Stochastic Modelling of Bacterial Dynamics:

Adhesion

&

Range Expansion

Dissertation

zur Erlangung des akademischen Grades
Doktor der Naturwissenchaften
der Naturwissenschaftlich-Technischen Fakultät
der Universität des Saarlandes

von

ERIK MAIKRANZ

Saarbrücken, 2021

Tag des Kolloquiums:

14.01.2022

Dekan:

Prof. Dr. Jörn Walter

Berichterstatter:

Prof. Dr. Ludger Santen

Prof. Dr. Dr. h.c. Heiko Rieger

Vorsitzende:

Prof. Dr. Karin Jacobs

Akademischer Beisitzer:

Dr. Jean-Baptiste Fleury

Abstract

Bacteria, as one of the three domains in the tree of life, play an important role in many phenomena such as biocorrosion, pipe clogging and infections. Since treatment with antibiotics or mechanical removal can be difficult, it is paramount to understand the initial attachment to a substrate and the subsequent colony growth. To this end, this thesis investigates first the adhesion process of *Staphylococcus aureus* by Monte Carlo simulations and helps to reveal that the bacterium uses different binding mechanisms on hydrophobic and hydrophilic substrates. On hydrophobic substrates, the bacterium's macromolecules bind freely. Subsequently, the bacteria show large cell-to-cell variation in adhesion forces but only small variations by repetitions with the same cell. On hydrophilic substrates, the macromolecules need to overcome a potential barrier. This leads to a comparable variability between repetitions with the same cell and the cell-to-cell variance. As a second model system, I investigated the competitive range expansion of microbial colonies with heterogeneous mechanical interactions by stochastic simulations. This is, for instance, realised by a network of piliated bacteria such as *Neisseria gonorrhoeae.* The simulations reveal that a heterogeneous susceptibility to division generated pushing significantly affects the competition dynamics of growing bacteria. Furthermore, homogeneous pushing leads to a small but standing variation of a disadvantaged subpopulation inside the expanding colony.

Zusammenfassung

Bakterien spielen in vielen Lebensbereichen wie beispielsweise Biokorrosion, Verstopfung von Rohren oder Infektionen eine zentrale Rolle. Da sich ihre Entfernung mittels Antibiotika oder mechanischer Methoden als schwierig erweisen kann, ist es wichtig die initiale Adhäsion und das nachfolgende Wachstum grundlegend zu verstehen. Zuerst wurde das Adhäsionsverhalten von *Staphylococcus aureus* auf hydrophilen und hydrophoben Oberflächen mittels Monte Carlo Simulationen untersucht. Es zeigt sich, dass die Adhäsion durch Makromoleküle der Zellwand vermittelt wird, von denen viele auf hydrophoben Oberflächen binden können. Dies resultiert in einer hohen Variabilität der Adhäsionskräfte innerhalb der Population, während Wiederholungen mit derselben Zelle ähnlich verlaufen. Auf hydrophilen Oberflächen selektiert jedoch eine Potentialbarriere stochastisch die bindenden Makromoleküle. Dies führt zu einer vergleichbaren Variabilität der Adhäsionskräfte zwischen Wiederholungen mit derselben Zelle und der Gesamtpopulation. Als zweites Modellsystem betrachtete ich das kompetitivem Koloniewachstum von pilierten *Neisseria gonorrhoeae* Bakterien. Zur Beschreibung dieser entwickelte ich ein minimales stochastisches Model von kompetitivem Koloniewachstum mit heterogenen mechanischen Wechselwirkungen. Die Simulationen zeigen, dass eine heterogene Suszeptibilität der Bakterien gegenüber Kräften, welche durch Zellteilung generiert werden, das kompetitive Wachstum maßgeblich beeinflussen.

Publications

Many results of this thesis are published in the following articles of peer-reviewed journals. Authors marked by † contributed equally.

Different binding mechanisms of Staphylococcus aureus to hydrophobic and hydrophilic surfaces
Nanoscale, 2020, 12, 19267-19275
Erik Maikranz†, Christian Spengler†, Nicolas Thewes, Alexander Thewes, Friederike Nolle, Philipp Jung, Markus Bischoff, Ludger Santen and Karin Jacobs

Theoretical modelling of competitive microbial range expansion with heterogeneous mechanical interactions
Physical Biology, 2021, 18, 016008
Erik Maikranz and Ludger Santen

Modelling bacterial adhesion to unconditioned abiotic surfaces
Frontiers in Mechanical Engineering, 2021, 7, 23
Christian Spengler†, Erik Maikranz†, Ludger Santen and Karin Jacobs

Some results are published as a preprint but not yet peer-reviewed.

The adhesion capability of S. aureus cells is heterogeneously distributed over the cell envelope
bioRxiv, 2021
Christian Spengler, Bernhard A. Glatz, Erik Maikranz, Markus Bischoff, Michael Andreas Klatt, Ludger Santen, Andreas Fery and Karin Jacobs

Contents

1 Introduction

Bacteria, as one of the three domains in the tree of life, play an important role in many applications. While they are productively used in bioreactors and wastewater treatment facilities they can clog pipes and increase biocorrosion [1, 2, 3, 4]. Furthermore, they can, among a plethora of other illnesses, give rise to implant-related infections on catheters, or joint prostheses or be the cause of sexually transmitted diseases such as gonorrhoea [5, 6, 7]. Since *Staphylococcus aureus*, as the main culprit for device-related infections, as well as *Neisseria gonorrhoeae*, as the causative agent of gonorrhoea, can be resistant to antibiotics, it is paramount to understand the initial steps of attachment to a substrate and subsequent colony growth [6, 8]. In the native setting, the aspect of colony growth and adhesion is imminently linked and certainly a better understanding of adhesion benefits a greater understanding of colony growth. While investigating the interplay of both is an interesting research direction this thesis investigates both aspects in two distinct model systems.

In the first model system, bacterial adhesion of *Staphylococcus aureus* is studied on abiotic surfaces, which while directly relevant for some applications, also provides a controlled system to gain insight into general principles of microbial adhesion. To this end, I develop and explore Monte Carlo simulations designed to mimic single-cell force spectroscopy experiments. These developments have been performed in close collaboration with the Jacobs group at Saarland University, which performed single-cell force spectroscopy experiments of *Staphylococcus aureus*. The resulting model is designed to provide a coarse-grained minimal description, which understands bacterial adhesion as primarily mediated by thermally fluctuating cell wall macromolecules. While in this approach deformations of the bacterium, typically associated with adhesion, are neglected, it allows modelling of adhesion to flat, curved and even rough surfaces when loading forces are negligible.

The second model system are microbial range expansion experiments on a homogeneous substrate. While range expansion experiments help to directly study the infection dynamics on a flat model substrate it also provides, due to short generation times, a toy model to investigate the link between pattern formation and evolutionary dynamics in general. In particular, I focus on the role of division induced pushing forces and the role of heterogeneous mechanical interactions. This is, for instance, realised by a network of piliated bacteria such as *Neisseria gonorrhoeae* which have been experimentally investigated by Zöllner et al. [9]. While my work has been solely stochastic simulations, they were designed to recreate those experiments.

The thesis is structured as follows: In chapters one and two I will introduce background information from Physics and Biology. This includes terminology, fundamental models and general background information, which are needed to understand the systems studied. Recent work, models, and the current understanding in the fields of bacterial adhesion and microbial range expansion will be presented in chapters four and five respectively. This will set my work, presented in chapters six and seven into the context of the present scientific research. The final chapter will summarize the achievements, draw conclusions from the presented work and will provide an outlook into possible future research programs combining both threads of investigation.

2 Fundamentals from Physics

This chapter introduces terminology, and basic models needed to understand the work developed in this thesis. Therefore, this chapter will serve as a brief reminder and references for a more in-depth presentation will be given. I start by introducing the classical models of colloidal science and contact mechanics. Then I introduce basic notions of stochastic processes, as well as polymer and surface growth models.

2.1 DLVO theory

Derjaguin, Landau, Verwey and Overbeek developed a theory for predicting the stability of the colloidal system nowadays named DLVO theory. It considers the repulsion of overlapping electrostatic double-layer forces around individual colloids and attractive van der Waals interactions.[1] Models for electrostatic double-layer forces can be complicated and in many instances not analytically solvable. I only present a simple model which considers a diffusive double layer in the limit of low surface potentials. This allows to formulate the concepts easily, while still providing qualitative explanations. If DLVO theory is to be applied in a quantitative manner these simplifications need to be dropped. The theory is nowadays applied outside the original scope and I will discuss the application to bacterial adhesion in section 4.2.1.

To describe the electrostatic potential around a single colloidal particle inside an electrolyte solution Poisson's equation from Electrostatics is combined with the Boltzmann

---

[1] Note that van der Waals interactions between bodies composed of different materials can also be repulsive. However, Hamaker [10] proved that the van der Waals interactions between identical materials inside a liquid are attractive as long as the liquid has no preferred orientation.

distribution for the charge density in an electrostatic potential (diffusive double layer). The resulting equation is the Poisson Boltzmann equation

$$\Delta\Phi = -\frac{e}{\epsilon}\sum_i z_i n_i e^{-\frac{z_i e\Phi}{k_B T}} \; [11].$$

Here Φ is the electrostatic potential, e the elementary charge, ϵ the absolute permittivity of the solution, z_i the valency and n_i the bulk concentration of the ith ion species. This non-linear equation can be linearized in the limit of $\frac{z_i e\Phi}{k_B T} \ll 1$ (Debye-Hückel approximation) to arrive at the Helmholtz equation

$$\Delta\Phi = \kappa^2\Phi \; ,$$

where $\kappa = \sqrt{\frac{2e^2 I}{\epsilon k_B T}}$ is the inverse Debye screening length and $I = \frac{1}{2}\sum_i n_i z_i^2$ the ionic strength. Consequently, this equation can be solved analytically for various geometries. An example is an infinite extended plane, where the potential decays $\propto e^{-\kappa x}$ and x is the distance perpendicular to the surface [11].

According to van Oss [12], the van der Waals interaction consists of the interactions between permanent-dipoles (Keesom interaction), permanent-dipoles and induced-dipoles (Debye interaction) and induced-dipole induced-dipole interactions (London interaction, dispersion force). All those interaction energies decay according to r^{-6}, where r is the distance of both molecules. On macroscopic scales, however, Hamaker [10] derived the van der Waals interaction energy between two macroscopic objects from a linear superposition of the molecular interactions as

$$V_{\text{vdW}}(r) \propto \int dV_1 \int dV_2 \frac{\rho(\vec{r}_1)\rho(\vec{r}_2)}{|\vec{r}_1 - \vec{r}_2|^6} \; .$$

This integral can be computed explicitly for various bodies, which results typically in a much weaker decay of the interaction energy than r^{-6}. For instance, the interaction energy between two semi-infinite plates decays as r^{-2} and therefore van der Waals interactions play a dominant role in colloidal science [12].

An important approximation for small separations, which can be performed for many body-body interactions is the Derjaguin approximation. In this approximation, the interaction energy is essentially approximated by the interaction energy between two parallel plates [11]. I want to emphasize that treating molecular interactions via simple superposition to arrive at the macroscopic interactions is not rigours and Lifshitz's created a more advanced theory, which uses the dielectric susceptibilities of the materials to compute the interactions [12]. The theory is, however, quite evolved and not necessary for a qualitative understanding and therefore I will not introduce it.

The DLVO theory combines the van der Waals attraction of colloidal particles with the repulsion from the overlap of the electrostatic double-layers. The balance between this attractive and repulsive interaction determines the typical distance between two colloids and therefore if the solution coagulates. As discussed earlier, the electrostatic potential and interaction energies are known. However, to describe the full thermodynamic behaviour also the entropy contributions need to be considered. This can be included by considering the Gibbs free energy[2]. The Gibbs free energy G of an electrostatic double-layer in the Debye-Hückel approximation is equal to $-\frac{1}{2}\sigma\Phi$ [13]. In the DLVO theory, the free energy of two double-layers is linearly combined with the van der Waals attraction [14]. If steric repulsion is neglected, this results in the limit of small separations in

$$G(x) = Ae^{-\kappa x} + \frac{B}{x^2}.$$

This shows (see figure 2.1) that at small distances the van der Waals attraction dominants, while at intermediate distances the electrostatic repulsion prevails. The repulsion can be tuned via the width of the electrostatic double-layer by changing the Debye screening length. Depending on this the free energy shows either only a primary minimum at small separations, which is followed by a potential barrier or an additional secondary minimum after the potential barrier. Inside the secondary minimum, the particles are only loosely attached and therefore if they can overcome the potential barrier by thermal motion, the system drops into the primary minimum and coagulates.

---

[2] Since for most applications fixed pressure and not volume is the more realistic situation Gibbs free energy and not Helmholtz free energy is used.

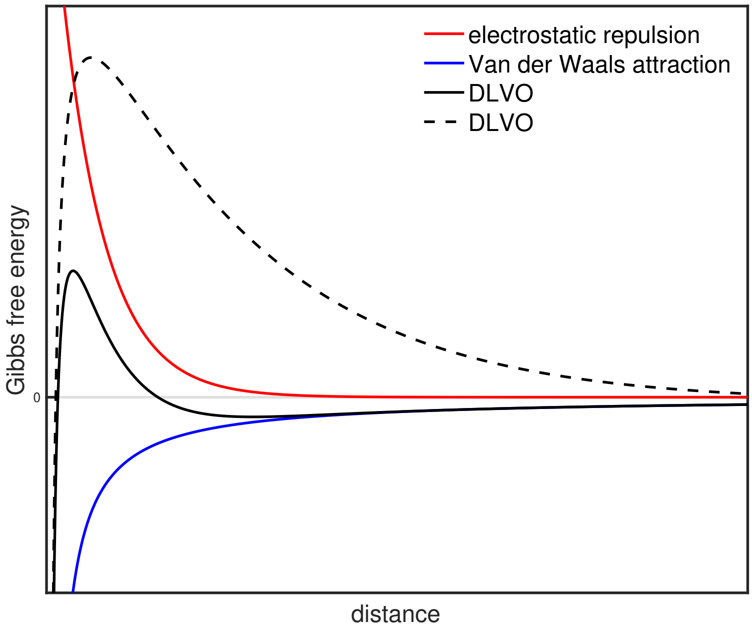

Figure 2.1: Gibbs free energy of pure electrostatic repulsion, van der Waals attraction and the DLVO free energy for two different Debye screening lengths.

2.2 Contact mechanics

Contact mechanics studies the mechanical behaviour of two continuous bodies in contact. General solutions for a plethora of axis-symmetric problems can be found in the book of Popov et al. [15]. This section, however, focuses on a sphere in contact with an infinite flat surface. I present the results for the Hertz model, which considers elastic friction less contact. Afterwards I extend the presentation to the JKR and DMT models which both address the role of adhesion forces in contact mechanics. I only sketch the derivations and refer for more details to the book of Popov [16].

The classical Hertz model considers an elastic sphere of radius R, reduced Young's modulus $E^* = \frac{E}{1-\nu^2}$, where E is the Youngs modulus and ν the Poisson ratio, pressing against a rigid flat surface.[3,4] If the sphere of radius R would penetrate up to depth d into the flat surface (see figure 2.2) the area inside the sphere below the surface needs to deform.

---

[3] If both bodies are elastic then $\frac{1}{E^*} = \frac{1-\nu_1^2}{E_1} + \frac{1-\nu_2^2}{E_2}$ where E_1, E_2 are the Youngs moduli and ν_1, ν_2 Poisson's ratios.

[4] Analogously the surface can be considered to be perfectly rigid and the sphere to be elastic. Closer to the applications in this thesis is the first situation.

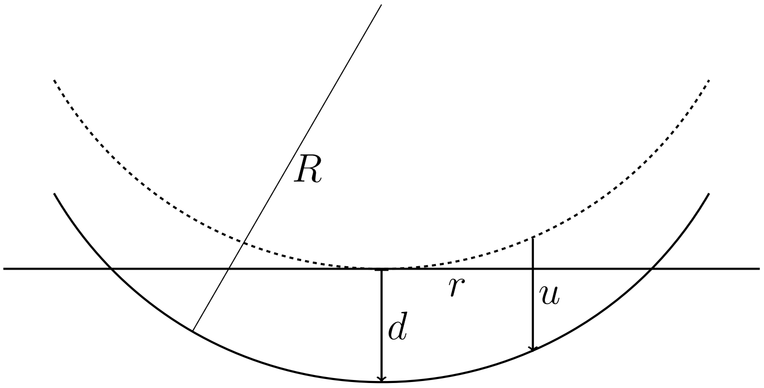

Figure 2.2: The geometry of the Hertz contact problem if a sphere of radius R would penetrate up to depth d into the flat surface.

From classical elasticity theory, the deformation into the direction normal to the surface is given by

$$u(x,y) = \frac{1}{\pi E^*} \iint \frac{p\left(x',y'\right)}{\sqrt{\left(x-x'\right)^2 + \left(y-y'\right)^2}} dx'dy' \ ,$$

where p is the pressure distribution arising from a force normal to the surface. For a known radial symmetric distribution the acting force is

$$F = 2\pi \int_0^a p(r)dr \ ,$$

where a determines the yet to be determined contact radius. Geometric considerations, in the limit of small indentation (i.e. $d \ll R$), show that the surface has to be displaced by

$$u = d - \frac{r^2}{2R} \ .$$

This determines the pressure field under the condition that the elastic energy[5] of the system is minimal at contact radius a. Following this procedure, the contact radius is computed to be $a_{\mathrm{Hertz}} = \sqrt{R \cdot d}$ and the acting force is

$$F_{\mathrm{Hertz}} = \frac{4E^*}{3R} a_{\mathrm{Hertz}}^3 \, .$$

Therefore, the force increases monotonously with increasing contact radius and shows without any external load a vanishing contact radius. This reflects the absence of any adhesion between the sphere and the substratum and predicts at the same time that no force is counteracting the separation of the sphere from the surface.

Derjaguin, Muller, and Toporov introduced the DMT model that incorporates adhesion. In their model, the Hertzian deformation remains valid, but it considers van der Waals forces acting outside the contact area. Therefore, the contact area remains the same as in the Hertz model but the acting force is derived by Maugis [17] to be[6]

$$F_{\mathrm{DMT}} = \frac{4E^*}{3R} a_{\mathrm{DMT}}^3 - 2\pi\gamma R \, .$$

Accordingly, the force increases monotonously with increasing contact radius as in the Hertz model, but for no external load, a finite contact radius of $\left(\frac{3\pi\gamma R^2}{2E^*}\right)^{\frac{1}{3}}$ is obtained (see figure 2.3). For contact radii smaller than this threshold the force becomes attractive until the maximal force $F_{\mathrm{DMT},A} = -2\gamma\pi R$ is reached. This maximal force is termed adhesion force and needs to be counteracted to separate the sphere from the surface.

Johnson, Kendall and Roberts extended the Hertz model to incorporate adhesion in a different way. The JKR model includes adhesion via a constant adhesive energy contribution inside the contact area. Using this energy contribution the pressure field is derived as before and the contact radius is determined by the equation

$$d = \frac{a_{\mathrm{JKR}}^2}{R} - \sqrt{\frac{2\gamma\pi}{E^*} a_{\mathrm{JKR}}} \, ,$$

---

[5] $\pi \int_0^a u(r)p(r)dr$

[6] In the Maugis model, a step function for the acting force is used. Strictly speaking, the derived force is not the adhesion force of the original DMT model and therefore sometimes denoted $F_{\mathrm{DMT\text{-}M}}$ [18, 19] .

where γ is the relative surface energy of sphere and surface. The acting force is derived to be

$$F_{\text{JKR}} = \frac{4E^*}{3R} a_{\text{JKR}}^3 - \sqrt{8\pi\gamma E^*} a_{\text{JKR}}^{\frac{3}{2}} \,.$$

Accordingly, the JKR model possesses, like the DMT model, a non zero contact radius for vanishing external load. For larger contact radii the force increase monotonously while below this critical contact radius the force becomes attractive but the strength varies non monotonously (see figure 2.3). The adhesion force obtained is $F_{\text{JKR},A} = -\frac{3}{2}\gamma\pi R$. Notably the JKR model has two solutions for negative indentation depths which indicates that the surface stays connected to the sphere, while the sphere is moving away from the surface. The surface detaches from the sphere once the minimal distance is reached. This minimal distance separates both branches of the curve, which depending on the starting indentation is chosen.

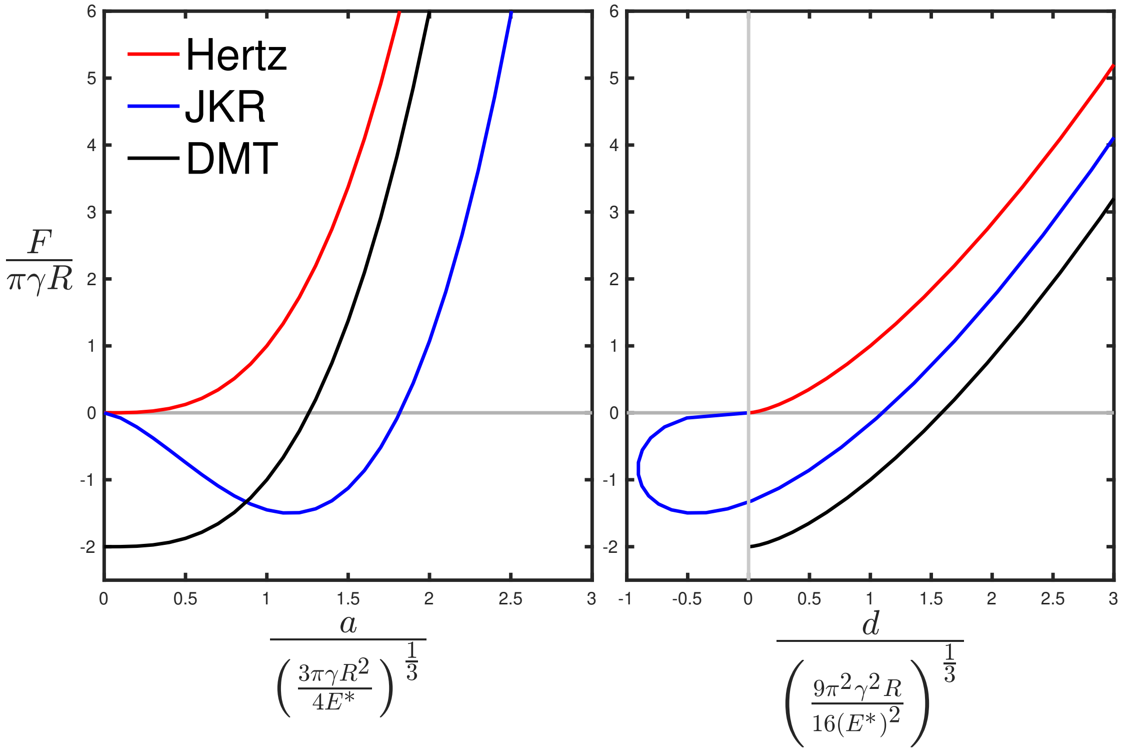

Figure 2.3: Normalized contact forces depending on the normalized contact areas (left) or indentation depths (right) of the Hertz, JKR and DMT model. The normalization is done according to Maugis [17]. The minimal value of the contact force is termed adhesion force.

These models are two examples taken from the vast literature about the role of adhesion in contact mechanics.[7] However, it was shown by Tabor [20] and Maugis [17] that these models are the limiting cases of a more general approach with a continuous transition from JRK to DMT model characterized by the Tabor Parameter $\mu = \sqrt[3]{\frac{R\gamma^2}{(E^*)^2 z_0^3}}$. Here z_0 denotes the equilibrium distance between atoms. While for soft materials with large surface energies and radii ($\mu \gg 1$) the JKR theory is the better approximation, for hard spheres with small radii and low surface energies ($0 < \mu \ll 1$) the DMT theory is [17].

2.3 Stochastic processes

Stochastic processes are a well-known approach to study and describe complex systems. While from the point of view of classical physics systems are perfectly predictable, the interactions of many parts in an often non-linear or even chaotic manner lead to a practical limit of this predictability [21]. Systems on macroscopic scales follow simple laws, like Boyle's law of a gas in a piston, or ordinary differential equations, e.g. population models like Lotka-Volterra. On mesoscopic scales, however, they are subject to fluctuations [21, 22]. Therefore effective descriptions by a few variables are chosen where the other degrees of freedom are effectively described as stochastic noise. With this the systems are explicitly or implicitly replaced by an ensemble of systems and a stochastic description is obtained [22]. The following introduction is based on the presentations of Gardiner [21] and Van Kampen [22].

A stochastic process is a collection of random variables S_t with a possible continuous set of indices t representing time.[8] This variable is defined by the family of distribution functions $p(s_n, t_n, \cdots, s_0, t_0)$[9] specifying the probability[10] of $(S_{t_0}, \ldots, S_{t_n})$ taking values $(s_0, \ldots, s_n)$ at times $(t_0, \ldots, t_n)$. Due to conditioning the distribution can be expressed as

$$p(s_n, t_n, \cdots, s_0, t_0) = p(s_n, t_n | s_{n-1}, t_{n-1}, \ldots, s_0, t_0) p(s_{n-1}, t_{n-1}, \cdots, s_0, t_0) \ , \qquad (2.1)$$

---

[7] For a review see for instance Ciavarella et al. [19].

[8] An equivalent view is that a stochastic process is a random variable that has functions as values.

[9] These finite-dimensional distributions, need to fulfil the Kolmogorov consistency conditions to define a stochastic process [23].

[10] In the case of continuous variables, it is a probability density. For the sake of brevity, I only refer to probabilities.

where $p(s_n, t_n|s_{n-1}, t_{n-1}, \ldots, s_0, t_0)$ is the probability of S_{t_n} having the value s_n if at times $(t_{n-1}, \ldots, t_0)$ $(S_{t_0}, \ldots, S_{t_{n-1}})$ had values $(s_0, \ldots, s_{n-1})$. A fixed time ordering $t_0 \leq t_1 \leq \cdots \leq t_n$ gives rise to interpreting the equation in terms of past events. The probability is then decomposed into conditional probabilities depending only on the past values and transitioning from the past into the current state. The most important classes of processes, which use this approach are Markov and Semi-Markov processes, where the transition probabilities only depend on the current state. They will be introduced in the next subsection and provide the workhorse for many applications. Since obtaining analytical expressions for the probability distributions is only possible in rare cases additionally sampling techniques are required.

2.3.1 Markov processes

A Markov process is defined by the property that if a given system is in a particular state, the transition into any other state only depends on the present state, i.e.

$$p(s_n, t_n|s_{n-1}, t_{n-1}, \ldots, s_0, t_0) = p(s_n, t_n|s_{n-1}, t_{n-1}) \ \forall n \ .$$

Then equation 2.1 can be fully decomposed into all transition probabilities $p(s_i, t_i|s_j, t_j)$ and the initial probability distribution $p(s_0, t_0)$. This can be used to derive the Chapman-Kolmogorov equation, a functional equation, relating all $p(s_i, t_i|s_j, t_j)$ to each other [21]. This equation limits the set of possible transition probabilities if the process is supposed to be Markovian. Often it is more convenient to derive a partial differential equation relating the probability distributions. I only present the situation where the system is characterised by a set of discrete variables in continuous time, i.e. continuous-time Markov chains (CTMC).[11]

Often it is easier to specify the short time probabilities of transitioning, i.e. transitioning rates, from state s to state s' in an infinitesimal time interval

$$\omega\left(s'|s, t\right) = \lim_{\Delta t \to 0} p(s', t + \Delta t|s, t) \ .$$

---

[11] For a mixed set of variables see Gardiner [21] who denotes the resulting equation "differential Chapman-Kolmogorov equation".

Using this definition the master equation

$$\frac{\partial p\left(s,t|s',t'\right)}{\partial t} = \sum_{s''}\left[\omega\left(s|s'',t\right)p\left(s'',t|s',t'\right) - \omega\left(s''|s,t\right)p\left(s,t|s',t'\right)\right] \tag{2.2}$$

$$p\left(s,t|s',t\right) = \delta\left(s-s'\right) \tag{2.3}$$

can be derived from the Chapman-Kolmogorov equation [21] . The master equation connects the conditional probability of being in sate s at time t when the system has been in state s' at t' with the probabilities of transitioning from all the states s'' into s and leaving sate s to an arbitrary state s''. Usually, a system is defined by imposing transition rates and it can be proven that every solution of the master equation, with reasonable rates, generates a set of probability densities, which satisfy the Chapman-Kolmogorov equation [21].

From equation 2.2 also

$$\frac{\partial p\left(s,t\right)}{\partial t} = \sum_{s''}\left[\omega\left(s|s'',t\right)p\left(s'',t\right) - \omega\left(s''|s,t\right)p\left(s,t\right)\right] \ , \tag{2.4}$$

which is an evolution equation for the single time probabilities, can be derived. Since this equation only relates single time-probabilities it does not fully define a Markov process. For this transition probabilities, i.e. two time-probabilities, need to be considered.

An important special case of Markov processes, which we only will consider in the following, are homogeneous Markov processes, i.e. processes with time-independent transition rates [21]. In this case, it is possible to study stationary processes, i.e. where the single time probabilities[12] are time-independent and $\frac{\partial p(s,t)}{\partial t} = 0\ \forall s$ is required. In the case of an ergodic Markov chain[13], it can be proven that all solutions tend independently of the initial conditions to the stationary solution [22]. In this case a sufficient, but not necessary, condition for stationarity can be identified from equation 2.4 as

$$\omega\left(s|s''\right)p\left(s''\right) = \omega\left(s''|s\right)p\left(s\right) \ .$$

This condition is named detailed balance. It states that there are no microscopic flows of probability between states and therefore models thermodynamic equilibrium. If a

---

[12] For the transition probabilities additional $p(s,t|s',t') = p(s,t-t'|s',0)$ is required [21].

[13] A Markov chain is ergodic if from any state every other state can in principle be reached.

system with a defined Hamiltonian H is given, this condition is equivalent to the equilibrium condition in statistical mechanics where a system is coupled to a heat bath with thermal energy β[14]. The probability is then given by the well known Boltzmann distribution

$$p\left(s\right)=\frac{e^{-\beta H(s)}}{Z}\ ,$$

where Z is the normalizing factor named partition function. Computing the partition function analytically, however, is for most systems not feasible and sampling techniques as introduced in section 2.3.2 are required.

At this stage it is worth emphasising that detailed balance is not a necessary condition for stationarity and systems in non-equilibrium steady states (NESS), i.e. states with a microscopic flow of probability, can be studied.

2.3.2 Sampling

Since obtaining analytical expressions for the probability distributions is only possible in rare cases sampling techniques are required. I briefly introduce how realisations of Markov chains in continuous time can be produced via the stochastic simulation algorithm (SSA). For this inverse transform sampling, which I introduce beforehand, is required. Then I introduce the Metropolis-Hastings algorithm, which constructs a Markov process to sample probability distributions, which are known up to the normalisation constant. This allows in particular to sample systems that are in thermodynamic equilibrium.

---

[14] $\frac{1}{\beta}=k_BT$

Inverse transform sampling

Let $F(x)$ be a known cumulative probability function[15], i.e. the probability that a random variable assumes a value smaller or equal x. Further, let U be a random variable uniformly distributed in [0,1). Then

$$X := F^{-1}(U)$$

is distributed according to F [24]. Here

$$F^{-1}(y) := \min\{x \in \mathbb{R} | F(x) \geq y\}$$

denotes the generalized inverse function. This definition is necessary to cover discrete and continuous situations at the same time. In the case of a continuous distribution, this reduces to the usual inverse function.

As an example consider the sampling of exponential distributed random variables with rate λ, i.e. the density is

$$\rho(t) = \lambda e^{-\lambda t} \ .$$

The cumulative probability function is

$$F(x) = \int_0^x \lambda e^{-\lambda t} \mathrm{d}t = 1 - e^{-\lambda x}$$

and its inverse

$$F^{-1}(x) = -\frac{1}{\lambda} \log(1 - x) \ .$$

Therefore $-\frac{1}{\lambda}\log(1-U)$ would sample the desired random variable. Since $1-U$ and U are both uniformly distributed in [0,1) it is, however, simpler to use

$$X = -\frac{1}{\lambda} \log(U) \ .$$

---

[15] This defines, up to measure zero, the probability density or in the discrete case the probability of a particular value.

In the case of a purely discrete distribution, each event can be mapped to a non-negative integer. The cumulative distribution then becomes

$$F\left(x\right) = \sum_{i=0}^{\lfloor x \rfloor} p_i \ ,$$

where p_i are the probabilities for the value i. The inverse is

$$F^{-1}\left(y\right) = x \Leftrightarrow \sum_{i=0}^{\lfloor x \rfloor - 1} p_i < y \leq \sum_{i=0}^{\lfloor x \rfloor} p_i \ .$$

Therefore inverse transform sampling for a discrete distribution consists of sampling U and finding the integer X such that

$$\sum_{i=0}^{X-1} p_i < U \leq \sum_{i=0}^{X} p_i$$

holds. This algorithm is also called tower sampling [25].

Stochastic simulation algorithm

Sampling of CTMCs with time-independent rates in continuous time is based on the fact that the transition probability densities, i.e. the probability densities of entering state s at time t if the system entered into state s' at time t_0 are distributed according to

$$\rho(s,t|s',t_0) = w(s|s')e^{-w(s|s')(t-t_0)} \text{ [26].} \tag{2.5}$$

According to Gibson and Bruck [26], three methods are utilizing the insight that the transition times to the next event are exponentially distributed:

1. First Reaction Method:
   If there are n transitions at time t_0 possible, this method generates transition times $T_1, \ldots T_n$ according to equation 2.5. Then the event of the smallest transition time is executed and system time propagated.

2. Direct Method:
   The following observations are used. The minimum of all transition times is again exponentially distributed i.e.

$$\min(T_1, \ldots, T_n) \sim \left(\sum_{i=1}^{n} w(s_i|s') \right) e^{-\left(\sum_{i=1}^{n} w(s_i|s')\right)(t-t_0)} \tag{2.6}$$

   and the probability that the transition into s_i was the fastest is

$$p_{s_i} = \frac{w(s_i|s')}{\sum_{i=1}^{n} w(s_i|s')} \ .$$

   The direct method utilises this and samples once the next reaction time according to equation 2.6 and the corresponding event independently by inverse transform sampling (tower sampling) as described before.

3. Next Reaction Method:
   This method samples not the time until the next transition but the absolute time for each event. This is equivalent to the first reaction method but allows to reuse already sampled event times. The method keeps track of all the event times and only samples new if the transition rates change. Reusing random numbers is in principle dangerous but Gibson and Bruck [26] show that in the case of exponential event times it is permissible.

The key issue in all presented algorithms is the efficient use and storage of already sampled event and transition times. While the next reaction method requires to sort the event times, the direct method requires constant updates of the probability distribution specifying possible events. Since in large systems this can become problematic numerous variants and approximation schemes are present in the literature [27].

Metropolis-Hastings algorithm

To sample from probability distributions, e.g. the Boltzmann distribution, where only the relative probabilities and not the normalization constant are known the Metropolis-Hastings algorithm can be used. The algorithm constructs a discrete-time Markov process, which in the limit of many steps follows the desired distribution $p(s)$. For this, the algorithm is constructed to fulfil detailed balance and each step consists of two sub-steps [25]:

1. if the system is in state s' propose a new state s with probability $A\left(s|s'\right)$
2. accept this proposed new state with probability $\min\left(1, \frac{p(s)A(s'|s)}{p(s')A(s|s')}\right)$

Since the acceptance probability only uses relative probabilities no normalisation constant is needed. There are two important special cases of this algorithm [25]:

- Metropolis:
  If the proposal distribution is symmetric i.e. $A\left(s|s'\right) = A\left(s'|s\right)$ and if the probability is given by the Boltzmann distribution, this reduces to the acceptance probability of the Metropolis-Algorithm $\min\left(1, e^{-\beta(H(s)-H(s'))}\right)$.
- Direct Sampling:
  If the proposal distribution is chosen as $A\left(s|s'\right) = p(s)\ \forall s'$, then the acceptance probability is always one. Note that this assumes the normalisation constant is known. The lack of this knowledge is the reason to use the Metropolis-Hastings algorithm in the first place.

Important to note is, that the Metropolis-Hastings algorithm generates a sequence of states which only in the limit of many steps converges to the desired distribution. The number of steps until convergence, whether it is independent of the initial condition, and if the algorithm samples the whole state space sufficiently depends on the energy landscape involved.[16] Dealing with these issues is part of the art of Monte Carlo simulations.

2.3.3 Semi-Markov processes

Let $(S_n)_{n\in\mathbb{N}}$ a collection of states and $(\tau_n)_{n\in\mathbb{N}}$ the corresponding waiting times between entering and leaving. The time entering a state is obtained by $T_n = \sum_{i=1}^{n} \tau_i$ and a Semi-Markov process is defined as

$$X_t = S_n : T_n \leq t < T_{n+1}$$

---

[16] Ergodicity, i.e. that a given algorithm samples all of the phase space independent of the initial condition can be analysed for given proposal distributions, however, systems can still be practically non-ergodic [25].

i.e. since the event time T_n, the system is in state S_n and leaves it at time T_{n+1} [28]. If the waiting times between transitions are exponentially distributed a time-homogeneous Markov process is obtained[17]. Therefore, Semi-Markov processes allow for non-exponential waiting times between transitions. This is useful in modelling, e.g. the division of a cell, where the time for cell division, immediately after a division is impossible. Sampling these models can be accomplished analogous to the next reaction method of Markov chains (see section 2.3.2), i.e. sampling and storing absolute event times for each event and executing the event with the closest time to the current time.

2.4 Polymer models

This section introduces some basic polymer models to set the worm-like chain (WLC) model into context. A polymer is described as N interacting units, called monomers, where the ith unit is connected to the $(i-1)$th unit by the bond vector $\vec{r}_i$ (see figure 2.4). I only present ideal chains, which neglect self-avoidance and correlations between distant[18] segments [29].

I will follow mostly the presentations of Rubinstein et al. [29] and Doi and Edwards [30], while reordering and condensing the material to what is needed to obtaining a basic understanding of polymer models, without being too detailed.

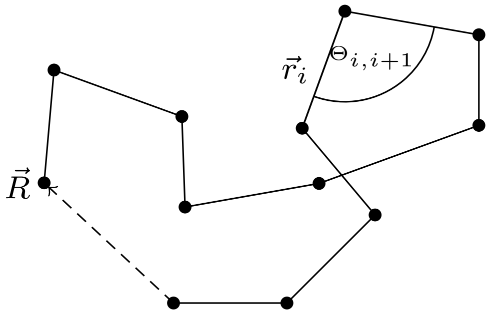

Figure 2.4: Exemplary polymer chain with vector $\vec{r}_i$ connecting the ith and $(i+1)$th monomer. $\Theta_{i,i+1}$ is defined as the angle between two consecutive monomers and $\vec{R}$ is the end-to-end vector.

---

[17] Note that Semi-Markov processes are also different from time inhomogeneous Markov processes, where the transition rates depend on global time. In a Semi-Markov process, the probability of leaving a state may depend on how long the system is in that particular state, while in Markov processes it does not.

[18] The distance is measured along the contour length.

The extension of the polymer can be characterized by the end-to-end vector which is simply given by $\vec{R} = \sum_{i=1}^{N} \vec{r}_i$. This is a stochastic quantity and can be characterized by the first and second moment as

$$\begin{aligned} \langle \vec{R} \rangle &= \sum_{i=1}^{N} \langle \vec{r}_i \rangle \\ \langle \vec{R}^2 \rangle &= \sum_{i=1}^{N} \sum_{j=1}^{N} \langle \vec{r}_i \cdot \vec{r}_j \rangle = \sum_{i=1}^{N} \sum_{j=1}^{N} \langle r_i r_j \cos \Theta_{ij} \rangle \ . \end{aligned}$$

Here, I introduced the bond length $|\vec{r}_i| = r_i$ and the angle Θ_{ij} between the monomers. I assume, in the following, that the bond length between the monomers remains constant i.e. $r_i = l \ \forall i$ and so the second moment can be expressed as

$$\langle \vec{R}^2 \rangle = l^2 N C_N \ ,$$

where C_N defines the Flory characteristic ratio $C_N := \frac{1}{N} \sum_{i=1}^{N} \sum_{j=1}^{N} \langle \cos \Theta_{ij} \rangle$.

The simplest polymer model is the freely joined chain (FJC), where $\langle \vec{r}_i \rangle = 0$ and no correlations between monomers, i.e., $\langle \cos \Theta_{ij} \rangle = 1 - \delta_{ij} \ \forall i, j$, are assumed. The first two moments can be evaluated to be

$$\begin{aligned} \langle \vec{R} \rangle &= 0 \\ \langle \vec{R}^2 \rangle &= l^2 N \ . \end{aligned}$$

A simple model that correlates the position of the monomers is the freely rotating chain (FRC), where the bond angle is fixed, i.e. $\vec{r}_i \cdot r_{i+1} = l^2 \cos \Theta \ \forall i, j$. Then

$$\langle \vec{r}_i \cdot \vec{r}_j \rangle = l^2 \langle \cos \Theta_{ij} \rangle = l^2 \cos^{|i-j|} \Theta$$

can be derived and the Flory characteristic ratio becomes

$$C_N = \frac{1 + \cos \Theta}{1 - \cos \Theta} + \frac{2 \cos \Theta}{N} \frac{1 - \cos^N \Theta}{(1 - \cos \Theta)^2} \ .$$

For $N \gg 1$ the second term is negligible and $\langle \vec{R}^2 \rangle \propto N$ is obtained. As in this ideal chain model, also other models display typically an exponential decay of their correlation over a characteristic length scale L_P, i.e.

$$\langle \cos \Theta_{ij} \rangle \propto e^{-\frac{l}{L_P}|i-j|} \ .$$

L_p is termed the persistence length and for those models $\langle \vec{R}^2 \rangle \propto N$ is obtained generally.

An important property of every ideal chain is, that it can be mapped to a FJC model by defining a new segment length b, the Kuhn-length, after which the monomers are mostly uncorrelated. The second moment of this new chain, consisting of M Kuhn segments of length b, simply is

$$\langle \vec{R}^2 \rangle = b^2 M \ ,$$

whereby matching moments and total length of the polymer M and b can be determined from the properties of the original ideal chain as $M = \frac{N}{C_N}, b = lC_N$.

The distribution of the end-to-end vector is generally unobtainable in a closed-form. However, if the segments are independent the distribution is a product of the individual bond vector distributions. If for instance the polymer is modelled as monomers connected by Hookean springs inside a heat bath, the energy contribution of each spring is quadratic in the relative distances of the monomers. Then utilising the bond vectors as coordinates leads to an independent Gaussian distribution of the individual bond vectors. This results in a Gaussian distributed (Gaussian chain) end-to-end vector. Due to the central limit theorem, the distribution of large chains ($N \gg 1$) is in general Gaussian and fully determined by the first and second moment.

2.4.1 Response to stretching

The response of a polymer to pulling can be derived by computing the free energy. For a general polymer model this is quite involved and for most models not analytically solvable.[19] Since for the FJC the energy is constant, a force $\vec{F} = f\hat{e}_z$ acting on the end-to-end vector can easily be computed. The resulting Gibbs free energy[20] is

$$G = -k_B T M \left(\ln 4\pi \sinh\left(\frac{fb}{k_B T}\right) - \ln \frac{fb}{k_B T} \right) \ .$$

From the thermodynamic relation $dG = -SdT - \langle \vec{R} \rangle \, df$ it is easy to see that

$$\langle \vec{R} \rangle = -\frac{\partial G}{\partial f} = bM \left(\cosh\left(\frac{fb}{k_B T}\right) - \frac{k_B T}{fb} \right) \ .$$

For small forces, a Hookean response with stiffness $\frac{3k_BT}{Mb^2}$ is obtained. Since this stiffness is temperature dependent the model is also named entropic spring.

2.4.2 Worm-like chain model

A simple model, which includes the bending rigidity between monomers, is the Kratky-Porod model. The Hamiltonian is given as

$$H = -\frac{\kappa}{2} \sum_{i=2}^{M} \frac{\vec{r}_{i-1} \cdot \vec{r}_i}{b^2} \ ,$$

where κ defines the bending rigidity. The worm-like chain (WLC) model is obtained in the continuum limit $b \to 0$, $Mb = L$ such that

$$H_{WLC} = \frac{\kappa}{2} \int_0^L \left(\frac{\partial \hat{t}}{\partial s} \right)^2 ds \ .$$

Here L is the contour length and $\hat{t}$ the tangential vector along the contour of the polymer. Therefore, the Hamiltonian describes the squared curvature integrated along the polymers contour. Note that a linear term would treat positive and negative curvatures differently, and therefore needs to vanish for isotropic bending. Hence, the WLC model

---

[19] Stretching at the end-to-end vector gives a linear contribution of each bond vector to the energy. For models with quadratic contributions to the energy, like Gaussian chains, this additional term can be easily treated by completing the square. For a general treatment see Doi and Edwards [30].

[20] Rubinstein et al. [29] give the helpful remark that analogous to the isothermal-isobaric ensemble (constant T,p), here the force and not the extension is constant and that is why the Gibbs free energy and not Helmholtz free energy is used. Note that in this analogy the signs of p and f do not match.

can also be understood as the approximation for an isotropic bending polymer up to second order in the curvature.

For the second moment

$$\langle \vec{R}^2 \rangle = \int_0^L \int_0^L \langle \hat{t}(s) \cdot \hat{t}(s') \rangle \, \mathrm{ds'ds} = \int_0^L \int_0^L e^{-\frac{|s-s'|}{L_p}} \mathrm{ds'ds} = 2L_pL\left(1 - \frac{L_p}{L}\left(1 - e^{-\frac{L}{L_p}}\right)\right)$$

is obtained [29, 31] . The same result can be found in the continuum limit ($l \to 0$, $\Theta \to 0$, $Nl = L$, $\frac{l}{\Theta^2} = \frac{L_p}{2}$) of the FRC model [29]. Two interesting limits are

$$\langle \vec{R}^2 \rangle = \begin{cases} L^2 & , L \ll L_p \\ 2LL_p & , L \gg L_p \end{cases}$$

showing that for polymers, which are much longer than the persistence length the results of the FJC with $b = 2L_p$ is recovered and for contour lengths much shorter than the persistence length rigid rod behaviour is retained. The result $b = 2L_p$ is generally obtained in the continuum limit of the FRC model and therefore generally used. From the second moment, the relation of the persistence length to the bending rigidity can be found to be $L_p = \frac{\kappa}{k_BT}$ [32].

To obtain the full distribution for the shape of the polymer the partition function $Z(\hat{t}, s|\hat{t}_0,0)$ needs to be computed. Since H is a functional the integration in the partition function runs over all possible tangential vectors, i.e. it is a path integral. This can be formally solved but is quite evolved and details can be found in the book by Yamakawa and Yoshizaki [31].

I am, however, primarily interested in the response of the polymer, when a force $\vec{F}$ acts onto one end of the polymer. This can be incorporated into the Hamiltonian by adding $-\int_0^L \vec{F} \cdot \hat{t}\mathrm{ds}$. The resulting path integrals are hard to treat but a Schrödinger type equation, with a fitting initial condition, can be derived for the partition function

$$\begin{aligned} \partial_s Z(\hat{t}, s|\hat{t}_0,0) &= \left[\frac{\vec{F}}{k_BT} \cdot \hat{t} + \frac{k_BT}{2\kappa}\Delta_{\hat{t}}\right] Z(\hat{t}, s|\hat{t}_0,0) \\ Z(\hat{t},0|\hat{t}_0,0) &= \delta(\hat{t} - \hat{t}_0) \text{ [33].} \end{aligned}$$

This can generally only be solved numerically, but Marko and Siggia [34] developed an approximation for a force acting along a single axis, i.e. $\vec{F} = f\hat{e}_z$. The approximated force under stretch $l = [\vec{r}(L) - \vec{r}(0)] \cdot \hat{e}_z$ is

$$f\left(\frac{l}{L}\right) = \frac{k_B T}{2b}\left(4\frac{l}{L} - 1 + \frac{1}{\left(1 - \frac{l}{L}\right)^2}\right) ,$$

where b is the Kuhn length computed as $b = 2L_P = \frac{2\kappa}{k_B T}$.

2.5 Surface growth

Many phenomena like the interface of a fluid in a porous medium, flame fronts, growing bacterial colonies, the deposition of snowflakes or even atoms in molecular beam epitaxy can be viewed and understood as growing surfaces [35]. While the application to bacterial colony growth will be made explicit in chapter 5, this section provides a brief introduction to the ideas and methods of this broad field of research. For a more extensive introduction see the monographs of Barabási and Stanley [35], Krug [36] and the review article of Halpin-Healy and Zhang [37].

This section presents how growing surfaces can be characterized by kinetic roughening. How universal, i.e. independent of the particular model in question, the characterisations are and introduces the important Eden model.

2.5.1 Kinetic roughening

Consider as an example for growth a deposition process with a fixed system size L as illustrated in figure 2.5a.[21] The global interface width[22], characterising the roughness of the surface, is defined as the root mean square fluctuations of the height, i.e. $w(t) = \sqrt{\langle \overline{\left(h - \overline{h}\right)^2} \rangle}$ [38]. Here $\bar{\cdot}$ denotes the spatial average over the entire system in a single realisation and $\langle \cdot \rangle$ the averaging over different realisations. This roughness, as shown in figure 2.5b, typically grows as a power law, with growth exponent β, until a

---

[21] In cellular growth the building blocks are generated by the already existing surface via cell division and do not enter from outside the system.

[22] One can also define a local interface width, where the average is performed over a window of size $l \leq L$. If the exponents are distinct from the exponents derived from the global width the process is said to displays anomalous roughening [38].

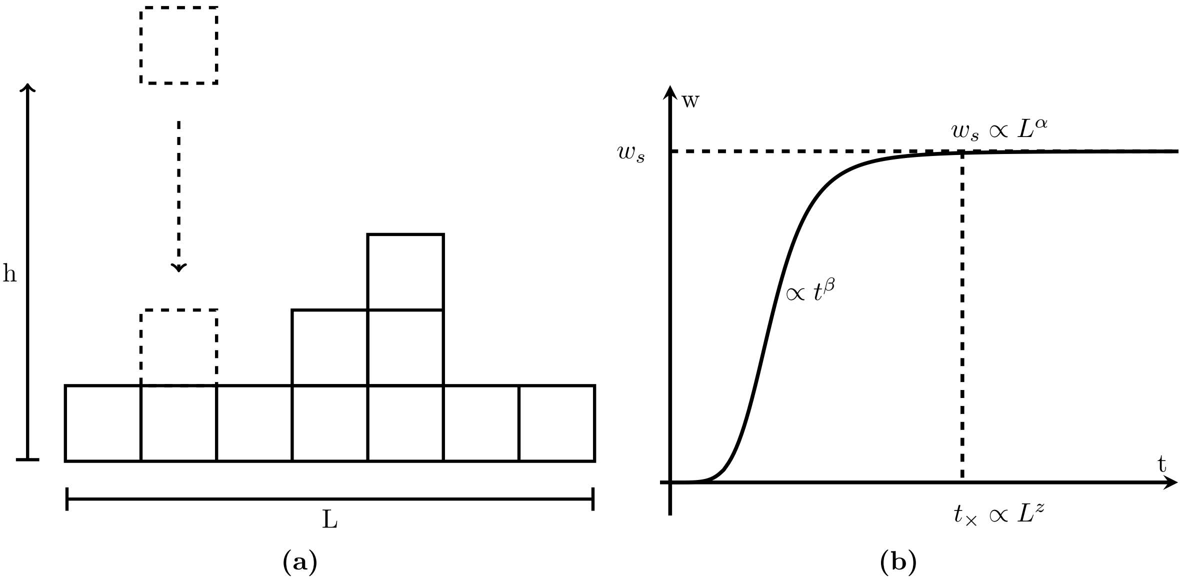

Figure 2.5: **(a)** Illustration of a possible surface growth model, with system size L and surface height h. Inspired by a figure from Barabási and Stanley [35]. **(b)** Typical behaviour of the surface roughness, characterized by the interface width w, displaying kinetic roughening with a typical roughness after the crossover time $t_\times$.

crossover time $t_\times \propto L^z$, with dynamic exponent z is reached. After this, the width has saturated to $w_s \propto L^\alpha$ with roughness exponent α.

These observations[23] can be summarized in the Family-Vicsek scaling relation $w(t) = L^\alpha f(\frac{t}{L^z})$, where f is a scaling function

$$f(x) = \begin{cases} x^\beta & , \ x \ll 1 \\ \text{const.} & , \ x \gg 1 \end{cases} .$$

The exponents are not independent of each other and from continuity at the crossover time $z = \frac{\alpha}{\beta}$ can be derived for all growth processes fulfilling the Family-Vicsek scaling. These exponents are universal for certain growth processes and can be predicted from stochastic continuum equations introduced in the next subsection. These neglect details of particular growth models in question and allow the classification of growth processes into different universality classes.

---

[23] In practice, this has to be confirmed by collapsing the data, under appropriate rescaling, for different system sizes to a master curve.

Universality classes and stochastic continuum equations

Stochastic continuum equations allow the description of growth processes in the hydrodynamic limit. According to Barabási and Stanley [35], the equations have the form

$$\frac{\partial h(\vec{x},t)}{\partial t} = G[h,\vec{x},t] + \eta(\vec{x},t) \ ,$$

where $\vec{x} \in \mathbb{R}^d$ is the spatial coordinate, G is a to be defined growth function and η is a white noise term[24] satisfying $\langle \eta(x,t) \rangle = 0$, $\langle \eta(x,t)\eta(x',t') \rangle = 2D\delta(t-t')\delta(x-x')$.

The function G can be construed by various symmetry principles nicely presented by Barabási and Stanley [35]. The invariance under time, height and space translation rules out explicit t, h, x dependences, such that G needs only be expanded in various combinations of $(\nabla^n h)$ and $(\nabla h)^m$. Further symmetries as, rotation, inversion of growth direction and up/down symmetry rule out further combinations. Since this equation represents a hydrodynamic limit, it can be shown from scaling arguments and dynamic renormalisation analysis that acceleration terms and spatial derivatives of higher order are negligible compared to lower ones [35].

The lowest order term that fulfils all requirements is $\nabla^2 h$ giving rise to the Edwards-Wilkinson (EW) equation

$$\frac{\partial h(\vec{x},t)}{\partial t} = \nu \nabla^2 h + \eta(\vec{x},t) \ .$$

From this equation, the exponents can be predicted via scaling or renormalisation and are found to be $\alpha = \frac{2-d}{2}$, $\beta = \frac{2-d}{4}$, $z = 2$ [35].

Barabási and Stanley [35] give a nice overview of further universality classes and their critical exponents. The important Kardar-Parisi-Zhang (KPZ) universality class will be introduced in the next section in detail. It is important to emphasise that not solely the symmetry principles determine the universality class, but also the interaction range and spatial-temporal correlations play a role. In particular, coloured or quenched noise, i.e. where the time dependence of the noise is replaced by the dependence of the surface height, can change the scaling exponents.

---

[24] Also coloured noise can be studied.

KPZ equation

Since the Edwards-Wilkinson equation, presented in the previous section, is linear it does not incorporate that the growth of a surface is typical along its local surface normal. If the height grows proportional to the amplitude of the surface normal $\sqrt{1+(\nabla h)^2} \overset{|\nabla h| \ll 1}{\approx} 1+\frac{1}{2}(\nabla h)^2$, the $(\nabla h)^2$ term needs to be considered to incorporate lateral growth [35, 39]. Adding this non-linear term to the EW equation leads to the Kardar-Parisi-Zhang (KPZ) equation

$$\frac{\partial h}{\partial t} = \nu \nabla^2 h + \frac{\lambda}{2}(\nabla h)^2 + \eta(\vec{x}, t) \ .$$

From this the scaling exponents for $d = 1$ can be computed as $\alpha = \frac{1}{2}$, $\beta = \frac{1}{3}$, $z = \frac{3}{2}$, but are for arbitrary dimensions unknown [35, 39].

The KPZ equation has connections to many fields of physics and mathematics like stochastic heat equation, random matrix theory, totally asymmetric simple exclusion process (TASEP) or directed polymers in random media [37, 39]. A nice recent introduction to these connections and the KPZ equation as a whole is given by Takeuchi [39]. Of note is, that strictly speaking the equation as given here is mathematical not well defined and the successful efforts for a rigorous definition have gained Hairer a Fields Medal in recent years [40]. In one dimension even analytic expressions for the height process can be found for various initial conditions [39, 40, 41, 42]. The solution, in the limit $t \to \infty$, is

$$h = v_\infty t + \mathrm{sgn}(\lambda)\,(\Gamma t)^{\frac{1}{3}}\,\chi \ ,$$

where v_∞, Γ are non-universal constants and χ is a random variable. The distribution of χ depends on growth geometry, i.e. flat or curved growth, and is given by the Tacy-Widoms distribution known from random matrix theory [40, 43].[25]

These results are quite remarkable and many models like the polynuclear growth model (PNG), the TASEP, which can be mapped to a growth model, belong to the KPZ universality class. Most importantly for this thesis, the Eden model, introduced in the next section, belongs to the KPZ universality class [39, 43, 44].

---

[25] For curved growth, this is the distribution for the largest eigenvalue of a random matrix from the gaussian unitary ensemble (GUE), while for flat growth it is from the gaussian orthogonal ensemble (GOE).

2.5.2 Eden model

Consider an arbitrary lattice, where occupying sites are forming the surface. For the following discussion the distinction between surface sites (occupied sites), periphery sites (surface sites with at least one empty next neighbour site) and perimeter sites (all empty sites which have at least one surface site as a next neighbour) are important. There exist three Eden models[26] named A, B and C in the literature [35, 36, 45]. To easily distinguish all models I present how the next site, which will be added to the surface, is chosen [36, 45]:

- A: chose a random perimeter site
- B: chose a random perimeter site proportional to the number of periphery sites i.e. proportional to its connections to the surface
- C: chose a random periphery site, and then choose one random site from its empty nearest neighbours

Unfortunately different publications define the B and C model in the opposite way warranting caution while consulting the literature [44, 46]. Since in this thesis, I am concerned with cellular growth the elements driving the surface growth are the occupied sites, and therefore the Eden C model is the most appropriate.

The Eden models, in one dimension, grown from a line shows the growth exponent $\beta = \frac{1}{3}$ consistent with KPZ universality. However, clusters grown from a single site, show radial growth and $\beta = 1$ for large grown clusters [46]. This deviation from the KPZ exponent is due to the lattice anisotropy producing for large clusters a diamond shape rather than a circle [46, 47]. If an off-lattice Eden Model is used the KPZ exponent is retained [48, 49]. In radial growth, the surface height is measured as the radial extension relative to a reference point. The choice of reference point, e.g. the origin or the centre of mass of the periphery sites, changes the growth exponent. Ferreira Jr and Alves [49] nicely demonstrated that the fluctuations of the centre of mass are non-negligible even in the asymptotic limit and only the origin as a reference point leads to KPZ scaling. Furthermore, Alves et al. [44] showed that the radial distribution function agrees with the Tracy-Widom distribution, for the on- and off-lattice model. This provides further evidence that the Eden model is indeed in the KPZ universality class.

---

[26] The original Eden model is B [45].

3 Fundamentals from Biology

In this chapter, I introduce terminology and general background information from Biology, that is needed to evaluate the content of this thesis. This includes information on the bacteria studied, basic information on biofilm formation and how bacterial adhesion is related to it, as well as a short introduction to the terminology and concepts of evolutionary population genetics.

3.1 Biofilm formation

Biofilms are not simply passive assemblages of cells that are attached to surfaces but are structurally and dynamically complex biological systems [5]. They develop after cells adhere to a surface, and then, depending on the bacterial strain, produce extracellular polymeric substances (EPS) that provide a matrix for further adhesion [3, 7]. Biofilms provide the main mode of living for many species and can be used in many engineering processes such as bioreactors or wastewater treatment systems [3]. However, their presence in some applications reduces efficiency. On ship hulls, they increase hydrodynamic friction, while in pipes they reduce flow rates of fluids and increase biocorrosion causing a reduced efficiency of cooling water systems in the processing industry [1, 2, 4]. If bacteria enter the body they can form biofilms as well and give rise to various infections, e.g. gum disease and device related infections on catheters or joint prostheses [5]. One main source of device-related infections is *Staphylococcus aureus* (*S. aureus*), which will be introduced in section 3.2.1 in more detail [7].

A nice overview of biofilm formation is given by Arciola et al. [7], which I briefly summarize (see figure 3.1b): Biofilm formation starts after the initial attachment of single bacteria or cellular aggregates to the surface, which at first can be reversible, but becomes irreversible, after excretion of EPS material [3]. This process termed adhesion can occur on abiotic, like implants, or biotic, like epithelia, materials. The adhesion typically takes place on preconditioned surfaces, i.e. they are covered by extracellular matrix (ECM) proteins and immune protein components when submerged in physiological fluids. The main ECM proteins bacteria bind to are collagens, fibronectins and fibrinogen and the class of proteins binding to them will be introduced in section 3.2.1. Since I study adhesion to abiotic, unconditioned surfaces the adhesion is unspecific and I will not go into details of specific protein-ligand binding.

After the initial adhesion cellular aggregation is enhanced by EPS production. Among the EPS molecules are exopolysaccharides, proteins, and extracellular DNA, wall teichoic and lipoteichoic acids forming the biofilm matrix [7]. The resulting microcolony grows, excretes more EPS and remodels the existing matrix until a mature biofilm is formed. This mature state, however, is not stationary and parts of the biofilm can disperse, where bacteria return to a planktonic lifestyle and become a source for further infections in the body.

In the mature stage, the biofilm is hard to treat by antibiotics. Three mechanisms have been proposed to explain this increased resistance. First, the extracellular matrix provides a barrier to biocidal agents and effectively dilutes them inside the biofilm. Second, the physiological state of bacteria is heterogeneous inside the biofilm, i.e. some regions of bacteria are dormant. Third, the presence of a small population of persister cells, which are immune against the antibiotic itself [5].

Since treatment of mature biofilms is challenging, it is paramount to stop biofilm formation in the early stages or inhibit/reduce initial bacterial adhesion altogether. To this end, bacterial adhesion, which I will present in chapter 4, has to be understood in detail.

3.2 Surface composition of bacteria

In this thesis, I will mention several experiments involving different microbial strains like baker's yeast *Saccharomyces cerevisiae* (*S. cerevisiae*), *Bacillus subtilis* (*B. subtilis*), *Escherichia coli* (*E. coli*), *Staphylococcus aureus* (*S. aureus*), *Staphylococcus carnosus* (*S. carnosus*) and *Neisseria gonorrhoeae* (*N. gonorrhoeae*). Therefore, this section will introduce the main structural features that are of interests to the experiments. These are only the surface structures and while these structures are present in many species,

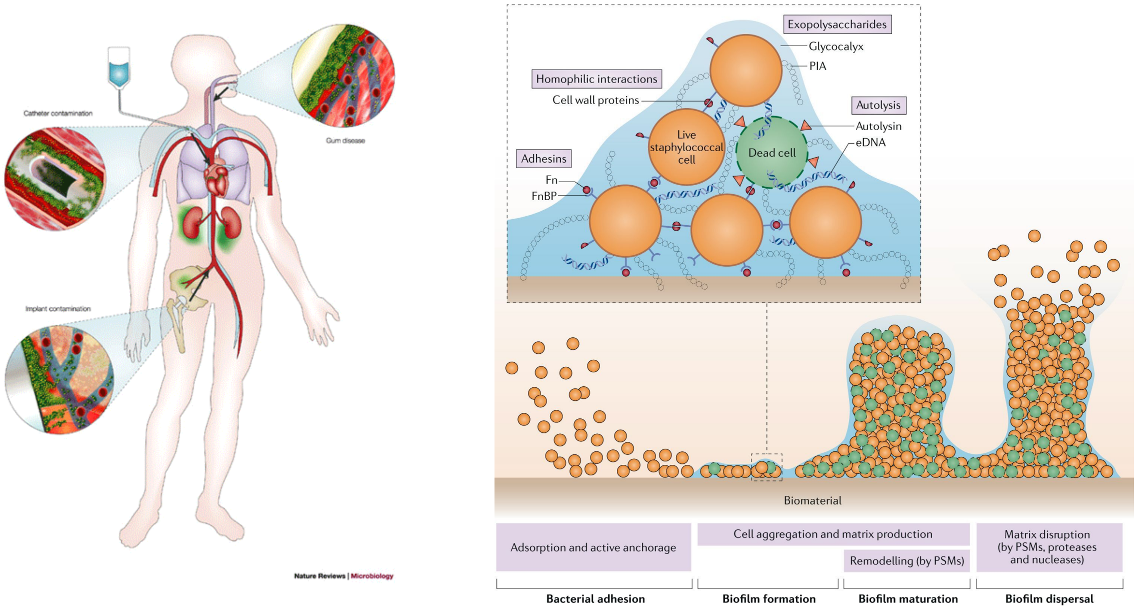

(a) (b)

Figure 3.1: **(a)** Illustration of possible infections, e.g. gum disease, catheter and implant contamination. Reprinted from Hall-Stoodley et al. [5] with permission from Springer Nature. **(b)** Phases of biofilm formation reprinted from Arciola et al. [7] with permission from Springer Nature.

I will focus for specifics on the gram-positive bacterium *S. aureus* and gram-negative bacterium *N. gonorrhoeae*.

3.2.1 Staphylococcus aureus

The surface structure of *S. aureus* is a highly complex and dynamic structure depicted in figure 3.2. It can be decomposed into three layers, which are as follows: Counting from the inside to the outside of the cell, the first layer consists of a lipid membrane. It contains freely moving proteins but also anchors polymers called lipoteichoic acids (LTAs), which protrude into the third layer. The second layer consists primarily of a highly cross-linked network of polymers termed peptidoglycan and is named the cell wall. This network covalently anchors wall teichoic acids (WTAs) and cell wall anchored proteins (CWAs). Additionally, it loosely binds ionically "secretable expanded repertoire adhesive molecules" (SERAMs). These acids and proteins extend into the third layer named capsule, which is composed of capsular polysaccharides such as poly-N-acetyl-D-glucosamine (PNAG).[1]

---

[1] The absence of a further lipid bilayer around the capsule classifies *S. aureus* as gram-positive.

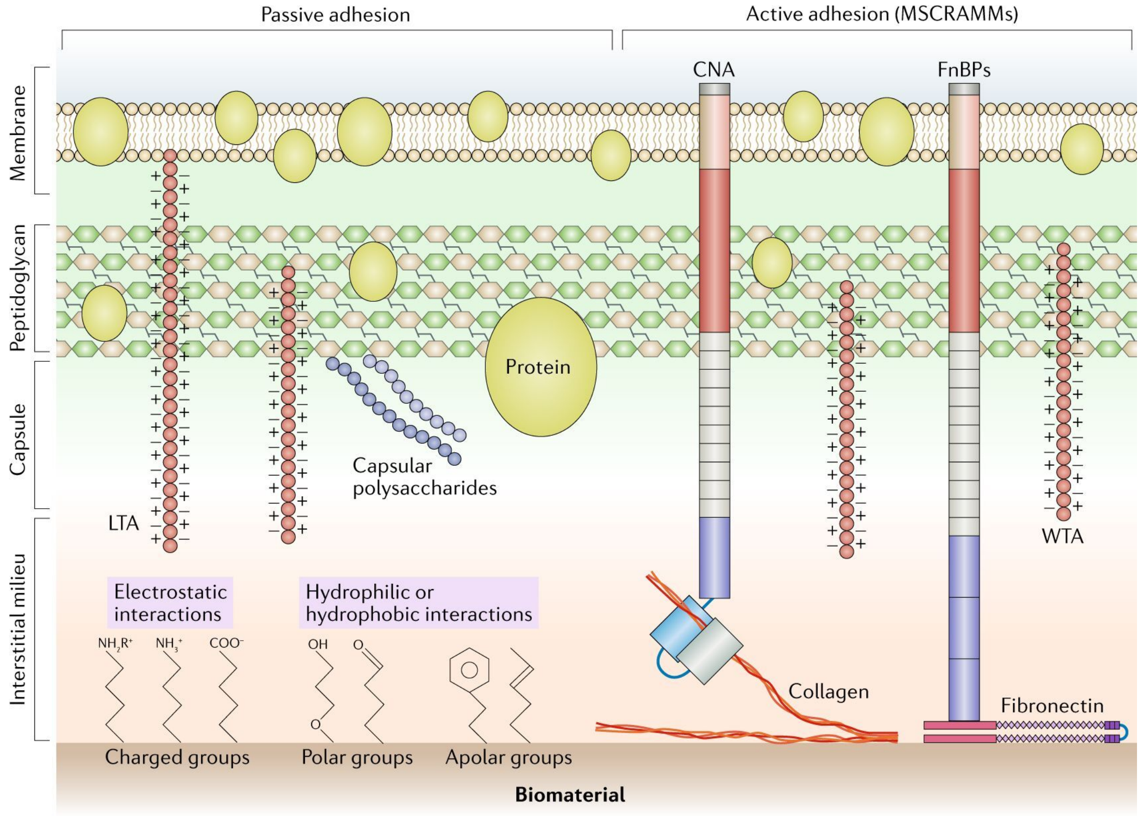

Figure 3.2: Cell wall composition of *S. aureus* illustrating structures important for adhesion to biomaterial. Reprinted from Arciola et al. [7] with permission from Springer Nature.

All these macromolecules contribute to the adhesion to abiotic and biotic material by electrostatic, hydrophilic or hydrophobic interactions. CWAs constitute a broad family and *S. aureus* expresses up to 24 different proteins depending on growth conditions [8]. First, it was thought that the binding to host surfaces is mediated by a class of CWAs termed "microbial surface components recognizing adhesive matrix molecules" (MSCRAMMs), which are binding to ECM proteins like collagens, fibronectins and fibrinogen. These CWA proteins, however, have additional functions to promote adhesion [8]. MSCRAMMs show functional redundancy, such that several MSCRAMMs bind to the same ECM protein and Foster et al. [8] proposed to classify them according to motifs derived from structure-function analysis. In this definition MSCRAMMs belong to one of four groups defined by molecular structure and resulting ligand-binding mechanism. Since this thesis is not concerned with specific binding to ECM proteins, I will refrain from giving more details and refer to the article of Foster et al. [8] for a nice overview. Important to note is, that for characterizing adhesion, it is not enough to characterize the individual adhesion contributions of distinct classes of CWAs. For instance, Staphylococcus Surfaces Protein G (SasG) can mask the binding of other CWAs [50].

In chapter 4, I will review the literature on adhesion to abiotic surfaces showing that adhesion can be understood in terms of the individual responses of macromolecules to stretching. Therefore, I give a brief introduction to the mechanical response of CWAs, in particular the G5-E repeat family, one of the four families defined by Foster et al. [8]. The aforementioned SasG belongs to this class and consists of G5-E-domains with individual folded lengths of 7 and 4.5 nm, respectively [51]. Several G5-E-domains repeat to form a continuous rode-like structure of various possible lengths (see figure 3.3) [50, 52]. Gruszka et al. [51] analysed the mechanical response of various SasG proteins to stretching. They found that the G5 and E subunits unfold, in the range of tested pulling speeds ($200-5000~\frac{\mathrm{nm}}{\mathrm{s}}$), independently of each other. The forces needed to unfold the E and G5 domains depend linearly on the retraction velocities and are 0.25 nN and 0.42 nN at a retraction velocity of $800~\frac{\mathrm{nm}}{\mathrm{s}}$, respectively. By fitting a WLC model, as introduced in section 2.4.2, with a persistence length of 0.4 nm to the force-stretch curves, they obtained a length increase of 14 nm and 21 nm for the E and G5 domain after unfolding [51].

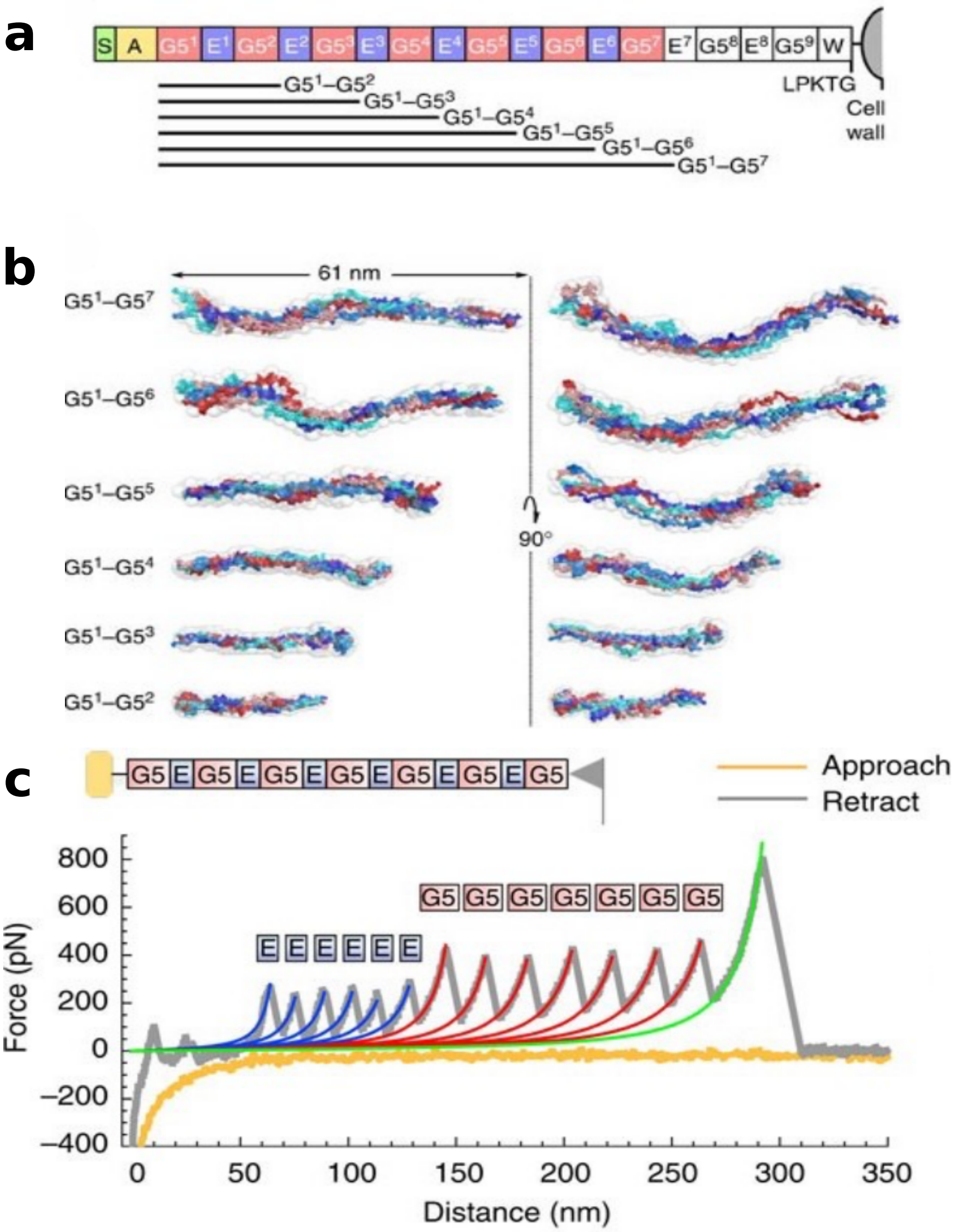

Figure 3.3: **(a)** Various length combinations of G5-E domains give rise to **(b)** continuous rode like structures of various sizes. **(c)** A WLC fit determined by persistence length of 0.4 nm to a retraction experiment, shows the independent unfolding of individual E and G5 domains. The figures are adapted from Gruszka et al. [51] under the CC BY 4.0 license.

3.2.2 Neisseria gonorrhoeae

The surface structure of *N. gonorrhoeae* consists of two lipid bilayers, with peptidoglycan in between.[2] While I presented the surface structure of *S. aureus* in quite some detail for *N. gonorrhoeae*, only the super molecular structure of type IV pili (T4P) is in this thesis of importance.

Type IV pili are 5-8 nm thick, have several micrometres in length and span from the inside to the outside of the cell (see figure 3.4). They withstand pulling forces greater than 100 pN and possess persistence lengths of about 5 μm [53]. They can actively be contracted and extended by polymerising and depolymerising subunits of the protein pileE. This poly-/depolymerisation is independently catalysed by assembly (pilF) and retraction (pilT) ATPases [53]. While this process is well-understood, I am only concerned with the consequences on the bacterial colony level. For details on the molecular mechanisms see Hospenthal et al. [54] and Craig et al. [53].

T4P structures meditate DNA uptake from the surrounding and enable surface mobility of the bacterium termed “twitching mobility”. They establish liquid-like order in growing colonies and govern their fusion dynamics [55, 56]. Furthermore, they mediate cell sorting in colonies with heterogeneous T4P interactions and determine the dynamics in competitive growing colonies [9, 57]. How these structures influence the sorting of strains with different piliation and the influence on competitive growth will be discussed in detail in chapter 5.

To understand the colony dynamics, it is important to know that the pilE gene producing the polymeric subunit of the T4P machinery undergoes phase- and antigenic variation. While these terms are used vaguely, according to Van Der Woude and Bäumler [58] phase variation refers in general to “a reversible switch between an ‘all-or-none’ (on/off) expressing phase”. This is distinguished from genetic noise by the existence of a genetic or epigenetic mechanism, which allows this variability to be inheritable. Antigenic variation refers, according to Van Der Woude and Bäumler [58] to “the expression of functionally conserved moieties within a clonal population that are antigenically” distinct. In the case of *N. gonorrhoeae* this is realised by silent pilS genes, which partially recombine into the pilE locus. The expression of this locus, depending on the state, leads to bacteria with normal, reduced, or no expressed T4P [9, 58].

---

[2] The second lipid bilayer classes *N. gonorrhoeae* gram-negative.

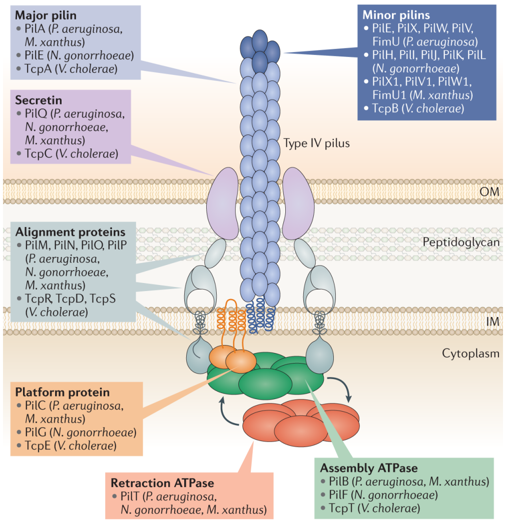

Figure 3.4: Illustration of the super molecular T4P machinery. The detailed T4P composition depends on the species. Reprinted from Craig et al. [53] with permission from Springer Nature.

3.3 Evolution and population genetics in well-mixed conditions

This section will introduce terminology and concepts from population genetics, which might not be too familiar to physicists. Population genetics studies how the frequency of genes change inside a population. Genes in population models refer to a variable that encodes a specific trait [59]. Different variants, termed alleles, can be present in a population. I only consider asexual reproduction of haploid organisms, i.e. each individual carries only one instance of each allele and passes this on to its offspring. Furthermore, this section only considers well-mixed growth, present in e.g. growing microbes in a liquid flask or a fixed spatial environment with high individual mobility. In such environments, all individuals compete with each other and spatial structure is not important. For the presentation, I mostly use the review articles of Blythe and McKane [59] and Korolev et al. [60] while reorganizing and focusing the material to set range expansion experiments, where the spatial structure is important into context. Range expansion experiments, however, will be presented in chapter 5.

3.3.1 Genetic drift

Consider a population with two alleles at its carrying capacity, i.e. the environment cannot sustain a larger population. At a fixed rate one individual of the population is chosen and replaced randomly by another allele. The choice and replacement occur proportional to the frequency inside the population, i.e. no selection bias for any allele is considered. This model is termed the Moran model and describes the fluctuations, named genetic drift, of the allele frequency. A master equation as described in section 2.3.1 can be constructed [59, 60]:

Let N be the maximal sustained population and n the number of individuals with allele one. Then the master equation reads

$$\frac{dp(n)}{dt'} = p_{2\to 1|n-1}p(n-1) + p_{1\to 2|n+1}p(n+1) - \left(p_{1\to 2|n} + p_{2\to 1|n}\right) p(n) \; \forall 0 < n < N,$$

where $p(n)$ is the probability of having n individuals of allele one at time t', and $p_{2\to 1|n}$ is the probability of choosing an individual of allele two and replacing it with an individual of allele one when n individuals of allele one are present. The other quantities are analogously defined. Note that $p_{1\to 2|n} + p_{2\to 1|n} \neq 1$, since one can choose an allele of type one and replace it with the same type. However, in the master equation only the contributions which lead to a change in the allele frequency are considered. In the Moran model, as described above, the transition probability is

$$p_{1\to 2|n} = \frac{n}{N}\frac{N-n}{N} \; ,$$

where $\frac{n}{N}$ is the probability of choosing one individual with allele one when n individuals have allele one, and $\frac{N-n}{N}$ is the probability of choosing one individual with allele two to replace it. Obviously $p_{1\to 2|n} = p_{2\to 1|n}$ and the master equation without boundaries is given as

$$\frac{dp(n)}{dt'} = \frac{n-1}{N}\frac{N-(n-1)}{N}p(n-1) + \frac{n+1}{N}\frac{N-(n+1)}{N}p(n+1) - 2\frac{n}{N}\frac{N-n}{N}p(n) \; \forall 0 < n < N \; .$$

In this equation, the time t' is measured in the typical time scale of the replacement process. To compare to experiments it is, however, more useful to measure time t in terms of the typical generation time τ_g of individual cells, i.e. $\frac{t}{\tau_g} = \frac{t'}{N}$.

In principle, this non-linear equation can be solved by a generating functional approach, but more often the interest is in the large population limit where an expansion in $\frac{1}{N}$ can be performed. In the limit of $N \gg 1$, the master equation can be approximated[3] by a diffusion equation

$$\frac{\partial p(f)}{\partial t} = \frac{1}{N\tau_g} \frac{\partial^2}{\partial f^2} f(1-f)p(f) \ , \tag{3.1}$$

where the allele frequency $f = \frac{n}{N}$ is considered to be a continuous parameter. The approximation neglects the terms $\mathcal{O}\left(\frac{1}{N^2}\right)$ and needs to be completed with absorbing boundary conditions at $f = 0, 1$. To characterise the frequency distribution, typically the mean frequency $F(t) = \langle f(t) \rangle$ and the average heterozygosity $H(t) = 2 \langle f(t)(1 - f(t)) \rangle$ are considered. The governing equations can be derived from equation 3.3.1 as

$$\begin{aligned} \frac{dF}{dt} &= 0 \\ \frac{dH}{dt} &= -\frac{2}{N\tau_g} H \ . \end{aligned}$$

These equations show that the mean frequency, consistent with the absence of selection, does not change in time. The average heterozygosity $H(t) = F_0(1 - F_0)e^{-\frac{2t}{N\tau_g}}$, however, decays exponentially fast to zero. This indicates fast extinction of one allele, while the other gets fixed i.e. it spreads through the full population. Particularly this occurs even if initially both alleles are present equally ($F_0 = 0.5$).

3.3.2 Selection

Selective advantage can be incorporated in the Moran model by introducing weights into the probability of replacing the alleles. Let, as before, n be the number of individuals with allele one. The probability for choosing an individual with allele one for replacement remains $\frac{n}{N}$ but the probability for replacing it with allele two becomes $\frac{w_2(N-n)}{w_1 n + w_2(N-n)}$ such that

$$p_{1\to 2|n} = \frac{n}{N} \frac{w_2(N-n)}{w_1 n + w_2(N-n)} = \frac{n}{N} \frac{N-n}{\frac{w_1}{w_2} n + (N-n)} \ .$$

---

[3] This is the well-known Kramers-Moyal expansion up to second order.

Since this depends only on the fraction $\frac{w_1}{w_2}$, w_2 is set to one. Note that in the case of $w_1 = 1$ this reduces to the case without any selection. In the next step, the fitness difference s is introduced as $w_1 = 1 + s$. For $s \geq 0$ allele one is advantageous while for $-1 \leq s < 0$ it is deleterious. This leads to a non-linearity in the transition probabilities. To deal with this, the weak selection limit $s \ll 1$ and the diffusion approximation is performed which results in

$$\frac{\partial p}{\partial t} = -\frac{s}{\tau_g}\frac{\partial}{\partial f}f(1-f)p + \frac{1}{N\tau_g}\frac{\partial^2}{\partial f^2}f(1-f)p \ , \tag{3.2}$$

where terms $\mathcal{O}\left(\frac{1}{N^2}\right), \mathcal{O}\left(s^2\right)$ and $\mathcal{O}\left(\frac{s}{N}\right)$ have been neglected. Equations for the mean frequency and average heterozygosity can be derived, but the equations do not close, i.e. the equation for the average heterozygosity depends on the third moment and so on. However, from equation 3.2 it is obvious that for $sN \gg 1$ the genetic drift can be neglected, and the process becomes deterministic[4]. The mean frequency then satisfies

$$\frac{dF}{dt} = sF(1-F) \ .$$

Therefore the advantageous allele grows logistically, i.e. $F(t) = \frac{F_0}{F_0 + (1-F_0)e^{-\frac{st}{\tau_g}}}$ and spreads through the population until it reaches fixation. This rapid growth is called selective sweep [59]. If the allele is, however, introduced via mutations, its initial frequency is small and genetic drift, which might lead to extinction, cannot be neglected. It can be shown that the fixation probability of an allele with initial frequency f_0 is

$$p_{\text{fix}} = \frac{1 - e^{-\frac{2Nsf_0}{\tau_g}}}{1 - e^{-\frac{2Ns}{\tau_g}}} \ .$$

For a single mutant $f_0 = \frac{1}{N}$ which leads in the limit $N \to \infty$ to

$$p_{\text{fix}} = \begin{cases} 1 - e^{\frac{-2s}{\tau_g}} \approx 2\frac{s}{\tau_g} & , 0 < \frac{s}{\tau_g} \ll 1 \\ 0 & , s \leq 0 \end{cases} ,$$

---

[4] Accoring to Gardiner [21] an equation of the form $\frac{\partial p(f,t)}{\partial t} = -\frac{\partial}{\partial f}A[f,t]p(f,t)$ has the solution $p(f,t) = \delta\left(f - F[f_0,t]\right)$ where $F = \langle f \rangle$ and is determined by $\frac{dF}{dt} = A[F,t]$.

since for deriving the equation the weak selection limit is considered. Also, the meantime for fixation can be computed as

$$\langle T_{\text{fix}} \rangle = \frac{2\tau_g \ln N}{s} \text{ [59].}$$

Therefore, a single mutation spreads relatively fast through a homogeneous population and genetic drift only plays a role for small populations.

4 Bacterial adhesion

While there exists extensive literature about bacterial adhesion to abiotic and biotic surfaces respectively, this thesis only concerns itself with adhesion to abiotic unconditioned surfaces. Therefore, this chapter, which got reworked in major parts into a mini-review with the title **Modelling bacterial adhesion to unconditioned abiotic surfaces** published in Frontiers in Mechanical Engineering, 2021, 7, 23 by Christian Spengler, **Erik Maikranz**,[1] Ludger Santen and Karin Jacobs [61], presents only the work on abiotic surfaces.

First, I introduce the typical experimental set-ups namely flow chamber and single-cell force spectroscopy (SCFS) experiments. Second, I present approaches that treat the bacterium-substratum interaction in a continuous manner. These approaches originating in colloidal science are surface thermodynamics and (x)DLVO theory. These models do not consider any deformations of the bacterium or surface and thus I present approaches from contact mechanics which take the deformation of the bacterium into account. I will discuss what these approaches can and cannot describe and present experimental studies and models which show the need for treating the bacterium-substratum interaction in a non-continuous manner i.e. mediated by individual macromolecules. Since my work presented in chapter 7 is based on one of those models I will present it in some detail.

4.1 Experimental set-ups

Bacterial adhesion is predominately studied with two kinds of experimental set-ups. In flow chamber experiments, bacteria are flushed into a chamber and after letting them settle onto a surface, the bacteria which do not adhere are washed off. The set-up allows to study many bacteria at the same time and allows to quantify how many

---

[1] The first authorship is shared by Christian Spengler and me.

bacteria stick to a given material under controlled shear flow conditions tangential to the surface. The flow conditions perpendicular to the surface are, however, uncontrolled and no repetitions with individual cells can be performed.

To perform repeated more controlled sticking experiments with the same bacterium single-cell force spectroscopy experiments are performed. In these experiments, individual cells are glued to a cantilever and moved towards or away from the surface. The deflection of the cantilever allows measuring the forces acting on the cell. The measurements result in force separation curves, as shown schematically in figure 4.1. A typical experimental approach and retraction cycle for *S. aureus* is as follows: The cantilever starts approaching the surface until the bacterium comes into the interaction range of the surface potential.[2] This leads to a sudden force increase named the snap-in.[3] The cantilever continues moving towards the surface until a prescribed force, the force trigger, is reached. After reaching this threshold the retraction starts, where the cantilever is moved away from the surface. The minimum of the retraction curve is named adhesion force and the last kink before measuring zero forces defines the rupture length, where the cell loses its last connection to the surface. Notice that real experimental curves do not need to follow the monotonous pattern shown here but can be highly irregular. Furthermore, it is noteworthy that the approach and retraction curves do not overlap and therefore display hysteresis.

SCFS allows studying the adhesion process natively by using a minimal force trigger.[4] Additionally possible deviations from a Hertzian contact can be investigated by choosing a force trigger such that the bacterium is pressed onto the surface. This is sometimes termed loading. Also, time-dependent strengthening of the adhesive contact can be investigated by introducing a prescribed waiting time before starting the retraction. I like to emphasize that the nature of the experiments allows to repeat the approach/retraction curves with the same bacterium. This allows to investigate the role of stochasticity in the adhesion process and in particular to distinguish its role from the variability inside a diverse population.

---

[2] The macromolecular appendages on the outside of the cell wall come into the range of the surface potential.

[3] The existence of a snap-in depends on the surface and bacteria used. For an explanation of the snap-in see section 4.3.

[4] Since the movement of the cantilever pushes the bacterium through eventual energy barriers a floating bacterium would experience, even SCFS experiments with minimal force triggers do not fully mimic flow chamber experiments.

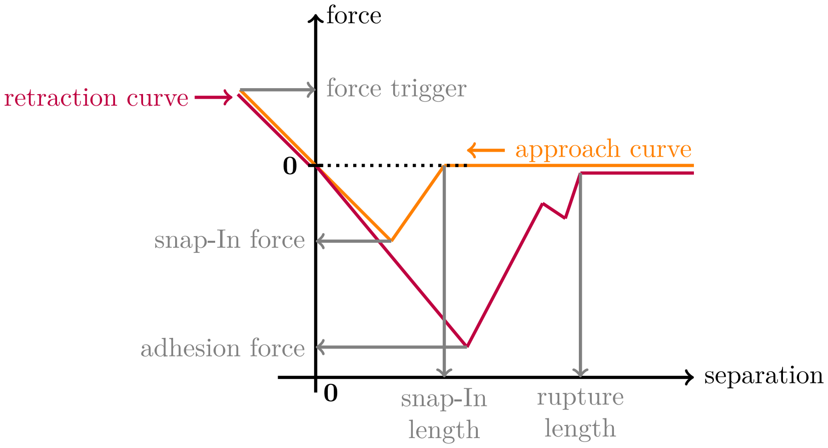

Figure 4.1: Schematic SCFS approach and retraction curves. The approach curve displays the typical snap-in behaviour, with corresponding separation and force which are named snap-in length and snap-in force respectively. The retraction curves are distinct from the approach curves (hysteresis). Its minimum is named adhesion force, while the last point of contact is termed rupture length. Note that the approach and retraction curves at large separations are both supposed to be zero.

By combining flow-chamber and SCFS experiments, the adhesion process can be studied on a cell individual as well populational level in various environmental conditions and on many substrates. For the comparison of individual studies and different experimental set-ups, not only well-defined growth conditions but also the characterization of surfaces is vital. These surfaces need not only be characterized by their roughness and surface hydrophobicity but also the underlying bulk substrate can influence the adhesion via van der Waals interactions and needs to be characterized [62].

4.2 Continuous interactions with the substratum

4.2.1 Approaches from colloidal science

The main goal of colloidal approaches is to predict if a given bacterium will stick to a particular surface. Its attempted scope of applicability are flow chamber experiments and therefore the theory does not attempt to describe a full approach retraction cycle of SCFS. The problem is phrased in the language of thermodynamics, where the Gibbs free energy is minimized in equilibrium. This renders the theory inherently reversible and hence it can't take eventual strengthening of adhesive bonds into account. An excellent review on thermodynamic and DLVO approaches has been conducted by Perni et al. [3] which I want to summarize briefly:

The simplest approach is surface thermodynamics, where the Gibbs free energy is computed as

$$G = A\left(\gamma_{BS} - \gamma_{BL} - \gamma_{SL}\right) \ .$$

Here A denotes the contact area and $\gamma_{BS}, \gamma_{BL}, \gamma_{SL}$ are the interfacial energies between bacterium-solid, bacterium-liquid and solid-liquid respectively. These energies can be determined from contact angle measurements via the Young–Dupre equation. Since the Gibbs free energy needs to be minimised in equilibrium, this model predicts adhesion for $\gamma_{BS} < \gamma_{SL} + \gamma_{BL}$. According to Perni et al. [3], this approach only works in some cases and is generally regarded as too simplistic.

A different approach to predict bacterial adhesion is DLVO theory, as introduced in section 2.1, but applied to the bacterium-plane geometry. Because various publications use different approximations for van der Waals and electrostatic double-layer forces respectively, I refrain from formulating the Gibbs free energy explicitly but discuss the situations which may occur in principle (see figure 4.2).

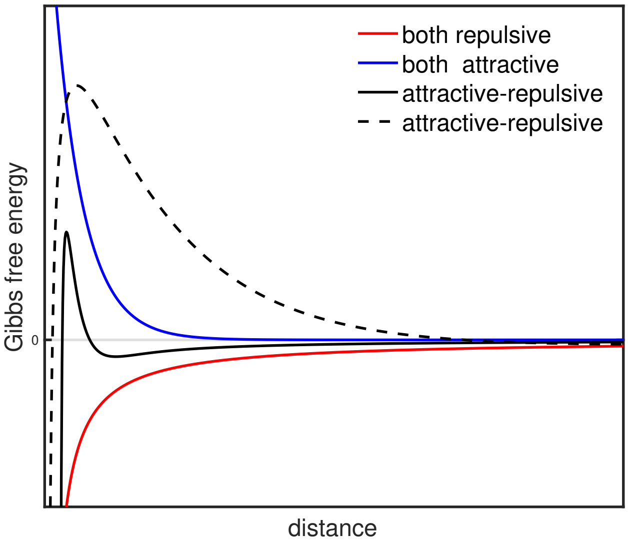

Figure 4.2: Schematic possibilities for the Gibbs free energies. Note that the different amplitudes were chosen to distinguish the curves easier and are not representative of the interactions.

If both potentials are either repulsive or attractive the potential is monotonically decreasing or increasing. Therefore, the energy is minimized at a maximal distance or zero distance from the surface.[5] In the latter case, adhesion is achieved. If, however, one of the interactions is repulsive and the other attractive the potential is non monotonic and displays a minimum close to the surface. Depending on the potential also a secondary minimum might be observed. As discussed for colloids in section 2.1 strong adhesion is achieved inside the global minimum and weak adhesion is achieved inside the secondary minimum. On experimental time scales the weak adhesion is visible as reversibility of the adhesion process.

DLVO theory, however, neglects acid-base interactions and the presence of polymers on the bacterium surface. These additional interactions have been considered in various cases and the extension is termed xDLVO theory. Acid-base interactions are extremely short-range i.e. they display an exponential decay [12]. Polymeric interactions, modelling steric repulsion of polymer brushes close to interfaces, are incorporated by de Gennes equation [63]. These extensions change quantitatively the interaction potential but the qualitative picture remains the same.

Perni et al. [3] list studies where (x)DLVO theory has been successfully applied to predict adhesion. However, he also list an equal amount of studies where this fails. The explanation for failure has according to Perni et al. [3] been attributed due to the neglection of shear forces and the underlying assumption of homogeneous bacterial surface composition.

While, a picture of heterogeneous surface composition, not only on the population but single-cell level becomes more evident, I want to emphasize that all colloidal models assume continuous interactions of the entire bacterium with the surface. This description neglects the stochasticity and the responses of individual macromolecules in the adhesion process, which section 4.3 will show are essential for certain aspects of bacterial adhesion.

As already mentioned (x)DLVO approaches have not been developed to describe the full approach retraction cycle of SCFS experiments. However, if the derivative of the Gibbs free energy is assumed to be the force experienced by the bacterium then, since the derivative is unique, no hysteresis can be observed. Furthermore, the interaction forces decay fast, such that the experimental observed snap-in on lengths of about 50-100 nm cannot be explained by DLVO forces [64]. The xDLVO theory, however, introduces the length of the polymer brush as an additional parameter and therefore could incorporate a snap-in on the observed length scale.

---

[5] Note that exclusion due to Pauli exclusion is not considered here.

4.2.2 Deformation and contact mechanics

Contact mechanics as described in chapter 2, considers the forces and deformations of two bodies in direct contact. The Hertz, JKR and DMT models introduced in section 2.2, have been initially developed for understanding the stress distribution and adhesion forces of non-biological particles in contact with a flat surface. The models assume homogeneity of the particles but nevertheless have been used to extract information about the elastic moduli of bacteria [65, 66]. Bacteria, as described in chapter 1, however, possess a non-homogeneous surface structure with cellular appendages, a cross-linked peptidoglycan layer and a lipid bilayer. While there exist many models in the contact mechanics which consider inhomogeneous particles they require numerical solutions and therefore previously know parameters such as the Youngs modulus [67, 68].

Chen et al. [65] developed a simple model which incorporates inhomogeneity and only assumes that the contact of the bacterium is formed by a cylinder whose volume does not change under loading. Chen et al. [65] applied this model to SCFS experiments with various bacterial strains[6] and the extracted Young's moduli are in the 8 to 50 kPa range and therefore a hundred times smaller than what would be extracted from a Hertz model. Furthermore, Chen et al. [69] applied this model to quantify the influence of nanoscale deformations on the adhesion force. To this end, the authors compared the adhesion forces of two wild type *S. aureus* strains on a glass surface with corresponding mutant strains lacking penicillin-binding proteins [69]. The penicillin-binding proteins play an important part in cross-linking the peptidoglycan and cells lacking these proteins are expected to be more easily deformable. Chen et al. [69] used loading forces in the 1−9 nN range and obtained adhesion forces in the 0.5−6 nN regime. The corresponding mutant strain showed for most loading forces an increased force accompanied by a height reduction due to deformation of about 100−200 nm and therefore Chen et al. [69] concluded that deformations influence the adhesion forces significantly. However, for one strain and high loading, the wild type strain showed higher adhesion forces than the mutant. Furthermore, by assuming that the short-range forces are proportional to the contact area, Chen et al. [69] extracted the van der Waals component of the adhesion force and found that it is three times larger for the more deformable strain. Therefore including deformation forces via contact mechanics into the description of bacterial adhesion seems necessary for loading forces of about 1nN.

---

[6] *S. aureus*, *S. epidermis* and *S. salivarius*

The Hertz, JKR and DMT model do not intent to describe a full approach and retraction cycle. While it is possible to consider the full approach and retraction cycle and solve the equations of contact mechanics for various interactions numerically Jasevičius et al. [70] choose a different approach. Jasevičius et al. [70] used the deformations forces of the DMT model when the bacterium is in contact with the substratum. To reproduce the snap-in van der Waals forces of a sphere-plane geometry (in the Derjaguin approximation) are added. Since the DMT model considers van der Waals interactions while in contact this is a straight forward extension. However, the snap-in force and distance are fitted from experiments and not obtained from the constitute equations of DLVO theory. Additional, the authors consider repulsive electrostatic double-layer forces and steric repulsion forces of polymer brushes at the surface of the bacterium. Phrased loosely, this model combines the Hertzian contact model, xDLVO theory and an ad hoc snap-in mechanism. To recreate the adhesion hysteresis and energy dissipation mechanism including plastic deformation is considered.[7]

Recently, this model has been extended to mimic flow chamber experiments and determined if a given bacterial strain will adhere to a given surface [72]. For this, the authors included viscous drag and an initial velocity into the model. Thus they predict that the bacterium *S. aureus* will stick to a glass surface. While this prediction is true, it was necessary to provide the model with many parameters, including the experimental adhesion force previously measured. Therefore, it remains elusive how this model can predict the adhesion capabilities of a wide range of strains to varying surfaces. Up to the point of publication, no such study was, to my knowledge, conducted. Furthermore, because the model considers the bacterial population to be homogeneous and that the adhesion process of an individual cell can be described by non-stochastic continuous interactions, it has the same disadvantages as the colloidal approaches.

4.3 The need for non-continuous interactions

Sjollema et al. [73] monitored in a flow chamber via a camera the displacement of several bacterial strains after they settled. The method, termed vibration spectroscopy combined with SCFS experiments, showed that with increased adhesion force the movement parallel to the surface decreased. These observations combined with an in silico

---

[7] To reproduce hysteresis energy dissipation or plastic deformation is sufficient. Note that this is necessary because the DMT model is used. Models from contact mechanics can show hysteresis without explicit dissipation or plastic deformation [18, 71].

model leads Sjollema et al. [73] to conclude, that the bacterium binds to the surface via multiple reversible binding tethers. These repeatedly detach and attach to the surface without detaching all at the same time. This study was extended by van der Westen et al. [74] via internal reflection microscopy, to determine if adhering bacteria also exhibit variations perpendicular to the surface. For bacteria without cellular appendages, van der Westen et al. [74] compared their results with predictions from DLVO theory and found that the potential displays a primary and secondary minimum where the potential barrier between both was considered to be too high to overcome by Brownian motion. On hydrophobic substrates, the authors observed asymmetric fluctuations inside the secondary minimum, where the amplitudes are independent of ionic strength but fitted to the width of the minimum.[8] For cells with fibrils[9] the bacteria showed symmetric fluctuations with five times smaller vibrational amplitudes. These amplitudes were independent from the hydrophobicity of the substrate and the tested ionic strength of the solution. This leads van der Westen et al. [74] to distinguish between "floating" and "tether-coupled" adhesion, where the first is dominated by the thermal motion inside the secondary minimum predicted from DLVO theory, while in the latter case the bacterium is bound to the surface by tethers.

A different set of studies showing the failure of (x)DLVO theory has been conducted by Thewes et al. [64, 75]. First Thewes et al. [75] demonstrated that SCFS experiments with the bacterium *Staphylococcus carnosus* (*S. carnosus*) display on hydrophobic surfaces force-distance curves which are characteristic for each bacterium. These curves are independent of their adhesion history and retraction velocities probed ($400-2400\ \frac{\mathrm{nm}}{\mathrm{s}}$). SCFS experiments, with a focus on the approach curves, have been extended to *S. aureus* on hydrophobic surfaces, which show that the initiation of bacterial contact starts as far as 50 nm (sometimes even 100 nm) above the substratum [64]. As already explained at these distances DLVO forces between the bacterium and the substratum are negligible and the snap-in is not explainable by DLVO theory.

Furthermore, Thewes et al. [64] investigated the approach-retraction cycle with varying force trigger (see figure 4.3). The force trigger sets the separation to the surface before the retraction starts such that a higher negative force trigger leads to closer separation to the surface. With increased initial separation the shapes of the retraction curves change, where for intermediate separations a bistable behaviour is observed. For low and high initial separations two classes of reproducible force-distance curves are obtained. While

---

[8] On hydrophilic surfaces, adhesion was too small to determine amplitudes.

[9] cellular appendages

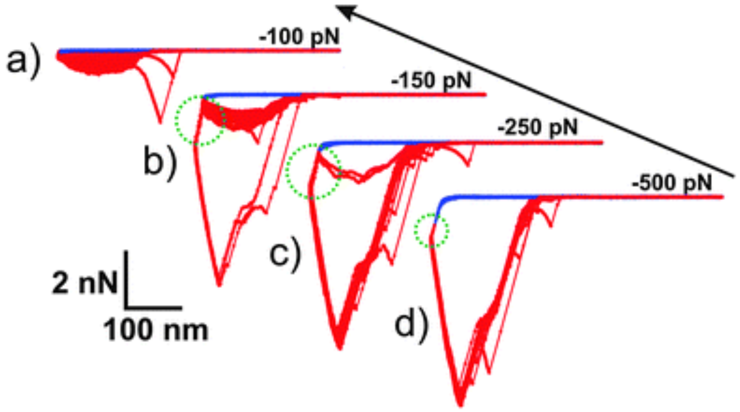

Figure 4.3: Partitioned force-distance curves on hydrophobised Si waver with varying force trigger (higher negative force trigger leads to lower separation to the surface). The red curves are individual retraction curves with the same cell, while the the blue curves are individual approach curves. The pulling regime is indicated by the green circle. The figure is reproduced from Thewes et al. [64] with permission from The Royal Society of Chemistry.

the rupture lengths in both classes are identical the adhesion forces for lower initial separations is larger. For intermediate initial separations, a force-distance curve of either one or the other class is obtained. Note, that this bistable behaviour is not due to the distinct behaviour of different cells, but since the same cell is used it reflects the internal stochasticity of the adhesion process. Additionally, the curves with low initial separation, display even though the retraction already started, an initial attraction to the surface. This region in the retraction curves is termed “pulling regime” .

To explain these observations, Thewes et al. [64] build a stochastic model (see figure 4.4). The bacterium is modelled as a hard sphere decorated with elastic springs modelling the macromolecules. One end of the springs is fixed to the bacterium, while the other end fluctuates thermally and interacts with the surface via an interaction potential. To mimic SCFS experiments, this sphere is connected to a cantilever, modelled as a spring, which moves toward/away from the surface. After each cantilever step, determined from the step size of the experimental Piezo motor, a prescribed number of Monte Carlo steps[10], to incorporate the thermal fluctuations, are performed. After this, the acting force, computed from the length of the connected springs and the deflection of the cantilever, is computed. The separation d of the sphere to the surface is then moved into the mechanical equilibrium position, computed from the restoring force of the cantilever F_C and the pulling force of the macromolecules F_M. I formulate the forces

---

[10] Metropolis steps according to section 2.3.2.

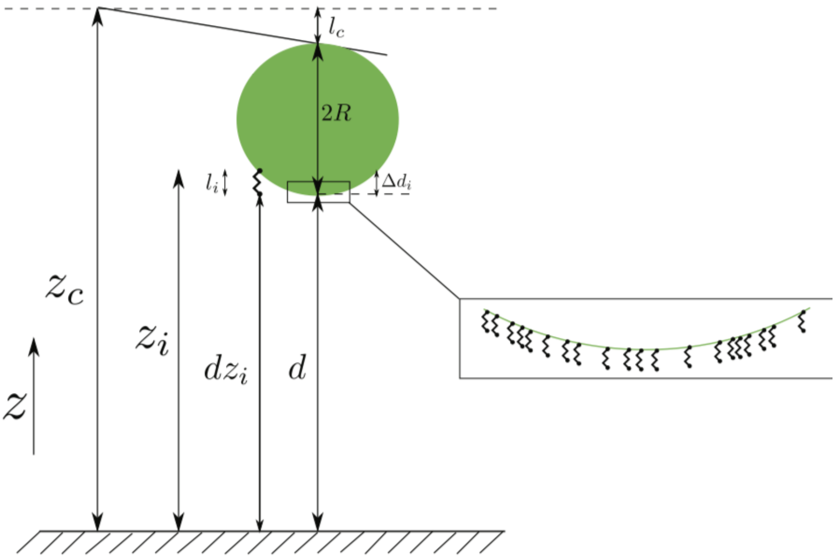

Figure 4.4: Model schematic of Thewes et al. [64]. Sphere of radius R decorated with springs of length l_i. One end of the springs are connected at fixed height Δd_i measured from the bottom of the sphere. The other ends thermally fluctuate, have distance dz_i to the surface and interact with the potential. In each step of the cantilever, its height z_c is changed and a new equilibrium position d for the sphere computed. The figure is adapted from Thewes et al. [64] with permission from The Royal Society of Chemistry.

acting at bacterium separation d, such that a generalisation to different force-stretch relation is obvious:

$$
\begin{aligned}
F_C &= k_c \cdot (z_c - d - 2 \cdot R - l_0^c) \\
F_M &= \sum_i k_i \left(d + \Delta d_i - dz_i - l_0^i \right) \ .
\end{aligned}
$$

Here k_c is the spring constant of the cantilever, l_0^c its rest length, z_c its distance to the surface R the radius of the bacterium. The sum of the molecule forces runs over all springs which are in the range of the interaction potential. The k_i denote the spring constants while l_0^i are the rest lengths. One end of the springs are connected at fixed height Δd_i measured from the bottom of the sphere. The other end thermally fluctuates, has distance dz_i above the surface and interacts with the potential. In other words, the deflection of the cantilever is given by $l_c = z_c - d - 2 \cdot R$, while the individual macromolecules are stretched as $l_i = d + \Delta d_i - dz_i$. Note that by separating the movement of the cantilever from the thermal fluctuations, it is assumed that the relaxations due to mechanical stretching decay much faster than thermal fluctuations and therefore the stretching of the macromolecules can be assumed to be quasi-static.[11]

This model connects the individual molecular binding of macromolecules with the macroscopic extensions in a single model. It reproduces the experimentally observed behaviour, i.e. the adhesion hysteresis, the snap-in and the bistable behaviour for the retraction curves with varying force trigger. The model shows that the distribution of spring constants is important for observing a snap-in, while the form of the interaction potential was not [64].

A similar model was studied by Ostvar and Wood [76]. It considers individual macromolecules with heterogeneous mechanical responses in a plane-plane geometry, but no thermal fluctuations nor a cantilever. This model reproduces the snap-in only if all macromolecules have the same extension and therefore come into contact with the surface at the same separation. Generally, a snap-in is not observed, which I attribute to the absence of a cantilever that allows the cell to abruptly approach the surface and hence leads to a cascade of interacting macromolecules. Furthermore, the model shows hysteresis but its origin is distinct from the origin of the hysteresis in the model of Thewes et al. [64]. While in the model of Ostvar and Wood [76] hysteresis is generated by the force balance of individual macromolecules interacting with a Lennard-Jones potential, which allows two stable solutions in the absence of thermal fluctuations, the square potential in the work of Thewes et al. [64] does not. In the model of Thewes et al. [64] the hysteresis is generated by the movement and flexibility of the cantilever. Nevertheless, both models demonstrate that the adhesion process can be described as the multi-scale interactions of heterogeneous macromolecules interacting with a surface.

Further investigations with SCFS have been performed by Spengler et al. [77, 78]. The size of the interaction area, i.e. which area of the bacterium contributes to the adhesion force for *S. aureus* and *S. carnosus* (see figure 4.5), has been determined [77]. Both strains have approximately the same radius of the interaction area of about 150−300 nm but *S. aureus* displays a three times larger adhesion than *S. carnosus*. Furthermore, if one compares several cells of the same strain, no correlation between the adhesion force and the interaction area is observed. Additionally, the study demonstrated a slight increase of interaction area with an increased loading force but the response is not Hertzian. An analysis comparing this to more sophisticated models of contact mechanics is missing.

---

[11] To ensure this a hundredths of the actual cantilever step size is used.

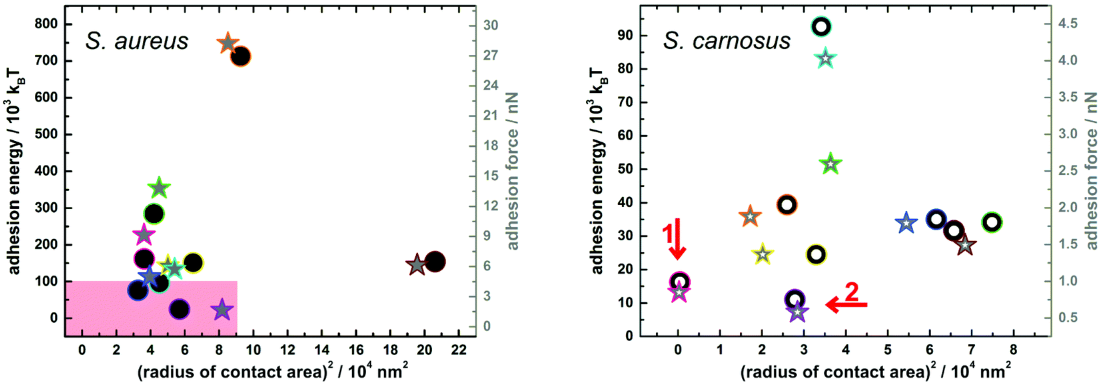

Figure 4.5: Adhesion energy (area under the retraction curve, black circles) and adhesion force (grey stars) of *S. aureus* (left) and *S. carnosus* (right) versus the radius of the interaction area squared. The reddish coloured rectangle displays the scale of *S. carnosus* cells. A force trigger of 0.3 nN was used. The figure is reproduced from Spengler et al. [77] with permission from The Royal Society of Chemistry.

The beforehand presented studies have been performed on smooth surfaces, however, many surfaces are not smooth and the roughness may have a significant influence on the adhesion. Indeed, Spengler et al. [78] demonstrated that even roughness on the nanoscale leads to a decrease in adhesion force with increasing roughness. While in classical adhesion models this is, at least for stiff spheres, attributed to a reduced contact area, Spengler et al. [78] explain this observation with reduced accessible binding area for macromolecules. Studies comparing the influence of roughness on stiff or elastic spheres with or without polymeric appendages is, to my knowledge, lacking. While including nano roughness into models which describe adhesion via individual macromolecules is quite easy, incorporating it into theories that treat the substratum bacterium interaction continuously seems quite challenging. Additionally, the study of Spengler et al. [78] nicely corroborates that adhesion can be understood mostly as a passive process since even though on rougher surfaces more cells died, the adhesion force was uncorrelated to the cells state.

4.4 Conclusion

This chapter reviewed the traditional approaches to bacterial adhesion on unconditioned abiotic surfaces. The literature demonstrates that traditional approaches from colloidal science and contact mechanics can be used to model bacterial adhesion. However, since they rely on continuous interactions of the entire bacterium with the substratum they cannot explain certain aspects of adhesion. Adhesion in the unloaded case is primarily mediated by the interaction of macromolecules, decorating the cells surface. Therefore, stochastic length fluctuation and the force response of individual macromolecules determine the adhesion process. I continue this interpretation of the adhesion process in chapter 7, where I show that an extension of the model proposed by Thewes et al. [64] can describe the retraction curves of *S. aureus* on hydrophobic and hydrophilic surfaces.

5 Range expansion

Microbial range expansion refers to the growth of microbes into previously uncolonised space. The main property distinguishing it from well-mixed growth, e.g. inside a liquid medium, is the interaction with a substratum. This results in a reduced mobility of individual cells such that each cell mostly competes with cells in its immediate surrounding. This is experimentally realised by growing microbes from an initial inoculation zone on hard surfaces such as agar plates. Since only individuals at the colony front divide the effective population size of competing microbes is small and genetic drift plays a pivotal role. Microbial range expansion has extensively been studied experimentally, mathematically and with the help of simulations and this chapter can only provide a brief introduction to this rich topic.

I will discuss the role of universality in colony growth and present the current understanding of genetic drift in spatial population genetics. A thorough understanding of this effect is necessary to evaluate the role of selection presented afterwards. I outline the role of selection advantages in reproduction statistics as well as the influence of mechanical interactions. Particular focus will be the experimental results for cell sorting populations, which I model in my work presented in chapter 6.

5.1 Colony growth and universality

Mono species range expansion experiments on solid substrates such as agar plates show divers macroscopic shapes. For the bacterium *B. subtilis* increased agar concentration leads to a reduction of cell individual mobility and depending on the nutrient and agar concentration various growth morphologies are observed (see figure 5.1). All phases can be captured by a simple reaction-diffusion model, coupling two mobility states with a nutrient field driving cell division [79, 80].

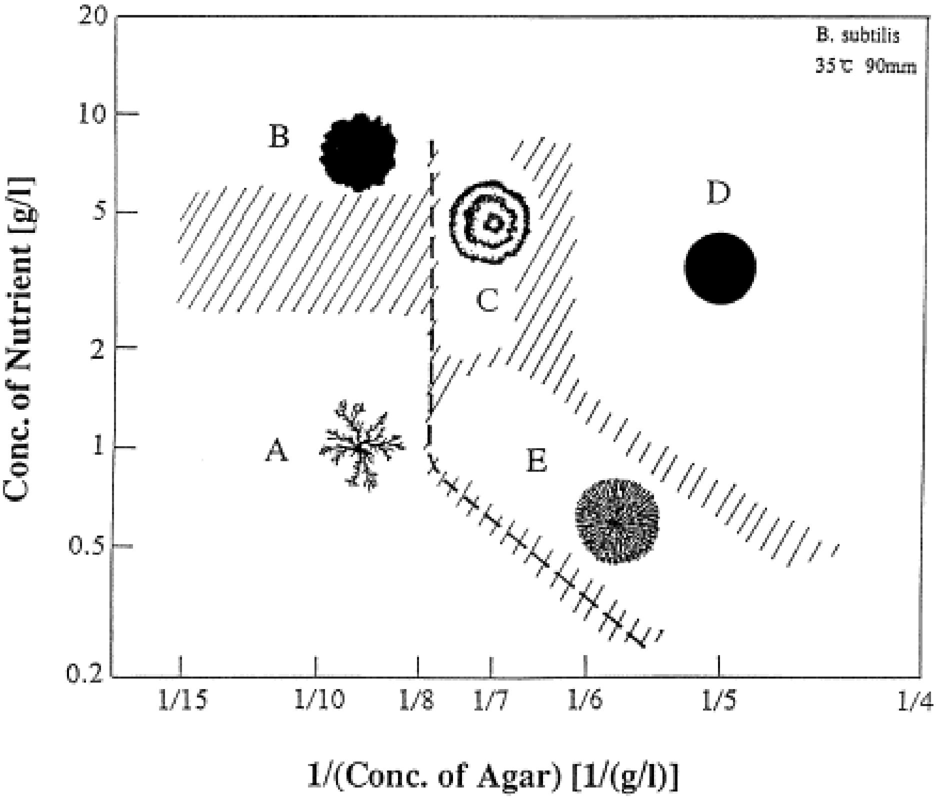

Figure 5.1: Colony morphology diagram of *B. subtilis*, for various agar and nutrient concentrations. Increased agar concentration leads to reduced mobility, such that in zone A and B the individual cells become immobile. The figure is reprinted from Matsushita et al. [79] with permission from Elsevier.

A low agar concentration leads to the dense branching morphology (DBM, phase E in figure 5.1) or with more available nutrients to its more compact variant with a smooth perimeter (phase D in figure 5.1). At intermediate agar concentrations, *B. subtilis* switches between mobile and immobile states resulting in a ring morphology (phase C in figure 5.1). At high agar concentration, no active movement is possible and either diffusion-limited aggregation (DLA, dendrite like structures, phase A in figure 5.1) or circular growth patterns with a rough perimeter are observed (phase B in figure 5.1).

This thesis is only concerned with immobile strains or conditions leading to immobility and the colonies have morphologies reminiscent of phase B or D in figure 5.1, i.e. they are disc-like with either a rough or smooth perimeter. Matsushita et al. [79] quantified the roughness exponent to be 0.78(2) and 0.5(01) in the B and D phase respectively. The exponent in phase D fits with KPZ predictions as introduced in section 2.5.1, while the origin of the large exponent in phase B remains contentious. Vicsek et al. [81] obtained similar roughness exponents for *E. coli* and *B. subtilis* (0.78(7) and 0.74(7)).

The large roughness exponent agrees with the exponent of the quenched KPZ class (qKPZ) at the pinning transition. The qKPZ class is defined by lateral growth in a heterogeneous medium, i.e. it has the same growth equation as the KPZ class but instead of the time-dependent noise space-dependent noise and a constant driving force are considered. The noise leads to locally pinned surfaces, which in the case of weak driving force results in a globally pinned surface. If the driving force is strong enough, the surface is not pinned and KPZ exponents are retained [35]. At the pinning transition, the roughness exponent $\alpha = \frac{3}{4}$ and the growth exponent $\beta = \frac{3}{5}$ are obtained [82]. Therefore the large exponent might be attributed to substrate heterogeneities.

However, also the coupling of two fluctuating interfaces can cause larger roughness exponents [35, 83]. The second interface can be realised by coupling the cellular growth to a nutrient field. Indeed, computer models incorporating limited growth due to nutrient depletion show without any substrate heterogeneity increased roughness exponents [84, 85]. While Bonachela et al. [84] did find agreement with the qKPZ predictions they did not find a regime that fits with KPZ values. The model of Santalla and Ferreira [85], however, showed KPZ exponents in the limit of weak coupling to nutrient depletion, while strong depletion agreement with qKPZ scaling was observed on intermediate time scales. On large time scales, however, neither KPZ nor qKPZ scaling could be obtained. Santalla et al. [86] revisited the growth of *E. coli* and *B. subtilis* in the B phase and their extensive analysis found neither agreement with KPZ nor qKPZ scaling. The authors attribute the increased roughness to the aforementioned coupling of cellular growth to nutrient consumption where depletion of nutrients leads to a diffusion instability resulting in effective but non-universal scaling on the observed time scales [86]. Therefore, neither *E. coli* nor *B. subtilis* show KPZ growth. However, other cells such as HeLa and Vero cells show scaling consistent with KPZ universality [87, 88, 89]. Furthermore, Huergo et al. [90] found for Vero cells growing in a gelled medium a transition from KPZ to qKPZ growth depending on the concentration of polymers inside the medium.[1]

Farrell et al. [91] investigated in an individual based mechanical model the roughness of a growing colony. The growth is coupled to a diffusion governed nutrient and the bacteria are modelled as rods growing at a constant speed as long as the nutrient supply is over a prescribed threshold. The growth occurs along the long axis of the bacterium until a Gaussian distributed critical length is reached. Then the cells divide and their orientation is perturbed to avoid growth along a straight line. The interaction of the bacteria is governed by overdamped equations of motion, where cells are subject to cell-substrate friction and repel each other according to forces from Hertzian contact theory. This model leads after an initial transient to growth with constant speed and the establishment of a growth zone with thickness h (see figure 5.2). The roughness decreases monotonously with the thickness of the growth layer and depends as expected on the system size. Farrell et al. [91], however, did not analyse the scaling behaviour and therefore a comparison to the previously presented experiments cannot be conducted.

5.2 The role of genetic drift

The growth of a range expanding colony is determined by the competition dynamics at the perimeter. If death inside the colony can be neglected this leads to a frozen record of past competitions. This can be visualised by mixing different fluorescent labelled, but otherwise identical microbial strains, and allows the qualitative and even quantitative study of genetic drift. The main experimental set-ups used are circular or line inoculations, where microbes are inoculated inside a circle or on a line respectively (see figure 5.3).

The initially well-mixed population grows into well-separated domains with fluctuating boundaries. Figure 5.3 shows this coarsening for non-motile *E. coli* and *S. cerevisiae*

---

[1] The exponents are $\alpha = 0.63(4)$, $\beta = 0.75(5)$ consistent with qKPZ [90].

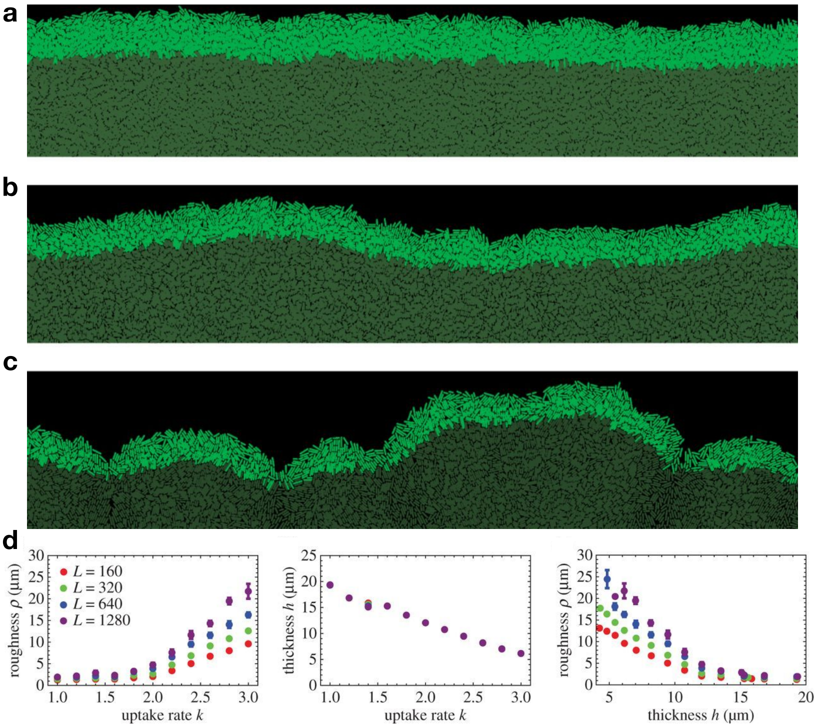

Figure 5.2: Simulation of the mechanical model by Farrell et al. [91] for update rate **(a)** $k = 1.8$, **(b)** $k = 2.2$, **(c)** $k = 2.6$. The bright green colour marks the growing layer. **(d)** Roughness and thickness of the growth layer h for various system sizes L. The figures are adapted from Farrell et al. [91] under the CC BY 4.0 license.

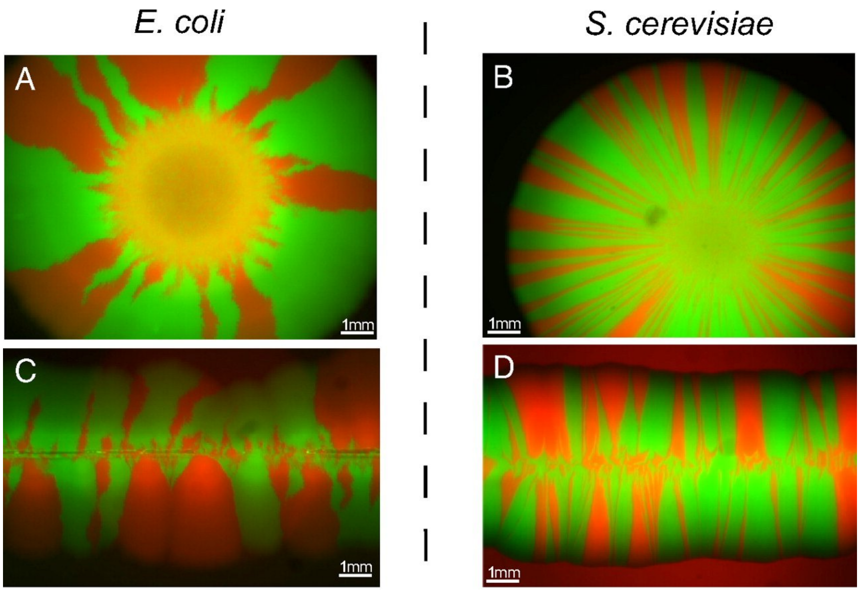

Figure 5.3: Range expansion of different fluorescent labelled but otherwise identical **(a,c)** *E. coli* and **(b,d)** *S. cerevisiae* cells. Figure **(a,b)** show circular inoculations while **(c,d)** show line inoculations. The figures are adapted from Hallatschek et al. [92] with permission of the National Academy of Sciences, U.S.A, Copyright (2007).

strains. While *S. cerevisiae* shows more sectors, *E. coli* displays more pronounced boundary fluctuations. As I will show in section 5.2.2, the sector statistic can be directly related to the behaviour of boundary fluctuations in a quantitative manner. In circular expansions, in addition to the fluctuations, the inflation of the colony needs to be considered. Understanding the system from boundary dynamics only provides insight into the effective macroscopic dynamic. It cannot be related to the classical well-mixed growth models and therefore the family of stepping stone models, which provides a stochastic continuum description closely related to the classical models will be introduced as well.

5.2.1 Stepping stone model and continuum theory

Stepping stone models are the extension of well-mixed growth models introduced in section 3.3 to spatial systems. They have a rich history and I only give a brief introduction. For this, I mostly follow the presentation of Blythe and McKane [59] and Korolev et al. [60]. To introduce spatial dependencies, the system is discretized into demes of typical size a. Inside each deme, well-mixed growth with maximal population N is considered. I focus on one-dimensional stepping stone models, where the demes are arranged along a line. The growth of the colony is reflected in the time dimension of the model and therefore the model is only applicable if the colony advances uniformly along its perimeter. Especially possible effects due to surface roughness are not captured.

I consider the case of two strains and label the occupation of each deme by the relative frequency of an arbitrary reference strain. Between neighbouring demes, strains migrate proportionally to their local frequency with migration rate m. While for well-mixed growth inside each deme many different microscopy models such as Moran model presented in section 3.3.1 can be considered. They reduce in the continuum limit as performed in section 3.3.1 to the same model. This continuum limit introduces a genetic diffusion constant $D_g = \frac{2a}{\tau_g N}$, where τ_g is the generation time. Analogously, a diffusion approximation for the migration dynamics introduces a spatial diffusion constant $D_s = \frac{ma^2}{2\tau_g}$. The resulting equation

$$\frac{\partial p}{\partial t} = \frac{D_g}{2}\frac{\partial^2}{\partial f^2} f(1-f)p - D_s \frac{\partial^2}{\partial x^2}\frac{\partial}{\partial f} fp \ ,$$

combines local genetic diffusion of the allele frequency with a spatial diffusive spread through the system.[2]

As introduced in section 3.3 the composition of the population can be characterised by the average frequency F and heterozygosity H, which are defined as

$$\begin{aligned} F(t,x) &= \langle f(t,x)\rangle \\ H(t,x_1,x_2) &= \langle f(t,x_1)(1-f(t,x_2)) + f(t,x_2)(1-f(t,x_1))\rangle \ . \end{aligned}$$

While F characterizes the population composition at position x, H is the probability of finding the reference strain at position x_1 while at the same time finding the other strain at position x_2. The equations of motion for these quantities can be derived as

$$\begin{aligned} \frac{\partial F}{\partial t} &= D_s \frac{\partial^2 F}{\partial x^2} \\ \frac{\partial H}{\partial t} &= D_s\left(\frac{\partial^2}{\partial x_1^2} + \frac{\partial^2}{\partial x_2^2}\right) H - D_g H \delta(x_1 - x_2) \ . \end{aligned} \tag{5.1}$$

The average frequency fulfils the diffusion equation, while the equation for the average heterozygosity combines diffusion with coalescence of domains. For spatially well-mixed initial conditions i.e. $F = F_0$, $H_0 = 2F_0(1-F_0)$, F remains constant, while H depends due to translation symmetry only on the relative distance $x = x_1 - x_2$. Solving equation 5.1 for an infinite system leads to

$$\begin{aligned} H &= H_0 - D_g \int_0^t dt' e^{-\frac{x^2}{8D_s(t-t')}} \frac{H(t',0)}{\sqrt{8\pi D_s(t-t')}} \\ H(t,0) &= H_0 \ \mathrm{erfc}\left(\sqrt{\frac{D_g^2 t}{8Ds}}\right) \ e^{\frac{D_g^2 t}{8Ds}} \ , \end{aligned}$$

where erfc is the complementary error function.

For $t \geq \frac{8D_s}{D_g^2} =: \pi T_{\text{fix}}$

$$H(t,0) \approx H_0 \sqrt{\frac{T_{\text{fix}}}{t}}$$

---

[2] Written as a stochastic Ito-Differential equation the coupling of spatial and frequency derivative is removed. In this form, the equation is known as the stochastic Fisher-Kolmogorov-Petrovsky-Piscounov (SFKPP) equation.

and therefore the heterozygosity decays locally algebraically to zero. This indicates local fixation of a single allele with fixation time $T_{\text{fix}} \sim N^2$. This is different from the non-spatial case, where the fixation occurs exponentially fast with a fixation time linear in N (see section 3.3).

For large separations, i.e. $x \gg 2\sqrt{2D_s t}$, H always approaches H_0. The change from zero to H_0 can be quantified by the average domain size l, for $t \geq \pi T_{\text{fix}}$. Korolev et al. [60] show that it is given by

$$l(t) = \frac{4D_s}{D_g}\frac{1}{H(t{,}0)} = \frac{\sqrt{2\pi D_s t}}{H_0} ,$$

which predicts unlimited[3] diffusive growth of the domains independent of the genetic diffusion constant.

To compare the system of finite extend L to the non-spatial case it is practical to consider the spatial average of the heterozygosity i.e. $H_L = \frac{1}{L}\int_0^L H(t,x)dx$. This encodes the probability to sample two different alleles in the entire population. For $t \gg \frac{L^2}{D_s}$, i.e. the time scale a domain boundary would need to spread through the full system, it can be shown that H_L follows the same dynamics as a well-mixed system with rescaled diffusion constant $\frac{D_g}{L}$. For $\pi T_{\text{fix}} \leq t \leq \frac{L^2}{D_s}$, however,

$$H_L = H_0 - \frac{D_g}{L}\int_0^t H(t'{,}0)dt' \approx H_0\left(1 - 4\frac{\sqrt{4D_s t}}{\sqrt{\pi}L}\right)$$

is obtained and therefore the total fraction of one allele performs a subdiffusive random walk[4] in frequency space and the influence of genetic drift reduces over time.

Radial expansions

Radial expansion of the colony can be treated by the one-dimensional stepping stone model if the growth dynamics remain quasi one dimensional i.e. the growth layer needs to be much smaller than the circumference. The spatial coordinate is then parameterized by the arc length $x = \varphi r$ where (r, φ) are the usual polar coordinates. The spatial distances inflate due to the radial growth of the colony. For this typically linear growth

---

[3] Strictly speaking the solution is only valid for an infinite system.

[4] Note that the variance of the total fraction simply is $\frac{H_0 - H_L}{2}$.

from an inoculation zone of radius r_0, i.e. $r(t) = r_0 + v_\parallel t$ is considered. The equation for the average heterozygosity is

$$\frac{\partial H}{\partial t} = \frac{2D_s}{r^2}\frac{\partial^2 H}{\partial \varphi^2} - \frac{D_g}{r}H(t{,}0)\delta\left(\varphi\right) \ , \tag{5.2}$$

which can be solved analytically but its solution is unwieldy. Important to note is, that $H(t{,}0)$ decays on time scales larger than $\frac{v_\parallel}{r_0}$ to zero according to t^{-1} and not $t^{-\frac{1}{2}}$ as in the case without inflation. This indicates faster local fixation due to inflation. Additional $H(t, \varphi)$ does not widen indefinitely but approaches for $t \to \infty$ a non-trivial limit shape. This can be understood from equation 5.2 by observing that on time scales larger than $\frac{r_0}{v_\parallel}$ domain boundary fusion stops. The angular domain size can be computed as

$$l(t) = \frac{4D_s}{D_g r}\frac{1}{H(t{,}0)} \ ,$$

in which for a long time the inflation of r and the linear decay of $H(t{,}0)$ cancel to give the finite result

$$l\left(\infty\right) = \frac{1}{H_0}\left(\frac{v_\parallel}{D_g} + \sqrt{\frac{r_0 v_\parallel}{2\pi D_s}}\right)^{-1} \ .$$

From this also the average number of domains $\langle N \rangle = \frac{2\pi}{l(t)}$ can be computed, which predicts the survival of a finite number of sectors in circular range expansions determined by the interplay of genetic drift and spatial mobility.

While comparing the predicted heterozygosity to fluorescence spectroscopy measurements remains challenging, Korolev et al. [93] observed qualitatively agreement. Also, the observed number of sectors agreed with the predictions and in particular, the boundaries followed a diffusive motion.

5.2.2 Sector statistics from boundary dynamics

Treating the boundaries of two neutral strains as a pure diffusion process is a simple but powerful approach. The problem of computing sector statistics is then reformulated as diffusion-limited annihilation, where heuristically the number of sectors is expected to decay inversely proportional to the area covered by a single boundary i.e. the root of the mean square displacement (MSD)

$$N \propto \frac{1}{\sqrt{\mathrm{MSD}\,(t)}} \; .$$

The typical time for fixation $\langle T_{\mathrm{fix}} \rangle$ is given by the spread of a single boundary over the full system size. If a system of size L and an $\mathrm{MSD}\,(t) \propto t^{2\gamma}$ with wandering exponent γ is assumed

$$\langle T_{\mathrm{fix}} \rangle \propto L^{\frac{1}{\gamma}}$$

is expected. Therefore, the fixation time decreases with an increasing wandering exponent.

For a detailed analysis in the diffusive case $\gamma = \frac{1}{2}$, I follow the presentation of Hallatschek and Nelson [94]. The relative distance of two boundaries is denoted by Z. This allows to study line inoculations ($Z = X$) and radial inoculations ($Z = \frac{\varphi}{r}$) at the same time, where the relative motion is either measured by the distance lateral to the expansion X or by the angular distance φ. Furthermore, as a time-like variable t either the surface height h or the radial extension r of the colony is used. If the individual boundaries are diffusions with time-dependent diffusion constant[5] $D(t) = \lim_{t_0 \to t} \frac{\langle Z^2 \rangle}{4(t-t_0)}$ the relative motion satisfies the diffusion equation[6]

$$\frac{\partial p}{\partial t} = 2D(t) \frac{\partial^2 p}{\partial z^2}$$

with absorbing boundary condition $p(0, t|z_0, t_0) = 0$. In the case of an infinite system the solution is[7]

$$p(z, t|z_0, t_0) = \frac{1}{\sqrt{2\pi\sigma}} e^{-\frac{(z-z_0)^2}{2\sigma^2}} \left(1 - e^{-\frac{2z_0 z}{\sigma^2}}\right) \tag{5.3}$$

with $\sigma^2 = 4 \int_{t_0}^{t} dt' D(t')$. In the case of the infinite allele model, where every cell is considered to be a different strain, the sector size distribution is given by the probability that two domains do not collide given that they start almost at the same position. This

---

[5] The time-dependent diffusion constant is necessary to describe inflation in radial inoculations.

[6] The factor two originates in the relative motion of two boundaries.

[7] For a finite system, a second boundary condition needs to be introduced. Solving this equation is possible but the resulting equations are much more unwieldy.

is obtained by a small ϵ expansion of solution 5.3, where $z = z_0 + \epsilon$. Normalizing the result over the half-open interval leads to

$$p\left(z, t|x_0\right) = \frac{z}{\sigma^2} e^{-\frac{z^2}{2\sigma^2}} \; .$$

The average sector size, therefore, is $\langle Z \rangle = \sqrt{\frac{\pi}{2}}\sigma$, which remarkably is $\frac{\pi}{2}$ larger than what is expected from individual non annihilating random walks. This can be understood by considering that the distribution describes the size of surviving sectors and therefore boundaries that stay apart contribute more to the statistics. The average number of sectors $\langle N \rangle$ for a system with only two alleles with initial heterozygosity H_0 and system size L is $\langle N \rangle = \frac{L H_0}{\langle Z \rangle}$. For well-mixed initial conditions $H_0 = \frac{1}{2}$ and line inoculations $D(t) = D$ which results in

$$\langle N \rangle = \frac{L}{2\sqrt{2\pi D\left(t - t_0\right)}} \overset{t\to\infty}{\longrightarrow} 0 \; .$$

This confirms the eventual fixation of a single allele on a time scale $\propto \frac{L^2}{D}$ as already obtained by the scaling analysis. For circular inoculations $D(t) = \frac{D}{t^2}$ and therefore

$$\langle N \rangle = \frac{\pi}{\sqrt{2\pi D\left(\frac{1}{t_0} - \frac{1}{t}\right)}} \overset{t\to\infty}{\longrightarrow} \sqrt{\frac{\pi t_0}{2D}} \; .$$

This shows the survival of different alleles. Note, that since equation 5.3 is only valid for an infinitive system the sector statistics are only an approximation. Furthermore, the analysis only considered the interactions of two domain boundaries which is an approximation by itself. For an analysis of several interacting sectors see for instance [95, 96, 97].

Boundaries in experiments

Korolev et al. [93] analysed the domain boundaries of non-motile *E. coli* bacteria in radial range expansions and found chiral behaviour, i.e. they turn always counter-clockwise. Chirality depends on the temperature *E. coli* are grown in [98]. Jauffred et al. [99] investigated the origin of chirality and demonstrated that neither the direction of cell wall synthesis nor the rod shape is sufficient to produce chiral colonies. The authors rather found that chirality is mediated by substrate interactions which can be masked by bacterial surface structures, such that removing them increases chirality.

Chirality can be included in the diffusion scheme by adding a growth $v_\perp$ speed perpendicular to the perimeter of the expanding colony. In the radial case, the resulting drift decreases with radial distance and results for the mean and variance in

$$\begin{aligned}\langle\varphi\rangle &= \varphi\left(r_i\right) + \frac{v_\perp}{v_\parallel}\ln\left(\frac{r}{r_0}\right)\\ \mathrm{Var}\left(\varphi\right) &= \frac{2D_s}{v_\parallel}\left(\frac{1}{r_0}-\frac{1}{r}\right)\ .\end{aligned}$$

Korolev et al. [93] confirmed that the mean and variances predicted fits the extracted boundaries. This drift of single boundaries, however, is cancelled in the relative movement of two boundaries and therefore does not influences the sector statistics.

Furthermore, Hallatschek et al. [92] analysed the boundaries of the same *E. coli* strain and found that they display superdiffusive wall wandering with wandering exponent $\gamma = 0.65(5)$ [92]. This does not agree with the radial diffusions observed by Korolev et al. [93]. This discrepancy may be the result of methodical differences in evaluating the MSD of single boundaries or due to slight changes in the growth conditions. So whether or under what conditions *E. coli* display superdiffusive wall wandering remains elusive.

Eventual superdiffusivity is explained, as argued by Hallatschek et al. [92], by the coupling of the boundary dynamics to the roughness of the colony growth which occurs along the local surface normal. A local tilt of the surface normal, which the boundary follows leads to an increased displacement from the average growth direction. Scaling arguments lead to a wandering exponent $\gamma = 1 + \beta\frac{\alpha-1}{\alpha}$ with growth and roughness exponents β and α. This predicts $\gamma = \frac{2}{3}$ for KPZ growth, which has been confirmed by simulations of Eden clusters as presented in the next section. Furthermore, this exponent is compatible with experimental observations of Hallatschek et al. [92]. Note, that for the exponents of *E. coli* presented in section 5.1 rather $\gamma = 0.56$ would be obtained. This does neither agree with the exponent of Hallatschek et al. [92] nor Korolev et al. [93]. However, in these experiments a different *E. coli* strain and growth conditions were used.

Boundary dynamics of Eden clusters

The boundary dynamics of two competing Eden clusters with identical growth rates has been studied by Ali and Grosskinsky [100]. The authors studied line inoculations on a cubic lattice with periodic boundary conditions lateral to the growth direction. Since the surface grows continuously the line geometry allows the use of the surface height h as a time variable for the boundary position X. They found that the distribution is consistent with a Gaussian distribution, with moments

$$\begin{aligned} \langle X_h \rangle &= 0 \\ \langle X_h^2 \rangle &\propto h^{\frac{4}{3}} \ . \end{aligned}$$

The exponent $\frac{4}{3}$ indicates superdiffusive wall wandering, which results from growth along the local surface normal, as discussed earlier. These observations are consistent with several continuous Gaussian processes, such as e.g. time changed Brownian motion, scaled Brownian motion and fractional Brownian motion. By using time changed Brownian motion, as the mathematically simplest model, understanding sector statistics from boundary dynamics reduces to the statistics of diffusion-limited annihilation as presented in the previous section. The correct scaling behaviour of the number of sectors, as well as the fixation time, has been confirmed by collapsing the simulated data to a master curve [100].

In biological systems, however, cells cannot divide immediately after a previous division. This can be incorporated by introducing a lag time $1-\delta$ between divisions such that a simple idealized division distribution is given by the lag exponential distribution i.e.

$$\rho(t) = \begin{cases} 0 & , t \leq 1-\delta \\ \frac{1}{\delta} e^{-\frac{t-1+\delta}{\delta}} & , t \geq 1-\delta \ . \end{cases}$$

The distribution is constructed such that the mean is one and the standard deviation is δ. For $\delta = 1$ the usual memoryless exponential distribution is retained, while $\delta < 1$ introduces a memory effect. This setting has been studied by Ali et al. [101], who obtained KPZ scaling exponents[8] for the surface growth and boundaries dynamics agreeing mostly with the memoryless case. The prefactor of the boundary MSD,

---

[8] Essentially the correlations from divisions are only short-range and therefore do not change the scaling behaviour.

depends monotonously on delta, such that a smaller delta[9] leads to smaller boundary fluctuations and more surviving sectors.

I like to emphasize that the wandering exponent $\frac{4}{3}$ is only obtained for flat initial condition i.e. starting from a compact line. Indeed, Derrida and Dickman [102] investigated the competitive growth of Eden clusters from a wedge initial condition for various opening angles and only found $\frac{4}{3}$ in the case of flat initial conditions. However, only a few angles were explored while Chu et al. [103] studied systematically the dependency of the wandering exponent on the initial angle. The authors found a continuous dependence, where $\frac{4}{3}$ is only obtained for opening angles close to a flat initial condition. After an initial transient, the wedge initial conditions lead to a closing of the initial gap and then the wandering exponent $\frac{4}{3}$ is recovered.

Mapping linear to radial inoculations

Let X_h be the boundary process in the flat expansion and Y_r in the radial case. This section presents literature, which shows that by rescaling the radial process such that distances are not measured according to the arc length but their angular distance both processes can be related via

$$X_{h(r)} \overset{\text{dist.}}{=} \frac{r_0}{r} Y_r \; r \geq r_0 \; . \tag{5.4}$$

The equal sign indicates equality of the probability law.[10] Hence, the single time point quantities of the stochastic process can be mapped to each other and radial inoculations can be understood from linear inoculations. In the case of Brownian motion, time changed Brownian motion and α-stable Lévy flights even all time correlations are mapped exactly [104, 105].

---

[9] more regular divisions

[10] Note that depending on the publication X and Y are differently defined [100, 104, 105].

For the mathematically simplest model consistent with the simulation from competing Eden clusters, i.e. the time changed Brownian motion, the mapping between flat and radial expansion can be derived analytically [100, 105]:

$$h(r) = \left(\gamma \int_{r_0}^{r} \left(\frac{r_0}{s}\right)^2 (s - r_0)^{\gamma-1} \mathrm{d}s\right)^{\frac{1}{\gamma}} \overset{r\to\infty}{\longrightarrow} r_0 \begin{cases} 1 & ,\gamma = 1 \\ \left[\frac{\gamma\pi(1-\gamma)}{\sin(\gamma\pi)}\right]^{\frac{1}{\gamma}} & ,1 \leq \gamma < 2 \\ \infty & ,\gamma \geq 2 \end{cases}$$

where $\langle X_h^2 \rangle \propto h^\gamma$ is assumed. Therefore the process $\frac{r_0}{r} Y_r$ has a finite MSD for all non-ballistic motions, i.e. $\gamma < 2$, and since the boundary grows linearly due to radial inflation fixation is typically not reached.

An analogous mapping can be found heuristically for all processes satisfying

$$dX_h \propto (dh)^{\frac{\gamma}{2}} \ (\gamma > 0) \ ,$$

where I introduce the factor $\frac{1}{2}$ to obtain for Brownian motion the wandering exponent $\gamma = 1$ [104, 105]. For those processes

$$h(r) = \int_{r_0}^{r} \left(\frac{r_0}{s}\right)^{\frac{2}{\gamma}} \mathrm{d}s \overset{r\to\infty}{\longrightarrow} r_0 \begin{cases} \frac{\gamma}{2-\gamma} & ,\gamma < 2 \\ \infty & ,\gamma \geq 2 \end{cases}$$

is obtained and therefore also in these cases, $\frac{r_0}{r} Y_r$ has a finite MSD for all non-ballistic motions. The mapping is confirmed numerically for Brownian motion, Lévy flights and fractional Brownian motion. These results can be extended to all geometries with time-dependent domain size and exact derivations exist for Brownian motions and Lévy flights [105]. For fractional Brownian motion, a different mapping can be derived analytically, which has numerical similar results. Note that for fractional Brownian motion both mappings only preserve one point quantities i.e. correlations at different surface heights are not mapped correctly.

5.2.3 Conclusion

In comparison to non-spatial models which predict exponential fast coalescence into a single surviving domain, the stepping stone model predicts local demixing into monoallelic domains on an algebraic time scale. As a consequence genetic drift can only act on the diffusing domain boundaries decreasing in strength as the population expands. The genetic diversity depends on the wandering exponent of domain boundaries and while diffusive wandering is observed in some experiments also superdiffusive wandering is observed in others [92, 93].

Colonies expanding from line inoculations display in the long time limit only one surviving allele, while for radial inoculations the inflation of the colony leads to the survival of a finite number of sectors. This increased genetic diversity on long time scales is remarkable, but I want to emphasize that also the formation of monoallelic domains and their increased survival in line inoculations is significant. Since this leads to a transient increase in genetic diversity it can be relevant in fast-changing environments.

While I presented range expansion experiments for a co-inoculation of strains often the second strain arises dynamically via mutations. This can be included in the presented stepping stone model and compared to well-mixed growth a higher mutant frequency is predicted. These predictions have been experimentally confirmed by Fusco et al. [106] using genetic sequencing for growing *E. coli* strains. The mutants occur either as sectors competing with the wild-type strain or stay behind the growth front and form bubbles. By considering the boundaries as random walks the authors' related successfully the boundary movement to the mutant frequency distribution. This illustrates the usefulness of the presented approaches which allow to set the effects of selection advantages into proper context and allows to better interpret the results of the following section.

To summarize, the previous investigations showed that in the case of neutral competition spatial models lead, compared to non-spatial models, to an increased genetic diversity in expanding populations. This is named allele surfing and can be understood heuristically from the observation that offspring of individuals which are born at the front tend to stay at the front of an expanding colony. Therefore this offspring has more access to nutrients and colonisable space than the offspring from individuals in the bulk. Hence, individuals at the front tend to be more successful in reproducing.

5.3 Selection

While in non-spatial systems only the growth rate determines the selective advantage, in spatial systems nutrient supply, microbe-substrate friction and access to colonisable space provide constraints for competing microbes. This section presents experiments, computer simulations and mathematical models elucidating the influence of these various factors on the selection dynamics. In particular, the focus will be on a small number of mutants competing with an existing wild type population. Since deleterious mutations, i.e. mutations that have a less selective advantage than the wild type, are connected to antibiotic resistance they are of particular importance [107].

5.3.1 Stepping stone model and continuum theory

The one-dimensional stepping stone models presented in section 5.2.1 can incorporate a selective advantage s due to faster reproduction quite easily. To this end, well-mixed growth with selection, as presented in section 3.3.2, is considered in each deme. Performing, as in the absence of selection (see section 5.2.1), the diffusion approximation for each deme and the continuum limit for the migration dynamics results in the equation

$$\frac{\partial p}{\partial t} = -\frac{s}{\tau_g}\frac{\partial}{\partial f} f\,(1-f)\,p + \frac{D_g}{2}\frac{\partial^2}{\partial f^2} f(1-f)p - D_s \frac{\partial^2}{\partial x^2}\frac{\partial}{\partial f} fp \; .$$

Furthermore, the moment equations for the average frequency and heterozygosity can be derived but the set of equations does not close. Nevertheless, the model can be analysed in two limiting cases as argued by Korolev et al. [60]: It is known from the non-spatial model the advantageous strain takes over the population at a time scale $\propto \frac{\tau_g}{s}$ and from the discussion of the pure genetic drift it is known that correlations occur at a time scale of $\frac{D_g^2}{D_s}$. Therefore, in the strong selection limit $\frac{s}{\tau_g} \gg \frac{D_g^2}{D_s}$ the same behaviour as in well-mixed growth is expected, while in the weak selection limit $\frac{s}{\tau_g} \ll \frac{D_g^2}{D_s}$ deviations are expected. For further analysis, Korolev et al. [60] consider two distinct initial conditions:

First consider the system initially separated into two domains i.e. $f(0,x) = 1 - \Theta(x)$. Then it can be shown that the more fit strain invades the domain of the less fit strain in form of a wave with speed $v_s = 2\sqrt{sD_s}$ in the strong selection limit and $v_w = \frac{2sD_s}{D_g}$ in the weak selection limit [60, 108]. The second initial condition is an initially well-mixed system. Now the selective sweep, in the weak selection limit, consists of two stages. In the first stage domains, controlled by genetic drift, are established as described in section 5.2.1. After the domains are established the fitter strain spreads as in the initially separated case with the weak wave speed into the other domain.

The selective sweep occurs, as in the non-spatial case, exponential fast but the time scale is $\propto \left(\frac{\tau_g}{s}\right)^2 \frac{D_g^2}{D_s}$ rather than $\left(\frac{\tau_g}{s}\right)$ [60]. And since the weak selection limit was considered selection is slower in range expansions.

Remarkably the question of the fixation probability, i.e. what is the probability that a given strain takes over the initial population has been solved analytically by Doering et al. [109]. For this, the duality between the one-dimensional stepping stone model and the birth-coagulation reaction-diffusion process $A \rightleftharpoons A + A$ is exploited. The fixation probability is

$$p_{\text{fix}} = 1 - e^{-\frac{2s}{D_g \tau_g} \int f(0,x) dx} ,$$

which does not depend on D_s but only in the limit $\frac{s}{D_g} \gg 1$ reduces to the well-mixed result [60, 109].

Note that since the model assumes constant front movement of all strains the predictions from the one-dimensional stepping stone model in the presence of selection should be treated with caution. In colonies, the growth advantage leads to local speed up of the growth velocity resulting in a non-uniform front motion visible by bulging of fronts that contain the faster-growing strain. However, to my knowledge, no quantitative comparison to experiments has been conducted.

5.3.2 Sector shape from boundary dynamics

Growing an initial small amount of an advantageous/deleterious strain inside a background population allows the easy study of selectional advantage in range expansion experiments. If the initial small population is advantageous it forms, as shown schematically in figure 5.4, sectors with fluctuating boundaries. First I introduce the local speed model which neglects fluctuations. Afterwards, the influence of genetic drift is analysed and finally the predictions compared to experiments.

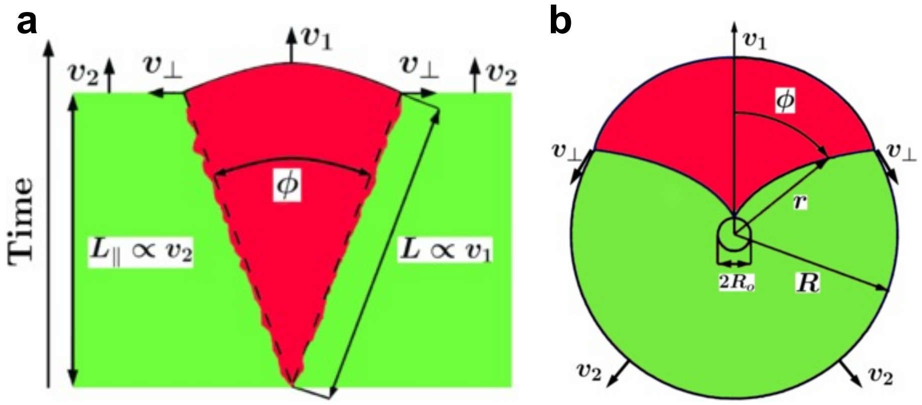

Figure 5.4: Illustration of the local speed model for **a** line or **b** circular inoculations. The growth speed of the strains are v_1 and v_2 respectively. Note the different definitions of the opening angle Φ depending on the geometry. The figures are adapted from Korolev et al. [110] with permission from IOP Publishing, Ltd.

Local speed model or equal time argument

This section presents a simple geometric model which predicts the sector shape of competing microbial stains. This is approach is known in the literature as the equal time argument or more recently as the local speed model [110, 111, 112].

Consider a colony growing from flat initial conditions as depicted in figure 5.4. The advantageous strain grows with velocity v_1 while the background strain grows with velocity v_2. The idealized resulting sector shape is an isosceles triangle with an opening angle Φ. The selective advantage is defined as $s = \frac{v_1}{v_2} - 1$. The equal time argument states that in the amount of time the less fit strain grows along the surface normal the advantageous strain grows the longer distance along the sector boundary. Therefore the sector boundary length L and the growth length of the colony $L_\perp$ are related by $L = \frac{v_1}{v_2} L_\perp$ and the relation to the opening angle is (see figure 5.4a)

$$\tan\left(\frac{\Phi}{2}\right) = \sqrt{\left(\frac{v_1}{v_2}\right)^2 - 1} = \sqrt{s\,(2+s)}\ .$$

The same reasoning can be applied for circular inoculations in the infinitesimal time interval (see figure 5.4 b). This results in a differential equation which has according to Korolev et al. [110] the solution

$$\Phi = \pm\sqrt{s\,(2+s)}\log\left(\frac{r}{r_0}\right)\ .$$

Here the initial colony radius is r_0 and the sign depends on the clockwise or anticlockwise turning direction of the boundaries. Note that in radial inoculations Φ is only half the full opening angle.

Including genetic drift

The influence of genetic drift was studied by Hallatschek and Nelson [94] by adding fluctuations to the motion of the sector boundaries. Since selection is considered a bias parameter $m_\perp$ is introduced such that the relative boundary motion is described as a diffusive random walker with drift, i.e.

$$\frac{\partial p}{\partial t} = 2D\frac{\partial^2 p}{\partial x^2} - 2m_\perp \frac{\partial p}{\partial x} \ , \tag{5.5}$$

where $p = p(x, t|x_0, t_0)$ is the probability distribution of having boundary separation x at time t when having separation x_0 at t_0. Note that t is a time-like variable i.e. the colonies height or radius.[11] Therefore the mean separation of the sector boundaries grows linearly in time i.e. $2m_\perp t$, whereby the standard deviation only grows diffusively. Therefore in the asymptotic limit, the bias parameter can be related to the opening angle as introduced for line inoculations in the previous section via $m_\perp = \tan\left(\frac{\Phi}{2}\right)$.

For an advantageous sector $(m_\perp > 0)$ the fixation probability can be computed from equation 5.5 to be

$$p_{\text{fix}} = \frac{1 - e^{-\frac{m_\perp x_0}{D}}}{1 - e^{-\frac{m_\perp L}{D}}} \ .$$

This result is under suitable identifications of parameters identical to the fixation probability of the non-spatial model but an analysis of the time dependence shows that the fixation time in the spatial model scales as $\frac{L}{D}$ while in the non-spatial case it scaled with $\ln L$. Furthermore, the equation predicts that in opposition to the deterministic case only a sector of size $x_0 \gg \frac{D}{m_\perp}$ certainly won't be extinct.

---

[11] Note that in the publication of Hallatschek and Nelson [94] the second moment is introduced as $2Dt$, which is inconsistent with their definitions in the backward equation. If $2Dt$ is introduced as the variance the publication remains consistent.

For a deleterious sector ($m_\perp < 0$) the sector will be eventually trapped and the average sector size can be computed to be

$$\langle A \rangle = \int_{t_0}^{\infty} dr \int_0^{\infty} dx\ x\ p(x,t|x_0,t_0) = \frac{x_0^2}{4|m_\perp|} + \frac{Dx_0}{2m_\perp^2}\ ,$$

where the first term reflects the deterministic expectation predicted from the local speed model, i.e. its the area of an isosceles triangle with width x_0 and height $\frac{x_0}{2|m_\perp|}$. Corrections to this deterministic expectation only play a dominant role for small sectors i.e. $x_0 \ll \frac{2D}{|m_\perp|}$.

Experiments

The predictions of the local speed model have been tested by Korolev et al. [110] with competition experiments of *S. cerevisiae* strains. First, the assumption of fixed growth speed was tested and only after an initial transient a constant growth speed was established. The authors attribute the transient to nutrient depletion and drying out of the agar gel. Subsequently, the sector shape was analysed for line and radial inoculations respectively and the asymptotic shape agrees with the predictions.

The equal time argument can also be applied to a deleterious strain but the extinction dynamics show a two phase behaviour [111]. First, the sector size decreases at a constant rate agreeing with the predictions of the local speed model but the sector boundaries don't collide leading to prolonged extinction times (see figure 5.5 a). This behaviour could be recreated by a two species KPZ equation and the authors, therefore, attribute the prolonged extinction times to surface tension avoiding infinity at the extinction point. Simulation of an individual based mechanical model, incorporating surface tension by nutrient-dependent growth rates and pushing due to cell division could also recreate the prolonged survival of sectors. While the authors claim this is due to the effective surface tension an Eden model did not reproduce the dynamics. Since the Eden model belongs to the KPZ universality class and KPZ growth contains surface tension this seems contradictory. However, the KPZ equation describes the Eden model only in the hydrodynamic limit, but here the finite sizes of the particles lead to avoidance of infinite surface tensions at coalescing boundaries. However, the experiments show that even non-dividing cells are transported 10 cell diameters in half

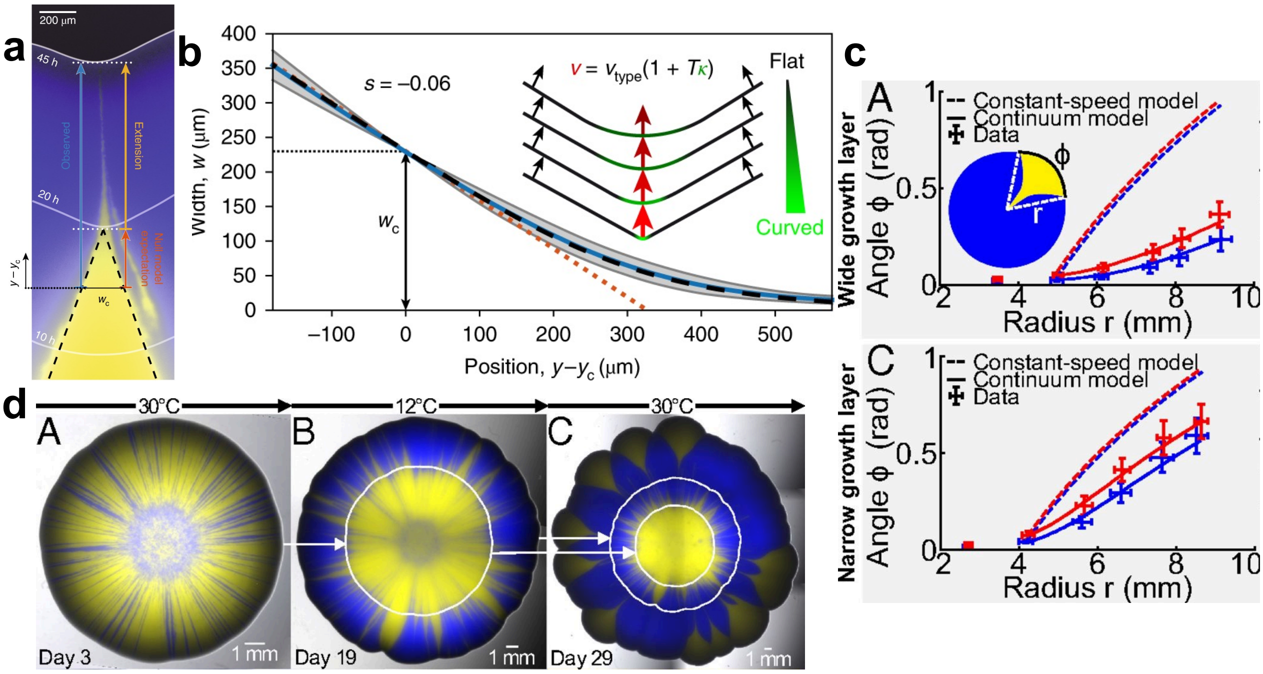

Figure 5.5: **(a)** Mutant (yellow) competing with wild type *S. cerevisiae* with relative fitness $s = -0.06$. y_c is defined as the colony height where both clone boundaries have a distance of 230 μm. **(b)** Distance between boundaries of clone sector of experiments (blue line with the grey area as standard deviation from 9 experiments), fitted interface model (black) and local speed model (red). **(c)** Fitted opening angles for wide and narrow growth layer for large (red) and small (blue) angles respectively. **(d)** Temperature depended range expansion illustrating evolutionary rescue in changing environments. The figures **(a)**, **(b)** are adapted from Kayser et al. [111] with the permission from Springer Nature. The figures **(c)**, **(d)** are adapted from Giometto et al. [112] by permission from Giometto.

a generation by division induced pushing of cells. This transport is not realized in a simple Eden model and likely the reason for the prolonged survival.

As Kayser et al. [111], Giometto et al. [112] also studied the competition of two *S. cerevisiae* and confirm the prolonged survival of the deleterious strain. Additionally, Giometto et al. [112] analysed the sector growth of an advantageous strain and found that it grows slower than the predictions from the local speed model. The authors introduce a hydrodynamic continuum model which treats the colony as a quasi-two-dimensional fluid at a constant density that is driven by a nutrient field $\vec{g}$. This couples the growth velocity $\vec{v}$ ($\nabla \cdot \vec{v} = \vec{g}$) via the Navier-Stokes equation to the pressure field $\nabla p = -\gamma \vec{v}$. Combining all assumptions leads to a Poisson equation with Dirichlet boundary condition at the perimeter which can easily be solved. A growth layer is implemented by specifying $\vec{g}$ as constant up to distance δ away from the perimeter and otherwise setting it to zero. Competing strains are then implemented by a simple two-species extension of the equations including the exclusion of both strains. In the limit $\delta \to 0$ the local speed model is retained. This model recreates the thin filaments and the slowed-down sector growth for narrow and wide growth layers respectively (see figure 5.5 c). Interestingly the model predicts faster sector growth for smaller growth layers which was also confirmed by experiments.

Both experiments demonstrate that collective division induced pushing forces significantly change the competition dynamics for sectors. For disadvantageous strains, this leads to sustained survival which can lead to evolutionary rescue in changing environments and promote the accumulation of deleterious mutations (see figure 5.5 d) [111, 112]. Since antibiotic resistance is typically acquired at a cost in growth speed this has interesting applications. Additionally, the overtake of advantageous mutants is slowed down leading to increased diversity inside expanding populations.

5.3.3 The fate of mutants

Since in range expansions genetic drift is increased, compared to well-mixed growth, selection is weaker. However, populations in well-mixed growth grow exponentially fast while range expansions from radial inoculations grow only proportional to the population at the colonies perimeter. Therefore, if the final population sizes are identical, selection has much more time to act in range expansions. This prompts the question if expansion promotes adaptation compared to well-mixed growth when the final population sizes are identical.

To this end, Gralka et al. [98] compared the final mutant frequency of a co-inoculation of mutant and wild type *S. cerevisiae* strain in range expansion experiments to growth in liquid flasks (see figure 5.6). They observed in range expansions an increased mutant frequency which rose with an increase in the selective advantage (see figure 5.6). While I only show the qualitative features the authors also quantified this by counting the number of sectors and computing their area. The qualitative features are mostly reproduced by an Eden-growth model. However, the area per sector increases only linearly in the Eden model while the experiments show a more rapid increase. This can be attributed to the absence of collective pushing as discussed in section 5.3.2.

Furthermore, the authors analysed the influence of selective advantage for various strains and growth conditions (see figure 5.7 b, d, f). They computed the surfing probability, i.e. which fraction of mutants at the perimeter of the inoculation zone form

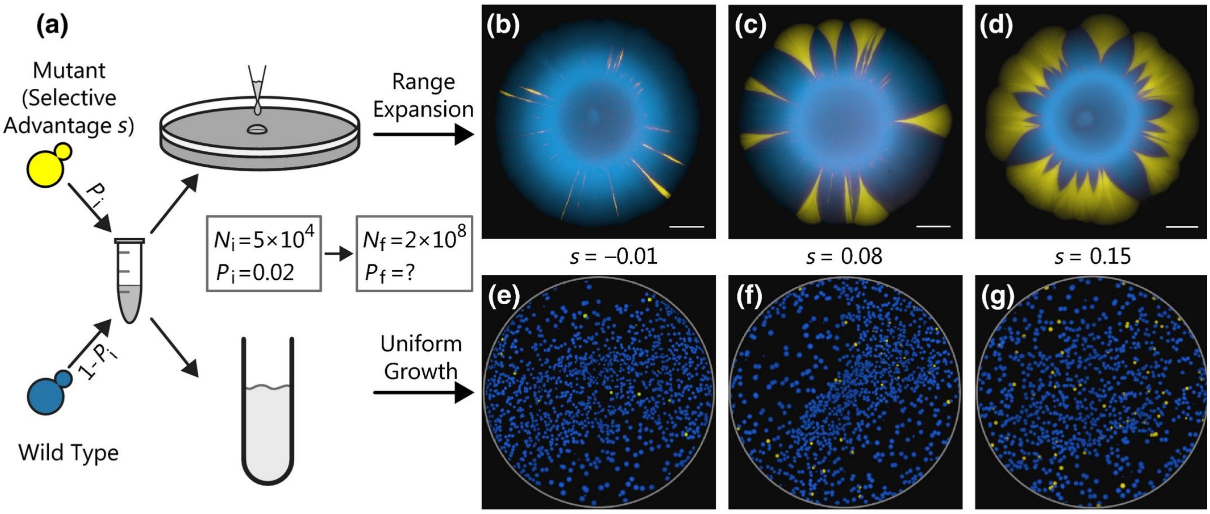

Figure 5.6: **(a)** Co-inoculation of *S. cerevisiae* strains with different selective advantages lead to more mutants in range expansion experiments (**(c)-(e)**) compared to growth in liquid flasks (**(f)-(h)**). The figure is adapted from Gralka et al. [98] with permission from WILEY.

surviving sectors. This quantity increases monotonously with an increased selective advantage for all analysed strains and growth conditions (see figure 5.7 g). The order of magnitude varies greatly between strains and growth conditions. The authors attribute this to the enormous difference in the genetic drift in neutral range expansions (see figure 5.7 a, c, d) which correlates with the number of surviving sectors when selective advantage is present (see figure 5.7 h).

The dynamical creation of mutants during range expansions has also been investigated by Gralka and Hallatschek [113] for an *E. coli* strain. The final mutant frequency displays rather similar behaviour to the results presented here. However, a detailed comparison is missing. More interestingly the authors also changed the underlying surface roughness, which changed the absolute growth speed of the competing strains but not their relative speeds. The rough surfaces had a roughness, defined as the standard deviation of the surface height, of 10 μm.[12] On the rough surface the mutant frequency stayed rather flat for even big selective advantages. These results could be recreated by an Eden model with quenched surfaces sites, i.e. sites chosen at the start of the simulation that are obstacles. These results nicely illustrate that in range expansion experiments, not just the position relative to the colony, i.e. bulk or perimeter, but also the position relative to the heterogeneities in the environment are important.

---

[12] This is approximately the tenfold radius of and individual *E. coli* bacterium.

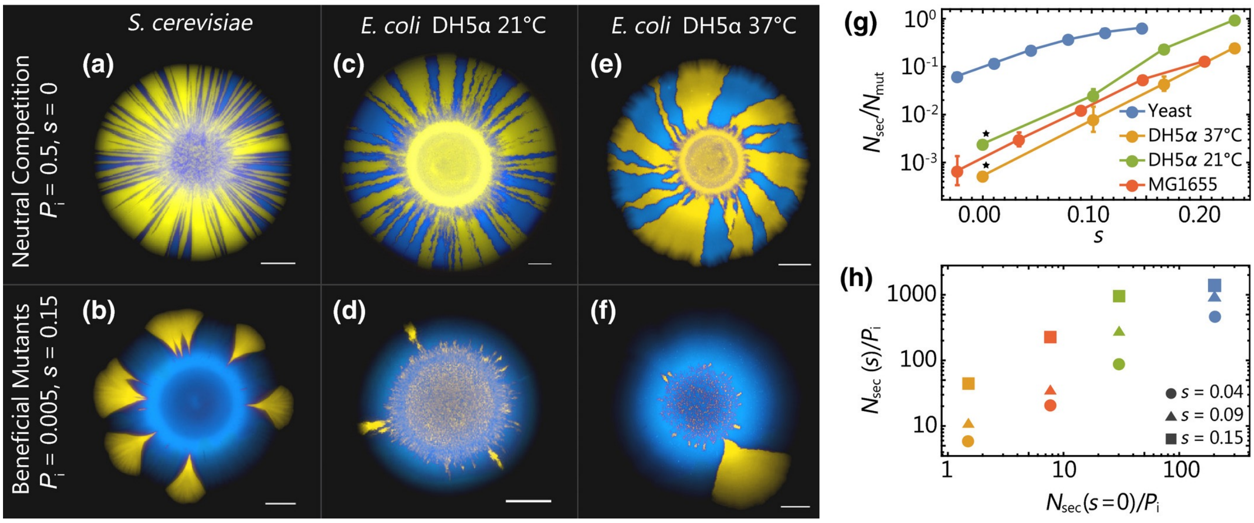

Figure 5.7: Competitive range expansion experiments with initial fraction P_i of mutants. **(a),(c),(d)** Neutral and **(b),(d),(e)** selective range expansion experiments with selective advantage $s = 0.15$. The selective advantage is defined as the relative growth rate in liquid culture. **(g)** Surfing probability as the fraction of surviving sectors per mutants at the perimeter of the inoculation zone for various selective advantages s. **(h)** Number of surviving sectors per initial mutant correlates with the values in neutral expansions. Scale bars 2 mm. The figure is reprinted from Gralka et al. [98] with permission from WILEY.

5.3.4 Selection advantage: mechanical properties

Reduced substrate adhesion increases the growth speed of *E. coli* colonies and leads, in competitive growth of a more and a less adhesive strain, to the out competition of the less mobile strain [114]. Colony growth can also be enhanced by the secretion of EPS (see figure 5.8 a), which leads to an increase in osmotic pressure. This enhances nutrient uptake and swelling of the colony [115]. The osmotic pressure was controlled by the agar concentration. Since this changes the stiffness the colony was grown on top of a semi-permeable membrane reducing the influence of the agars stiffness. However, EPS production also leads to stripe formation (see figure 5.8 a), which has been linked to a mechanical instability mediated by the interplay of nutrient consumption, EPS production and biofilm substratum friction [116]. Since EPS production can enhance the friction of the colony with the membrane the aforementioned growth advantage is even more noteworthy.

Furthermore, Yan et al. [115] investigated if non EPS producing cells could benefit from the EPS production of other cells in a co-inoculation. Interestingly, they observed cell sorting where the non EPS producing cells are pushed to the perimeter of the colony and subsequently get displaced by the bulk while staying at the front (see figure 5.8 b).

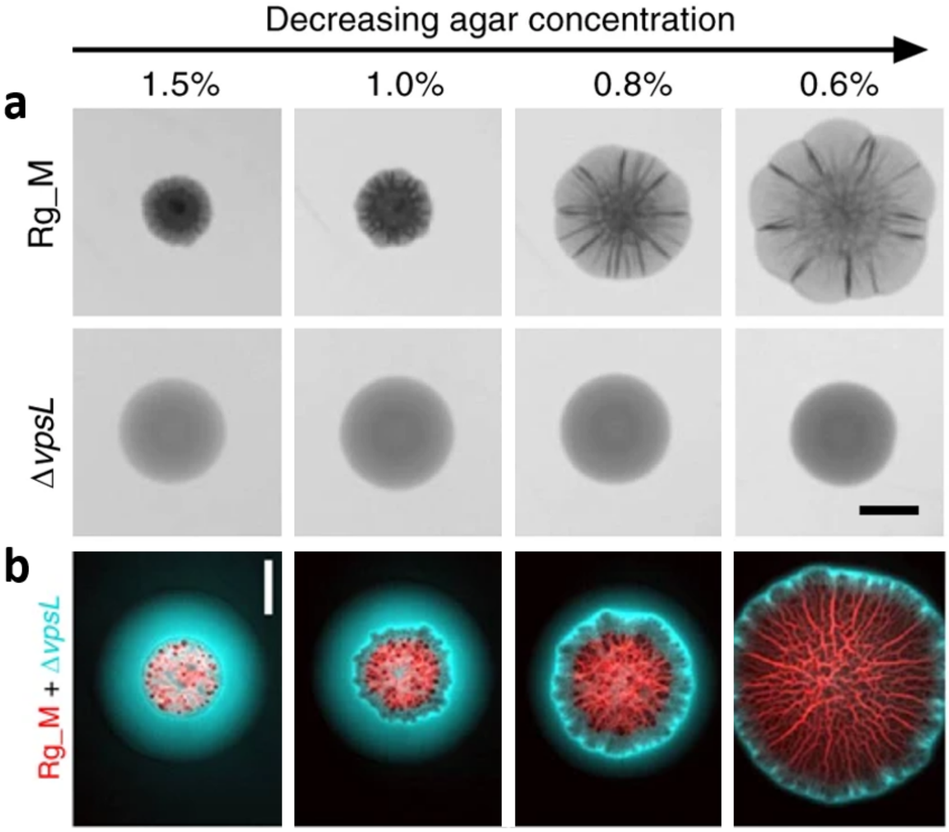

Figure 5.8: **(a)** Range expansion of high and non EPS producing Rg_M ΔvpsL strains. Different osmotic pressures are realized by variable agar concentration. Scale bar 0.5 cm. **(b)** Mixture of EPS producing and non producing strain. Scale bar 0.3 cm. The figures are adapted from Yan et al. [115] under the CC BY 4.0 license.

The authors hypothesize that this sorting is mediated by local swelling of the colony, which transports the cells towards the colonies perimeter. This affects mostly non EPS producers since EPS producing cells are more likely to be connected to EPS which they produced. The connection to the EPS likely reduces the strain's susceptibility to pushing forces generated by cell divisions and local swelling.

Systematic simulation studies on the influence of mechanical interactions in competitive range expansion are scares. However, at the end of section 5.1 presented model of Farrell et al. [91] is such a study. Farrell et al. [91] demonstrate that only mutations occurring at the perimeter of the growing colony have a reasonably high chance of surfing. This surfing probability is influenced by the roughness of the surface. More specifically the local roughness, as the roughness computed over a window of finite size instead of the full system size, provides a collapse of the surfing probability for different system sizes. The local roughness is influenced by growth and mechanical factors such as the thickness of the growth layer and friction anisotropy. While it is obvious that also the local roughness should be influenced by cellular alignment and varying aspect ratios, the authors did not quantify this. Friction anisotropy, however, is quantified and only in the isotropic case a clear decrease of the surfing probability with increased roughness is observed. Experimentally the decay of the surfing probability with increasing local roughness is confirmed for *E. coli*, while for *S. cerevisiae* this is not observed. Farrell et al. [91] attribute this failure to the minimal changes in roughness in the tested experimental conditions.

Cell sorting

As introduced in section 3.2.2 *N. gonorrhoeae*, possess extracellular polymers named type IV pili which undergo phase and antigenic variation. If populations with different levels of piliation are grown in liquid flasks the colonies display distinct patterns shown in figure 5.9 a-d [57]. These patterns are consistent with the “differential adhesion hypothesis” (DAH), which treats adhesion analogous to the mixture of liquids [117]. The predicted patterns are determined by the difference in the surface free energy of the involved phases and are intermixing, self-isolating, spreading complete or incomplete (a-d in figure 5.9). This hypothesis has been critiqued by Harris [118]: He argues that treating adhesion as a thermodynamically reversible process that minimizes the contact area between different phases is too simplistic. This approach neither considers eventually strengthening of adhesive bonds, nor the possibility of heterogeneous distributed adhesion capabilities, such that a minimization of the contact area would not necessarily minimize the free energy. He puts forward the “differential strength of adhesion hypothesis” (DSAH), treating the adhesion as an active process where cell sorting is caused by the rupture of the weakest bonds. Oldewurtel et al. [57] quantified the rupture forces of the involved strains and confirmed that they fit with the observed patterns. Since the patterns fail to be realised if the active retraction of pili is inhibited by deleting the pilT gene, Oldewurtel et al. [57] concluded that this indicates the validity of the DSAH rather than the DAH. I like to point out that by deleting the pilT gene the mobility of the cells is greatly reduced. This mobility, however, is also a key ingredient in the DAH and therefore without determining the remaining mobility the conclusion of Oldewurtel et al. [57] seems premature.

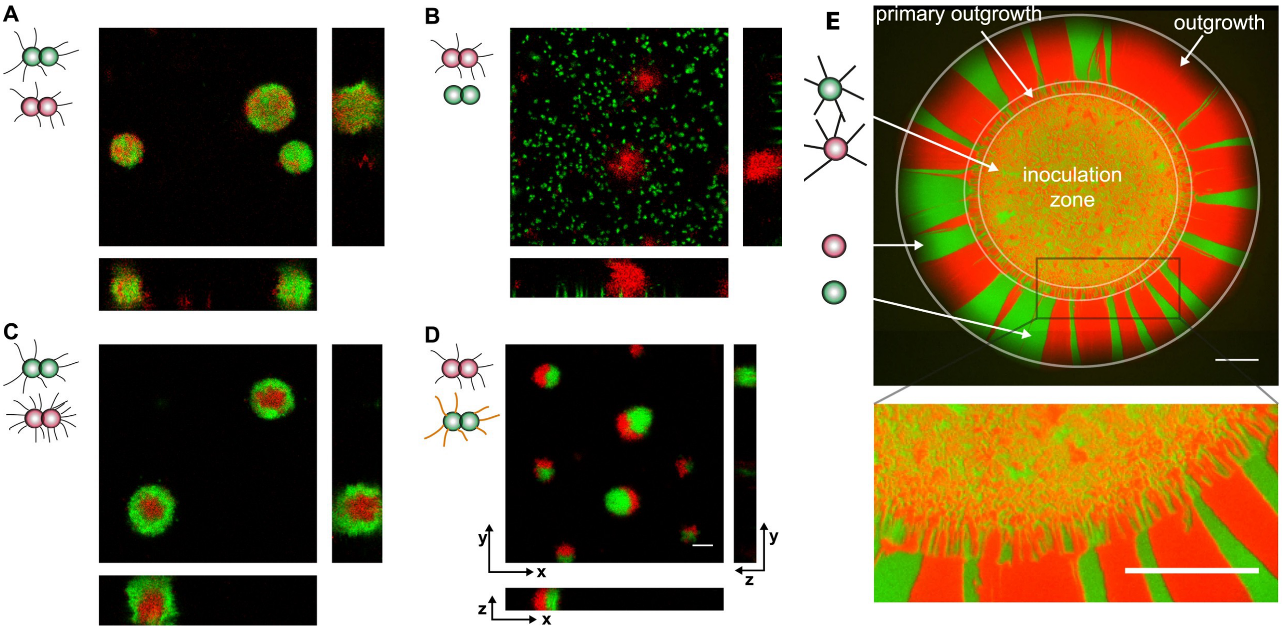

Figure 5.9: Pattern formation in a liquid flask of *N. gonorrhoea* bacteria with different levels of piliation (**A**-**D**). Depending on the pilus density and post-translational modifications **(A)** intermixing, **(B)** self-isolating, **(C)** complete and **(D)** incomplete spreading is observed. Patterns consistent with predictions from DAH and DSAH as determined from rupture forces. **(E)** Range expansion of *N. gonorrhoea* bacteria with **identical levels of piliation** after 48 h. Scale bar: 500 μm. The figures **(A)**-**(D)** are adapted from Oldewurtel et al. [57] while the figure **(E)** is adapted from Zöllner et al. [9]. All figures are adapted under the CC BY 4.0 license.

Zöllner et al. [9] investigated the influence of piliation on range expansion by co-inoculating different fluorescent labelled, but otherwise identical piliated, *N. gonorrhoeae* bacteria (see figure 5.9 e). After 48 hours they observed inside the inoculation zone a random mixture of both strains, while the primary outgrowth forms many small sectors. After $\approx 150\ \mu$m the number of sectors is greatly reduced and the sector boundaries appear rather straight. While it is not clear how the initial densities in this experiments are related to the densities used to create figure 5.3, the sudden strong reduction of sectors seems to distinguish both experiments. Indeed an analysis of the outgrowth by immunofluorescence and morphology inspection revealed that the sectors consist of unpiliated clones, which arise naturally from phase and antigenic variation [9]. Note that in opposition to the claim of the publication, morphology inspection is according to their citation only able to distinguish between piliated and under piliated but not non-piliated morphology [119]. Therefore, the experiments do not rule out that the mutants are under piliated, which will be important for my work presented in chapter 6.

The study furthermore investigated the role of cell sorting on colony growth by co-inoculating a piliated and non-piliated strain (see figure 5.10) in various initial ratios r_{in}. As discussed the non-piliated strain gets sorted to the perimeter of the colony, while additionally Zöllner et al. [9] demonstrated that the non-piliated strain gets displaced by piliated cells during cell division but stay at the front. Analogous to genetic surfing, the authors refer to this transport as surfing. The sorting and transport results in a clear outcompetition of the piliated strain by the non-piliated strain for identical growth rates. Tuning the strain-specific growth rate, by their distinct sensitivity to the antibiotic concentration, showed remarkably that the non-piliated strain could outcompete the piliated strain even with twice as large mean division times.

Sometimes, red sectors with rather moderate opening angles were observed inside the non-piliated outgrowth (see figure 5.10). These are formed by non or under piliated mutants. The dominance of the outgrowth by the unpiliated slow-growing strain is even retained for a colony that initially consists of a hundred times more piliated cells. However, the frequency of non-piliated mutants grows with the initial population of piliated cells, and the mutants become able to compete with the non-piliated outgrowth.

In order to study the interplay of two sorting strains, Dong and Klumpp [120] introduced an Eden-like growth model incorporating cell division and swapping of cells with each other as well as the surrounding medium (see figure 5.11). Events are executed according

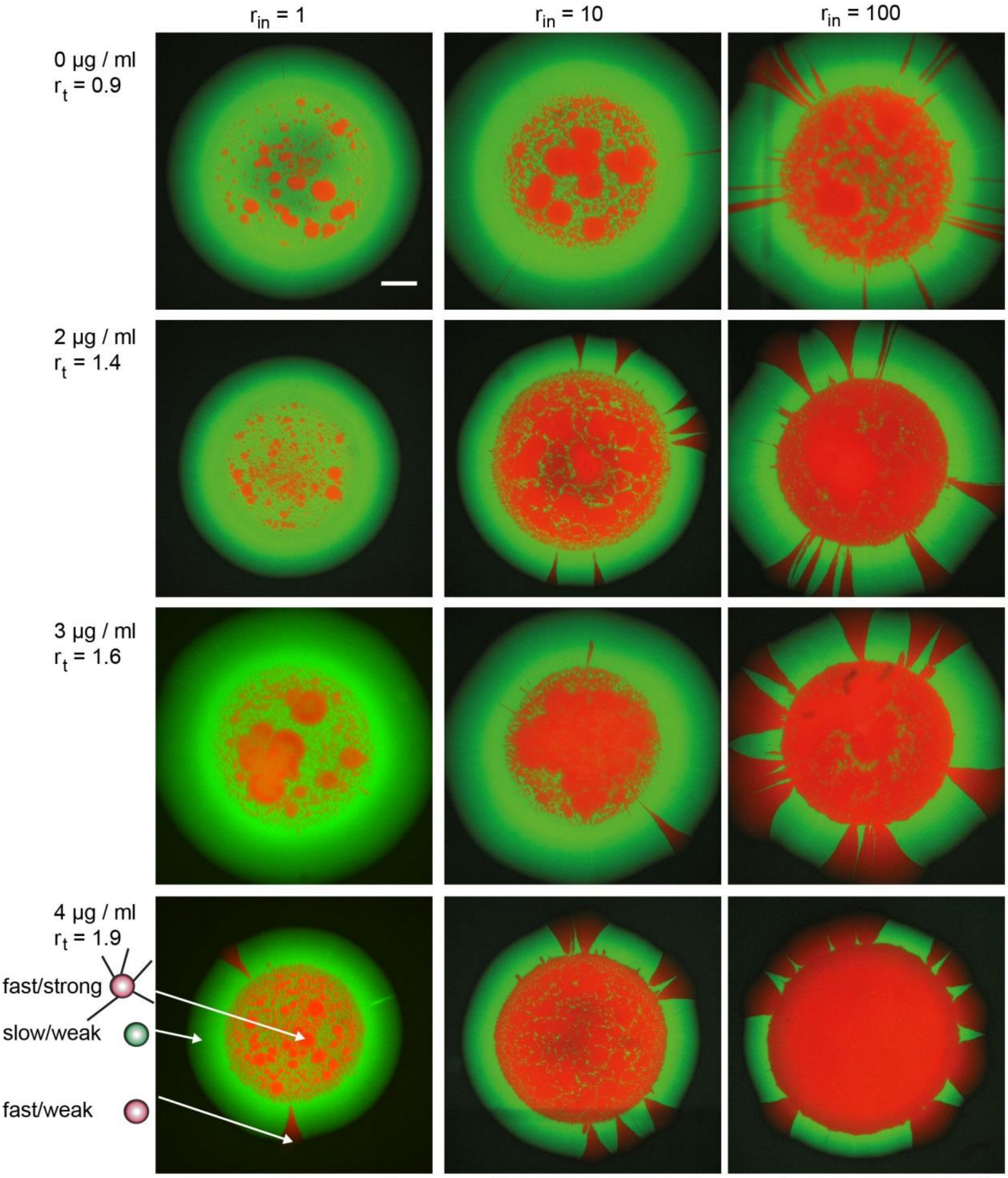

Figure 5.10: Range expansion of *N. gonorrhoea* bacteria with no piliation (green) and piliation (red) after 68-70 h. Scale bar: 500 μm. r_{in} initial fraction of piliated to non-piliated cells. r_t fraction of mean division time of non-piliated to piliated cells. The figure is adapted from Zöllner et al. [9] under the CC BY 4.0 license.

to the stochastic simulation algorithm introduced in section 2.3.2 and swap attempts are accepted according to the Metropolis algorithm. The energy of the system is computed via simple pair-pair interaction energies of both bacterial strains and the surrounding medium. Due to the swapping mechanism, the radius of a colony consisting of a single strain shows two distinct growth speeds. In the strong adhesion case, swapping with empty sites is suppressed and the radius grows linearly with the growth rate, while in the weak adhesion limit the radius grows diffusively. In the case of two non-dividing strains, the model confirms the predictions of the DAH if the particle number is conserved but not if cell division is included.

In the case of dividing cells, the system is initialised as a compact circle, where the less-adhesive cells take up a small wedge (see figure 5.11d). If division rates are identical the less-adhesive cells always engulfed the more-adhesive cells. The interior shows either mixed or fully phase-separated morphology depending on the adhesion energy. Dong and Klumpp [120] argue that engulfment of the more adhesive cells will be typical as long as the effective growth of the less adhesive strain is greater. Because of the two distinct growth regimes, this is expected as long as $4\sqrt{D}u_{\text{strong}} > \sqrt{u_{\text{weak}}}$, where u are the mean division times and D the diffusion constant.[13] The argument predicts engulfment for twice as low division times as long as $D > \frac{1}{2}$. It neglects the effects of inflation on a growing colony and presumes diffusive-like spread of the less-adhesive strain which in the experiments of Zöllner et al. [9] is not observed.

Furthermore, the initial condition confines the fast-growing cells into a sector, which provides the less-adhesive strain with an advantage. This confinement does not reflect the experimental condition of Zöllner et al. [9]. Dong and Klumpp [120] already suspected that the experimentally observed pushing of cells plays a vital role in the competition dynamics. This presumption will be confirmed by my work presented in chapter 6, which designs a stochastic model analysing the influence of pushing on the competition dynamics.

---

[13] The publication states the inequality without $4D$ which is dimensionally inconsistent. Reworking their argument with the previous definition of growth speed leads to the stated equation. The dimension of the diffusion constant is distance^2 per mean division time of the strong interacting strain.

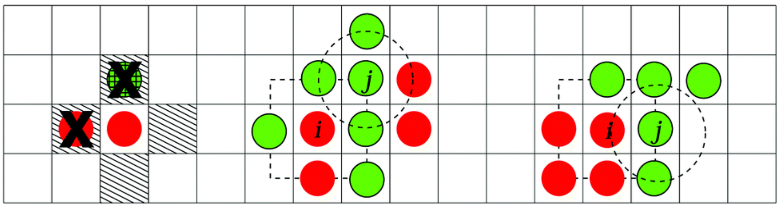

(a) division (b) swap attempt (c) swap attempt

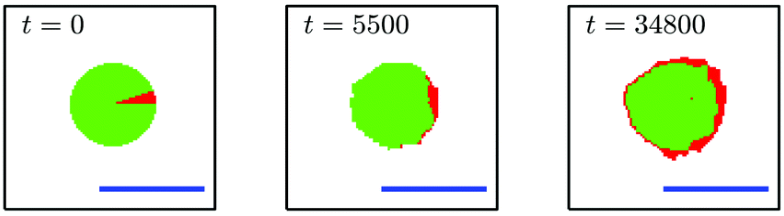

(d) Range expansion with identical growth rates starting from a wedge initial condition

Figure 5.11: Model and simulation results for a range expanding cell sorting population. **(a)** Cell division occurs only to empty nearest neighbour sites. **(b,c)** Possible swap attempt of cell i and j. The neighbouring cells which contribute to the energy calculation are marked in a circle and square respectively. Note, that the swapping considers nearest and next-nearest neighbours (Moore neighbourhood) and swaps to empty sites can occur. The figures and captions are adapted from Dong and Klumpp [120] with permission from The Royal Society of Chemistry.

5.4 Conclusion

This chapter presented the influence of selective advantages on expanding populations by experiments and simulations. It demonstrated the strong effects of genetic drift and the enormous extent to which it is understood. The role of reproduction statistics of individual microbes as a selection advantage has been explored extensively. Mechanical properties, while remaining mainly unexplored, show a strong influence on the structure of growing populations. In particular pushing of microbes due to division generated forces or osmotic pressure differences greatly affected the colony growth. The introduction of competing cell sorting strains provided a new model system that allows investigating the influence of mechanical interactions on the competition dynamics. Remarkably, even if the strong interacting strain divided twice as fast it could not outperform the weaker interacting strain. My work, presented in chapter 6, constructs and analyses a minimal stochastic model, which provides a framework for understanding the influence of division induced pushing as a selection advantage.

6 Modelling competitive range expansion with heterogenous mechanical interactions

In section 5.3.4, I presented competitive range expansion experiments of two *N. gonorrhoea* strains, with different mechanical interactions and tunable reproduction statistics. These experiments show that in neutral competitions (equal mean division times) the weak interacting strain outcompetes the strong interacting strain. This distinguishes this model system from other well studied microbial model systems where in the neutral case no outcompetition is observed. Even more remarkable the outcompetition is still observed when the strong interacting strain divides twice as fast. While the different mechanical interactions induce cell sorting of the weaker interacting strain toward the perimeter it is unclear if this mechanism is sufficient to explain the experimentally observed patterns. As a second mechanism, the heterogeneous interactions could facilitate distinct susceptibilities to division induced pushing of cells. To discern the influence of these distinct mechanisms, this chapter constructs and analyses a minimal stochastic growth model which allows investigating the influence of cell sorting and heterogeneous pushing on competitive growth. I will cover radial inoculations as in the range expansion experiments of two *N. gonorrhoea* strains as well as sector formation from line inoculations.

This chapter is based on the article **Theoretical modelling of competitive microbial range expansion with heterogeneous mechanical interactions** published in Physical Biology, 2021, 18, 016008 by **Erik Maikranz** and Ludger Santen [121]. Section 6.3.3 has not been published and investigates if division induced pushing can lead to filamentous sector growth and corresponding prolonged survival as observed by Kayser et al. [111].

6.1 Model

I model range expansion as Eden-like growth on a two-dimensional hexagonal lattice in continuous time. I consider three cell types with different interactions (corresponding to the degree of piliation) and mean division times. The waiting time between divisions is Weibull distributed with scale parameter λ and form parameter k (Weib(λ, k)), i.e. $(t \geq 0)$

$$\rho(t) = \frac{k}{\lambda}\left(\frac{t}{\lambda}\right)^{k-1} e^{-\left(\frac{t}{\lambda}\right)^k} \,. \tag{6.1}$$

The Weibull distribution reduces to the exponential distribution for $k = 1$, which is often used to model cell division times. The exponential distribution, however, implies that the most probable division time is instantly after the last division. This is biologically not reasonable. The distribution of waiting times between divisions for real cells shows that the minimal time between divisions is comparable to the mean division time [122]. Therefore I will compare the results for an exponential distribution to a regularized distribution with $k = 2$ (see figure 6.1).

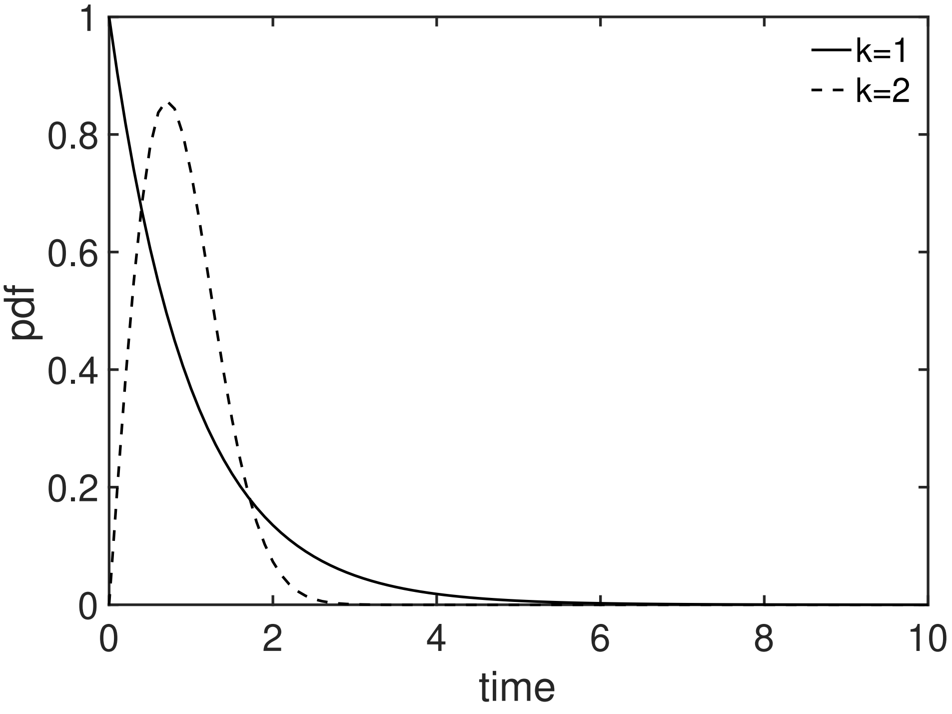

Figure 6.1: Probability density function of the Weibull distribution with scale parameter $\lambda = 1$ and shape parameter k. The figure and caption is reprinted from Maikranz and Santen [121].

The moments of the Weibull distribution are

$$\langle T^n \rangle = \lambda^n \Gamma\left(1+\frac{n}{k}\right) \ , \tag{6.2}$$

where Γ is the Gamma function. Hence, the relative moments of two independent Weibull distributed random variables T_1, T_2 ($\mathrm{Weib}(\lambda_1, k)$, $\mathrm{Weib}(\lambda_2, k)$) are $(\lambda_1/\lambda_2)^n$. As a consequence, I can fix in competitive growth either the relative mean values or scale parameters as long the distribution for all strains uses the same form parameter.

In the following simulations, the strong interacting strain (SI-strain, red) has many pili and divides with scale parameter λ_r, while the weakly interacting strain (WI-strain, green) has no pili and divides with different scale parameter λ_g. Through most of section 6.2, this will be the only strains considered but in section 6.2.2 also a mutant strain (M-strain, yellow) as the progeny of a SI-cell will be introduced. The mutant arises during division and inherits the division statistics of the SI-cell but it loses some of its pili. This leads to a weakening of the mechanical interactions in comparison to the SI-strain. In these experiments of Zöllner et al. [9], the SI-strain was constructed to show only a weak dependence on the antibiotic concentration while the mean division time of the WI-strain was varied. Accordingly, the scale parameter of the SI-strain sets the reference time scale i.e. $\lambda_g = r_d \cdot \lambda_r$ and in accordance with the experiments, I choose $\lambda_r = 1\ h$.

Besides cell divisions also swapping of SI-cells with M- and WI-cells with rate $1/\mu_s$ is considered whereby $\mu_s = r_s \cdot \lambda_r$. All events (divisions and swaps) are selected analogously to the next reaction method of the stochastic simulation algorithm (SSA) presented in section 2.3.2.

6.1.1 Swapping

As presented in section 5.3.4 different levels of piliation lead to cell sorting. I implement this by swapping SI-cells with M- and WI-cells with rate $1/\mu_s$ (swapping of WI- and M-cells is not considered). However, swapping is only allowed if a swap increases the number of neighbouring SI-cells (see figure 6.2 b). Note that this swapping mechanism introduces a subtle asymmetry between SI- and WI-cells at the perimeter of the colony. Since only the number of SI-strain SI-strain interactions are optimized the WI-cells will be most likely sorted to the perimeter with more empty neighbour sites. This asymmetry is also observed in the experiments presented in section 5.3.4, where the WI-strain is always sorted towards the colonies perimeter.

6.1.2 Cell division

The model considers two cases of cell division: In the first case the dividing cell has at least a single empty neighbour site (see figure 6.2 a), while in the second case the neighbour sites are fully occupied (see figure 6.2 d).

In the first case cell division from site I to one of the empty sites J is selected with relative weight

$$w^d_{I \to J} := \sum_j s_j \sum_{i \in <I,J>} I_{S_i = P_j} + \sum_{i \in <I,J>} I_{S_i = E} \ .$$

Here $\sum_{<I,J>}$ denotes the sum over **common** neighbour sites of site I and J. Furthermore, $I_{S=P_j}$ and $I_{S=E}$ indicate if a cell of type j is occupying the site or if it is empty. The stickiness of a given cell type is controlled by the s_j which give additional weight to a neighbour site (see figure 6.2 c).

In the second case, a cell division occurs if the translation of at most P cells leads to a valid configuration, i.e. the last particle of the chain occupies a previously empty site. The strain-specific interaction strengths are reflected by their susceptibility to pushing. While WI-cells can in principle always be pushed I will consider for SI- and M-cells various possibilities. It turns out that to recreate the experimental patterns SI-cells will not be pushable while M-cells can only be pushed to an empty site.

The construction of the push chain occurs in steps such that in each step[1] a cell is translated onto an occupied site or empty next neighbour site (see figure 6.2 d). Note that each pair of sites has three common next neighbour sites. Hence after a translation to a new site, there are only three neighbour sites previously not considered for a translation. To illustrate this consider the first translation where, out of the pushable neighbours of the dividing cell (0th step cell), one random cell is chosen. This chosen cell has six neighbour sites from which only three are not also next neighbours of the dividing cell (0th step). Therefore, I choose the next position only among the accessible

---

[1] Besides the 0th layer which is defined as the dividing cell.

(empty or pushable) three new sites. This is continued such that in the nth step a cell can only be translated onto a site that has been previously not considered for a translation. From this set of accessible sites (empty or pushable) a random site is chosen and the chain continued. The construction of the chain ends if an empty site is found or the maximal chain length P is reached. If the chain cannot be continued because there are no pushable cells or the maximal length is reached the construction goes back to the previous step and chooses randomly a different accessible site to continue the chain. This method guarantees that an empty site is always found if it is within range of the maximal amount of pushes P.

In both cases of cell division, the newly placed cell can mutate with probability p_m into a different cell type. In the present model, I consider only the mutation of a SI-cell into a M-cell.

6.1.3 Initialisation and reference parameters

If not otherwise mentioned the simulations are initialized with 500 cells of the SI- and WI-strain. The cells are randomly distributed in a circular patch at fixed density $\rho_0 = 0.1$. The reference parameters are collected in table 6.1.

Table 6.1: Reference parameters and symbols. The table is reprinted from Maikranz and Santen [121].

initial number of SI-cells	500
initial number of WI-cells	500
initial density ρ_0	0.1
scale parameter of SI-strain	1 h
mean swap time relative to scale parameter of SI-strain r_s	0.1
stickiness of M- and WI-strain s_g, s_y	1
stickiness of SI-strain s_r	1
mutation probability (in division) of SI- to M-strain p_m	0
mean division time of WI-strain relative to mean division time of SI-strain	r_d
maximal amount of cells that can be pushed by the WI-strain	P

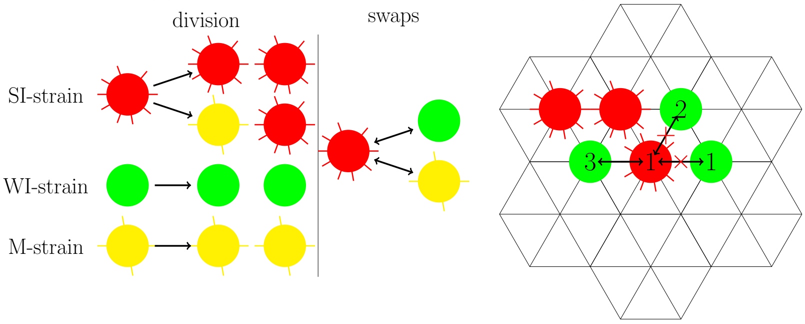

(a) particle dynamics

(b) swapping

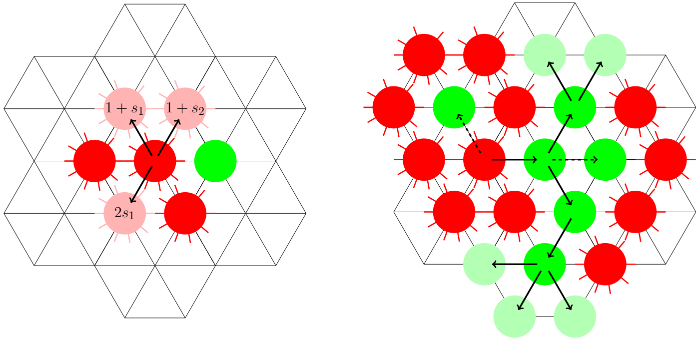

(c) division to empty site

(d) division to occupied site

Figure 6.2: The green cells represent the slow growing weakly interacting strain (WI-strain), while the red cells represent the strong interacting fast growing strain (SI-strain). The yellow cells (M-strain) are the progeny of the red cells which are weaker interacting but are growing as fast as the SI-strain. **(a)** All cell types produce offspring of the same type by cell division but red cells can also produce yellow mutants as offspring. Due to different cell-cell interactions red cells can swap places with yellow and green cells. **(b)** Example of configuration-dependent swap possibilities. The double headed arrow indicates pairs of cells that could swap, whereby the red crosses rule out swaps in which the red particle would have less red neighbours than before the swap. The digit inside the cells denotes the number of surrounding red particles. **(c)** Example of configuration-dependent division weights for a division to an empty site. **(d)** Cell division to occupied sites is possible by pushing neighbouring cells. While in this example the red cells cannot be pushed, the red cell is able to push the green cells and create one of the push paths indicated by the arrows. The paths resulting in a division are marked by continuous black arrows and non-viable paths by dotted arrows. Note, that I construct the final path by following a path until it fails to find an empty side. In particular branching is only considered when the current path fails. In this example the algorithm would **either** find two empty sites (upper path) **or** three empty sites (lower path). The figure and caption is reprinted from Maikranz and Santen [121].

6.2 Effects of division induced pushing in competitive radial range expansion

First, I study the competition between the WI- and SI-strain. Both strains are allowed to be pushed and neither strain is mutating. Therefore, the strong interactions of the SI-strain are only considered by swapping with the WI-strain (see section 6.1.1). The typical colony compositions after 60 h of growth time are shown in figure 6.3 a and are quantified by the mean fraction of WI-cells at radial distance R (MFR) to the origin inside the inoculation zone (see figure 6.3 b).

Competition of cells with equal mean division times ($r_d = 1$):
If neither strain has a divisional advantage a compact random mixture of both strains inside the inoculation zone after 60 h of growth time is observed. The MFR of 0.5 inside the inoculation zone confirms that the inoculation zone is equally filled with both strains. Out of the inoculation zone, the strains grow as monoallelic sectors reminiscent of neutral range expansions presented in section 5.2.1. The MFR, however, shows a monotonic increasing dominance of the WI-strain. This is different from the situation without swapping, where a constant mean fraction of 0.5 is predicted from symmetry considerations as well as from the stepping stone model introduced in section 5.2.1. I attribute this increasing dominance to the asymmetry of the swapping mechanism as already discussed in section 6.1.1. The swapping leads to a systematic reduction of the number of neighbouring empty sites for the SI-strain resulting in a starting advantage for the WI-strain. Furthermore, the swapping stabilises the monoallelic interfaces leading to a slow increase of the MFR. If the cells can push, the initial advantage of the WI-strain is amplified and additionally, the sector interfaces can be overcome. This leads to increasing dominance of the WI-strain with increasing P, but particularly for small values of P long-living SI-strain sectors are observed.

The regularisation ($k = 2$) of division times has two effects: First, it results in smaller radial extensions of the colony. Since the mean division time is $\sqrt{\pi}/2$ times smaller than for $k = 1$ bigger radial extension would be expected (see equation 6.2). However, the growth of the colony is determined by the competition for vacant sizes by many cells at the same time. This minimal time can be computed (see appendix equation A.4) for the Weibull distribution and is significantly shorter for an exponential distribution ($k = 1$) than for $k = 2$. Second, the MFR for $k = 2$ is larger than for $k = 1$. This indicates

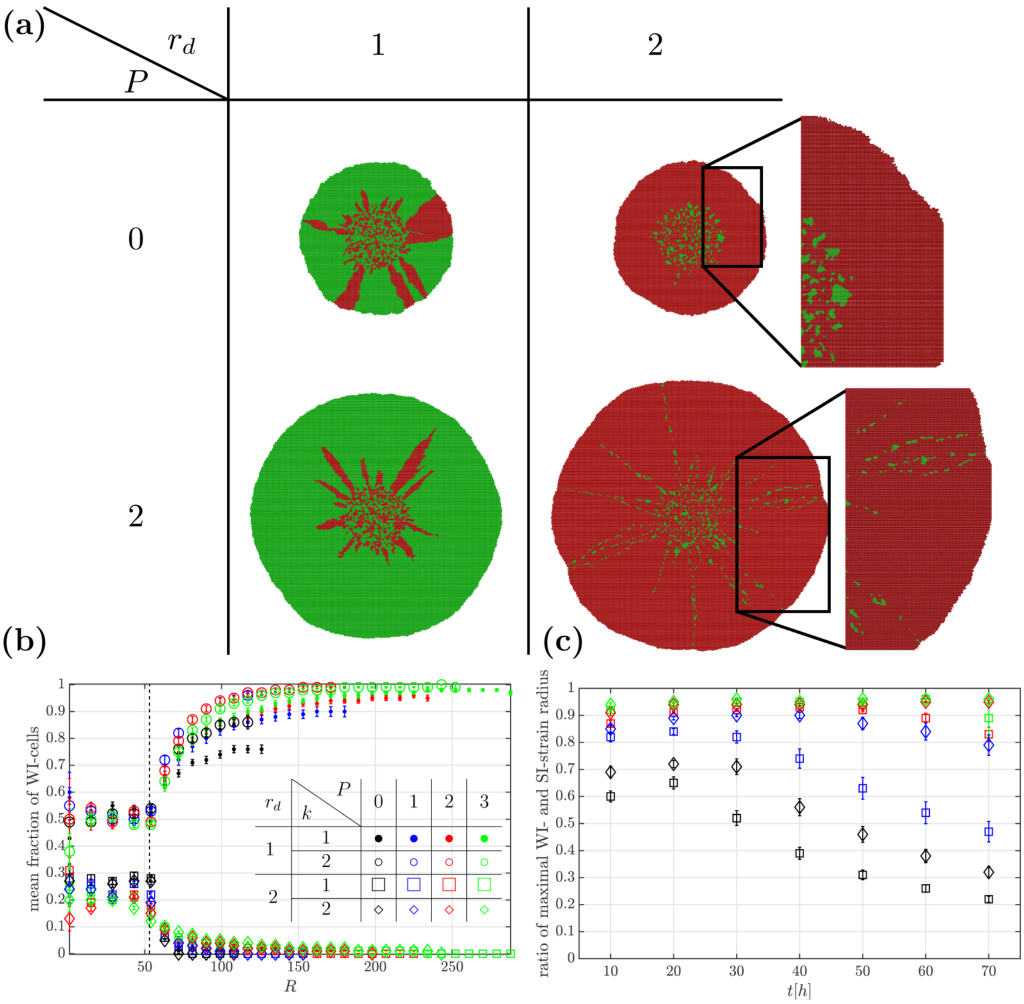

Figure 6.3: Range expansion simulation of weakly interacting slow growing (WI, green) and fast growing strong interacting (SI, red) strains with relative mean division times r_d and maximal allowed pushes P. Here, **both** strains can be pushed equally and swapping is considered. **(a)** Typical phases for shape parameter $k = 2$ where for $k = 1$ I observe similar results. For $P = 2$ and $r_d = 1$ sectors still grow to the perimeter of the colony but die out for $P = 3$. **(b)** Mean fraction of WI-cells up to radial distance R, after 60 h of growth time. The dotted line indicates the initial radius of the inoculation zone. **(c)** Mean fraction of the maximal radial distances of the WI-strain. Values close to one indicate survival. Values for $r_d = 1$ would be greater one and are not shown. The figure and caption is reprinted from Maikranz and Santen [121].

faster annihilation of outgrowing sectors with varying P. Indeed, the SI-sectors get annihilated for $P = 2$, while for $k = 1$ the sectors still reach the colony frontier and get extinct for $P = 3$.

Impact of divisional advantage ($r_d = 2$):

In the case of a substantial divisional advantage ($r_d = 2$) the SI-strain dominates the colony for all values of P. Quantitatively, this is represented in an MFR below 0.5 inside the inoculation zone, while outside the inoculation it decreases monotonically to zero. Note that this dominance is naively expected but it does deviate from the experimental results presented in section 5.3.4 where the WI-strain dominated. Therefore swapping is not sufficient to recreate the observed patterns but nevertheless, some interesting results are obtained for $P \neq 0$:

While for $P = 0$ the WI-strain becomes completely extinct, for $P \neq 0$ the expanding population of SI-cells transports a small population of WI-cells (see figure 6.3 a). This results in a sustained standing variation of strains inside the expanding population and is not predicted by continuum theories. The MFR, due to the stochastic radial position and small population size, is not a good quantity to characterise survival. Therefore, I calculate for every colony the maximal radial distances of all WI- and SI-cells respectively and use their fraction to characterize survival. Values close to one indicate the existence of WI-cells at the current perimeter of the growing colony and hence sustained transport. In figure 6.3 c the mean values of this fraction at different times are shown for $r_d = 2$. The aforementioned transport indicates survival and increases with an increasing P. Furthermore, the regularisation of the division distribution enhances the observed survival.

6.2.1 Effects of mechanical heterogeneity

Mechanical heterogeneity in this section is realized by different pushing susceptibilities of SI- and WI-cells. In the case of $P = 0$ this is the same scenario as in the previous section, but for $P \neq 0$ only the WI-strain can be pushed. As in section 6.2, the typical phases of the colony are shown in figure 6.4 a and are quantified by the mean fraction of WI-cells at radial distance R (MFR) to the origin inside the inoculation zone (see figure 6.4 b).

If I consider no divisional advantage for any strain ($r_d = 1$), the behaviour inside the inoculation zone is equivalent to the homogeneous case. Outside the inoculation zone, the MFR increases much faster and reaches one already for $R \gtrsim 57$. The regularisation (k dependence) and an increasing amount of pushes have for $P \neq 0$ only a minor effect on the MFR.

Now I turn to the situation, where the heterogeneous susceptibility to pushing can compensate for slower divisions. I focus as in the previous section on $r_d = 2$: As previously

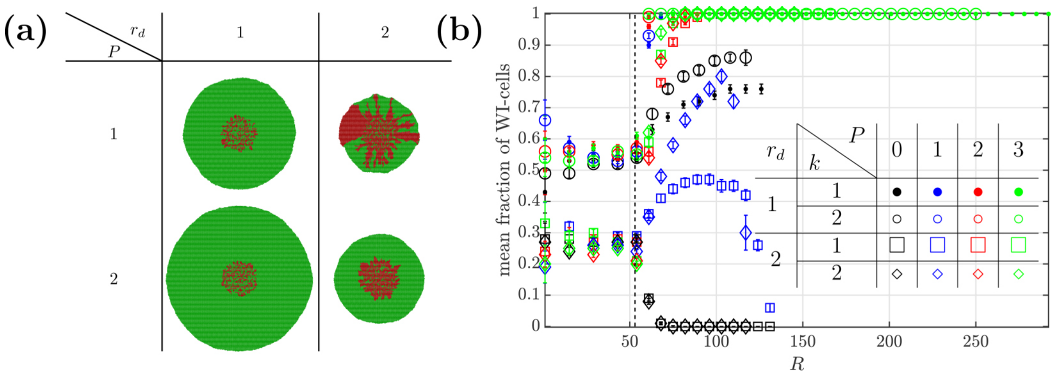

Figure 6.4: Range expansion simulation of weakly interacting slow growing (WI, green) and fast growing strong interacting (SI, red) strains with relative mean division times r_d and maximal allowed pushes P. Here, **only** the WI-strain can be pushed. **(a)** Typical phases of the range expansion for shape parameter $k = 2$. We observe similar results for $k = 1$. **(b)** Mean fraction of WI-cells up to radial distance R, after 60 h of growth time. The dotted line indicates the initial radius of the inoculation zone. The figure and caption is reprinted from Maikranz and Santen [121].

mentioned for $P = 0$ a strong dominance of the SI-strain is observed. For $P = 1$ the pushing supports the outgrowth of the WI-strain which results in a comparable or even higher MFR than the SI-strain below $R \lesssim 100$. The higher MFR is observed for $k = 2$, which shows, as already discussed in section 6.2, that the regularization supports the outgrowth of the disadvantaged WI-strain. For $R > 100$, however, the sectors of the SI-strain dominate the population and the MFR drops fast almost to zero. For $P \geq 2$ the WI-strain dominates the colony growth in almost the same manner as it would possess no divisional disadvantage.

The results demonstrate that larger passive mobility, which I introduced by selective pushing, can beat an extreme divisional disadvantage. This was observed in the experiments introduced in section 5.3.4, and already studied with the help of simulations by Dong and Klumpp [120]. While this work considered swapping cells to energetically favourable positions and diffusion of cells to empty sites the authors did not consider pushing. Furthermore, Dong and Klumpp [120] already observed outcompetition despite divisional disadvantage but I like to emphasize that this strongly depends on the initial conditions. In particular, in their setup, the fast-growing cells were contained in a single compact sector and not randomly placed inside a circular inoculation zone as in the experiments. This discrepancy, especially together with the previous section where no dominance of the slow-growing strain could be observed highlights the importance of selective pushing.

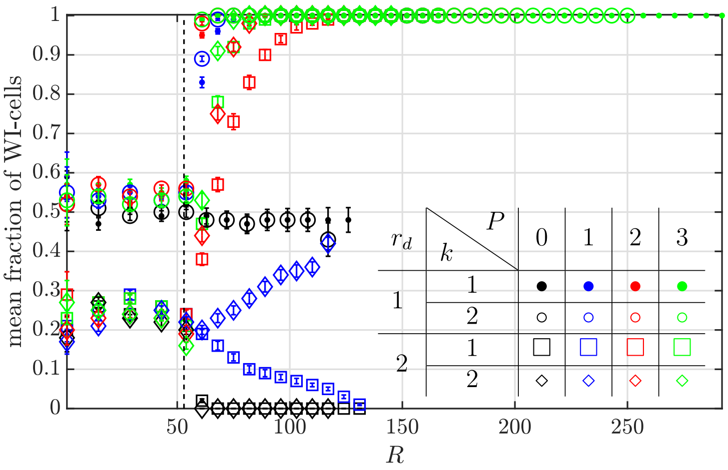

Figure 6.5: Mean fraction of WI-cells up to radial distance R, after 60 h of growth time. The dotted line indicates the initial radius of the inoculation zone. Here, **only** the WI-strain can be pushed and cells were not able so swap. The figure and caption is reprinted from Maikranz and Santen [121].

Next, I investigated the questions if selective pushing is sufficient for the dominance of the slower-growing strain or if swapping is needed as well. To this end I repeated the simulations without swapping (see figure 6.5): First, I consider the neutral case $r_d = 1$. For $P = 0$ both strains have identical properties and the MFR is ≈ 0.5, as expected. Note that this result shows that the dominance of the WI-strain observed for the same parameters but with activated swapping is caused by the asymmetry of the swapping rule. For $P > 0$ comparable patterns to the case with swapping are obtained and the MFR reaches one shortly after the inoculation zone. As in the case with swapping, also only a weak dependence on the parameters k and P is observed.

In the second scenario, I consider $r_d = 2$. The case $P = 1$ nicely demonstrates the strong influence of the waiting time distribution. While in the exponential case ($k = 1$) the MFR decreases, it increases linearly for $k = 2$. For $P \geq 2$ the dominance of the slow-growing strain outside the inoculation zone is obtained. This demonstrates that the mechanical heterogeneity of the pushing is sufficient for the outcompetition and swapping is indeed not needed.

Together, these results suggest that the outcompetition observed in the experiments of Zöllner et al. [9] can be attributed to the heterogeneous transduction of division induced pushing forces, and not to cell sorting of WI-cells to the perimeter of the inoculation zone. While it is unclear if the transduction of pushing forces is related to pili retraction it is known that blocking active pili retraction inhibits cell-sorting [57, 123]. Hence, repeating the experiments with pilT knockout mutants would be a first step in testing this hypothesis.

6.2.2 Radial range expansion with mutants

Now that I could recreate the experimentally observed patterns of Zöllner et al. [9] by considering selective pushing of only WI-cells I investigated the influence of naturally occurring SI-cell mutants. To this end, I consider a finite mutation probability $p_m = 0.001$ of SI- to M-cells and a configuration of pushes where the WI-strain outcompetes the strong interacting strain. Comparing to the previous sections shows that no pushing of the SI-strain and $P = 2$ for the WI-strain is sufficient. Furthermore, Zöllner et al. [9] characterized the properties of the M-strain such that the division statistics remain unchanged from the parent strain but they lose their pili. This suggests that M- and WI-cells possess the same mechanical properties i.e. they should be pushed equally. Simulations with these properties show (see figure 6.6 right column) that the resulting opening angles are much larger than the experimentally observed angles. If the M-cells retain the identical properties of the SI-strain (no push) they get trapped as their parent strain (see figure 6.6 left column). Only if I considered an intermediate amount of pushes (single push) for the mutant strain I obtained M-strain sectors with opening angles comparable to the experimental results.

This indicates that the mutants in the experiments are rather underpiliated and not unpiliated as claimed by Zöllner et al. [9].

6.3 The fate of mutants

The previous section demonstrates that differential passive mobility induced by cell division induced pushing is an important factor in colony growth. I now investigate more in-depth how differential pushing influences the development of a small subpopulation of cells, which are embedded in a larger population. To only investigate the influence of pushing swapping will not be considered. Furthermore, I start the simulations from an initial line where the smaller population (M-/SI-cell) is placed as a compact region inside a background of WI-cells. I use periodic boundary conditions perpendicular to the direction of growth (x-direction $x \in [0,499]$) and a half-open system in y-direction

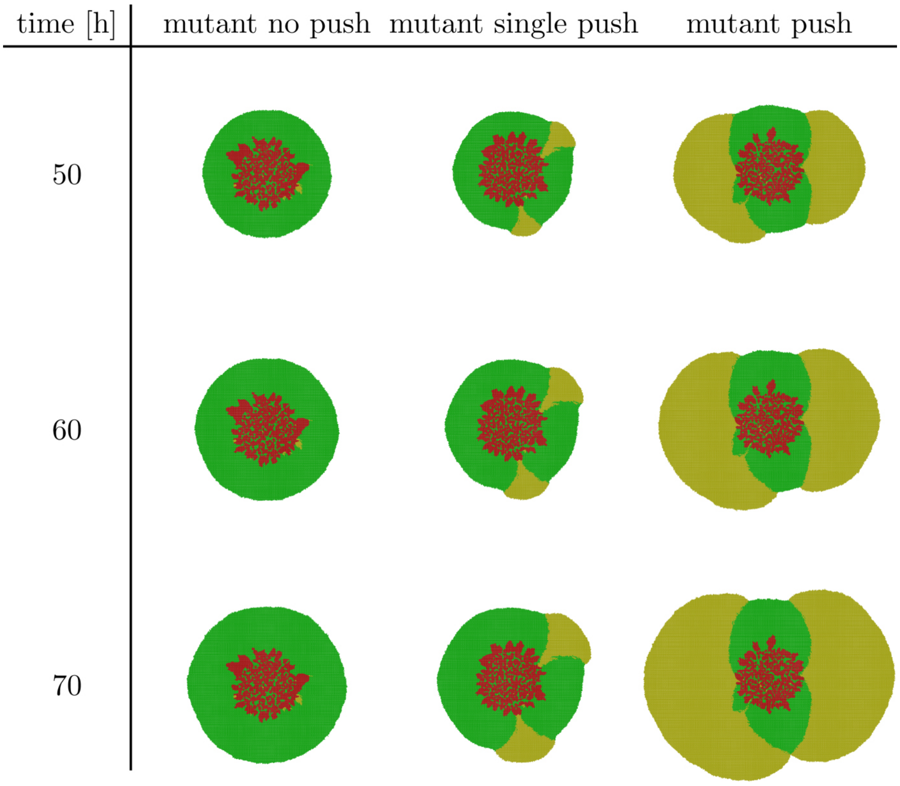

Figure 6.6: Example configurations of mutating SI-cells competing with WI-cells after 50, 60 and 70 hours of growth time. We consider Weibull distributed divison times with $k = 2$, $r_d = 2$ amd $P = 2$ for the WI-strain. The mutation probability is given by $p_m = 10^{-3}$. Configurations are shown for different pushing capabilities of the M-strain (P_M = 0,1,2 from left to right). The figure and caption is reprinted from Maikranz and Santen [121].

($y \in [0, \infty)$).[2] The SI-strain (red) cannot be pushed, while a single M-strain (yellow) can be pushed according to min $(1, P)$. As I have presented in section 5.3.2 such experiments typically lead to growing sectors which can be quantified by their opening angle. To this end, the first subsection will detail how the opening angle is computed and the subsequent subsection will present the results.

---

[2] The coordinates are hexagonal. The conversion to Cartesian coordinates is presented in section 6.3.1.

6.3.1 Computation of sector angles

To compute the opening angles of a sector first the left and right endpoint of the sectors (see figure 6.7) need to be determined. For this, I convert from hexagonal grid coordinates (x', y') to cartesian coordinates by

$$x = x' + \frac{y'}{2}$$
$$y = \frac{\sqrt{3}}{2} y'.$$

To compute the interface height y, I count the number of WI-cells per layer. Subsequently, y is determined as the first layer where the mean and slope change significantly (see figure 6.7b). This can be conveniently performed by the MATLAB function 'findechangepts'. The corresponding x values are then obtained by finding the left and right closest points to the origin in layer y.

From the coordinates (x_i, y) of the left and right endpoint the corresponding left and right angles α_l, α_r are computed via $\alpha_i = \arctan \frac{y}{|x_i|}$. The full opening angle α is obtained by $\alpha := 180° - (\alpha_l + \alpha_r)$.

6.3.2 Advantageous mutants

The small population, here 10 cells, is placed as a compact region inside a background of WI-cells. Consider first the mechanical homogeneous case, i.e. every strain can be pushed equally. This is shown in figure 6.8 a for $P = 0$ and $r_d = 2$. In this situation, always compact sectors are observed which I quantified by their opening angles α. These angles are mostly determined by the divisional advantage r_d, while P and k have only a small influence (see figure 6.8 b). Although the influence of P is much weaker than the influence of the divisional advantage, still a systematic difference between $P = 0$ and $P \geq 1$ can be observed: Since pushing facilitates the occupation of space it increases the opening angle if it has any influence at all.

For heterogeneous pushing, I consider two different scenarios: First, the competition of a small population of the M-strain with the WI-strain. The WI-strain can be pushed according to P while the M-strains pushing capabilities are given by $\min(1, P)$. Therefore, only the cases $P \geq 2$ constitute new scenarios. For $P = 2$ and $r_d \leq 1.6$ the sector

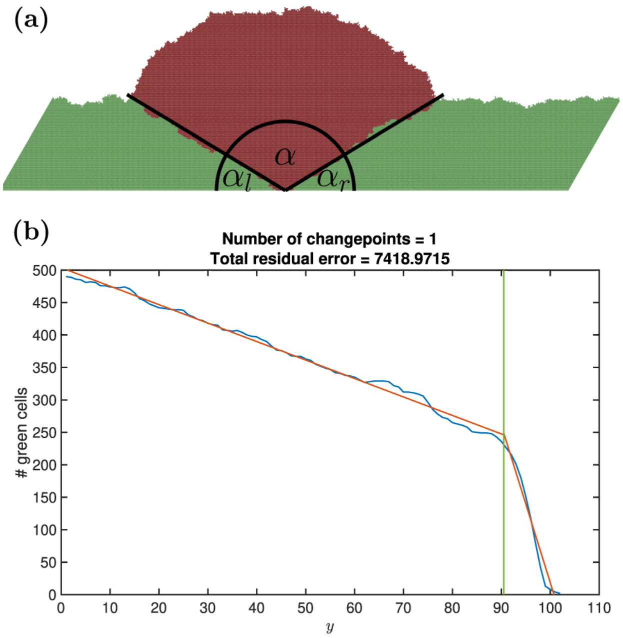

Figure 6.7: **(a)** Opening angle α quantifies the growth advantage of two competing strains. To find α , we compute the angles α_l, α_r via the slope of the lines connecting the origin to the endpoints. **(b)** For computing the y coordinate of the endpoints, we compute the number of WI-cells in layer y and find the first layer where the mean and slope change significantly. The figure and caption is reprinted from Maikranz and Santen [121].

annihilates and only for $r_d \geq 1.8$ do I observe stable sector formation (see figure 6.8 b). For already $P = 3$ and up to $r_d = 2$ the WI-strain background dominates leading to either annihilation or only non increasing opening angles (see figure 6.8 a right column). Note, that the sectors remained monoallelic for all parameters irrespective of outcome (growth or annihilation). In the second scenario, the WI- strain competes with SI-cells which cannot be pushed. For up to $r_d = 2$ and $P \geq 2$ the sectors generally annihilate. In the case of $P = 1$, however, the sectors grow in a dendrite-like shape and survive at least 70 h of growth time. The absence of a monoallelic sector complicates the interpretation of the opening angle which is much smaller than for the compact sectors. To quantify the divisional advantage needed to establish surviving domains for $P = 2$ I varied r_d in the range of three to five (see figure 6.8 a middle column). The simulations show only sector formation for $r_d \geq 4$. Interestingly, these sectors are not monoallelic but rather show a mixture of SI- and WI-cells despite the dominance of SI-strain. This high persistence of WI-cells inside the expanding SI-strain domain is reminiscent of the transport of WI-cells in radial range expansions (see section 6.2). It is caused by the transport of WI-cells towards the colonies surface and demonstrates that heterogeneous

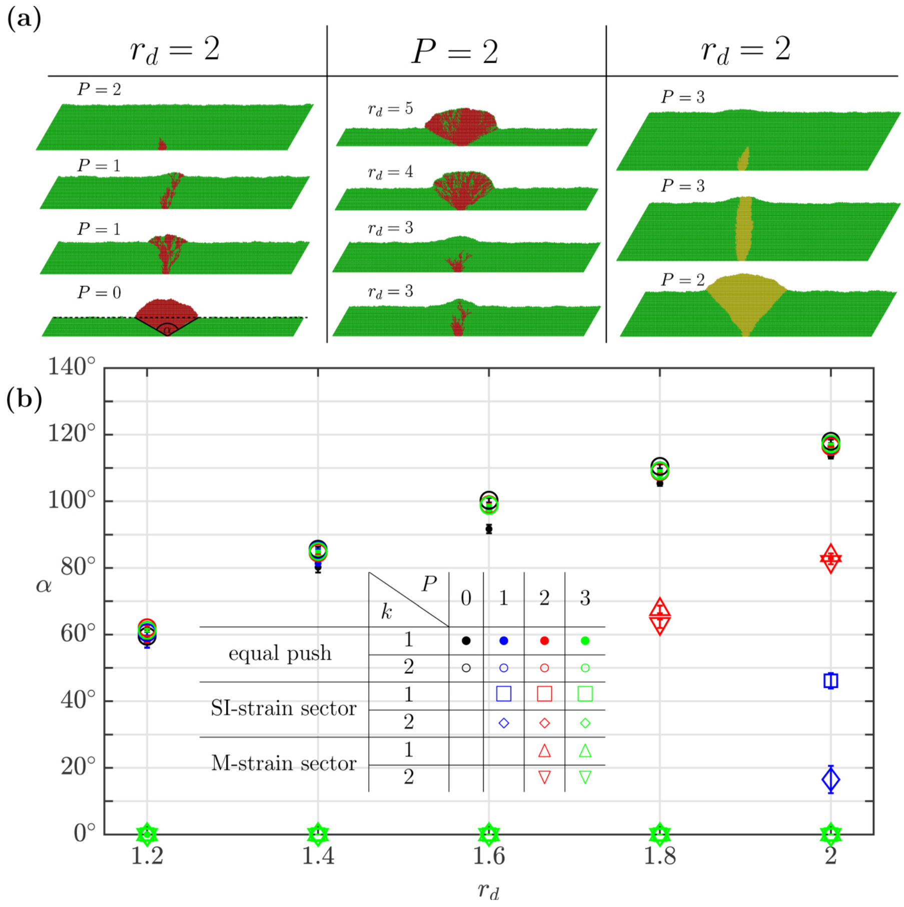

Figure 6.8: Range expansion simulation with 70 h of growth time of a small population inside a bigger population of WI-cells starting from a line inoculation. The simulation uses periodic boundary conditions perpendicular to the growth directions and none of the strains are able to swap. The WI-strain (green) can be pushed according to P , while the M-strain (yellow) can just be pushed according to $\min(1, P)$ and the SI-strain (red) cannot be pushed at all. r_d is the relative division time of the WI-strain with respect to the small initial sub-population. I quantify the sector growth by the opening angle α. **(a)** Illustration of sector dynamics for shape parameter $k = 2$. **(b)** Opening angle α quantifies the relative fitness of the strains. Angles of domains which die out are plotted as zero. The figure and caption is reprinted from Maikranz and Santen [121].

mechanical interactions can establish a standing variation of strains inside the growing sector which is not observed for homogeneous mechanical interactions.

6.3.3 Deleterious mutants and enhanced survival

The small population, here 50 yellow cells, is placed as a compact region inside a background of WI-cells. To investigate if the observed prolonged survival presented in section 5.3.2 could be induced by division driving pushing, I only consider the mechanical homogeneous case, i.e. both strains can be pushed equally. Note that these results have not been published. I consider $r_d = 0.95$, i.e. the slower growing strain (yellow) is embedded in a background of faster growing cells (green cells). As depicted in figure 6.9 the sectors for $P = 0$ form an isosceles triangle compatible with the predictions of the local speed model presented in section 5.3.2. Division induced pushing ($P \neq 0$), however, leads to longer survival and the creation of filamentous sector growth. I quantity this as Kayser et al. [111] (see figure 5.5 b) by the sector width at height y after 100 h of simulated time. At this time all the dynamics in the colonies bulk have ceased and I obtain well-defined values. Since the sectors are not compact I define the sector width as the maximal distance of two yellow cells at height y. Figure 6.9, indeed, shows for $P = 0$ an almost constant sector shrinkage, while for $P \neq 0$ slowed down extinction is observed. This slowed down extinction is enhanced by an increased amount of pushing.

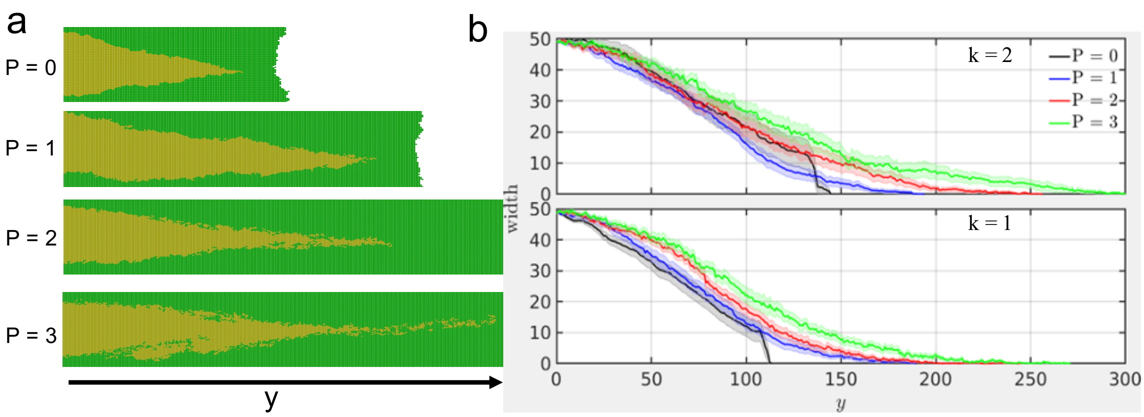

Figure 6.9: Range expansion simulation with 100 h of growth time of a small population inside a bigger population of WI-cells starting from a line inoculation. The simulation uses periodic boundary conditions perpendicular to the growth directions and none of the strains is able to swap. Note that the yellow cells are not M-cells and are pushed identically to the green cells according to P. $r_d = 0.95$ is the relative division time of the green train with respect to the small initial sub-population, i.e. the small sub-population grows more slowly. I quantify the sector survival by the width of the sector. **(a)** Illustration of sector dynamics for shape parameter $k = 2$. Only the figure segment showing the small initial sub-population are shown. **(b)** Width of the sector at height y for non-exponential waiting times ($k = 2$) and exponential division times ($k = 1$).

The constant shrinkage and sustained survival can be observed for exponential ($k = 1$) and non-exponential division times ($k = 2$), whereby the regularisation leads at fixed P to an always comparably prolonged survival.

To summarize, I demonstrated that to observe filamentous growth and corresponding prolonged survival of deleterious mutants inside an expanding colony, division induced pushing is sufficient. In particular, surface tension, a concept ill-defined on the length scale of discrete cells, is in opposition to the claim of Kayser et al. [111] not necessary.

6.4 Conclusion

My work established a coarse-grained stochastic growth model that focuses on the role of division induced pushing in range expanding populations. Particularly, I focused on the role of strain-dependent mechanical and growth specific properties in the competitive growth of several strains starting from line inoculations as well as circular inoculations. All results demonstrate the importance of passive mobility induced by division generated pushing forces in expanding populations. This shows the shortcomings of the often-used growth rate specific fitness definition in mechanical heterogeneous populations and therefore has interesting implications for the growth of microbial colonies but also for the field of evolutionary population genetics as a whole. In particular, I showed:

In circular inoculations for divisional neutral competitions between cell-sorting strains, a subtle detail in the swapping mechanism leads to a broken symmetry between WI- and SI-cells at the perimeter of the colony. This asymmetry leads to the sorting of the WI-cells to the perimeter resulting in a starting advantage for colonising empty space. Subsequently, the WI-cells dominate the outgrowth of the colony. Furthermore, the regularization of division times, i.e. non-exponential distribution, reduces the growth speed of the entire colony and enhances the impact of different mean division times. Since individual cell divisions occur faster, this is remarkable. In particular, it highlights that range expansions need to be understood as a competition about colonizable space. In opposition to the experimental result for *N. gonorrhoea*, the dominance of the WI-strain could be overcome by a strong divisional advantage of the SI-strain. But even in this case, the division induced pushing leads to a standing variation of slower dividing cells inside the outgrowth as a noteworthy result. These standing variations of strains can lead to the evolutionary rescue in changing environments, and as argued by Kayser et al. [111], promotes the accumulation of deleterious mutations inside a growing colony. This contributes to the development of antibiotic resistance which usually comes at a cost in growth speed.

The dominance of the WI-strain in the presence of strong divisional disadvantage could be reproduced by introducing strain-specific susceptibilities to division induced pushing. With these, the experimentally observed patterns could be recreated even in the absence of an explicit cell sorting mechanism. Note that already Dong and Klumpp [120] constructed a model that could reproduce the dominance of the slower-growing strain. However, they used a special initial condition where the faster-growing cells a starting from a compact sector inside a larger domain of slower-growing cells. My results suggest that for the initial conditions fitting to experiments their model will fail to recreate the dominance of the slower-growing strain. In addition, I studied the dynamical creation of SI-cell mutants and found that the experimentally observed patterns can only be recreated with a susceptibility to pushes that lies between the SI- and WI-cells. This leads to the conclusion that the mutants are not unpiliated as claimed by Zöllner et al. [9] but rather underpiliated.

Furthermore, I investigate the role of pushing on the development of an initially small compact domain in line inoculations. The competition of SI- and WI-cells leads either to the extinction of the advantageous sector or to dendrite like structures. By contrast, the competition of M- and WI-cells or cells with equal pushing susceptibilities always leads to essentially compact sectors. For the competition of a deleterious sector with equal pushing susceptibilities, the division induced pushing leads to deviations from the local speed model. In particular, I recreate the filamentous sector growth and corresponding prolonged survival observed by Kayser et al. [111].

7 Modelling single-cell force spectroscopy experiments

This chapter presents single-cell force spectroscopy (SCFS) experiments of *S. aureus* to hydrophobic and hydrophilic abiotic unconditioned surfaces. First, the results on flat surfaces are presented in section 7.1. This section is based on the article **Different binding mechanisms of Staphylococcus aureus to hydrophobic and hydrophilic surfaces** published in Nanoscale, 2020, 12, 19267-19275 by **Erik Maikranz**, Christian Spengler, Nicolas Thewes, Alexander Thewes, Friederike Nolle, Philipp Jung, Markus Bischoff, Ludger Santen and Karin Jacobs [124]. Note that the first authorship is shared with Christian Spengler and that section 7.1.4 provides additional material not yet published.

The second set of experiments investigated the heterogeneous distribution of adhesion capabilities of *S. aureus.* To this end, SCFS experiments were performed on sinusoidal surfaces and the model correspondingly extended. Some first model extensions and results are based on the article **The adhesion capability of S. aureus cells is heterogeneously distributed over the cell envelope** published as a preprint in bioRxiv, 2021 by Christian Spengler, Bernhard A. Glatz, **Erik Maikranz**, Markus Bischoff, Michael Andreas Klatt, Ludger Santen, Andreas Fery and Karin Jacobs [125]. The results and model extension presented in section 7.2 are however much more exhaustive than the already published material.

7.1 SCFS on flat surfaces

The experiments for flat surfaces, presented in section 7.1.1, have been performed by several members of the Jacobs group at Saarland University. However, Christian Spengler and I analysed the obtained force-distance curves. The various results will set my main work of modelling SCFS experiments, presented in section 7.1.2 and afterwards, into context.

7.1.1 Experimental data

The experimentally obtained retraction curves on hydrophobic and hydrophilic surfaces[1] are fundamentally different (see figure 7.1). While on hydrophobic surfaces cup-shaped retraction curves are obtained the curves on hydrophilic surfaces show several peaks which display non-linear force stretch behaviour. Non-linear force stretch curves are commonly observed in single-molecule force spectroscopy experiments for various proteins as introduced in section 3.2.1. They are often described by the worm-like chain model from polymer physics and therefore I will refer to them as ‘WLC-like peaks’. In the experiments presented here most likely, several macromolecules are stretched at the same time. These WLC-like peaks can also be observed on hydrophobic surfaces at separations close to the rupture length (see in particular the inset of figure 7.1 a). This, in addition to the reasons presented in chapter 4, suggests that the adhesion process on both surfaces is to be understood as a stochastic tethering of individual macromolecules.

The following section presents an in-depth analysis of the adhesion characteristics on both hydrophilic and hydrophobic surfaces. In total 64 cells on hydrophobic surfaces and 71 cells on hydrophilic surfaces have been analysed. The experiments can be performed with or without a surface delay time, i.e. time spent above the surface before retraction starts. Note that a nominal surface delay time of 0 s amounts to a ‘real’ contact time below 0.5 s [75, 126]. While on hydrophobic surfaces reliable force-distance curves could be obtained without delay time, on hydrophilic surfaces 19 cells were probed without surface delay time and display no significant adhesion. Since an increased surface delay time can increase the adhesion additionally 52 cells were probed with a surface delay time of 5 s [127]. For curves with surface delay time, the approach speed was set to 100 nm/s, while without any surface delay time it was set to 800 nm/s. For all cells 30 repeated full approach and retraction cycles are performed and analysed:

As described in section 4.1 approach and retraction curves are characterized by the snap-in force (maximum attractive force), snap-in separation (separation at which the

---

[1] The investigated hydrophobic surface has a water contact angle of 5(2)°, while the hydrophilic substrate has an advancing contact angle of 111(1)° and a receding angle of 107(2)°.

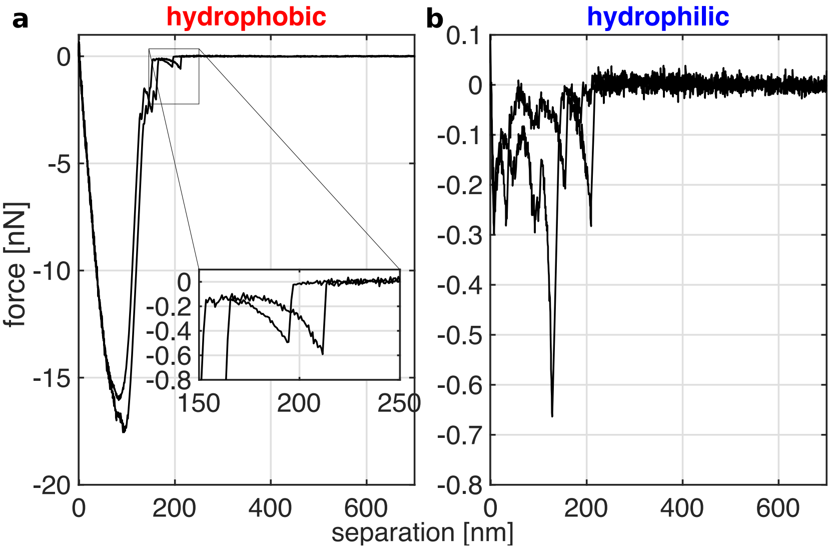

Figure 7.1: Force-separation curves of two repeated SCFS experiments with one specific bacterium (per surface) on a hydrophobic **(a)** and a hydrophilic surface **(b)**. The figure and caption is reprinted from Maikranz et al. [124] with permission from The Royal Society of Chemistry.

sudden attraction starts), adhesion force (maximum force needed to detach an individual cell from the surface) and rupture length (separation at which bacterium and surface lose contact). While the computation of forces is obvious the snap-in separation and rupture length are, due to noise, more difficult to obtain (observe the baseline noise in figure 7.1 b). Therefore, I define the snap-in separation and rupture length as the largest separation where the root mean square of the signal changed the first time[2] significantly from the background noise. This computation is conveniently performed via the Matlab function ‘findchangepts’.

To characterize the stochasticity of the adhesion process all quantities were extracted for every repetition of each cell. Subsequently, mean values and standard deviations are computed for every cell. Additionally, a mean curve was constructed for every cell: To this end, I interpolated along a given grid of separation values and subsequently calculate for each grid point the corresponding mean and standard deviation. The resulting mean curves are plotted with a shaded area representing the standard deviation. Note that the positive forces indicated by parts of the shaded area are only an artefact of the symmetrical display of the standard deviation and the values are, besides the baseline noise, never positive. Furthermore, the entire population was characterized by computing histograms of the mentioned quantities as well as a mean curve from all cells and

---

[2] Both approach and retraction curves are analysed starting from large separations where besides baseline noise no force is observed.

their repetitions. The adhesion forces for repeated measurements with the same cell on hydrophobic surfaces are strongly correlated. Therefore, the errors in the histogram are only divided by the square root of the number of cells.

Approach Curves

All approach curves were analysed as described in section 7.1.1. While the snap-in is rarely observed on hydrophilic surfaces on hydrophobic surfaces nearly all approach curves display it. Therefore, only the curves that feature a reliable snap-in are pooled and the populations' properties calculated (see figure 7.2). As can be already suspected from the different incidences of the snap-in, rather strong differences between curves on hydrophilic and hydrophobic surfaces are observed: On hydrophobic surfaces, the snap-in separation is 51.9(4) nm and hence around four times larger than on hydrophilic surfaces (13.5(4) nm). Even more strikingly the mean snap-in force on hydrophobic surfaces is almost one order of magnitude stronger compared to hydrophilic surfaces (4.2(1) nN vs. 0.06(1) nN).

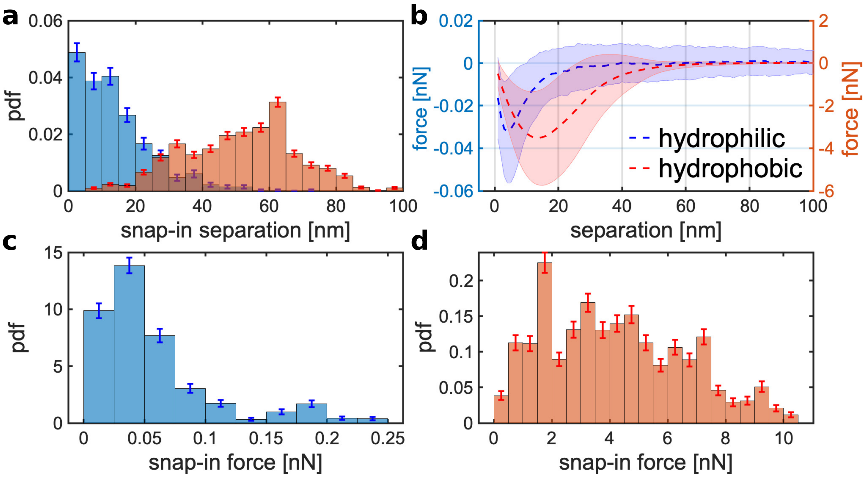

Figure 7.2: (a,c,d) Probability density histograms of snap-in separation and snap-in force of each tested cell on hydrophilic (blue) and hydrophobic (red) surfaces (where histograms overlap, a mixed colour is displayed). **(b)** Corresponding mean approach curve (shaded area is standard deviation) calculated from all tested cells calculated as described in section 7.1.1. The figure and caption is reprinted from Maikranz et al. [124] with permission from The Royal Society of Chemistry.

As explained in section 4.3 the snap-in is mediated by the fast subsequent binding of macromolecules and therefore these observations already hint towards different interaction mechanisms of *S. aureus* on hydrophobic and hydrophilic surfaces. This perception will be corroborated in the successive sections which analyse the retraction curves.

Adhesion to hydrophilic surfaces

As already mentioned in section 7.1.1, force-distance curves on hydrophilic surfaces show without surface delay time no significant adhesion. Therefore, as a first step, I compare the mean retraction curves for 0 s (purple) and 5 s (blue) surface delay time (see figure 7.3 a coloured lines). Both curves show qualitatively similar behaviour: First, the force decreases as the separation increases until it reaches a minimum from which it relaxes back to zero if the separation is increased further. By increasing the delay time the standard deviation increases markedly, the minimum is wider and reached at larger separations. Furthermore, the relaxation to zero starts at much higher separations. I quantify these observations by the adhesion force and rupture length as described in section 7.1.1 (see figure 7.3 b and c). Note that the mean values in the adhesion force histograms do not agree with the corresponding values of the mean curve. This is the case because the positions of the minima are varying. Hence the adhesion force of the mean curve is smaller than the mean of the adhesion forces of individual bacteria.

The rupture lengths vary in both delay times from several tens of nm to a few hundred nm, where for the longer surface delay time larger rupture lengths are observed more frequently. Most notable the adhesion forces a rather different: While for 0 s surface delay time the adhesion forces are mostly close to 0 pN for 5 s delay time the maximum occurrence is at about 700 pN. Furthermore, the maximal observed forces for 0 s are hundreds of pN while for 5 s delay time values up to several nN are observed.

Since without any delay time adhesion is weak if observed at all, in the following I will focus on retraction curves with 5 s delay time. To characterize the stochasticity of the adhesion process of individual bacteria I computed the mean retractions curves for some cells and mean rupture length and adhesion force for all cells (see figure 7.4). Every cell shows a distinct mean curve but their standard deviation overlap. The reason for this high variance can be seen in the inset. It shows two successively recorded force-separation curves of the same cell. While both curves show WLC-like peaks, they are obviously very distinct. This high variability of individual cells is also reflected in the mean adhesion forces and rupture lengths: While rupture lengths vary around 150 nm

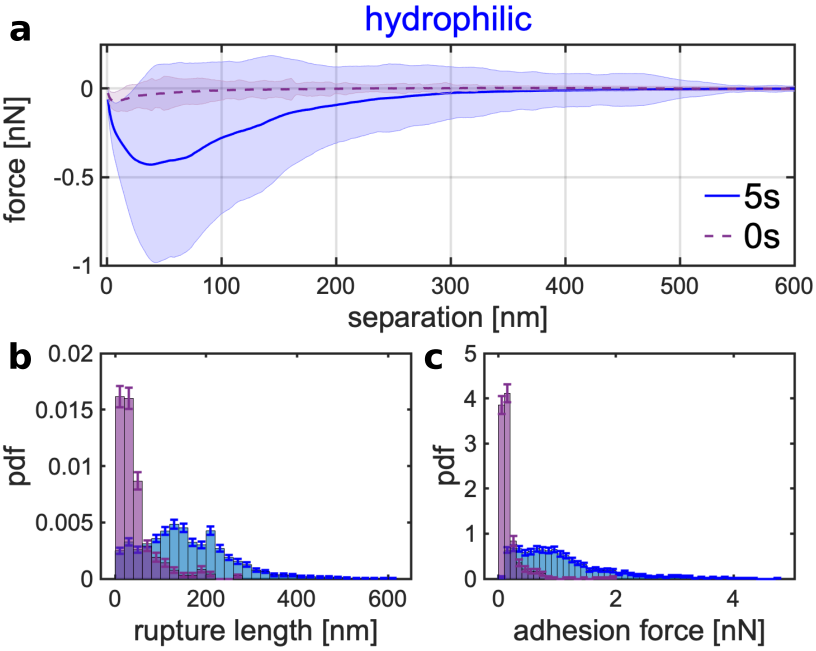

Figure 7.3: (a) Mean SCFS retraction curves (calculated as described in section 7.1.1) with surface delay times of 0 s (purple, 19 cells) and 5 s (blue, 52 cells) on hydrophilic surface (shaded area is standard deviation). **(b,c)** Rupture length and adhesion force probability density histograms extracted from single SCFS retraction curves with to (a) corresponding colours. The figure and caption is reprinted from Maikranz et al. [124] with permission from The Royal Society of Chemistry.

and possess huge error bars of more than 100 nm (see figure 7.4 c), the adhesion forces vary from 0.1 to 1.7 nN with error bars (depicting the standard deviation) between 0.5 and 1 nN (see figure 7.4 b). Therefore, the variance of repetitions with the same cells is as large as the variations from cell-to-cell.

The shape of the retraction curves and the magnitude of the adhesion forces, as well as the rupture lengths, will be discussed in the next section where they can be directly compared to the results on hydrophobic surfaces.

Adhesion to hydrophobic surfaces

As already mentioned the force-distance curves on hydrophobic surfaces show for 0 s surface delay time a significant amount of adhesion. Therefore, no additional surface delay time will be considered. Analogously to the data on hydrophilic surfaces the mean retraction curves of several single cells are depicted in figure 7.5 a. Every cell

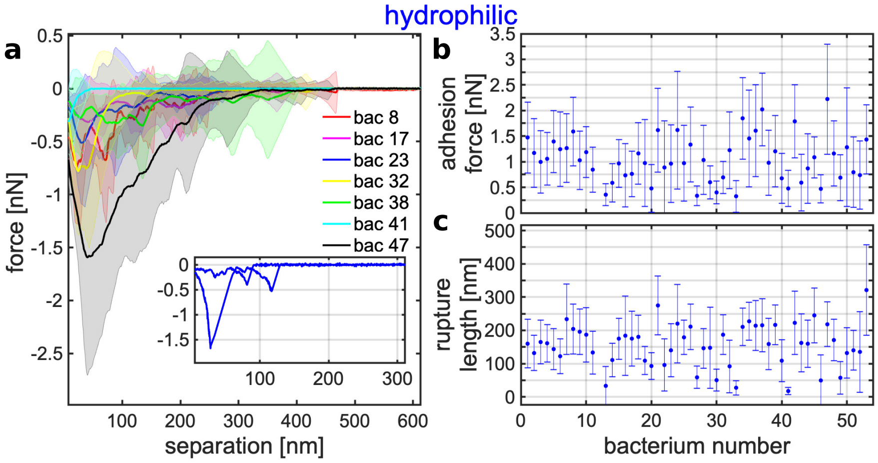

Figure 7.4: **(a)** Mean SCFS retraction curves(calculated as described in section 7.1.1) of 7 exemplary individual bacteria on the hydrophilic surface for a surface delay time of 5 s (shaded area is standard deviation). The inset depicts two exemplary force-distance curves of cell no. 23, whose mean curve is shown in blue in the main diagram. **(b,c)** Mean adhesion forces and rupture lengths extracted from single SCFS retraction curves of 52 cells (error bars are standard deviation). The figure and caption is reprinted from Maikranz et al. [124] with permission from The Royal Society of Chemistry.

shows a ‘cup-shaped’ retraction curve with a very small standard deviation and a well-defined minimum. This is explicitly shown in the inset for two consecutive curves which display almost identical shapes. Subsequently, also the mean adhesion forces are highly cell-specific while the rupture lengths vary between repetitions (see figure 7.5 b, c). The magnitude and variability of the rupture lengths are similar to the behaviour on hydrophilic surfaces while the mean adhesion forces range from 5 to 70 nN with most error bars in the order of a few nN.

To compare the adhesion properties of a typical population of bacteria I compare the mean retraction curves and relevant histograms of all cells measured (see figure 7.6): Remarkably the mean retraction curves look, besides their completely different force scales, rather similar. Note that the larger extent of the standard deviation on hydrophilic surfaces is just an optic effect of the strongly different force scales. The mean adhesion force is about a factor 25 (1.1(0) nN vs 28(2) nN) larger on hydrophobic surfaces than on hydrophilic surfaces. Furthermore, the adhesion forces on hydrophilic surfaces range from hundreds of pN up to several nN (see figure 7.6 c, d) while on hydrophobic surfaces, they are several tens of nN.

The rupture lengths, as already mentioned before, differ much less than the adhesion forces: While on hydrophobic surfaces the rupture length histogram is clearly shifted

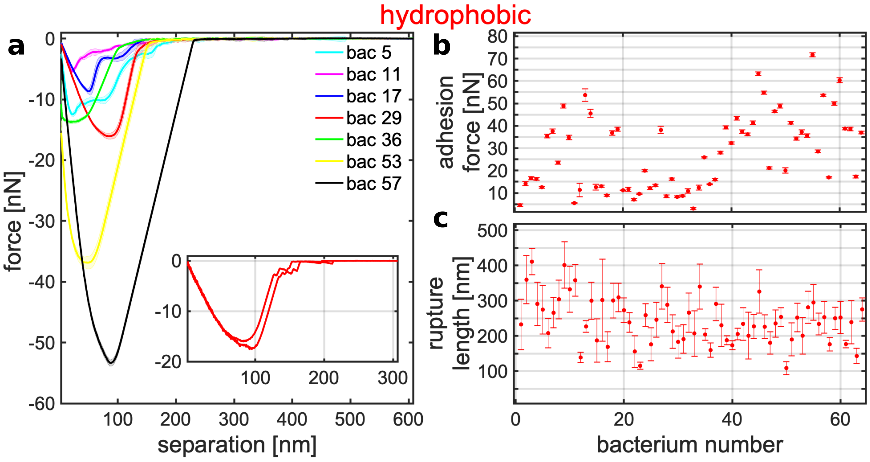

Figure 7.5: **(a)** Mean SCFS retraction curves (calculated as described in section 7.1.1) of 7 exemplary bacteria on the hydrophobic surface for 0 s surface delay time (shaded area is standard deviation). The inset depicts two exemplary force-distance curves of cell no. 29, whose mean curve is shown in red in the main diagram. **(b,c)** Mean adhesion forces and rupture lengths extracted from single SCFS retraction curves of 64 cells (error bars are standard deviation). Note the different scales in this figure and Figure 7.4 for the adhesion forces, but identical scale for the rupture lengths. The figure and caption is reprinted from Maikranz et al. [124] with permission from The Royal Society of Chemistry.

to larger lengths, the mean value differs only by a factor of approximately 1.5 (from 160(2) nm on hydrophilic surfaces to 242(2) nm on hydrophobic surfaces). Especially the large rupture lengths with values greater than 400 nm are notable on abiotic surfaces where cell wall macromolecules can just tether non-specifically to the surface. In single-molecule force spectroscopy experiments with proteins typically 0.36 nm length contribution per amino acid is considered [128, 129]. The measured rupture lengths are therefore comparable to the fully unfolded length of different *S. aureus* surface proteins, like Serine-aspartate repeat-containing protein C (SdrC, 360 nm [129]), clumping factor A (ClfA, 285 nm [130]), and *S. aureus* surface protein G (SasG, 505 nm [50]). Forces needed to unfold proteins are typically in the range of 0.1–0.4 nN [51, 131, 132], but are structure and pulling speed specific. As already discussed in section 3.2.1 unfolding forces for the *S. aureus* proteins SasG are 0.25 nN and 0.42 nN for the E and G5 domains respectively [51]. These values might even depend on the Zn^{2+} concentration [133]. Note that since some proteins detach before fully unfolding the rupture length does not necessarily correspond to the fully unfolded length. While for instance Cna or SdrC do not unfold fully before detaching [129, 134], ClfA has a folded length of 25 nm and unfolds fully to a length of 285 nm before detaching [130]. Furthermore, as introduced in section 3.2.1 the rupture lengths might also result from tethering of other

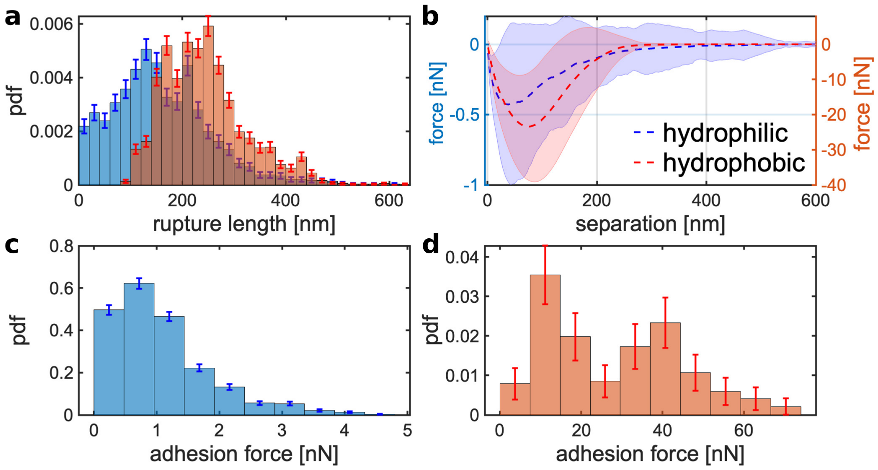

Figure 7.6: **(a,c,d)** Probability density histograms of rupture lengths and adhesion force of each tested cell on hydrophilic (blue) and hydrophobic (red) surfaces (where histograms overlap, a mixed colour is displayed). **(b)** Corresponding mean retraction curve (shaded area is standard deviation and very small) calculated from all tested cells calculated as described in paragraph 4.3. Note the different scales of the y-axes. The figure and caption is reprinted from Maikranz et al. [124] with permission from The Royal Society of Chemistry.

cell surface macromolecules such as extracellular polysaccharides, like poly-N-acetyl-D-glucosamine (PNAG), or glycolipids (teichoic acids).

7.1.2 Model

To investigate the origin of the different adhesion behaviour of *S. aureus* on hydrophilic and hydrophobic surfaces I extended the model of Thewes et al. [64], presented in chapter 4. The model by Thewes considers the bacterium as a hard-sphere decorated with thermally fluctuating macromolecules. To mimic SCFS experiments this bacterium is connected to a moving cantilever modelled as a Hookean spring. The interaction of the molecules with the surface is given by a simple square well potential of potential depth V and interaction range r. In between every cantilever step, the forces of the deflected cantilever and bound molecules are balanced. The shape of the retraction curves on hydrophilic surfaces indicated the necessity of a non-linear force stretch relation. And while in principle several polymer models could be used in single-molecule force spectroscopy the WLC model as presented in section 2.4.2 is the most prevalently used. Therefore I consider the WLC model as a force-stretch relation in the usual approximation of Marko and Siggia [34] and account for the compression of the macromolecules by introducing the rest length l_0. Below this length, the macromolecules behave as

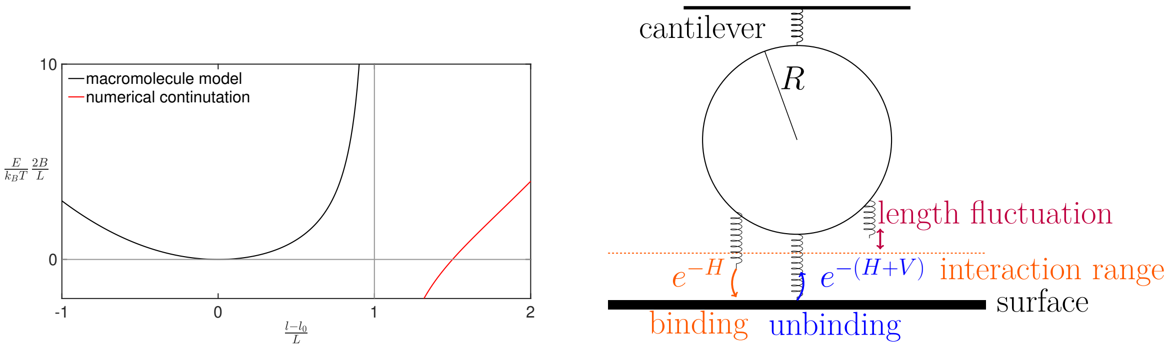

(a) **(b)**

Figure 7.7: **(a)** Energy of the macromolecule with length L, Kuhn length B, and stretch l. At $l = L + l_0$ the energy diverges and should be infinite but numerically the function continuous as indicated in red. This sudden non-physical drop of energy needs to treated explicitly in the simulations. **(b)** Model schematic depicting the adhesion as mediated by thermally fluctuating macromolecules binding to a surface with binding energy $H + V$ if the potential barrier of H can be overcome.

Hookean springs. For simplicity, I use the radius of gyration as the rest length such that $l_0 = \sqrt{\frac{L \cdot B}{6}}$ where L is the contour length and B the Kuhn length of a polymer. By continuity, this results at length l in the energy E and corresponding force f (see figure 7.7a):

$$E(l) = k_BT\frac{L}{2B}\left(\frac{l-l_0}{L}\right)^2 \begin{cases} 2 + \frac{1}{1-\frac{l-l_0}{L}} & , l_0 \leq l \\ 3 & , 0 \leq l \leq l_0 \end{cases} \tag{7.1}$$

$$f(l) = -\frac{k_BT}{2B} \begin{cases} 4\frac{l-l_0}{L} - 1 + \frac{1}{\left(1-\frac{l-l_0}{L}\right)^2} & , l_0 \leq l \\ 6\frac{l-l_0}{L} & , 0 \leq l \leq l_0 \ . \end{cases} \tag{7.2}$$

Since the force model is non-linear, the equilibrium position of the bacterium needs to be calculated numerically, by bisection. This energy function has been briefly explored within the model of Thewes et al. [64] which shows the expected non-linear behaviour [135]. However, the divergence at $l = l_0 + L$ requires careful treatment in the simulations since numerical errors can lead to non-physical larger lengths (see figure 7.7a red line).

A key change to the model of Thewes et al. [64] is the introduction of a potential barrier. In particular, I do not allow the binding of macromolecules to the surface by being merely in the proximity of the surface. Here once the macromolecule is in the interaction range of the surface, it overcomes a potential barrier with probability e^{-H} before it binds. Once the molecule is bound, its energy decreases by the potential depth V but can also spontaneously detach with probability $e^{-(V+H)}$ (see figure 7.7b).[3]

The effects of this potential barrier will be discussed in detail in the result section. Most notable it introduces another source of stochasticity into the simulations. To mimic the unknown distribution of macromolecules on the bacterium's surface a fixed number of molecules are uniformly distributed[4] over the surface of the sphere. However, for a better numerical performance only a lower section of the sphere, having a chance of interacting with the surface, will be decorated. The parameters of the macromolecules will be sampled from distributions as presented in the following section.

Parameters

Since I investigate unspecific binding the binding energy can be estimated to be in the low tenth of $k_B T$. The Kuhn lengths of proteins are typically in the range of $0.1-1$ nm [132, 136, 137]. And while also teichoic acids or capsular polycarbonate may contribute to the adhesion the literature did not provide any values. Therefore, I will sample the Kuhn length from a uniform distribution with corresponding maximal and minimal values. As already mentioned in section 7.1.1, estimating the relevant contour lengths is more difficult: First of all, it is not clear which proteins are expressed in the SSA113 strain investigated here. Second, the proteins have folded and unfolded length. Forces to unfold proteins are typically $0.1-0.4$ nN [51, 131, 132], but are structure and pulling speed specific and might even depend on the concentration of ions in the solution as for SasG [133]. Furthermore, the proteins might detach before unfolding as Cna or SdrC [129, 134] or just partially unfold as SasG which forms fibrils of 53 nm length with several domains that, depending on the loading rate, can unfold independently to give a fully unfolded length of 505 nm [50, 51, 52]. Third, the proteins are initially anchored at the height of the membrane, but it is not clear if proteins stay or change their height within the membrane due to the synthesis of new peptidoglycan. Fourth, capsular polycarbonates and teichoic acids contribute to adhesion for which I was not

---

[3] The detaching probability is chosen such that the detailed balance is fulfilled.

[4] Uniformly in the sense of a probability distribution not equidistant.

able to find any information on contour lengths. Therefore, I sample the contour length L from a Weibull distribution for form-parameter k and scale parameters λ, i.e.

$$\rho\left(L\right) = \frac{k}{\lambda}\left(\frac{L}{\lambda}\right)^{k-1} e^{-\left(\frac{L}{\lambda}\right)^{k}} .$$

The model parameters used in the following, if not stated differently, are given in table 7.1. An overview of the simulation steps is provided in the appendix as pseudo code (see appendix B). Furthermore, to avoid artefacts from the instantaneous cantilever steps, I subdivided each experimental cantilever step into a hundred sub-steps inside the simulation.

Table 7.1: Reference Parameters and Symbols. The table is reprinted from Maikranz et al. [124] with permission from The Royal Society of Chemistry.

number of macromolecules N	5000
minimum macromolecule Kuhn-length	0.2 nm
maximum macromolecule Kuhn-length	1 nm
scale parameter for macromolecule length	125 nm
form parameter for macromolecule length	1.5 nm
radius of bacterium	500 nm
decorate area height (from bottom of bacterium)	50 nm
Spring constant of the cantilever	0.6 nN/nm
$k_B T$	4.1 pN nm
interaction range of surface potential r	2 nm
change of macromolecule length Δl	1 nm
macromolecule stretch	l [nm]
macromolecule Kuhn length	B [nm]
macromolecule contour length	L [nm]
macromolecule rest length	$l_0 = \sqrt{\frac{L \cdot B}{6}}$ [nm]
potential barrier	H $[k_B T]$
potential depth	V $[k_B T]$

7.1.3 Monte Carlo simulations

Since the measured *S. aureus* cells have been grown under the same conditions all results should be reproducible by only varying the potential depth and surface height. At first, I show that the experimental mean curves and the waiting-time dependence on both surfaces can be reproduced (see figure 7.8). The simulated mean curves (magenta line) display the correct force scale and rupture lengths. And while also the waiting-time dependence on hydrophilic surfaces can be reproduced the standard variation on hydrophobic surfaces as well as on hydrophilic surfaces with 5 s surface delay time is much lower than in the experiments. This lack of populational heterogeneity, especially on hydrophobic surfaces is a result of several model assumptions: Every cell is decorated with a large identical number of macromolecules which all use the same simple force stretch relation and binding energy. In particular, it is reasonable to assume that the behaviour of polycarbonates and teichoic acids deviates from proteins that can unfold. However, implementing these specific responses and binding energy requires experimental characterisation of the force stretch relation of said macromolecules. To my knowledge, this characterisation is still lacking. Further, I distributed the macromolecules uniformly over the entire surface of the bacterium but since in SCFS experiments only a particular section of a bacterium will come into contact with the surface any heterogeneous distribution of adhesion capabilities will increase the populational heterogeneity. For instance Serine-aspartate repeat-containing protein G (SdrG) on *S. epidermis* and Collagen adhesin (Cna) protein on *S. aureus* form nanodomains on the bacteria's surface [128, 134]. The heterogeneous distribution of adhesion capabilities will be further studied in section 7.2.

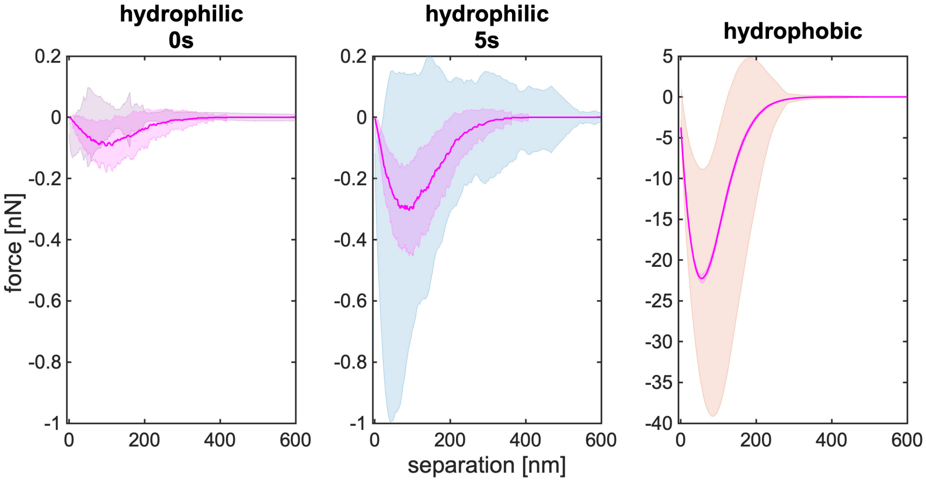

Figure 7.8: Comparison of the simulated mean retraction curves (pink) that match the experimental results (blue, purple, red). We used 17 $k_{\mathrm{B}}T$ (0 $k_{\mathrm{B}}T$) for the potential barrier and 50 $k_{\mathrm{B}}T$ (20 $k_{\mathrm{B}}T$) binding energy for hydrophilic (hydrophobic) surfaces. Note the different scales of the right panel in comparison with the others and the remarkably small standard deviation. The figure and caption is reprinted from Maikranz et al. [124] with permission from The Royal Society of Chemistry.

Next, I investigated the stochasticity of repeated SCFS experiments with the same bacterium depending on the potential depth V and barrier height H (see figure 7.9).

For low potential barriers and sufficiently large potential depths, all repetitions with the same cell (blue, red, green line) show quasi deterministic cup-shaped retraction curves as in the experiments on hydrophobic surfaces. The adhesion force as is expected increases with larger potential depths. For larger potential barriers the repetitions with the same cell vary significantly. Furthermore, the curves display 'WLC-like peaks' matching the behaviour observed on hydrophilic surfaces. As already discussed in the experimental results this indicates the tethering of a few macromolecules.

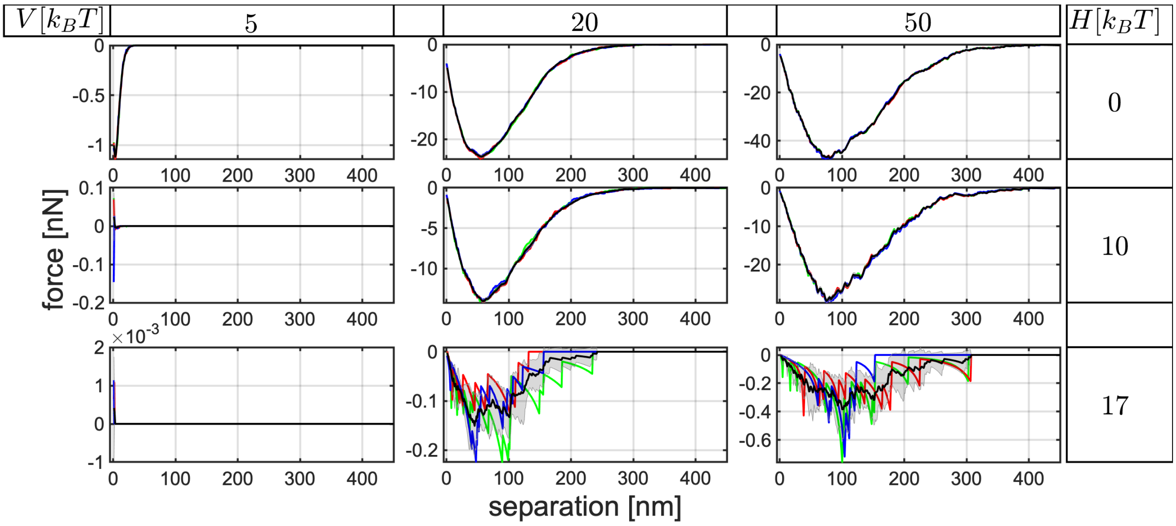

Figure 7.9: Simulation results: Single (coloured) and mean retraction curves (black) for different potential depths V and potential barriers H and fixed bacteria. Surface delay time is 5 s. The figure and caption is reprinted from Maikranz et al. [124] with permission from The Royal Society of Chemistry.

To substantiate this intuition I counted the number of macromolecules that are attached to the surface (see figure 7.10). Indeed for both surface delay times, the number of attached macromolecules is mostly influenced by the barrier height, while the influence of the potential depth levels of once a sufficiently large depth is reached. Furthermore, for low barriers, thousands of molecules tether to the surface while for larger barriers this reduces to only tenths of molecules. The influence of additional surface delay time dependence strongly on the size of the potential barrier. While for small potential barriers the number of attached molecules does not increase markedly with additional surface delay time, for large barriers the amount increases substantially. This is reflected in the corresponding adhesion curves (see figure 7.11), which show for increased barrier heights only a substantially increased adhesion force when a surface delay time is considered. Note that for no potential barrier still a small surface delay time dependence is observed.

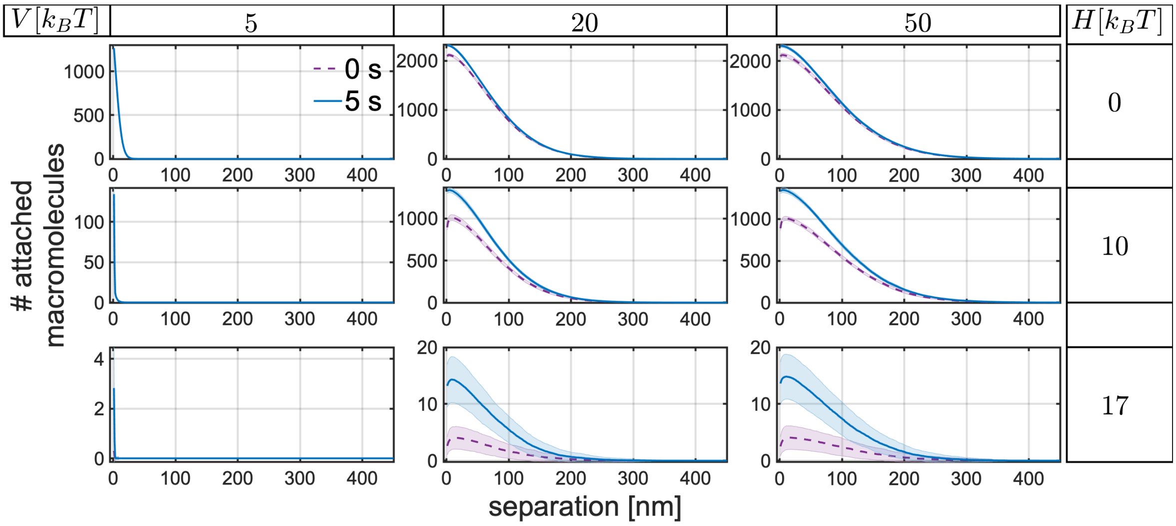

Figure 7.10: Ensemble mean of the number of attached macromolecules for different potential depths V and barriers H, extracted from the first 10 retractions of 20 simulated cells. Shaded area is standard deviation. While blue solid lines indicate 5 s of surface delay time, purple dashed lines indicate 0 s. The figure and caption is reprinted from Maikranz et al. [124] with permission from The Royal Society of Chemistry.

In summary, the simulations show that the cell individual stochasticity within repetitions, the shape of the retraction curves (cup-shaped or WLC-like) and the surface delay time dependence can be explained by the presence of a potential barrier. This barrier selects on hydrophilic surfaces only a few macromolecules which leads to the large variability of consecutive curves and a significant surface delay time dependence. On the other hand, on hydrophobic surfaces many molecules can bind leading to almost identical retraction curves. The next section will substantiate that this behaviour is independent of the contour length parameter variation.

Contour length dependence

In this section, additional simulations investigating the influence of the unknown length distribution is presented. To this end, I vary the scale parameter of the Weibull distribution and analyse the mean retraction curves as well as the mean number of attached macromolecules (see figure 7.12, 7.13). Note that the scale parameter not only influences the mean but also the variance of the distribution.

While the initial part of the retraction curve shows no significant change, the adhesion force reaches with increasing scale parameter larger values. Furthermore, the separation

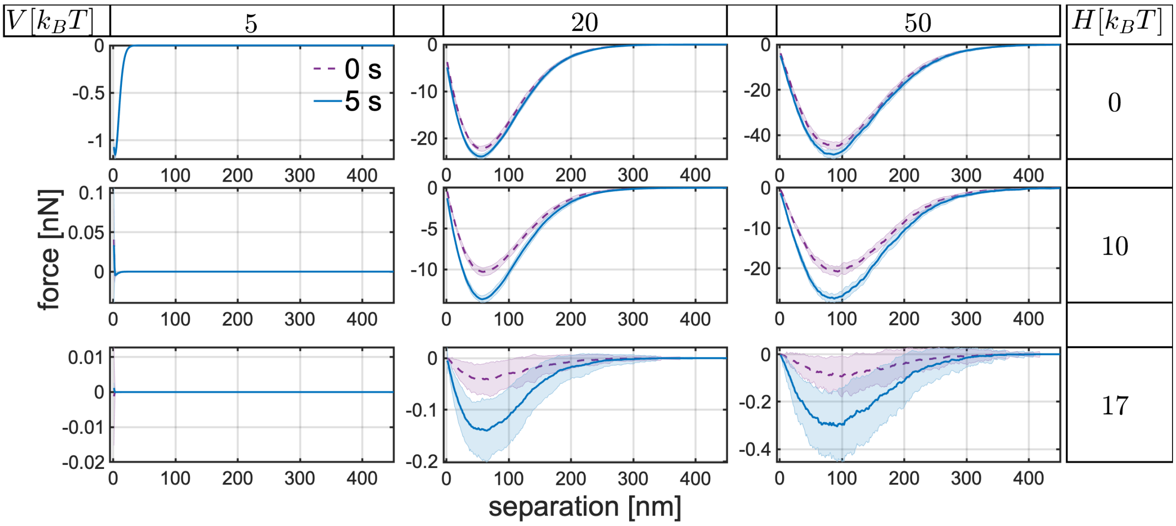

Figure 7.11: Mean retraction curves for different potential depths V and barriers H, extracted from the first 10 retractions of 20 simulated cells. Shaded area is standard deviation. While blue solid lines indicate 5 s of surface delay time, purple dashed lines indicate 0 s. The figure and caption is reprinted from Maikranz et al. [124] with permission from The Royal Society of Chemistry.

at which the adhesion force is measured, as well as the rupture lengths, shift to larger separations. The number of attached macromolecules (see figure 7.13) increases with larger scale parameter and more macromolecules stay attached to larger separations. Both behaviours are observed for a broad range of potential depths and all tested barrier heights. At large barrier heights, however, the standard variation increases substantially leading to the overlapping of the mean forces and number of attached molecules.

The behaviour is explained as follows: Since the interaction with the surface is only short-range more macromolecules come into the interaction range when more of them are longer. Correspondingly more will tether initial to the surface and since they are also longer obviously stay longer attached to the surface. This also explains the increased adhesion force and its' shift to larger separations. If more macromolecules with larger contour length bind naively also a change in the initial part of the retraction curve would be expected. This is, as already mentioned, not observed. Since the molecules utilize the WLC-like force-stretch relation they contribute to the measured force only when they are significantly stretched relative to their contour lengths. This lack of large forces at small stretches is the reason why the initial part of the retraction curves shows no sensitivity to the changing scale parameter although more macromolecules bind to the surface.

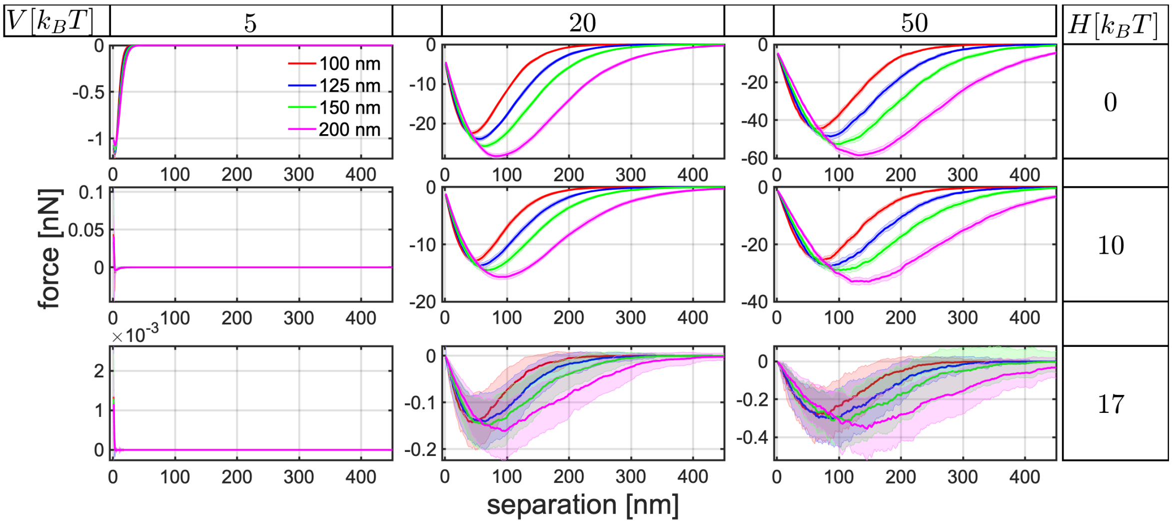

Figure 7.12: Mean retraction curves for different potential depths V and barriers H, extracted from the first 10 retractions of 20 simulated cells with surface delay time of 5 s. Shaded area is standard deviation. Different colors correspond to scale parameters as indicated in the first panel. The figure and caption is reprinted from Maikranz et al. [124] with permission from The Royal Society of Chemistry.

7.1.4 Retraction curves for an infinitely stiff cantilever

In the case of a rigid cantilever, the retraction curves can be described by a set of master equations. Because it is rigid the separation s of the bacterium to the surface can be used as a time-like variable. Then the master equation for the probability p of an individual macromolecule being attached at separation s is

$$\frac{dp}{ds} = -w[E(s)]p \ .$$

Here E is the energy of the macromolecule at separation s and it is assumed that once the macromolecule detaches it never attaches back to the surface. The solution $p(s) = e^{-\int_0^s w[E(s')]ds'}$, is for the Kramers' rate[5]

$$w[E(s)] = \omega_0 e^{\frac{E(s)-E(s-\delta)}{k_BT} - V}$$

a highly non-linear function but the integral can be computed numerically to obtain $p(s)$. The results for a macromolecule with $E(s)$ given by equation 7.1 and $\omega_0 = 1$, $\frac{\delta}{L} = 0.02$, $L = 100$ nm, $B = 20$ nm are shown in figure 7.14a.

---

[5] In the unbound state the molecule can be initially significantly stretched. This stretch is controlled by the parameter δ.

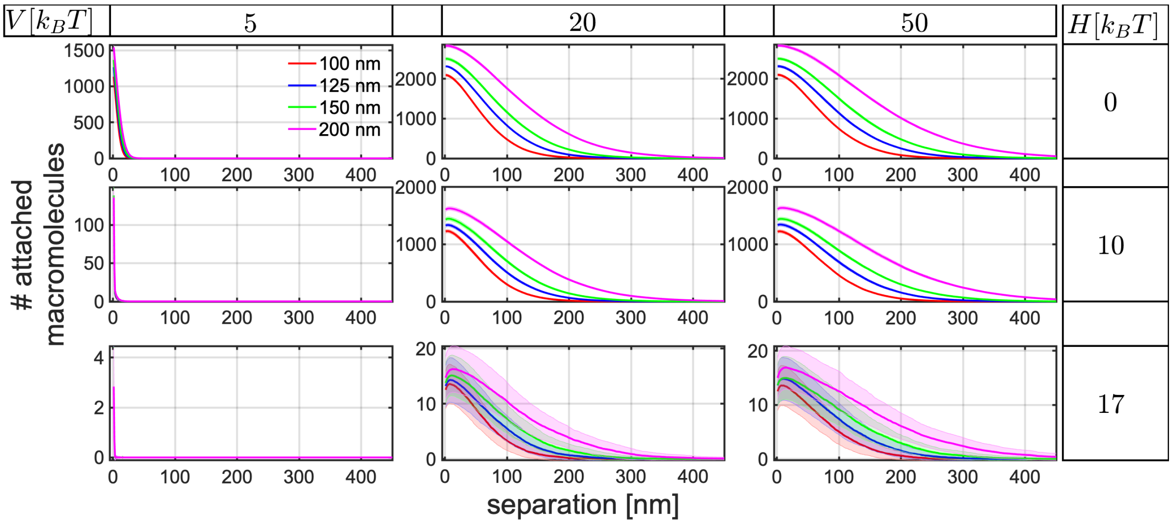

Figure 7.13: Ensemble mean of the number of attached macromolecules for different potential depths V and barriers H, extracted from the first 10 retractions of 20 simulated cells with surface delay time of 5 s. The shaded area is standard deviation. Different colors correspond to scale parameters as indicated in the first panel. The figure and caption is reprinted from Maikranz et al. [124] with permission from The Royal Society of Chemistry.

An increasing potential depth has two effects on the probability of being attached: First, the stretch at which the macromolecule is likely no longer attached shifts for larger potential depths to larger values. This shift, however, is non-linear and an ever more increasing potential depth is required to increase this probability significantly. Second, the shape changes to a step-function predicting the quasi deterministic attachment for sufficiently deep potentials. Both behaviours can be attributed to the non-linear divergence of the force-stretch relation at the contour length.

This approach can be generalized to N initially attached molecules. If f_i is the acting force of molecule i the entire force acting on the bacterium is $f(s) := \sum_{i=1}^{N} f_i(s)\mathbb{1}_{X_i=1}$, where $\mathbb{1}_{X_i=1}$ indicates if the molecule is still attached. The average retraction curve becomes

$$F(s) = \langle f(s) \rangle = \sum_{i=1}^{N} f_i(s) p_i(s)$$

which can be computed once the probabilities of being still attached i.e. the $p_i(s)$ are known.

To mimic the Monte Carlo simulations I sampled the properties of the molecules from the same distribution as described in section 7.1.2. To mimic the curvature of the

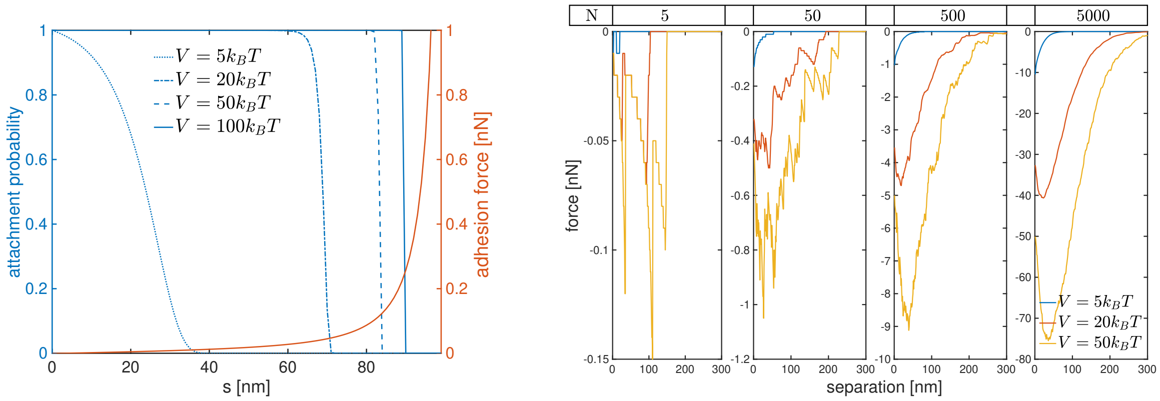

(a) **(b)**

Figure 7.14: **(a)** Probability of being attached (left axis), and corresponding force (right axis) at stretch s for $\omega_0 = 1$, $\frac{\delta}{L} = 0.02$, $L = 100$ nm, $B = 20$ nm, and various potential depths V. As energy equation 7.1 is used. **(b)** Numerical solution for the average retraction curve $F(s)$ for N initially attached macromolecules. The properties of the molecules are sampled from the same distributions as in the Monte Carlo simulations.

bacterium I sampled an initial stretch uniformly in the interval [0,50] nm. The resulting average retraction curves (see figure 7.14b) show with increasing potential depth an increase in adhesion force, as well as a transition from WLC-like peaks (N=5) to cup-shaped retraction curves (N=5000). This behaviour is the same as in the Monte Carlo simulations substantiating the result that on hydrophobic surfaces indeed many macromolecules bind while on hydrophilic surfaces only a few. However, in opposition to the Monte Carlo simulations, the force-distance curves have a non zero force for zero distance to the surface. This is due to the distribution of prescribed initial stretches.

7.1.5 Conclusion

I analysed the adhesion characteristics on hydrophilic and hydrophobic surfaces for a large number of single *S. aureus* SA113 cells. These characteristics could be, besides the large populational heterogeneity of adhesion forces on hydrophobic surfaces, quantitatively reproduced by Monte Carlo simulations. These simulations mimic the adhesion process in SCFS experiments and allow the interpretation of the experimentally observed force-distance curves. The simulations utilized reasonable parameters for the properties of the macromolecules, as well as the magnitude of the surface potential.

The model reproduces the distinct retraction curve shapes, adhesion force scales and stochasticities on hydrophobic as well as hydrophilic surfaces. In particular, the investigations show that the different cell individual stochasticity on hydrophobic and hydrophilic abiotic surfaces can be reproduced by the introduction of a potential barrier. On hydrophobic surfaces many macromolecules bind weakly while on hydrophilic surfaces few macromolecules get selected by the potential barrier and tether strongly to the surface. This leads on hydrophobic surfaces to a small variation between repetition with the same cell, while the barrier on hydrophilic surfaces leads to variations between the repetitions which are as large as the cell-to-cell variation.

These results are corroborated by a set of master equations describing the mean retraction curves in the limit of an infinitely stiff cantilever. These show that the quasi deterministic retraction curves are caused by the divergence of the force-stretch relation. Therefore, the stochasticity in the repetitions needs to be produced by a stochastic initial attachment to the surface. This is realised by a potential barrier stochastically selecting the binding molecules. The origin of this barrier is unclear but it is reasonable to assume a relation to possible conformational changes of the macromolecules and the disruption of the hydrogen bond network close to the surface. It depends on the structure of the water network and the atomic structure of the involved macromolecules. Hence, this question is not approachable by effective models but could be investigated by molecular dynamics simulations.

The work presented here was limited to the bacterium *S. aureus* SA113, however the same observations hold for *S. aureus* JE2 and N313 [124]. Furthermore, I expect the results to be valid for all gram-positive bacteria where, due to the peptidoglycan layer, the involved macromolecules cannot freely diffuse inside the lipid membrane. These results are a first step towards reducing the binding of bacteria to surfaces. Note, however, that depending on the application preconditioning of the surface by biological material can enable specific binding of macromolecules. In those situations, the presented analysis may not be applicable.

7.2 SCFS on sinusiodal surfaces

To investigate the distribution of adhesion capabilities of *S. aureus* Christian Spengler designed and performed SCFS experiments on abiotic hydrophobic sinusoidal surfaces (see figure 7.15 a). Depending on the position of the bacterium relative to the surface different parts of the bacterium can interact with the surface. The bacterium is then moved parallel to the periodicity of the surface and force-distance curves for every point along the surface are recorded.[6] From these, the adhesion force is extracted and mapped to the position relative to the periodicity of the surface. Afterwards, the curves are averaged pointwise to obtain the adhesion profiles displayed in figure 7.15 b. The resulting profiles show several features: Cells 1−13 show the maximum adhesion force in the minimum of the surface. Outside of the surface minimum the adhesion force drops significantly by about 30−60 %. The profiles show either a 'bathtub-like shape' (cells 1−8) or peaked adhesion capabilities (cells 9−14). Furthermore, even 'bathtub-like' profiles show a reflection asymmetry with respect to the origin (i.e. $F(x) \neq F(-x)$). Hence, the adhesion capabilities are clearly heterogeneously distributed over the cell envelope.

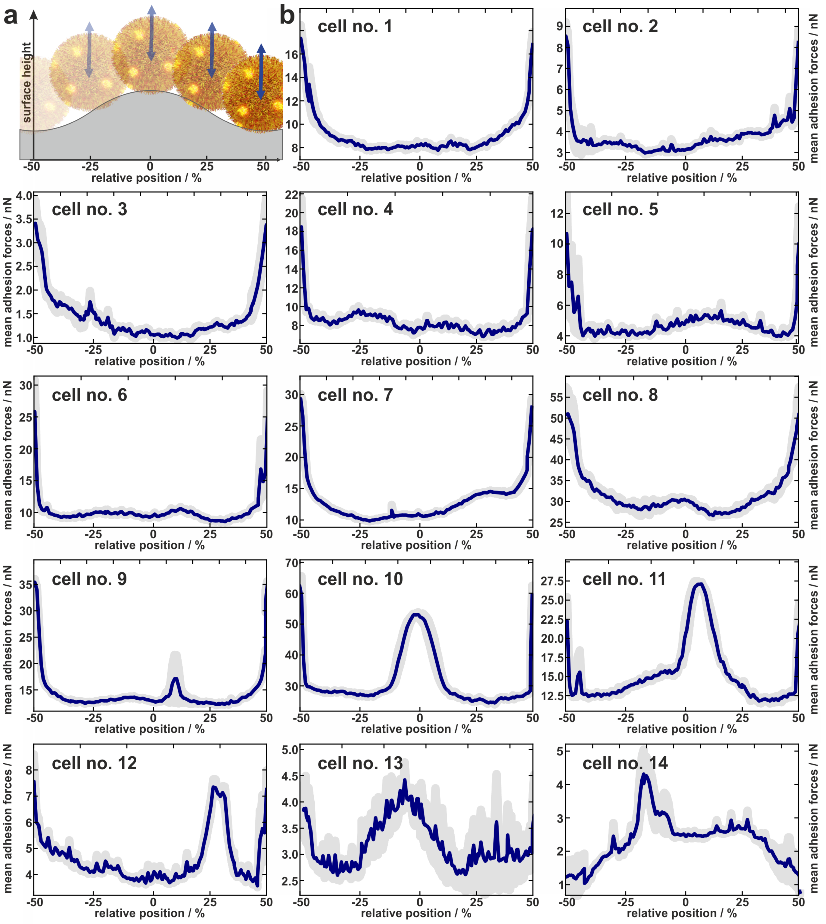

Figure 7.15: **(a)** Sketch that illustrates how the position in one period along the surface probes different parts of the bacterium's surface. **(b)** Adhesion profiles, i.e. adhesion forces averaged over several periods of the wrinkled surface relative to the topographical maximum of the surface periods. The shaded area depicts the standard error of the mean. The figure and caption is reprinted from Spengler et al. [125].

---

[6] The distance in the force-distance plots is measured perpendicular to a flat reference surface.

To further analyse the adhesion profiles I constructed a mean profile from all cells which show, besides the peaks in the surfaces minima, no peaked adhesion capabilities i.e. cells 1−8 in figure 7.15.

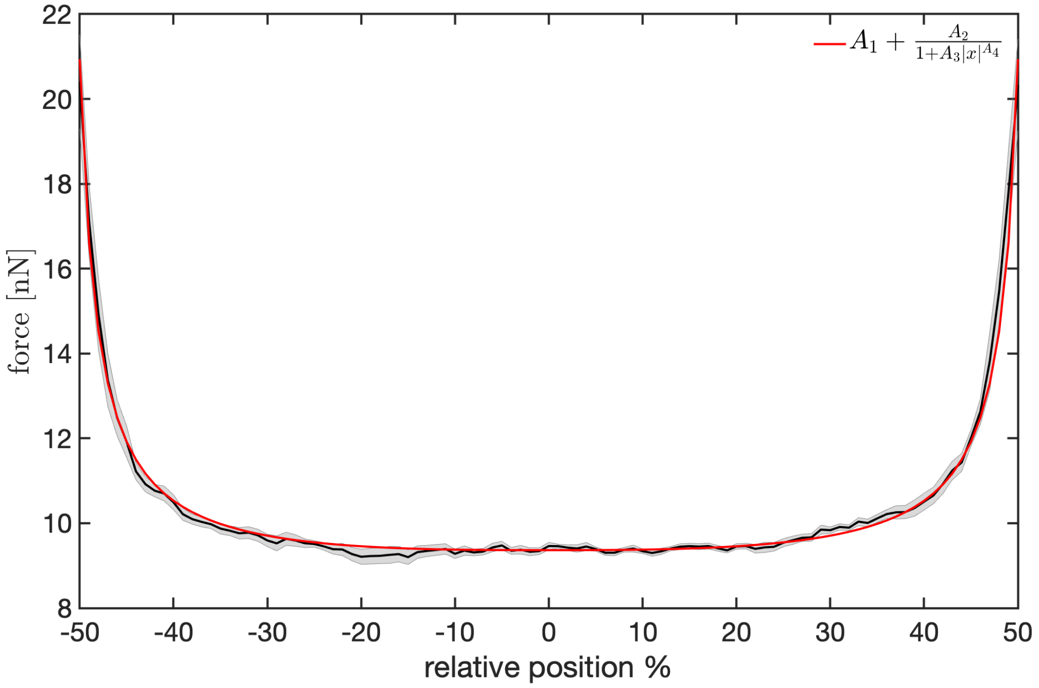

Figure 7.16: Mean curve of cells 1-8, with standard deviation as shaded area. The fit was performed via a constrained non-linear optimization of squared residuals as implemented by MATLAB's 'lsqnonlin' function. The constrains for fit parameters have been set to $|A_1| \leq 100, |A_2| \leq 100, |A_3| \leq 10, 0 \leq A_4 \leq 10$ and this results for a broad range of initial conditions in A_1 = 8.1, A_2 = 1.3, A_3 = -6.4, A_4 = 2.8. For this particular fit the initial values (A_1, A_2, A_3, A_4) = (0,0,0,1) have been used.

A phenomenological fit function for a homogeneous distribution of adhesion capabilities is

$$F(x) = A_1 + \frac{A_2}{1 + A_3\,|x|^{A_4}} \ ,$$

where F is by construction symmetric around the origin. A_1 and A_2 can be directly related to the functions values at the origin and boundaries respectively, i.e. $F(0) = A_1 + A_2$, $\lim_{x\to\pm\infty} F(x) = A_1$. A_4 and A_3 characterize the range of the flat adhesion profile and the sharp increase at the boundaries. From these the length scale $l = \frac{1}{\sqrt[A_4]{|A_3|}}$ over which the profile is flat, i.e. $F(x) \overset{|x|\ll l}{\approx} F(0)$ can be identified. As figure 7.16 shows, this function fits the experimental obtained profile reasonable well (for the fit details see the caption of figure 7.16). The parameters for the length scale are A_3 = -6.4 and A_4 = 2.8 which leads to l = 0.52. Hence, this length scale is larger than the domain of definition and not useful in characterizing the profile.

This reference curve allows characterizing the adhesion peaks of cells 9-13. In particular, the excess adhesion force, i.e. the force larger than the force expected from a non-peaked profile and the widths of the peaks can be computed. To this end a baseline $aF(x) + b$ is linearly fitted to the adhesion profiles of cells $9-14$.[7]. To weaken the influence of the boundaries I only fit over the range $|x| < 0.49$ (neglecting the outmost points). Since the presence of the peaks distorts the baseline the fit is performed in two iterations: In the first iteration, the fit considers the entire domain (see figure 7.17 a green lines) and subsequently the difference of the profile and the fit is computed (see figure 7.17 b green lines). I refer to this difference as the residual-profile. The zeros closest to the peak's maximum in the residual-profile defines the domain excluded in the second fit iteration (see figure 7.17 b green dashed lines). Hence in the second iteration, the peak is excluded, which allows a more accurate fit of the baseline (see figure 7.17 a red lines). From the residual-profile in the second fit iteration (see figure 7.17 b red lines) the characteristics of the peak are computed.

The excess adhesion is obtained as the peaks maximum in the residual-profile and the half width of the peak as the distance of the peaks maximum to its nearest zero.[8] The characteristics of the peaks are shown in figure 7.18, from which no correlation between the excess adhesion force and the peaks half width can be inferred. However, correlating the excess adhesion force and the half width to properties of adhesive patches on the bacterium's surface is not trivial. In particular, it is unclear how the size of an adhesive patch corresponds to a given half width. Furthermore, to properly interpret the excess adhesion force the homogeneous adhesion profiles need to be understood.

To this end, I extended the previously presented model to take curvature effects of the bacterium and the surface into account. Furthermore, Michael Klatt and I derived a computational inexpensive 'geometric model' that neglects the mechanical properties of the macromolecules. This model only considers the varying interacting area of the bacterium along the surface and allows to separate this influence from the impact of the curvature on the forces exerted by the macromolecules.

---

[7] a, b are the fit parameters

[8] The half width is used because the residual-profile in the second iteration does not necessarily produces two zeros characterizing the peak.

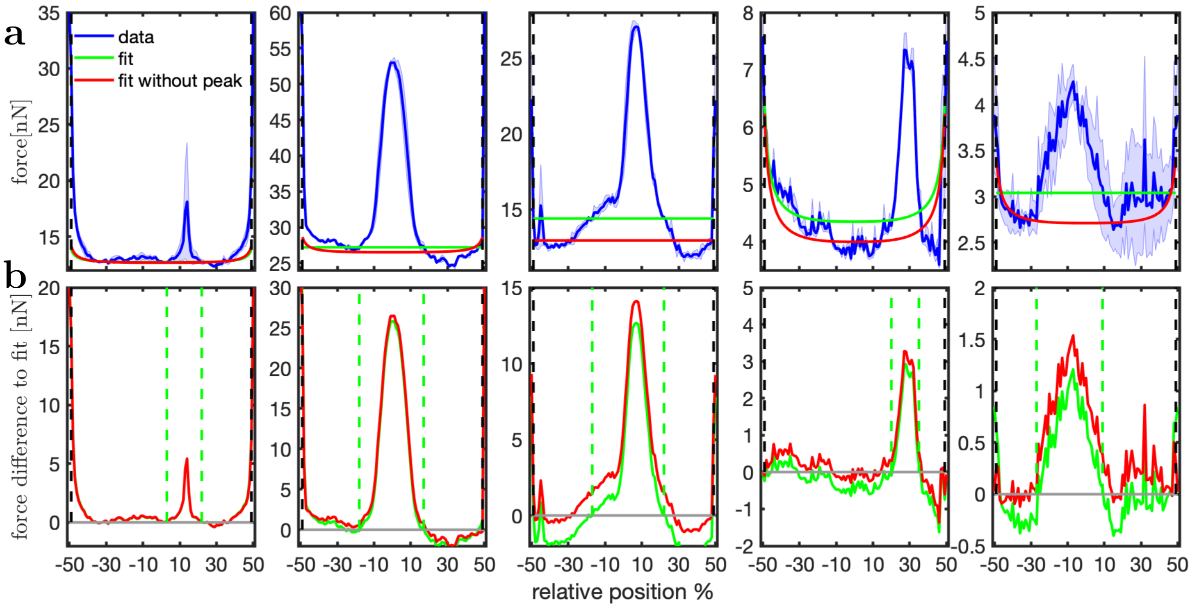

Figure 7.17: **(a)** Adhesion profiles of cells 9−13 (blue) with fit range ($|x| < 0.49$) indicated by the black dashed lines. Green shows the first iteration of the fit over the full domain, while for the second iteration, i.e. the red fit, the domain of the peak was excluded. **(b)** The residual-profiles, i.e. the difference of the fits to the adhesion profiles. The dashed green lines indicate, the zeros of the first fit, and defines the domain excluded for the second fit.

7.2.1 Geometric model

In the geometric model a bacterium is decorated with N rods of fixed length l pointing into the normal direction of their position on the bacterium's surface. Each rod has an adhesive weight $w_i, i = 1, \ldots, N$. For each position x along the sinusoidal surface, the sphere is positioned above the surface, such that only a single point touches the surface. This is termed the tangential contact. The relative adhesion force $F(x)$ is then computed via

$$F(x) = \frac{\sum_j w_j}{\sum_{i=1}^{N} w_i} ,$$

where the j-summation runs over all rods that intersect with the surface. This model only provides relative adhesion strengths and in essence computes the adhesion strength by the bacterium's surface area can interact with the surface. In particular, cooperative effects due to simultaneous stretching of macromolecules are not considered.

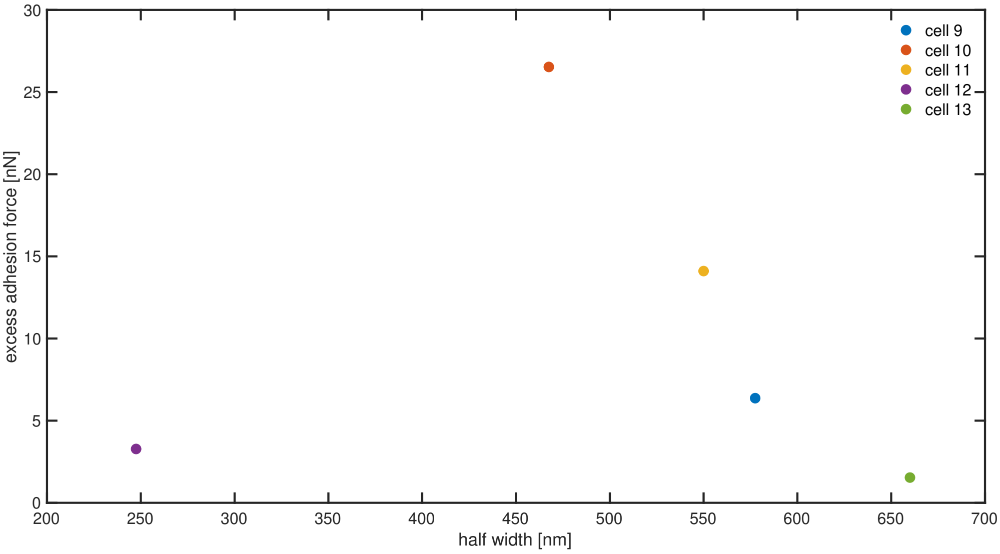

Figure 7.18: Characteristics of the peak extracted from figure 7.16 b as the excess adhesion force (maximum of the residual-profile) and the half width (distance of the maximum to closest zero of the residual-profile). The residual-profile is defined as the difference between the adhesion profile and the fitted baseline.

Tangential contact

Every point on the bacterium's surface is parametrised by

$$\vec{B} = R \begin{pmatrix} \cos\varphi \sin\Theta \\ \sin\varphi \sin\Theta \\ \cos\Theta + 1 \end{pmatrix} + \begin{pmatrix} x \\ 0 \\ s \end{pmatrix} ,$$

where (R, Θ, φ) are the usual spherical coordinates, x is the relative position along the surface and s the distance from the minimum of the surface to the bottom of the bacterium (see figure 7.19). In order to bring the bacterium at position x in tangential contact I need to compute s^* such that the bacterium barley touches the surface (see figure 7.19). More precisely the bacterium is placed into tangential contact. In formulas, s^* is the maximal distance such that

$$h(R\cos\varphi\sin\Theta + x, R\sin\varphi\sin\Theta) = R\,(\cos\Theta + 1) + s^* \ \forall\varphi, \Theta$$

holds. This can be reformulated into a maximisation problem with solution (see appendix C)

$$s^* = \max\{h(x), h(x \pm R\sin\Theta) - R\,(\cos\Theta + 1)\} ,$$

where Θ needs to be determined to solve $\pm \cot \Theta\ h'(x \pm R \sin \Theta) + 1 = 0$.

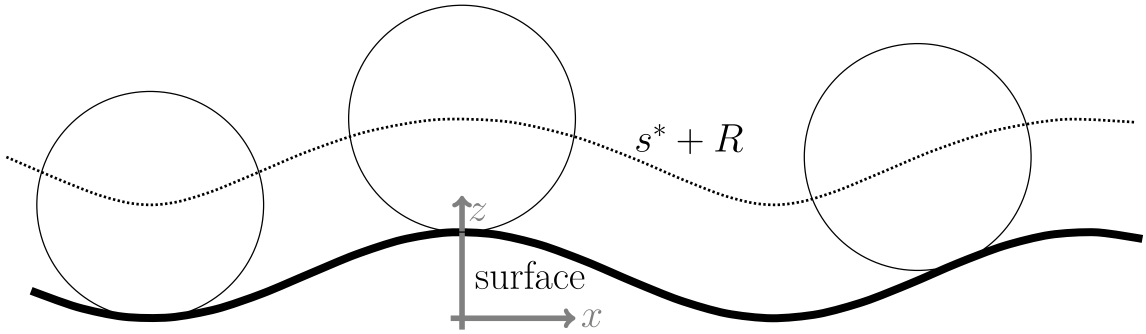

Figure 7.19: Tangential contact for various positions along the sinusoidal surface. s^* is the minimal distance of the bacterium's bottom to the minimum of the surface, such that the sphere is in tangential contact. Note that the bacteria and surface dimensions are scaled according to the experimental setting and therefore for better visibility $s^* + R$, i.e. the height of the bacterium's centre is plotted.

7.2.2 Monte Carlo model extension

To interpret the experimentally obtained adhesion forces on sinusoidal surfaces I extended the previously presented model to curved surfaces. The macromolecule is placed on the bacterium's surface at position $\vec{r}$ relative to the bacterium's centre (see figure 7.20 a). The molecule has length l and orientation $\hat{P}$. At the beginning of the simulation, $\hat{P}$ points along the local surface normal defined by $\vec{r}$. The length fluctuations of the molecule occur along $\hat{P}$. Furthermore, both ends of the molecule relative to the global coordinate system are denoted by $\vec{r}_1$ and $\vec{r}_2$ as indicated in figure 7.20 a. Thereby the end connected to the bacterium is denoted by $\vec{r}_1$ while the freely moving end is $\vec{r}_2$.

A macromolecule can bind to the surface if the shortest distance of $\vec{r}_2$ to the surface is smaller than the interaction range.[9] How this shortest distance is computed is described in the next section. However, once the molecule is bound to the surface its length and orientation can change by moving the bacterium (see figure 7.20 b). This stretch leads to a force acting along $\hat{P}$ such that the cantilever only measures its z-projection i.e. $F(l)\hat{P} \cdot \hat{e}_z$, where $F(l)$ denotes the magnitude of the force at stretch l. Note, that this stretching changes the orientation of the molecule.

Additionally, I consider two kinds of interactions with the surface. The first kind is identical to the previous model, i.e. the energy of a bound molecule decreases by the

---

[9] The presence of a potential barrier is possible.

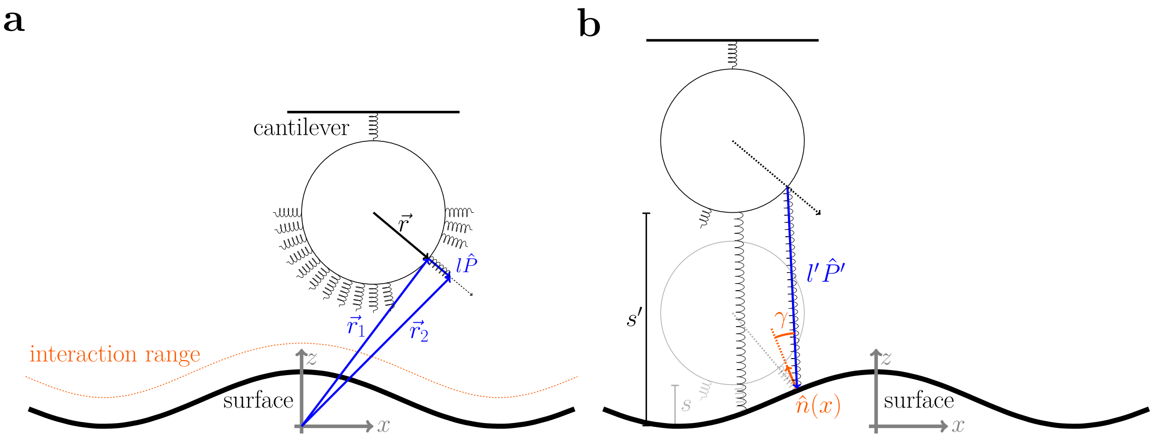

Figure 7.20: Illustration of the extended model elements on a sinusoidal surface. **(a)** The macromolecules are oriented along their local surface normal given by their position $\vec{r}$ relative to the centre of the bacterium. Their length l and orientation $\hat{P}$ are determined by their position $\vec{r}_1$ on the bacterium and the free moving end $\vec{r}_2$. If $\vec{r}_2$ is in the interaction range of the surface it can bind and be stretched. **(b)** If the bacterium is moved from $s \mapsto s'$ perpendicular to the surface the molecules which are bound to the surface are stretched to length l' and change their orientation to $\hat{P}'$. The binding strength to the surface is determined by the angle γ between the local surface normal and the orientation $\hat{P}'$ of the macromolecule. Furthermore, the force of the molecule acts along $\hat{P}'$ such that the cantilever only measures its z-projection. Note that while the bacteria and surface dimensions are scaled according to the experimental setting the spring and cantilever are not.

potential depth V. In the second kind of interaction, the potential depth depends on the angle between the orientation of the molecule and the local surface normal. In particular, I consider for a molecule with orientation $\hat{P}$ that binds at position x the potential

$$V(x) = V\cos\gamma = -V\hat{n}(x)\cdot\hat{P}$$

where $\hat{n}(x)$ denotes the surface normal at position x (see figure 7.20 b).[10] The surface normal can be obtained from the surface height h as

$$\hat{n}(x) = \frac{1}{\sqrt{1+h'(x)^2}}\begin{pmatrix}-h'(x)\\0\\1\end{pmatrix},$$

where I assumed that the h remains constant along the y-direction.

---

[10] Note the minus sign for the orientation $\hat{P}$ such that both vectors are properly aligned.

To compute all changes in configurations it is convenient to choose the usual spherical coordinates (R, Θ, φ) to determine $\vec{r}$. Furthermore, to be able to include in the future fluctuations of the orientation easily, it is convenient to specify the orientation $\hat{P}$ with respect to the bacterium's surface normal i.e. $\vec{r}$. Therefore, to convert from the coordinates with respect to the local surface normal to the global coordinate system[11], I introduced the matrix

$$R = \begin{pmatrix} \cos\varphi\cos\Theta & -\sin\varphi & \cos\varphi\sin\Theta \\ \sin\varphi\cos\Theta & \cos\varphi & \sin\varphi\sin\Theta \\ -\sin\Theta & 0 & \cos\Theta \end{pmatrix} .$$

Using this matrix, the position of both ends of the macromolecule are given by

$$\begin{aligned} \vec{r}_1 &= \vec{r} + (R + s)\hat{e}_z + x\hat{e}_x \\ \vec{r}_2 &= \vec{r}_1 + lR\hat{P} \ , \end{aligned}$$

where x denotes the position along the surface and s is the distance from the lowest point of the surface to the bottom of the bacterium. From these equations all changes in positions, and lengths can be computed:

First, I consider thermal length fluctuations of each macromolecule along their respective normal i.e. $l \mapsto l'$, $\vec{r}_2 \mapsto \vec{r}_2' = \vec{r}_1 + l'R\hat{P}$. Second, if the cantilever is moved from $s \mapsto s'$, $\vec{r}_1 \mapsto \vec{r}_1' = \vec{r} + (R + s')\hat{e}_z + x\hat{e}_x = \vec{r}_1 + (s' - s)\,\hat{e}_z$. If the molecule is not attached $(l, \hat{P}$ fix$)$ $\vec{r}_2 \mapsto \vec{r}_2' = \vec{r}_1' + lR\hat{P}$. However, if the molecule is attached the molecule is stretched ($\vec{r}_2$ fix) i.e. $l \mapsto l'$, $\hat{P} \mapsto \hat{P}'$. I now determine $l', \hat{P}'$ from $\vec{r}_2 = \vec{r}_2'$ which leads to

$$\begin{aligned} l'\hat{P}' &= l\hat{P} + R^{-1}\,(s - s')\,\hat{e}_z = l\hat{P} + (s - s') \begin{pmatrix} -\sin\Theta \\ 0 \\ \cos\Theta \end{pmatrix} \\ \Rightarrow l' &= \sqrt{l^2 + (s - s')^2\,(R^{-1}\hat{e}_z)^2 + 2l\,(s - s')\,\hat{P}\cdot R^{-1}\hat{e}_z} \\ &= \sqrt{l^2 + (s - s')^2 + 2l\,(s - s')\,(\cos\Theta P_z - \sin\Theta P_x)} \ . \end{aligned}$$

More conveniently the macromolecule dynamics are summarized as follows:

---

[11] To rotate the global z-axis onto the surface normal, first rotate the amount Θ around the y-axis and then the amount φ around the new z-axis. Hence, $R = R_z(\varphi)\,R_y(\Theta)$ where R_z, R_y are the usual rotation matrices around the z- and y-axes respectively.

- length fluctuations: $l \mapsto l'$, $\vec{r}_2 \mapsto \vec{r}_2' = \vec{r}_1 + l' R\hat{P}$
- cantilever movement: $s \mapsto s'$, $\vec{r}_1 \mapsto \vec{r}_1' = \vec{r}_1 + (s'-s)\,\hat{e}_z$
  - molecule is attached:

$$l \mapsto l' = \sqrt{l^2 + (s-s')^2 + 2l\,(s-s')\,(\cos\Theta P_z - \sin\Theta P_x)}$$

$$\hat{P} \mapsto \hat{P}' = \frac{l}{l'}\hat{P} + \frac{s-s'}{l'}\begin{pmatrix} -\sin\Theta \\ 0 \\ \cos\Theta \end{pmatrix}$$

  - molecule is not attached: $\vec{r}_2 \mapsto \vec{r}_2' = \vec{r}_2 + (s'-s)\,\hat{e}_z$

Since the bacterium interacts with a curved surface the potential interaction area and therefore the number of involved macromolecules increases substantially. To increase computation time I parallelised computations and removed macromolecules, which most likely will not come into contact with the surface. For this, the bacterium is placed for every position along the surface into tangential contact (as in the geometrical model). Afterwards, the closest distance of each macromolecule to the surface is computed and if this distance is smaller than 70 nm the molecule is removed.[12]

Minimal distance to surface

Finding for a given position (x_p, y_p, z_p) above the surface the point (x, y, z) on the surface which minimizes the distance between them is a minimization problem with condition $z = h(x, y)$. I obtain (see appendix D)

$$\begin{aligned} x &= x_p + (z_p - h(x,y))\,\partial_x h(x,y) \\ y &= y_p + (z_p - h(x,y))\,\partial_y h(x,y) \\ z &= h(x,y) \end{aligned}$$

---

[12] Since the molecules have a fluctuating length, I consider the position on the bacterium, i.e. $\vec{r}_1$ as the position of the molecules. Note that the mean length of the molecules in the unbound state is given by the rest length $\sqrt{\frac{L\cdot B}{6}}$ and not the contour length L. Therefore, even though some molecules have contour lengths that are the size of the threshold, their actual length is significantly smaller. However, if the rest length is differently defined this threshold should be adjusted.

as implicit equations in (x, y) which can be solved numerically by bisection. The corresponding shortest distance is

$$d = |z_p - h(x, y)| \sqrt{h_x^2(x, y) + h_y^2(x, y) + 1} \; .$$

7.2.3 Simulations

As a first step, I generated a bacterium where the properties of the molecules are sampled from the same distribution as for flat surfaces. For this fixed bacterium, the adhesion profile is simulated for both interaction potentials (see figure 7.21). Both models, i.e. with and without angle-dependent substratum interactions, approximately recreate the correct force scale. The shape of the adhesion profiles, however, differs from the experimentally obtained profile in several ways. First, the maximal adhesion force is not obtained in the minimum of the surface but rather slightly next to it. This is, as I will demonstrate later, an effect of the spatial distribution and the properties of macromolecules of the particular bacterium considered. Second, I observe that the adhesion force with angular interactions is, compared to the model without angular interactions, always smaller. This is expected since the angular interaction decreases the binding energy for most molecules and positions along the surface. Third, the 'bathtub-like' shape is only recovered for the model with angular interactions. This will become more evident in the subsequent discussion. However, the size of the plateau, i.e. the domain over which it is constant, is much shorter than in the experiments.

Since the geometric effects of the models should be more pronounced at shorter contour lengths, I repeated the simulations with shorter molecules. To better analyse the influence of stretching at different positions along the surface all molecules possess, in the following simulations, the identical contour length of 45 nm and a Kuhn length of 0.4 nm (see figure 7.22). The resulting adhesion forces are, compared to the simulations where the molecule properties are drawn from a distribution, substantially increased. This is caused by the synchronous stretching of many macromolecules at the same time. Additionally, the maximal force is now obtained in the minimum of the surface. The most important observation, however, is emphasised by switching to adhesion profiles normalized by the maximal observed force (see figure 7.22 b). This shows that a 'bathtub-like' shape is observed for angular interactions but not without them. However, also for much shorter molecules the drop in adhesion force, as well as the extent of the plateau, is smaller than in the experiments.

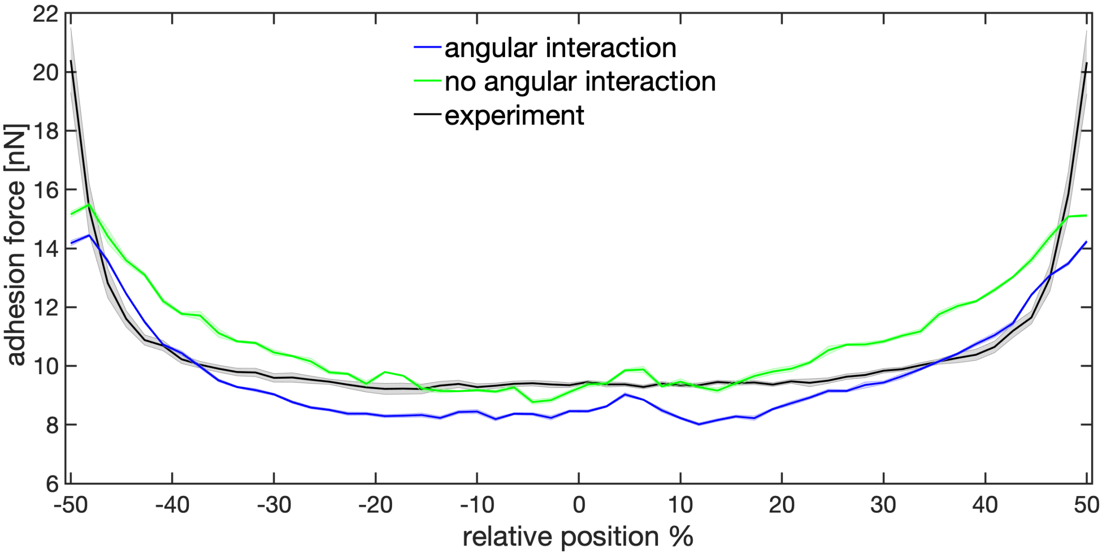

Figure 7.21: Adhesion profile along the surface averaged over five repetitions for a single bacterium. The molecules have properties as for the flat surfaces, i.e. the scale parameter for contour length distribution is $\lambda = 125$.

By comparing both models to the result of the geometric model, additional insight can be obtained. This shows that if the profile would be determined by only the accessible surface area (geometric model) along the surface a 'bowl-like' shape is expected. This predicted profile is smooth and, except near the maximum of the surface, always overestimates the adhesion force relative to the thermally fluctuating molecules. In particular, it does not show a plateau as is observable for angular interactions. To include angular interactions into the geometric model, I divided the relative adhesion force in the geometric model by $\sqrt{1 + h'(x)^2}$, i.e. the normalisation constant of the surface normal. Here x denotes the position of the contact point along the surface. This modification introduces a plateau close to the maximum of the surfaces, but it underestimates the extent of the plateau and overestimates the adhesion outside of the plateau. Hence for both kinds of interaction potentials, the stretching of the macromolecules gives, except close to the surfaces maximum, a non-trivial contribution.

To gain more knowledge about the origin of the adhesion profile, I tracked the configurations of the molecules. This allows establishing which part of the bacterium contributes to the adhesion force and how the molecules are stretched at different positions along the surface. To more easily understand the subsequent figures, I want to emphasize that the polar angle of the contact point changes along the surface (see figure 7.23). This angle defines the centre of a surface patch that in the geometric model is able to interact

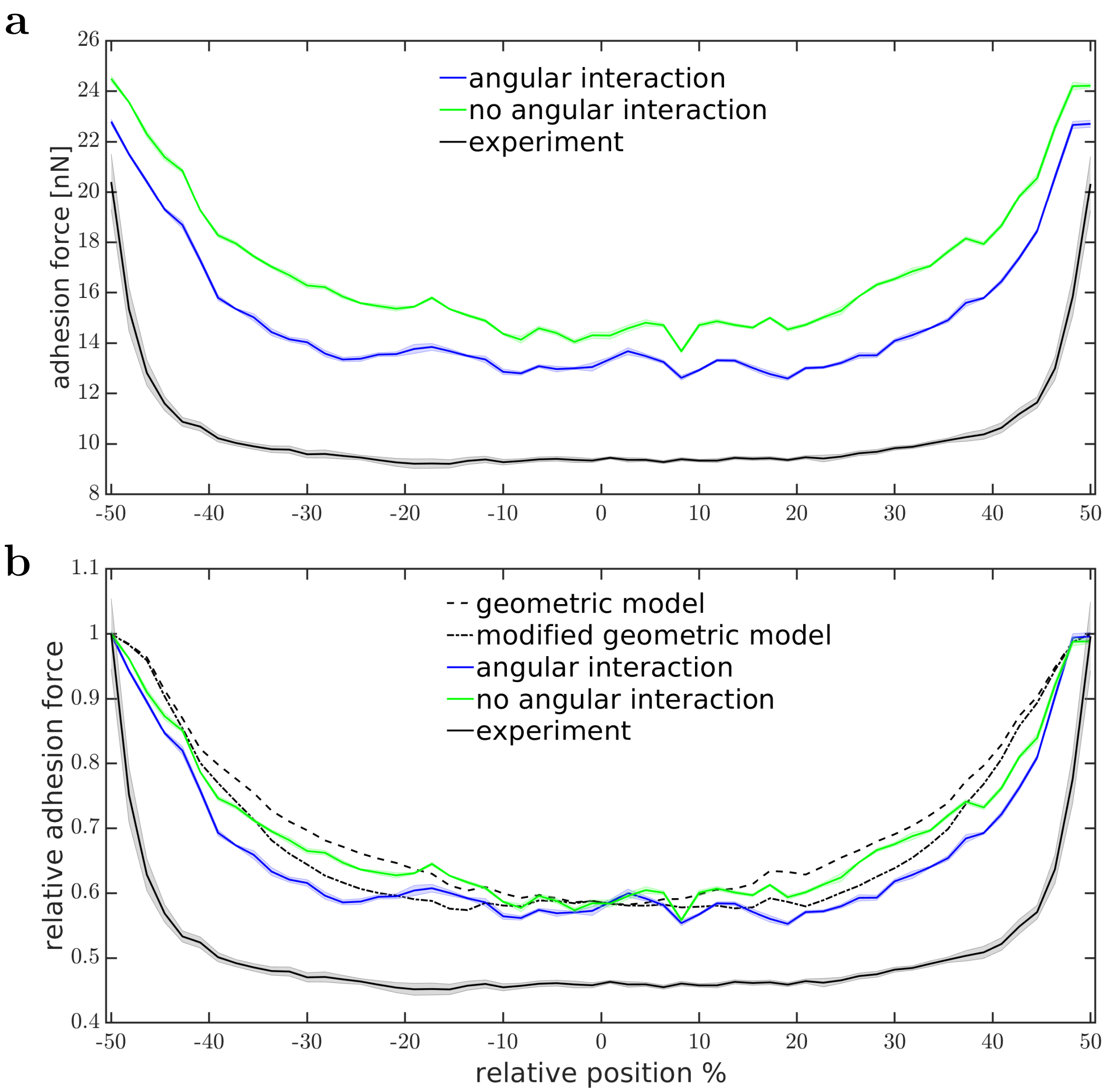

Figure 7.22: Adhesion profile along the surface with **(a)** absolute adhesion force and **(b)** adhesion force normalized by the maximal force. In the modified geometric model the relative adhesion force of the geometric model is divided by $\sqrt{1+h'(x)^2}$. All molecules have a contour length of 45 nm and a Kuhn length of 0.4 nm.

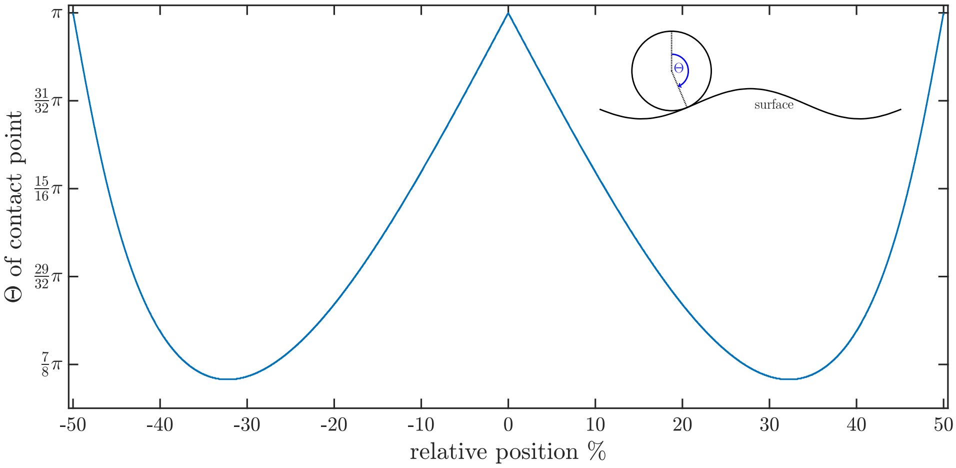

Figure 7.23: Polar angle of the contact point as depicted in the inset. The angle is computed as described in section 7.2.1.

with the surface. Since the polar angle is not injective on the domain [−50%,0%] the same contact point is reached twice when moving from the minimum of the surface to its maximum. However as presented in figure 7.22 b, the size of the interacting area is distinct in both instances. Interestingly, the minimum of the polar angle is assumed approximately at the start of the plateau observed in the experimentally obtained adhesion profiles.

I use the bacterial surface normal at the contact point to define the z-axis of a local coordinate system. I define the coordinate system in the same manner as the local coordinate system defined for individual macromolecules in section 7.2.2. Hence, I can convert with $R^{-1} = R^T$ all global coordinates to the local system.[13] The such constructed local coordinate system allows defining an azimuthal and polar angle for all points on the bacterium. And since the geodesic distance on a sphere is given by a great circle the polar angle defines the geodesic distance[14] to the contact point.

Until now I presented only the resulting adhesion profiles, and not how different parts of the bacterium contribute to them. In accordance with the previous results, the bacterial surface area contributing to the adhesion force is, for the thermally fluctuating molecules, always smaller than in the geometric model (compare purple to other colours in figure 7.24). Figure 7.24 shows that in the plots the contributing areas are elliptical around the contact point. These are, however not ellipses in real space. Since this polar plot uses polar and azimuthal angles on a sphere it describes a curved patch.

---

[13] In section 7.2.2, I converted with R from the local coordinate system to the global system.

[14] In units of the bacterial radius.

Nevertheless, a smaller area in the polar plot indicates a smaller bacterial surface area. The reduced area can be attributed to two effects. First, the effective length of the fluctuating macromolecules is much smaller than the interaction radius considered in the geometric model. Second, the geometric model considers the interacting molecules at the point of contact, while the adhesion force for thermally fluctuating molecules is obtained at a certain distance to the surface. And since some molecules detached during retraction, not all initially bound molecules contribute to the adhesion force. This is particularly well highlighted by comparing both interaction potentials (compare figure 7.24 a and b). For angular interactions, the area contributing to the force is not simply connected, but close to the contact point, the molecules are mostly detached. This is caused by the effectively smaller potential depth experienced by most of the molecules, which leads to earlier detachment. Interestingly, as can be observed by the relative stretch $\frac{l-l_0}{L}$, the molecules are stretched symmetrically around the contact point. Increasing the geodesic distance (radial coordinate in figure 7.24) the molecules are stretched more until they are detached (white space in figure 7.24). Furthermore, all molecules are mostly aligned along the global z-axis such that the force experienced by the molecules is mostly measured by the cantilever (geometric factor in figure 7.24))

As I already mentioned the size of the interacting area changes along the surface. However, figure 7.24 shows also that the ellipses major axes turn when moving along the surface. Since the local coordinate system turns along the surface caution is warranted in the interpretation. However, the first and last columns, as well as the second and third have approximately the same contact point. Hence, comparing for these the orientation of the ellipses is straightforward. This shows, that in the minimum of the surfaces mostly the molecules pointing along the periodicity of the surface contribute to the attachment. When the bacterium moves out of the minimum of the surface the patch turns. Now the molecules pointing along the trench contribute to the adhesion force. Hence, incorporating a bending rigidity into the model of the macromolecules would enhance the detachment when the bacterium is moved from the minimum of the surface towards the maximum. This effect, while not be explored in the limits of this thesis, seems to be the most promising candidate in widening the plateau of constant adhesion and hence recreating the experimentally observed profiles.

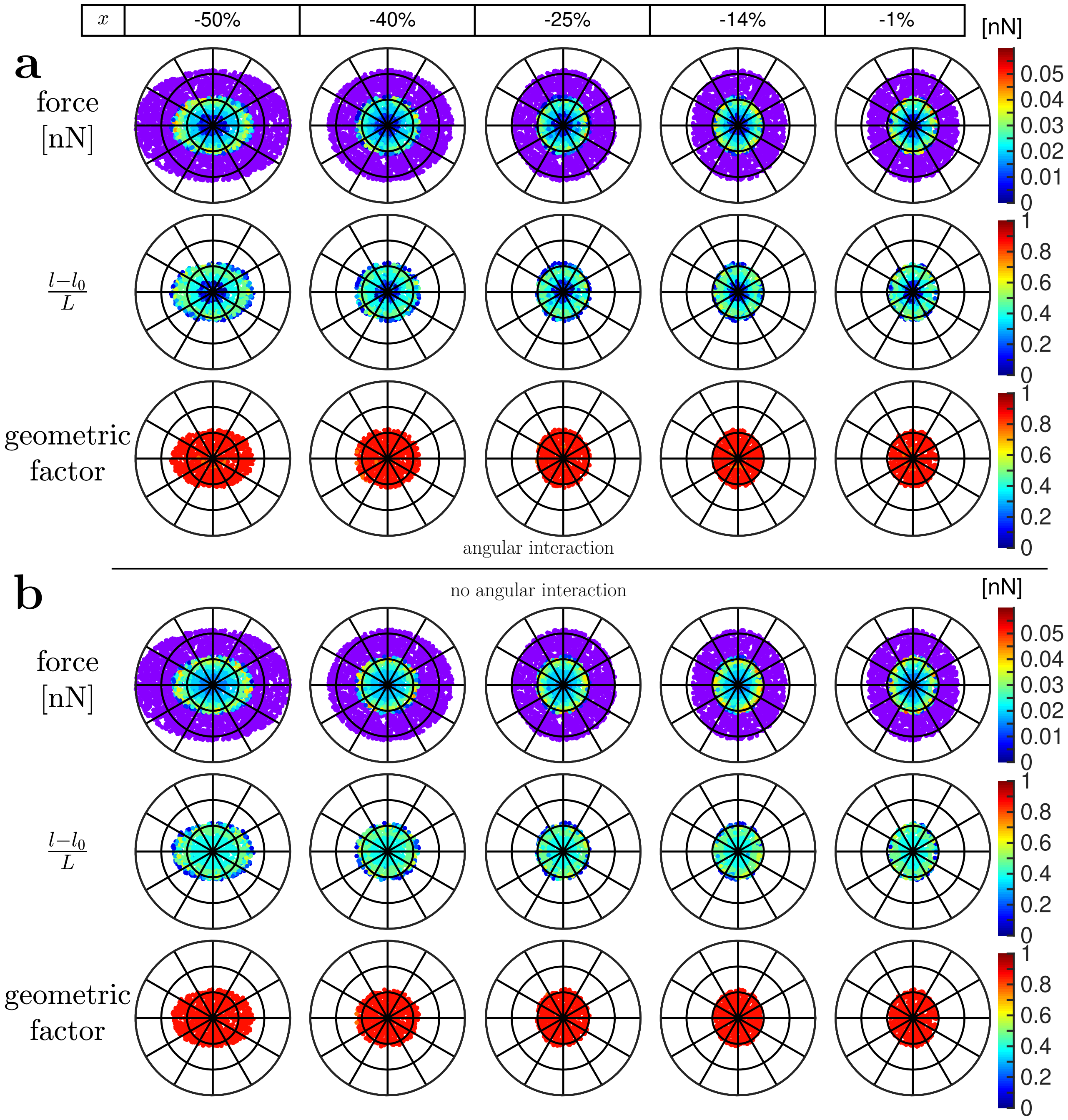

Figure 7.24: Molecule properties contributing to the adhesion force for the model including **(a)** angular interactions and **(b)** no angular interactions. The coordinate system changes along the x-coordinate, such that the z-axis matches the surface normal of the contact point. The required turning angle is depicted in figure 7.23. The radial coordinate is the polar angle while the angular coordinate is the azimuthal angle in the new coordinate system. Therefore, the radial coordinate depicts the geodesic distance to the contact point, whereby the lines of constant angle are 100 nm apart. Purple depicts the molecules which contributed to the force according to the geometric model. Molecules are only plotted when they contribute to the adhesion force, i.e. $\langle \text{force} \rangle \neq 0$. The geometric factor is P_z with respect to the global coordinate system and measures how much of the force experienced by the molecules is transmitted onto the cantilever. All molecules have a contour length of 45 nm, a Kuhn length of 0.4 nm and the data is averaged over five retractions.

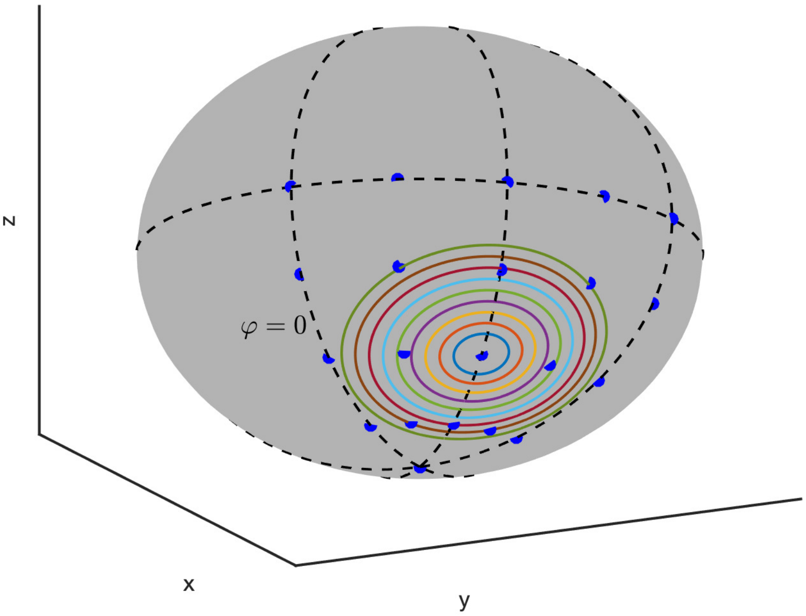

Figure 7.25: Illustration of the patches positions in figure 7.26. The radii of the patch are up to scale and match the colours in figure 7.26. Note that in the simulations $\varphi = 0$ aligns with movement parallel to the surfaces periodicity.

Peaked adhesion capabilities

To get the first idea of how a single patch of increased adhesion capabilities would influence the adhesion profiles, I used the modified geometric model and placed a patch systematically on the bacterium's surface. I vary (Θ, φ) in the usual spherical coordinates. Since the patch needs to be able to interact with the surface, I only considered $\Theta \geq \frac{\pi}{2}$, and because of the reflection symmetry of the surface, I only consider $0 \leq \varphi \leq \frac{\pi}{2}$. For a better illustration of where the patches have been positioned see figure 7.25. Inside the patch, the adhesion is increased ten-fold.

The resulting adhesion profiles can be seen in figure 7.26. If the patch is placed in the x-y plane of the bacterium, the standard 'bathtub-like' adhesion profiles are obtained for all considered radii. If the patch is facing along the x-axis ($\varphi = 0$) and is lowered (increasing Θ), parts of the patch come left of the surfaces maximum into contact. This leads to asymmetric adhesion profiles where the maximal amount of adhesion is not at the minimum of the surface. As the patch approaches the bottom of the bacterium,

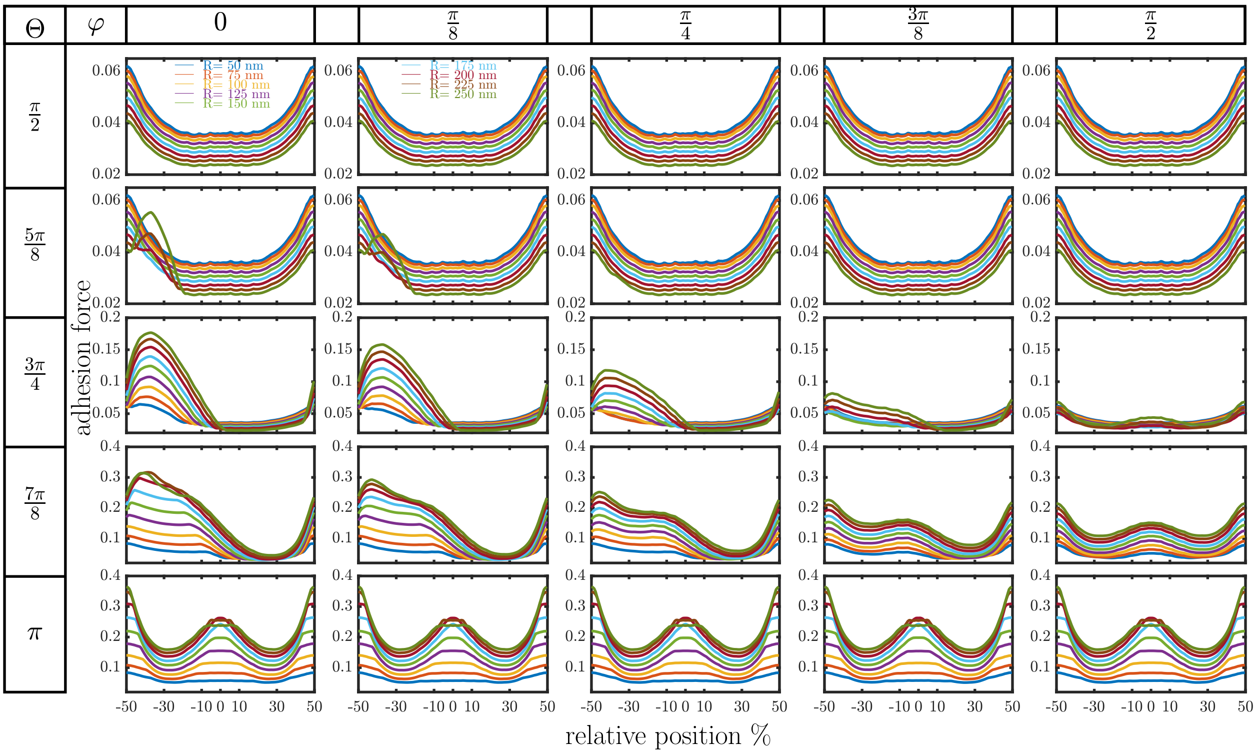

Figure 7.26: Adhesion profiles in the modified geometric model with a single patch of radius R and ten-fold increased adhesiveness positioned at position (Θ, φ). Note that in the modified geometric model the adhesion force of the geometric model is used and divided by $\sqrt{1 + h'(x)^2}$. The bacterial radius is 500 nm.

smaller radii are sufficient to obtain asymmetric adhesion profiles. However, since the adhesion is always increased over a wide domain, the profiles are never reminiscent of the experimentally obtained adhesion profiles. If the patch is placed directly at the bottom of the bacterium symmetric profiles are obtained where, depending on the patches radius, increased adhesion at the maximum of the surface is observed. When the patch is not at the bottom of the bacterium and turned such that it does not align with the x-axis, the asymmetry of the profiles is less pronounced. If the patch is turned such that it points along the y-axis, symmetric adhesion profiles are obtained for all considered radii.

7.2.4 Conclusion

The SCFS experiments reveal that the adhesion capabilities of *S. aureus* are heterogeneously distributed over the cell envelope. In particular, a reflection asymmetry around the maximum of the surface and locally increased adhesion is observed. If this is due to an increased number of molecules or their specific properties remains unknown. However, already adhesion profiles which, besides the increased adhesion in the minimum of the surface, show no locally increased adhesion display 'bathtub-like' adhesion profiles. This is, compared to the predictions of a model considering the accessible bacterial surface area, remarkable in two ways: First, immediately next to the surfaces minima the adhesion force decreases much faster. Secondly, near the maximum of the surface, the adhesion force decreases much less. This leads to a plateau of constant adhesion forces over a large domain of the surface. Monte Carlo simulations, considering the different stretches of macromolecules depending on their position relative to the surface, could not reproduce both behaviours. Only a heterogeneous interaction potential inversely proportional to the local surface normal could reproduce the plateau of adhesion forces next to the maximum of the surface. However, the extent of the plateau is much smaller than in the experimentally obtained profiles.

By tracking in the simulations which molecules contribute to the adhesion force, I could identify a possible missing detail. In the minimum of the surface, the molecules contributing to the adhesion force point mostly along with the periodicity of the surface. While outside of the minimum the contributing molecules are pointing along the trench. Hence, considering a lateral bending rigidity of the molecules could facilitate varying detachment along the surface and might result in an extended plateau. The simulations, however, also neglect other possible effects. For instance, deformations of the PDMS substratum, as well as the bacterium are not considered. While the deformation of the substratum during compression can be included by the usual deformation theory, the high local forces during retraction might require a coupling of the macromolecules stretch to the substratum deformation. The necessity for this can be evaluated by measuring adhesion profiles on substrates that are less deformable than PDMS. Another neglected factor could be the possible distinct behaviours of wall teichoic acids, capsular polysaccharides and proteins. Proteins, which can unfold in several domains, might unfold differently depending on the angle relative to the surface. The potential influence of unfolding is hard to estimate and possibly even depends on the synchronous or asynchronous unfolding of other proteins. Nevertheless, this could be investigated by repeating the experiments with mutants lacking cell-wall anchored proteins.

8 Summary & Conclusion

I investigated in this thesis two aspects of microbial dynamics, i.e. range expansion and bacterial adhesion on abiotic surfaces. The characterization of the adhesion process has been performed in a combined approach of simulations and SCFS experiments. I modelled the adhesion process, performed the simulations and analysed the experimentally obtained force-distance curves recorded by several members of the Jacobs group at Saarland University. In particular, I investigated the adhesion process of the bacterium *S. aureus* to abiotic surfaces. The results demonstrate, that *S. aureus* uses two different binding mechanisms on hydrophobic and hydrophilic surfaces [124]. The retraction curves on hydrophilic and hydrophobic surfaces show several distinct behaviours: First, the curves on hydrophilic surfaces show several small peaks of similar magnitude, while on hydrophilic surfaces the curves are cup-shaped with only a single major peak. Second, the typical maximal forces on hydrophilic surfaces are hundreds of pN up to several nN while on hydrophobic surfaces, they are several tens of nN. And third, on hydrophobic surfaces, the experiments show a large variability of adhesion forces in the bacterial population but only a low variability between repetitions with the same cell. Bacteria on hydrophilic surfaces, however, show a comparable variability between repetitions with the same cell and the entire population. I analysed the origin of this behaviour by extending a previously developed model that mimics SCFS experiments by Monte Carlo simulations. In these simulations, the bacterium is treated as a rigid sphere decorated by fluctuating macromolecules that, once bound to the substrate, mediate the acting forces. I added a WLC like force-stretch relation to mimic the characteristic curves known from single-molecule force spectroscopy of polymers and introduced a potential barrier that stochastically selects the binding macromolecules. By varying the binding strength of the molecules and the potential barrier height the correct force scales, distinct curve shapes and distinct stochastic behaviours on both kinds of surfaces are obtained. Furthermore, I substantiated the necessity of this potential barrier by a simple set of master equations. These demonstrate that the stochastic response of the macromolecules to stretching is negligible. This is caused by the divergence of force-stretch relation due to the finite extension of the macromolecules. While the model could capture the stochasticity and force-response of single cells very well, it could not reproduce the vast differences in adhesion forces different bacteria display on hydrophobic surfaces. I attributed this to the simple universal force-stretch relation of all the involved macromolecules and that they are distributed homogeneously over the cell envelope.

By performing the SCFS experiments on shifting positions on a sinusoidal surface, the adhesion force of varying parts of the bacterial surface area can be probed. Hence, this set of experiments allows characterizing the distribution of adhesion capabilities over the cell envelope. To better understand the resulting adhesion profiles, I extended the model of thermally fluctuating molecules to curved surfaces. Additionally, I consider a simple geometric model of the accessible bacterial surface area along the surface. This allows evaluating the distinct influences of accessible area and variable stretching along the surface. Experimentally observed are, with respect to the surfaces maximum asymmetric adhesion profiles and peaks on varying positions along the surface. Therefore the adhesion capabilities are heterogeneously distributed over the cell envelope. This explains to some extent the lack of vast differences in adhesion forces on flat surfaces, but also has interesting implications for the adhesion process in flow chambers. Since the bacteria are embedded in a liquid environment the most adhesive part might reorient towards the surface such that the adhesion capabilities are increased. This should be observable in increased adhesion forces and including this additional degree of freedom into the model is an interesting direction for future research. Apart from the asymmetry and peaks, the adhesion profiles show further interesting behaviour. They display, relative to the predictions from the accessible bacterial surface area, two remarkable features. First, when moving out of the minimum of the surface, the adhesion force decreases much faster. Second, this steep decrease is followed by a wide plateau of constant adhesion where geometric considerations predict a constant decrease. While the adhesion profiles of the thermally fluctuating molecules are more rugged, the overall shape and relative magnitude agree with the accessible surface area. Hence variable stretching alone does not explain the observed plateau. However, including angle-dependent interactions of the macromolecules with the surface could reproduce the plateau. But the extent of the plateau is much narrower than in the experimentally obtained profiles. By tracking which molecules contribute to the adhesion force, I could identify a promising effect not included in the present models. I observed that in the minimum of the surface, the molecules contributing to the adhesion force point mostly along with the periodicity of the surface. While outside of the minimum the molecules contributing to the adhesion force are pointing along the trench. Hence, introducing a lateral bending rigidity of the molecules could facilitate varying detachment along the surface and might result in an extended plateau. If this also leads to the fast decrease of adhesion force remain to be explored in the future. Other not explored possibilities are distinct force-stretch behaviours of wall teichoic acids, capsular polysaccharides and proteins, as well as the deformability of the bacterium and substratum. The influence of these factors could be investigated with more rigid substrates and mutants lacking cell-wall anchored proteins.

The second topic I investigated are microbial range expansion experiments with heterogeneous mechanical interactions. Range expansions are toy systems to understand the invasion dynamics of microbes and due to their low generation time provide also a suitable framework to study the evolution of expanding populations. My work was inspired by the experiments of Zöllner et al. [9] with *N. gonorrhoea* bacteria. The wild-type strain of these bacteria possess pili where naturally arising mutants show different levels of piliation. A mixture of piliated and non-piliated bacteria sort, in liquid flasks, on time scales where cell division is negligible, such that the piliated strain lies entirely in the inside of the spherical colony. In range expansion experiments the non-piliated strain outcompetes the piliated strain even if it divides twice as slow. This distinguishes this model system from many other microbial range expansion experiments. The origin of this outcompetition has been attributed to the aforementioned cell sorting, but in the simulations only compact wedge initial conditions i.e. the fast-growing strong piliated strain is contained in a small sector, have been used [120]. These conditions don't mimic the experiments where both strains are inoculated into a circular domain. In particular, in the experiments, the initial density is rather small and the spatial distribution of both strains is well-mixed. My work demonstrates that in those initial conditions cell-sorting is not sufficient to reproduce the experimentally observed patterns. To investigate the interplay of these different strains I implemented an extension of the classical Eden model including cell division induced pushing and swapping of cells. The simulations reveal, as already mentioned, that for reproducing the experimentally observed patterns a pure swapping mechanics is not sufficient [124]. Rather strong interactions of the piliated bacteria with each other, as well as the substrate, are leading to heterogeneous pushing susceptibilities that reproduce the patterns even in the absence of any swapping. Furthermore, the model showed that homogeneous pushing leads to a small but standing variation of a disadvantaged subpopulation inside the expanding colony. This survival is enhanced when instead of the often used exponential distribution of the division times a more biological peaked distribution is considered. Enhanced survival of disadvantaged mutants is highly important for the development of antibiotic resistance and in changing growth conditions these mutants can even dominate the population. This sustained survival has been described before by concepts from continuum theories like surface tension and pressure differences inside growing microbial colonies [111, 112]. On the length scale of individual microbes, however, pressure fields and in particular surface tension are not well-defined concepts. The application of my model shows that the enhanced survival can be entirely understood on a cell individual level by the division induced pushing of cells. In my model, however, the pushing is achieved by an ad hoc translation of cells over the grid. Therefore, extending the model to an off-lattice version, where pushing forces are generated by the cells is an interesting direction for future research. Furthermore, since heterogeneities of the cells influence the colony growth also mechanical heterogeneities of the environment should strongly influence the growth dynamics. This could be investigated for instance in hydrogels which allow for the creation of controlled heterogeneous environments.

Combining both threads of investigation, i.e. studying how adhesion influences colony growth, is a promising research direction. While in this thesis adhesion of *S. aureus* was investigated, it is also known for *E. coli* that the adhesion capabilities are heterogeneously distributed over the cell enveloped [138]. Furthermore, this heterogeneity determines the transition from two-dimensional to three-dimensional growth and further analysis could provide some insights into colony formation and therefore bacterial infections [139]. Therefore characterizing the adhesion capabilities of other bacteria, like *N. gonorrhoea*, is a prime task. In particular, the pili distribution would be interesting to obtain. Since for the rod-shaped bacterium *Pseudomonas aeruginosa*, the distinct pili expression levels, have been shown to determine the colony spread in two dimensions and the transition from two-dimensional to three-dimensional growth [140]. This is in particular, interesting since these transitions can be understood by the theory of active nematics and topological defects arising in them. And while *N. gonorrhoea* is a round bacterium a heterogeneous pili distribution would make them effectively nematic. Moreover, *N. gonorrhoea* often occurs as a diplococcus, i.e. in pairs. Thus, even if the pili density is homogeneous nematic effects could be relevant. In this regard, the theory of active nematic could be extended to investigate the influence of nematic cells that can split into two non-nematic cells. This is in particular interesting in the view of *N. gonorrhoea* mutants, which display reduced pili expression. Those mutants might preferentially transition from two-dimensional to three-dimensional growth, adding a literal additional dimension to the study of mutants and antibiotic resistance inside expanding microbial populations.

Bibliography

[1] Carla CCR De Carvalho. Biofilms: recent developments on an old battle. *Recent patents on biotechnology*, 1(1):49–57, 2007.

[2] Carsten U Schwermer, Gaute Lavik, Raeid MM Abed, Braden Dunsmore, Timothy G Ferdelman, Paul Stoodley, Armin Gieseke, and Dirk De Beer. Impact of nitrate on the structure and function of bacterial biofilm communities in pipelines used for injection of seawater into oil fields. *Applied and Environmental Microbiology*, 74(9):2841–2851, 2008.

[3] Stefano Perni, Emily Callard Preedy, and Polina Prokopovich. Success and failure of colloidal approaches in adhesion of microorganisms to surfaces. *Advances in Colloid and Interface Science*, 206:265 – 274, 2014. ISSN 0001-8686. doi: https://doi.org/10.1016/j.cis.2013.11.008. URL `http://www.sciencedirect.com/science/article/pii/S0001868613001619`. Manuel G. Velarde.

[4] Jayaraman Narenkumar, Mohamad S AlSalhi, Arumugam Arul Prakash, Subramani Abilaji, Sandhanasamy Devanesan, Aruliah Rajasekar, and Akram A Alfuraydi. Impact and role of bacterial communities on biocorrosion of metals used in the processing industry. *ACS omega*, 4(25):21353–21360, 2019.

[5] Luanne Hall-Stoodley, J William Costerton, and Paul Stoodley. Bacterial biofilms: from the natural environment to infectious diseases. *Nature Reviews Microbiology*, 2(2):95–108, 2004.

[6] Sarah Jane Quillin and H Steven Seifert. Neisseria gonorrhoeae host adaptation and pathogenesis. *Nature Reviews Microbiology*, 16(4):226, 2018.

[7] Carla Renata Arciola, Davide Campoccia, and Lucio Montanaro. Implant infections: adhesion, biofilm formation and immune evasion. *Nature Reviews Microbiology*, 16(7):397, 2018.

[8] Timothy J Foster, Joan A Geoghegan, Vannakambadi K Ganesh, and Magnus Höök. Adhesion, invasion and evasion: the many functions of the surface proteins of staphylococcus aureus. *Nature Reviews Microbiology*, 12(1):49–62, 2014.

[9] Robert Zöllner, Enno R Oldewurtel, Nadzeya Kouzel, and Berenike Maier. Phase and antigenic variation govern competition dynamics through positioning in bacterial colonies. *Scientific Reports*, 7(1):12151, 2017.

[10] H.C. Hamaker. The london-van der waals attraction between spherical particles. *Physica*, 4(10):1058 – 1072, 1937. ISSN 0031-8914. doi: https://doi.org/10.1016/S0031-8914(37)80203-7. URL `http://www.sciencedirect.com/science/article/pii/S0031891437802037`.

[11] G.J. Lauth and J. Kowalczyk. *Einführung in die Physik und Chemie der Grenzflächen und Kolloide*. Springer Berlin Heidelberg, 2015. ISBN 9783662470176. URL `https://books.google.de/books?id=bYxyrgEACAAJ`.

[12] C.J. van Oss. *Interfacial Forces in Aqueous Media*. Taylor & Francis, 1994. ISBN 9780824791681.

[13] EJW Verwey and J Th G Overbeek. Theory of the stability of lyophobic colloids. elsevier, amsterdam. *Theory of the stability of lyophobic colloids. Elsevier, Amsterdam.*, 1948.

[14] RTWDW Hogg, To Wo Healy, and Douglas W Fuerstenau. Mutual coagulation of colloidal dispersions. *Transactions of the Faraday Society*, 62:1638–1651, 1966.

[15] Valentin L. Popov, Markus Heß, and Emanuel Willert. *Handbook of contact mechanics : exact solutions of axisymmetric contact problems*. Springer, Berlin, Heidelberg, 2019. doi: 10.1007/978-3-662-58709-6. URL `https://doi.org/10.1007/978-3-662-58709-6`.

[16] Valentin L. Popov. *Contact Mechanics and Friction : Physical Principles and Applications*. Springer, Berlin, Heidelberg, 2017. doi: 10.1007/978-3-642-10803-7.

[17] Daniel Maugis. Adhesion of spheres: The jkr-dmt transition using a dugdale model. *Journal of Colloid and Interface Science*, 150(1):243 – 269, 1992. ISSN 0021-9797. doi: https://doi.org/10.1016/0021-9797(92)90285-T. URL `http://www.sciencedirect.com/science/article/pii/002197979290285T`.

[18] JA Greenwood. Adhesion of elastic spheres. *Proceedings of the Royal Society of London. Series A: Mathematical, Physical and Engineering Sciences*, 453(1961): 1277–1297, June 1997. doi: 10.1098/rspa.1997.0070.

[19] M. Ciavarella, J. Joe, A. Papangelo, and J. R. Barber. The role of adhesion in contact mechanics. *Journal of The Royal Society Interface*, 16(151):20180738, 2019. doi: 10.1098/rsif.2018.0738. URL `https://royalsocietypublishing.org/doi/abs/10.1098/rsif.2018.0738`.

[20] D Tabor. Surface forces and surface interactions. *Journal of Colloid and Interface Science*, 58(1):2 – 13, 1977. ISSN 0021-9797. doi: https://doi.org/10.1016/0021-9797(77)90366-6. URL `http://www.sciencedirect.com/science/article/pii/0021979777903666`. International Conference on Colloids and Surfaces.

[21] C. W. Gardiner. *Handbook of stochastic methods for physics, chemistry and the natural sciences.* Springer Series in Synergetics. Springer-Verlag, second edition, 1985.

[22] Nicolaas Godfried Van Kampen. *Stochastic processes in physics and chemistry*, volume 1. Elsevier, 1992.

[23] Joseph Leo Doob. *Stochastic processes.* New York Wiley, 1953.

[24] *Inversionsmethode*, pages 85–95. Vieweg+Teubner, Wiesbaden, 2008. ISBN 978-3-8348-9290-4. doi: 10.1007/978-3-8348-9290-4_8. URL `https://doi.org/10.1007/978-3-8348-9290-4_8`.

[25] Werner Krauth. *Statistical mechanics: Algorithms and Computations.* Oxford University Press, 2006.

[26] Michael A Gibson and Jehoshua Bruck. Efficient exact stochastic simulation of chemical systems with many species and many channels. *The journal of physical chemistry A*, 104(9):1876–1889, 2000.

[27] Yang Cao and David C Samuels. Discrete stochastic simulation methods for chemically reacting systems. *Methods in enzymology*, 454:115–140, 2009.

[28] Nikolaos Limnios and Gheorghe Oprisan. *Semi-Markov processes and reliability.* Springer Science & Business Media, 2012.

[29] Michael Rubinstein, Ralph H Colby, et al. *Polymer physics.* Oxford university press New York, 2003.

[30] Masao Doi and Samuel Frederick Edwards. *The Theory of Polymer Dynamics*, volume 73. Oxford University Press, 1986.

[31] Hiromi Yamakawa and Takenao Yoshizaki. *Helical wormlike chains in polymer solutions*, volume 1. Springer, 1997.

[32] C. P. Broedersz and F. C. MacKintosh. Modeling semiflexible polymer networks. *Rev. Mod. Phys.*, 86:995–1036, Jul 2014. doi: 10.1103/RevModPhys.86.995. URL `https://link.aps.org/doi/10.1103/RevModPhys.86.995`.

[33] Christina Kurzthaler and Thomas Franosch. Exact solution for the force-extension relation of a semiflexible polymer under compression. *Physical Review E*, 95(5): 052501, 2017.

[34] John F. Marko and Eric D. Siggia. Stretching dna. *Macromolecules*, 28(26):8759–8770, 12 1995. doi: 10.1021/ma00130a008. URL `https://doi.org/10.1021/ma00130a008`.

[35] A-L Barabási and Harry Eugene Stanley. *Fractal concepts in surface growth.* Cambridge university press, 1995.

[36] H Krug. Kinetic roughening of growing surfaces. *Solids far from equilibrium*, pages 479–582, 1991.

[37] Timothy Halpin-Healy and Yi-Cheng Zhang. Kinetic roughening phenomena, stochastic growth, directed polymers and all that. aspects of multidisciplinary statistical mechanics. *Physics reports*, 254(4-6):215–414, 1995.

[38] José J Ramasco, Juan M López, and Miguel A Rodríguez. Generic dynamic scaling in kinetic roughening. *Physical review letters*, 84(10):2199, 2000.

[39] Kazumasa A Takeuchi. An appetizer to modern developments on the kardar–parisi–zhang universality class. *Physica A: Statistical Mechanics and its Applications*, 504:77–105, 2018.

[40] Tomohiro Sasamoto. The 1d kardar–parisi–zhang equation: height distribution and universality. *Progress of Theoretical and Experimental Physics*, 2016(2): 022A01, 2016.

[41] Pasquale Calabrese and Pierre Le Doussal. Exact solution for the kardar-parisi-zhang equation with flat initial conditions. *Phys. Rev. Lett.*, 106:250603, Jun 2011. doi: 10.1103/PhysRevLett.106.250603. URL `https://link.aps.org/doi/10.1103/PhysRevLett.106.250603`.

[42] Ivan Corwin. The kardar-parisi-zhang equation and universality class, 2011.

[43] Sidiney G Alves, Tiago J Oliveira, and Silvio C Ferreira. Non-universal parameters, corrections and universality in kardar–parisi–zhang growth. *Journal of Statistical Mechanics: Theory and Experiment*, 2013(05):P05007, may 2013. doi: 10.1088/1742-5468/2013/05/p05007. URL `https://doi.org/10.1088/1742-5468/2013/05/p05007`.

[44] Sidiney G Alves, Tiago J Oliveira, and Silvio C Ferreira. Universal fluctuations in radial growth models belonging to the kpz universality class. *EPL (Europhysics Letters)*, 96(4):48003, 2011.

[45] R Jullien and R Botet. Surface thickness in the eden model. *Physical review letters*, 54(18):2055, 1985.

[46] LR Paiva and SC Ferreira Jr. Universality class of isotropic on-lattice eden clusters. *Journal of Physics A: Mathematical and Theoretical*, 40(1):F43, 2006.

[47] MT Batchelor, BI Henry, and SD Watt. Surface width scaling in noise reduced eden clusters. *Physical Review E*, 58(3):4023, 1998.

[48] CY Wang, PL Liu, and JB Bassingthwaighte. Off-lattice eden-c cluster growth model. *Journal of physics A: Mathematical and general*, 28(8):2141, 1995.

[49] SC Ferreira Jr and SG Alves. Pitfalls in the determination of the universality class of radial clusters. *Journal of Statistical Mechanics: Theory and Experiment*, 2006(11):P11007, 2006.

[50] Rebecca M Corrigan, David Rigby, Pauline Handley, and Timothy J Foster. The role of staphylococcus aureus surface protein sasg in adherence and biofilm formation. *Microbiology*, 153(8):2435–2446, 2007.

[51] Dominika T. Gruszka, Fiona Whelan, Oliver E. Farrance, Herman K. H. Fung, Emanuele Paci, Cy M. Jeffries, Dmitri I. Svergun, Clair Baldock, Christoph G. Baumann, David J. Brockwell, Jennifer R. Potts, and Jane Clarke. Cooperative folding of intrinsically disordered domains drives assembly of a strong elongated

protein. *Nature Communications*, 6(1):7271, 2015. doi: 10.1038/ncomms8271. URL `https://doi.org/10.1038/ncomms8271`.

[52] Dominika T Gruszka, Justyna A Wojdyla, Richard J Bingham, Johan P Turkenburg, Iain W Manfield, Annette Steward, Andrew P Leech, Joan A Geoghegan, Timothy J Foster, Jane Clarke, et al. Staphylococcal biofilm-forming protein has a contiguous rod-like structure. *Proceedings of the National Academy of Sciences*, 109(17):E1011–E1018, 2012.

[53] Lisa Craig, Katrina T Forest, and Berenike Maier. Type iv pili: dynamics, biophysics and functional consequences. *Nature Reviews Microbiology*, 17(7):429–440, 2019.

[54] Manuela K Hospenthal, Tiago RD Costa, and Gabriel Waksman. A comprehensive guide to pilus biogenesis in gram-negative bacteria. *Nature Reviews Microbiology*, 15(6):365, 2017.

[55] Anton Welker, Tom Cronenberg, Robert Zöllner, Claudia Meel, Katja Siewering, Niklas Bender, Marc Hennes, Enno R. Oldewurtel, and Berenike Maier. Molecular motors govern liquidlike ordering and fusion dynamics of bacterial colonies. *PRL*, 121(11):118102, September 2018. URL `https://link.aps.org/doi/10.1103/PhysRevLett.121.118102`.

[56] Wolfram Pönisch, Christoph A Weber, Guido Juckeland, Nicolas Biais, and Vasily Zaburdaev. Multiscale modeling of bacterial colonies: how pili mediate the dynamics of single cells and cellular aggregates. *New Journal of Physics*, 19(1): 015003, 2017.

[57] Enno R Oldewurtel, Nadzeya Kouzel, Lena Dewenter, Katja Henseler, and Berenike Maier. Differential interaction forces govern bacterial sorting in early biofilms. *eLife*, 4:e10811, 2015.

[58] Marjan W Van Der Woude and Andreas J Bäumler. Phase and antigenic variation in bacteria. *Clinical microbiology reviews*, 17(3):581–611, 2004.

[59] Richard A Blythe and Alan J McKane. Stochastic models of evolution in genetics, ecology and linguistics. *Journal of Statistical Mechanics: Theory and Experiment*, 2007(07):P07018, 2007.

[60] K. S. Korolev, Mikkel Avlund, Oskar Hallatschek, and David R. Nelson. Genetic demixing and evolution in linear stepping stone models. *Rev. Mod. Phys.*, 82:

1691–1718, May 2010. doi: 10.1103/RevModPhys.82.1691. URL `https://link.aps.org/doi/10.1103/RevModPhys.82.1691`.

[61] Christian Spengler, Erik Maikranz, Ludger Santen, and Karin Jacobs. Modelling bacterial adhesion to unconditioned abiotic surfaces. *Frontiers in Mechanical Engineering*, 7:23, 2021.

[62] Peter Loskill, Hendrik Hähl, Nicolas Thewes, Christian Titus Kreis, Markus Bischoff, Mathias Herrmann, and Karin Jacobs. Influence of the subsurface composition of a material on the adhesion of staphylococci. *Langmuir*, (18):7242–7248, 05 2012. doi: 10.1021/la3004323. URL `https://doi.org/10.1021/la3004323`.

[63] P.G. de Gennes. Polymers at an interface; a simplified view. *Advances in Colloid and Interface Science*, 27(3):189 – 209, 1987. ISSN 0001-8686. doi: https://doi.org/10.1016/0001-8686(87)85003-0. URL `http://www.sciencedirect.com/science/article/pii/0001868687850030`.

[64] Nicolas Thewes, Alexander Thewes, Peter Loskill, Henrik Peisker, Markus Bischoff, Mathias Herrmann, Ludger Santen, and Karin Jacobs. Stochastic binding of staphylococcus aureus to hydrophobic surfaces. *Soft Matter*, 11:8913–8919, 2015. doi: 10.1039/C5SM00963D. URL `http://dx.doi.org/10.1039/C5SM00963D`.

[65] Y Chen, W Norde, H C van der Mei, and H J Busscher. Bacterial Cell Surface Deformation under External Loading. *mBio*, 3(6):e00378–12, 2012.

[66] Peter Loskill, Pedro M Pereira, Philipp Jung, Markus Bischoff, Mathias Herrmann, Mariana G Pinho, and Karin Jacobs. Reduction of the peptidoglycan crosslinking causes a decrease in stiffness of the staphylococcus aureus cell envelope. *Biophysical journal*, 107(5):1082–1089, 2014.

[67] A Onur Sergici, George G Adams, and Sinan Müftü. Adhesion in the contact of a spherical indenter with a layered elastic half-space. *Journal of the Mechanics and Physics of Solids*, 54(9):1843–1861, 2006.

[68] Gheorghe Stan and George G Adams. Adhesive contact between a rigid spherical indenter and an elastic multi-layer coated substrate. *International journal of solids and structures*, 87:1–10, 2016.

[69] Y Chen, A K Harapanahalli, H J Busscher, W Norde, and H C van der Mei. Nanoscale Cell Wall Deformation Impacts Long-Range Bacterial Adhesion Forces on Surfaces. *Applied and Environmental Microbiology*, 80(2):637–643, 2014.

[70] Raimondas Jasevičius, Romas Baronas, and Harald Kruggel-Emden. Numerical modelling of the normal adhesive elastic-plastic interaction of a bacterium. *Advanced Powder Technology*, 26(3):742 – 752, 2015. ISSN 0921-8831. doi: https://doi.org/10.1016/j.apt.2015.04.010. URL `http://www.sciencedirect.com/science/article/pii/S0921883115000862`. Special issue of the 7th World Congress on Particle Technology.

[71] IG Goryacheva and Yu Yu Makhovskaya. Adhesive interaction of elastic bodies. *Journal of Applied Mathematics and Mechanics*, 65(2):273–282, 2001.

[72] Raimondas Jasevičius and Harald Kruggel-Emden. Numerical modelling of the sticking process of a s. aureus bacterium. *International Journal of Adhesion and Adhesives*, 77:15 – 28, 2017. ISSN 0143-7496. doi: https://doi.org/10.1016/j.ijadhadh.2017.03.015. URL `http://www.sciencedirect.com/science/article/pii/S0143749617300660`.

[73] Jelmer Sjollema, Henny C. van der Mei, Connie L. Hall, Brandon W. Peterson, Joop de Vries, Lei Song, Ed D. de Jong, Henk J. Busscher, and Jan J. T. M. Swartjes. Detachment and successive re-attachment of multiple, reversibly-binding tethers result in irreversible bacterial adhesion to surfaces. *Scientific Reports*, 7(1):4369, 2017. doi: 10.1038/s41598-017-04703-8. URL `https://doi.org/10.1038/s41598-017-04703-8`.

[74] Rebecca van der Westen, Jelmer Sjollema, Robert Molenaar, Prashant K. Sharma, Henny C. van der Mei, and Henk J. Busscher. Floating and tether-coupled adhesion of bacteria to hydrophobic and hydrophilic surfaces. *Langmuir*, 34 (17):4937–4944, 05 2018. doi: 10.1021/acs.langmuir.7b04331. URL `https://doi.org/10.1021/acs.langmuir.7b04331`.

[75] Nicolas Thewes, Peter Loskill, Philipp Jung, Henrik Peisker, Markus Bischoff, Mathias Herrmann, and Karin Jacobs. Hydrophobic interaction governs unspecific adhesion of staphylococci: a single cell force spectroscopy study. *Beilstein Journal of Nanotechnology*, 5:1501–1512, 2014. ISSN 2190-4286. doi: 10.3762/bjnano.5.163.

[76] Sassan Ostvar and Brian D. Wood. Multiscale model describing bacterial adhesion and detachment. *Langmuir*, 32(20):5213–5222, 05 2016. doi: 10.1021/acs.langmuir.6b00882. URL `https://doi.org/10.1021/acs.langmuir.6b00882`.

[77] Christian Spengler, Nicolas Thewes, Philipp Jung, Markus Bischoff, and Karin Jacobs. Determination of the nano-scaled contact area of staphylococcal cells. *Nanoscale*, 9:10084–10093, 2017. doi: 10.1039/C7NR02297B. URL `http://dx.doi.org/10.1039/C7NR02297B`.

[78] Christian Spengler, Friederike Nolle, Johannes Mischo, Thomas Faidt, Samuel Grandthyll, Nicolas Thewes, Marcus Koch, Frank Müller, Markus Bischoff, Michael Andreas Klatt, and Karin Jacobs. Strength of bacterial adhesion on nanostructured surfaces quantified by substrate morphometry. *Nanoscale*, 11: 19713–19722, 2019. doi: 10.1039/C9NR04375F. URL `http://dx.doi.org/10.1039/C9NR04375F`.

[79] M Matsushita, J Wakita, H Itoh, Ismael Rafols, T Matsuyama, H Sakaguchi, and M Mimura. Interface growth and pattern formation in bacterial colonies. *Physica A: Statistical Mechanics and its Applications*, 249(1):517 – 524, 1998. ISSN 0378-4371. doi: https://doi.org/10.1016/S0378-4371(97)00511-6. URL `http://www.sciencedirect.com/science/article/pii/S0378437197005116`.

[80] A. M. Lacasta, I. R. Cantalapiedra, C. E. Auguet, A. Peñaranda, and L. Ramírez-Piscina. Modeling of spatiotemporal patterns in bacterial colonies. *Phys. Rev. E*, 59:7036–7041, Jun 1999. doi: 10.1103/PhysRevE.59.7036. URL `https://link.aps.org/doi/10.1103/PhysRevE.59.7036`.

[81] Tamás Vicsek, Miklós Cserző, and Viktor K Horváth. Self-affine growth of bacterial colonies. *Physica A: Statistical Mechanics and its Applications*, 167(2):315 – 321, 1990. ISSN 0378-4371. doi: https://doi.org/10.1016/0378-4371(90)90116-A. URL `http://www.sciencedirect.com/science/article/pii/037843719090116A`.

[82] Z Csahók, K Honda, E Somfai, M Vicsek, and T Vicsek. Dynamics of surface roughening in disordered media. *Physica A: Statistical Mechanics and its Applications*, 200(1-4):136–154, 1993.

[83] Albert-László Barabási. Dynamic scaling of coupled nonequilibrium interfaces. *Phys. Rev. A*, 46:R2977–R2980, Sep 1992. doi: 10.1103/PhysRevA.46.R2977. URL `https://link.aps.org/doi/10.1103/PhysRevA.46.R2977`.

[84] Juan A Bonachela, Carey D Nadell, João B Xavier, and Simon A Levin. Universality in bacterial colonies. *Journal of Statistical Physics*, 144(2):303–315, 2011.

[85] Silvia N. Santalla and Silvio C. Ferreira. Eden model with nonlocal growth rules and kinetic roughening in biological systems. *Phys. Rev. E*, 98:022405, Aug 2018. doi: 10.1103/PhysRevE.98.022405. URL `https://link.aps.org/doi/10.1103/PhysRevE.98.022405`.

[86] Silvia N. Santalla, Javier Rodríguez-Laguna, José P. Abad, Irma Marín, María del Mar Espinosa, Javier Muñoz García, Luis Vázquez, and Rodolfo Cuerno. Nonuniversality of front fluctuations for compact colonies of nonmotile bacteria. *Phys. Rev. E*, 98:012407, Jul 2018. doi: 10.1103/PhysRevE.98.012407. URL `https://link.aps.org/doi/10.1103/PhysRevE.98.012407`.

[87] M. A. C. Huergo, M. A. Pasquale, A. E. Bolzán, A. J. Arvia, and P. H. González. Morphology and dynamic scaling analysis of cell colonies with linear growth fronts. *Phys. Rev. E*, 82:031903, Sep 2010. doi: 10.1103/PhysRevE.82.031903. URL `https://link.aps.org/doi/10.1103/PhysRevE.82.031903`.

[88] M. A. C. Huergo, M. A. Pasquale, P. H. González, A. E. Bolzán, and A. J. Arvia. Dynamics and morphology characteristics of cell colonies with radially spreading growth fronts. *Phys. Rev. E*, 84:021917, Aug 2011. doi: 10.1103/PhysRevE.84.021917. URL `https://link.aps.org/doi/10.1103/PhysRevE.84.021917`.

[89] M. A. C. Huergo, M. A. Pasquale, P. H. González, A. E. Bolzán, and A. J. Arvia. Growth dynamics of cancer cell colonies and their comparison with noncancerous cells. *Phys. Rev. E*, 85:011918, Jan 2012. doi: 10.1103/PhysRevE.85.011918. URL `https://link.aps.org/doi/10.1103/PhysRevE.85.011918`.

[90] M. A. C. Huergo, N. E. Muzzio, M. A. Pasquale, P. H. Pedro González, A. E. Bolzán, and A. J. Arvia. Dynamic scaling analysis of two-dimensional cell colony fronts in a gel medium: A biological system approaching a quenched kardar-parisi-zhang universality. *Phys. Rev. E*, 90:022706, Aug 2014. doi: 10.1103/PhysRevE.90.022706. URL `https://link.aps.org/doi/10.1103/PhysRevE.90.022706`.

[91] Fred D Farrell, Matti Gralka, Oskar Hallatschek, and Bartlomiej Waclaw. Mechanical interactions in bacterial colonies and the surfing probability of beneficial mutations. *Journal of The Royal Society Interface*, 14(131):20170073, 2017.

[92] Oskar Hallatschek, Pascal Hersen, Sharad Ramanathan, and David R. Nelson. Genetic drift at expanding frontiers promotes gene segregation. *Proceedings of the National Academy of Sciences*, 104(50):19926–19930, 2007. ISSN 0027-8424. doi: 10.1073/pnas.0710150104.

[93] Kirill S Korolev, Joao B Xavier, David R Nelson, and Kevin R Foster. A quantitative test of population genetics using spatiogenetic patterns in bacterial colonies. *The American Naturalist*, 178(4):538–552, 2011.

[94] Oskar Hallatschek and David R Nelson. Life at the front of an expanding population. *Evolution: International Journal of Organic Evolution*, 64(1):193–206, 2010.

[95] Thomas O Masser and Daniel Ben-Avraham. Correlation functions for diffusion-limited annihilation, a+ a→ 0. *Physical Review E*, 64(6):062101, 2001.

[96] Farinaz Roshani and Mohammad Khorrami. Annihilation-diffusion processes: An exactly solvable model. *Journal of Mathematical Physics*, 43(5):2627–2635, 2002. doi: 10.1063/1.1466532. URL `https://aip.scitation.org/doi/abs/10.1063/1.1466532`.

[97] Ranjiva Munasinghe, R. Rajesh, Roger Tribe, and Oleg Zaboronski. Multi-scaling of the n-point density function for coalescing brownian motions. *Communications in Mathematical Physics*, 268(3):717–725, December 2006. ISSN 1432-0916. URL `https://doi.org/10.1007/s00220-006-0110-5`.

[98] Matti Gralka, Fabian Stiewe, Fred Farrell, Wolfram Möbius, Bartlomiej Waclaw, and Oskar Hallatschek. Allele surfing promotes microbial adaptation from standing variation. *Ecology Letters*, 19(8):889–898, 2016. doi: 10.1111/ele.12625.

[99] Liselotte Jauffred, Rebecca Munk Vejborg, Kirill S Korolev, Stanley Brown, and Lene B Oddershede. Chirality in microbial biofilms is mediated by close interactions between the cell surface and the substratum. *The ISME journal*, 11(7):1688–1701, 2017.

[100] Adnan Ali and Stefan Grosskinsky. Pattern formation through genetic drift at expanding population fronts. *Adv. Compl. Sys.*, 13(3):349–366, 2010. doi: 10.1142/S0219525910002578.

[101] Adnan Ali, Ellák Somfai, and Stefan Grosskinsky. Reproduction-time statistics and segregation patterns in growing populations. *Physical Review E*, 85(2):021923, 2012.

[102] B Derrida and R Dickman. On the interface between two growing eden clusters. *Journal of Physics A: Mathematical and General*, 24(4):L191, 1991.

[103] Sherry Chu, Mehran Kardar, David R. Nelson, and Daniel A. Beller. Evolution in range expansions with competition at rough boundaries. *Journal of Theoretical Biology*, 478:153 – 160, 2019. ISSN 0022-5193. doi: https://doi.org/10.1016/j.jtbi.2019.06.018. URL `http://www.sciencedirect.com/science/article/pii/S002251931930253X`.

[104] Adnan Ali, Robin C Ball, Stefan Grosskinsky, and Ellák Somfai. Scale-invariant growth processes in expanding space. *Physical Review E*, 87(2):020102, 2013.

[105] Adnan Ali, Robin C Ball, Stefan Grosskinsky, and Ellak Somfai. Interacting particle systems in time-dependent geometries. *Journal of Statistical Mechanics: Theory and Experiment*, 2013(09):P09006, 2013.

[106] Diana Fusco, Matti Gralka, Jona Kayser, Alex Anderson, and Oskar Hallatschek. Excess of mutational jackpot events in expanding populations revealed by spatial luria–delbrück experiments. *Nature communications*, 7:12760, 2016.

[107] Bruce R. Levin, Véronique Perrot, and Nina Walker. Compensatory mutations, antibiotic resistance and the population genetics of adaptive evolution in bacteria. *Genetics*, 154(3):985–997, 2000. ISSN 0016-6731. URL `https://www.genetics.org/content/154/3/985`.

[108] Oskar Hallatschek and K. S. Korolev. Fisher waves in the strong noise limit. *Phys. Rev. Lett.*, 103:108103, Sep 2009. doi: 10.1103/PhysRevLett.103.108103. URL `https://link.aps.org/doi/10.1103/PhysRevLett.103.108103`.

[109] Charles R Doering, Carl Mueller, and Peter Smereka. Interacting particles, the stochastic fisher–kolmogorov–petrovsky–piscounov equation, and duality. *Physica A: Statistical Mechanics and its Applications*, 325(1-2):243–259, 2003.

[110] Kirill S Korolev, Melanie J I Müller, Nilay Karahan, Andrew W Murray, Oskar Hallatschek, and David R Nelson. Selective sweeps in growing microbial colonies. *Physical Biology*, 9(2):026008, apr 2012. doi: 10.1088/1478-3975/9/2/026008. URL `https://doi.org/10.1088/1478-3975/9/2/026008`.

[111] Jona Kayser, Carl F Schreck, Matti Gralka, Diana Fusco, and Oskar Hallatschek. Collective motion conceals fitness differences in crowded cellular populations. *Nature ecology & evolution*, 3:125–134, December 2018. ISSN 2397-334X. doi: 10.1038/s41559-018-0734-9.

[112] Andrea Giometto, David R Nelson, and Andrew W Murray. Physical interactions reduce the power of natural selection in growing yeast colonies. *Proceedings of the National Academy of Sciences of the United States of America*, 115:11448–11453, November 2018. ISSN 1091-6490. doi: 10.1073/pnas.1809587115.

[113] Matti Gralka and Oskar Hallatschek. Environmental heterogeneity can tip the population genetics of range expansions. *Elife*, 8:e44359, 2019.

[114] Craig Watson, Paul Hush, Joshua Williams, Angela Dawson, Nikola Ojkic, Simon Titmuss, and Bartlomiej Waclaw. Reduced adhesion between cells and substrate confers selective advantage in bacterial colonies (a). *EPL (Europhysics Letters)*, 123(6):68001, 2018.

[115] Jing Yan, Carey D Nadell, Howard A Stone, Ned S Wingreen, and Bonnie L Bassler. Extracellular-matrix-mediated osmotic pressure drives vibrio cholerae biofilm expansion and cheater exclusion. *Nature communications*, 8(1):327, 2017.

[116] Chenyi Fei, Sheng Mao, Jing Yan, Ricard Alert, Howard A. Stone, Bonnie L. Bassler, Ned S. Wingreen, and Andrej Košmrlj. Nonuniform growth and surface friction determine bacterial biofilm morphology on soft substrates. *Proceedings of the National Academy of Sciences*, 117(14):7622–7632, 2020. ISSN 0027-8424. doi: 10.1073/pnas.1919607117. URL `https://www.pnas.org/content/117/14/7622`.

[117] Malcolm S. Steinberg. Reconstruction of tissues by dissociated cells. *Science*, 141 (3579):401–408, 1963. ISSN 0036-8075. doi: 10.1126/science.141.3579.401. URL `https://science.sciencemag.org/content/141/3579/401`.

[118] Albert K Harris. Is cell sorting caused by differences in the work of intercellular adhesion? a critique of the steinberg hypothesis. *Journal of theoretical biology*, 61(2):267–285, 1976.

[119] Cornelis Vink, Gloria Rudenko, and H. Steven Seifert. Microbial antigenic variation mediated by homologous DNA recombination. *FEMS Microbiology Reviews*, 36(5):917–948, 09 2012. ISSN 0168-6445. doi: 10.1111/j.1574-6976.2011.00321.x. URL `https://doi.org/10.1111/j.1574-6976.2011.00321.x`.

[120] J. J. Dong and S. Klumpp. Simulation of colony pattern formation under differential adhesion and cell proliferation. *Soft Matter*, 14:1908–1916, 2018.

[121] Erik Maikranz and Ludger Santen. Theoretical modelling of competitive microbial range expansion with heterogeneous mechanical interactions. *Physical Biology*, 2020.

[122] Johan H. van Heerden, Hermannus Kempe, Anne Doerr, Timo Maarleveld, Niclas Nordholt, and Frank J. Bruggeman. Statistics and simulation of growth of single bacterial cells: illustrations with b. subtilis and e. coli. *Scientific Reports*, 7 (1):16094, 2017. doi: 10.1038/s41598-017-15895-4. URL `https://doi.org/10.1038/s41598-017-15895-4`.

[123] Matthew Wolfgang, Peter Lauer, Hae-Sun Park, Laurent Brossay, Jacques Hébert, and Michael Koomey. Pilt mutations lead to simultaneous defects in competence for natural transformation and twitching motility in piliated neisseria gonorrhoeae. *Molecular Microbiology*, 29(1):321–330, 1998. doi: 10.1046/j.1365-2958.1998.00935.x. URL `https://onlinelibrary.wiley.com/doi/abs/10.1046/j.1365-2958.1998.00935.x`.

[124] Erik Maikranz, Christian Spengler, Nicolas Thewes, Alexander Thewes, Friederike Nolle, Philipp Jung, Markus Bischoff, Ludger Santen, and Karin Jacobs. Different binding mechanisms of staphylococcus aureus to hydrophobic and hydrophilic surfaces. *Nanoscale*, 12:19267–19275, 2020. doi: 10.1039/D0NR03134H. URL `http://dx.doi.org/10.1039/D0NR03134H`.

[125] Christian Spengler, Bernhard A. Glatz, Erik Maikranz, Markus Bischoff, Michael Andreas Klatt, Ludger Santen, Andreas Fery, and Karin Jacobs. The adhesion capability of s. aureus cells is heterogeneously distributed over the cell envelope. *bioRxiv*, 2021. doi: 10.1101/2021.01.05.425282. URL `https://www.biorxiv.org/content/early/2021/01/05/2021.01.05.425282`.

[126] Audrey Beaussart, Philippe Herman, Sofiane El-Kirat-Chatel, Peter N Lipke, Soňa Kucharíková, Patrick Van Dijck, and Yves F Dufrêne. Single-cell force spectroscopy of the medically important staphylococcus epidermidis-candida albicans interaction. *Nanoscale*, 5:10894–10900, November 2013. ISSN 2040-3372. doi: 10.1039/c3nr03272h.

[127] Henny C van der Mei, Minie Rustema-Abbing, Joop de Vries, and Henk J Busscher. Bond strengthening in oral bacterial adhesion to salivary conditioning films. *Applied and Environmental Microbiology*, 74(17):5511–5515, 2008.

[128] Philippe Herman, Sofiane El-Kirat-Chatel, Audrey Beaussart, Joan A Geoghegan, Timothy J Foster, and Yves F Dufrêne. The binding force of the staphylococcal adhesin sdrg is remarkably strong. *Molecular Microbiology*, 93:356–368, July 2014. ISSN 1365-2958. doi: 10.1111/mmi.12663.

[129] Cécile Feuillie, Cécile Formosa-Dague, Leanne MC Hays, Ophélie Vervaeck, Sylvie Derclaye, Marian P Brennan, Timothy J Foster, Joan A Geoghegan, and Yves F Dufrêne. Molecular interactions and inhibition of the staphylococcal biofilm-forming protein sdrc. *PNAS*, 114:3738–3743, April 2017. ISSN 1091-6490. doi: 10.1073/pnas.1616805114.

[130] Philippe Herman-Bausier, Cristina Labate, Aisling M Towell, Sylvie Derclaye, Joan A Geoghegan, and Yves F Dufrêne. Staphylococcus aureus clumping factor a is a force-sensitive molecular switch that activates bacterial adhesion. *Proceedings of the National Academy of Sciences of the United States of America*, 115:5564–5569, May 2018. ISSN 1091-6490. doi: 10.1073/pnas.1718104115.

[131] M Rief, M Gautel, F Oesterhelt, J M Fernandez, and H E Gaub. Reversible unfolding of individual titin immunoglobulin domains by afm. *Science*, 276:1109–1112, May 1997. ISSN 0036-8075. doi: 10.1126/science.276.5315.1109.

[132] F Oesterhelt, D Oesterhelt, M Pfeiffer, A Engel, HE Gaub, and DJ Müller. Unfolding pathways of individual bacteriorhodopsins. *Science*, 288:143–146, April 2000. ISSN 0036-8075. doi: 10.1126/science.288.5463.143.

[133] Cécile Formosa-Dague, Pietro Speziale, Timothy J Foster, Joan A Geoghegan, and Yves F Dufrêne. Zinc-dependent mechanical properties of staphylococcus aureus biofilm-forming surface protein sasg. *Proceedings of the National Academy of Sciences*, 113(2):410–415, 2016.

[134] Philippe Herman-Bausier, Claire Valotteau, Giampiero Pietrocola, Simonetta Rindi, David Alsteens, Timothy J Foster, Pietro Speziale, and Yves F Dufrêne. Mechanical strength and inhibition of the staphylococcus aureus collagen-binding protein cna. *mBio*, 7(5):e01529–16, 2016.

[135] Alexander Thewes. *Modellierung und Simulation von bakterieller Adhäsion und intrazellulärem Transport in realer Geometrie*. PhD thesis, Universität des Saarlandes, 2019.

[136] A F Oberhauser, P E Marszalek, H P Erickson, and J M Fernandez. The molecular elasticity of the extracellular matrix protein tenascin. *Nature*, 393:181–185, May 1998. ISSN 0028-0836. doi: 10.1038/30270.

[137] M Rief, J Pascual, M Saraste, and H E Gaub. Single molecule force spectroscopy of spectrin repeats: low unfolding forces in helix bundles. *Journal of molecular biology*, 286:553–561, February 1999. ISSN 0022-2836. doi: 10.1006/jmbi.1998.2466.

[138] Teun Vissers, Aidan T. Brown, Nick Koumakis, Angela Dawson, Michiel Hermes, Jana Schwarz-Linek, Andrew B. Schofield, Joseph M. French, Vasileios Koutsos, Jochen Arlt, Vincent A. Martinez, and Wilson C. K. Poon. Bacteria as living patchy colloids: Phenotypic heterogeneity in surface adhesion. *Science Advances*, 4(4), 2018. doi: 10.1126/sciadv.aao1170. URL `https://advances.sciencemag.org/content/4/4/eaao1170`.

[139] Marie-Cécilia Duvernoy, Thierry Mora, Maxime Ardré, Vincent Croquette, David Bensimon, Catherine Quilliet, Jean-Marc Ghigo, Martial Balland, Christophe Beloin, Sigolène Lecuyer, et al. Asymmetric adhesion of rod-shaped bacteria controls microcolony morphogenesis. *Nature communications*, 9(1):1–10, 2018.

[140] O. J. Meacock, A. Doostmohammadi, K. R. Foster, J. M. Yeomans, and W. M. Durham. Bacteria solve the problem of crowding by moving slowly. *Nature Physics*, 17(2):205–210, 2021. doi: 10.1038/s41567-020-01070-6. URL `https://doi.org/10.1038/s41567-020-01070-6`.

Appendix

A Characteristics of the Weibull distribution

The Weibull distribution (Weib(λ, k)) is defined by the probability density function ($t \geq 0$)

$$\rho(t) = \frac{k}{\lambda}\left(\frac{t}{\lambda}\right)^{k-1} e^{-\left(\frac{t}{\lambda}\right)^k} \ ,$$

where λ is termed the scale parameter and k the form parameter (see figure A1).

This distribution reduces to the exponential distribution for $k = 1$.

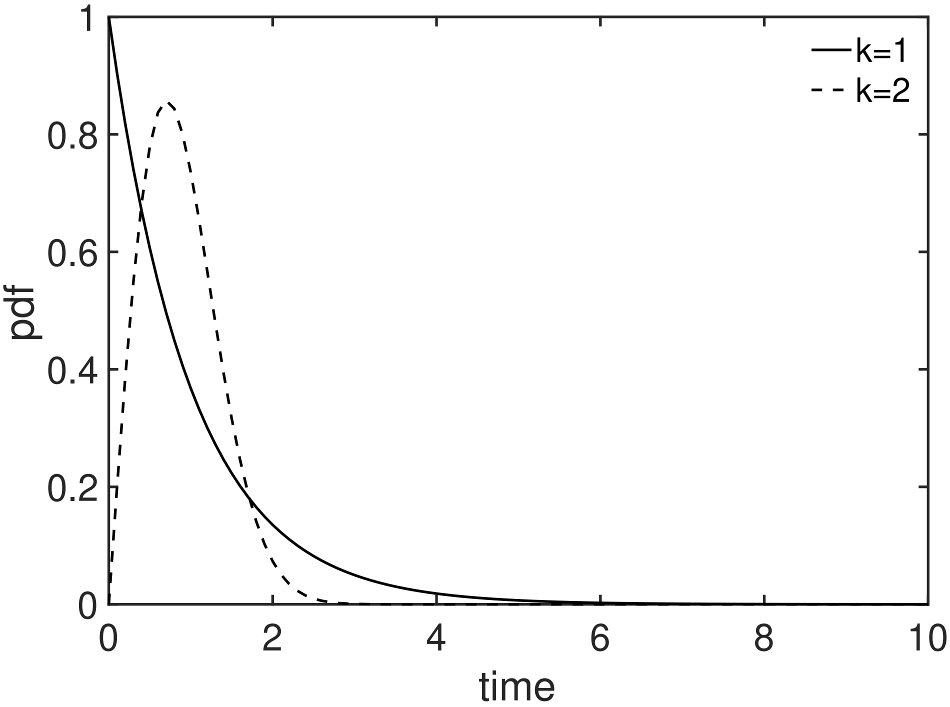

Figure A1: Probability density function of the Weibull distribution with scale parameter $\lambda = 1$ and shape parameter k. The figure and caption is reprinted from Maikranz and Santen [121].

The cumulative distribution function F and moments $\langle T^n \rangle$ can be derived by integration to be

$$\begin{aligned} F(t) &= 1 - e^{-\left(\frac{t}{\lambda}\right)^k} \\ \langle T^n \rangle &= \lambda^n \Gamma\left(1 + \frac{n}{k}\right) \ , \end{aligned}$$

where Γ is the Gamma function.

A.1 Minimum of Weibull distributed random variables

Let T_1 and T_2 be two independent Weibull distributed random variables $(\mathrm{Weib}(\lambda_1, k), \mathrm{Weib}(\lambda_2, k))$. Then $\min(T_1, T_2)$ is distributed according to

$$\begin{aligned} P\left[\min(T_1,T_2) \leq t\right] &= 1 - P\left[\min(T_1,T_2) > t\right] = 1 - P\left[T_1 > t, T_2 > t\right] = 1 - P\left[T_1 > t\right] P\left[T_2 > t\right] \\ &= 1 - \left(1 - F_1(t)\right)\left(1 - F_2(t)\right) \ , \end{aligned}$$

where I used in the second last step the independence of the random variables and in the last step the definition of the cumulative distribution F. Using F for Weibull distributed random variables I obtain

$$P\left[\min(T_1,T_2) \leq t\right] = 1 - e^{-\left(\frac{t}{\lambda_1}\right)^k} e^{-\left(\frac{t}{\lambda_2}\right)^k} = 1 - e^{-\left(\frac{t}{\lambda}\right)^k} \ ,$$

where $\lambda = 1/\sqrt[k]{\frac{1}{\lambda_1^k} + \frac{1}{\lambda_2^k}}$. This demonstrates that the minimum of two Weibull distributed random variables with identical form parameter is again Weibull distributed with the same form parameter k but new scale parameter λ. The probability of T_1 being the smaller random variable is

$$P\left[T_1 \leq T_2\right] = \int_0^\infty \rho_{T_1} \left(1 - F_{T_2}\right) dt \qquad \text{(A.1)}$$

$$\overset{u=\frac{t}{\lambda_1}}{=} \int_0^\infty k u^{k-1} e^{-u^k\left(1+\left(\frac{\lambda_1}{\lambda_2}\right)^k\right)} du \qquad \text{(A.2)}$$

$$= \frac{1}{1+\left(\frac{\lambda_1}{\lambda_2}\right)^k} \ . \qquad \text{(A.3)}$$

Note that for $\lambda_1 = \lambda_2$ the k dependence is removed.

Lets consider now the minimum of l independent random variables which are Weibull distributed with identical scale parameter λ and form parameter k i.e. $\min(T_1, \ldots, T_l)$. It is obvious from the previous discussion that this variable is again Weibull distributed with form parameter k but scale parameter $\frac{\lambda}{\sqrt[k]{l}}$. Therefore, its mean value is

$$\langle \min(T_1, \ldots, T_l) \rangle = \frac{\lambda}{\sqrt[k]{l}} \Gamma\left(1 + \frac{1}{k}\right) \ . \qquad \text{(A.4)}$$

For the exponential distribution ($k = 1$) this simplifies to the well known result $\langle \min(T_1, \ldots, T_l) \rangle_{k=1} = \frac{\lambda}{l}$.

Now, lets compare the mean value of $\min(T_1, \ldots, T_l)$ for $k = 2$ to $k = 1$ (see figure A2). Noting that $\Gamma\left(\frac{3}{2}\right) = \frac{\sqrt{\pi}}{2}$ leads to the observation that the mean value for $k = 2$ is smaller for $l = 1$ but larger for $l \geq 2$.

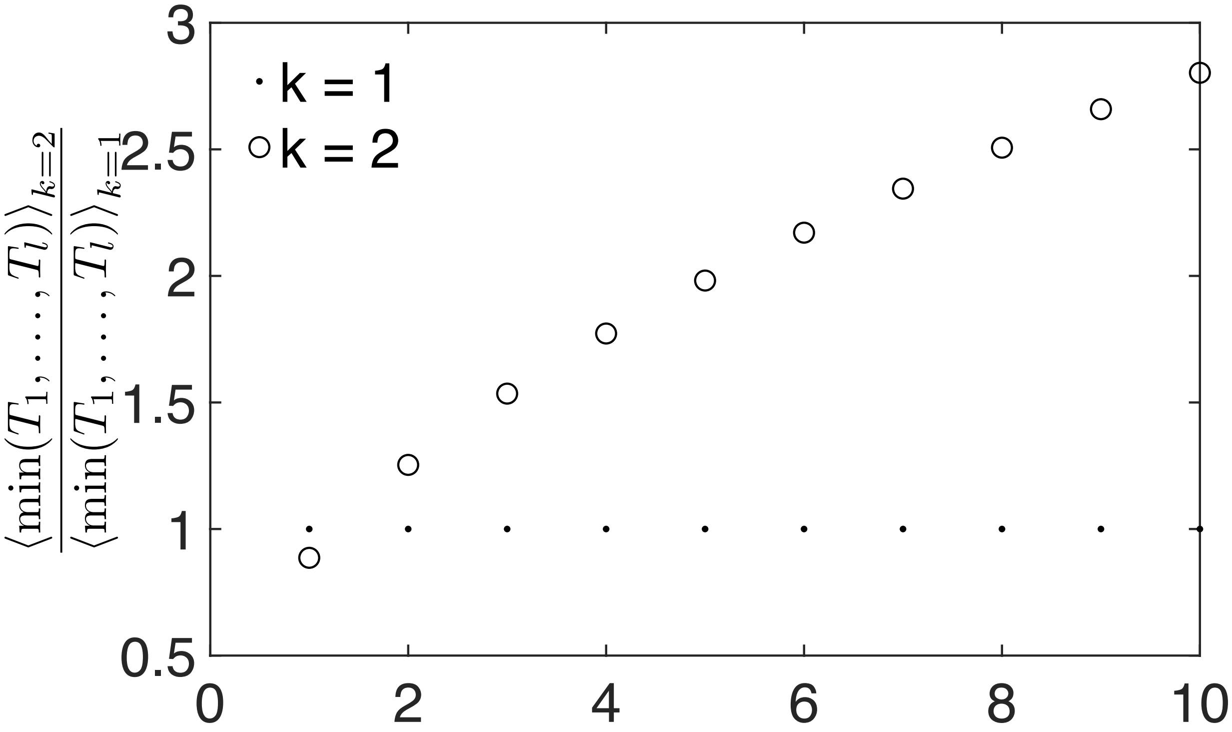

Figure A2: Relative value of the mean of l independent Weibull distributed random variables with form parameter k to form parameter $k = 1$.

B Pseudo code for SCFS simulations

Reprinted from the supplemental material of Maikranz et al. [124]:

Algorithm 1 SCFS-Simulation

```
procedure Initialization

procedure Approach
    while force trigger not reached & step possible do
        cantileverHeight ← cantileverHeight − stepSize
        procedure MainUpdates
        if wantToMeausure then
            procedure take measurement
        end
    end

procedure Waiting
    for given number of iterations do
        procedure MainUpdates
    end

procedure Retraction
    while inital cantilverHeight is not reached do
        cantileverHeight ← cantileverHeight + stepSize
        procedure MainUpdates
        if wantToMeausure then
            procedure take measurement
        end
    end
```

```
procedure MainUpdates
    for 200 iterations do
        for number of macromolecules do
            chose a random macromolecule & propose a random change in the stretch $l \mapsto l + U\Delta l$ where U is uniformly distributed in [−1,1]
            if proposed length and distance to surface > 0 then
                accept $l$ according to Metropolis algorithm
            end
            if macromolecule in range of surface potential then
                if macromolecule is attached then
                    bind with probability $e^{-H}$
                else
                    unbind with probability $e^{-(H+V)}$
                end
            else
                unbind
            end
        end
        update bacterium position by force balance of cantilever and all bound macromolecules via bisection and threshold $10^{-4}$ nm
    end
```

C Tangential contact

Every point on the bacterium is defined by

$$\vec{r} = R \begin{pmatrix} \cos\varphi \sin\Theta \\ \sin\varphi \sin\Theta \\ \cos\Theta + 1 \end{pmatrix} + \begin{pmatrix} x \\ 0 \\ s \end{pmatrix} ,$$

where (R, Θ, φ) are the usual spherical coordinates x the relative position along the surface and s the distance from the minimum of the surface to the bottom of the bacterium. In order to bring the bacterium from above the surface into tangential contact I need to compute the maximal distance s such that

$$s = h(r_x, r_y) - R\,(\cos\Theta + 1) + \ \forall \varphi, \Theta \ .$$

Therefore, I define $f := h(r_x, r_y) - R\,(\cos\Theta + 1)$ and compute the maximum value of f in terms of Θ, φ. If h is a constant this problem is obviously solved for $\Theta = \pi$ and arbitrary φ. Therefore, in the following I assume a non constant h and additionally $\partial_2 h = 0$. Thus I will write $\partial_1 h = h'$. The necessary conditions for the extrema are:

$$\frac{\partial f}{\partial \Theta} = R\left(\cos\varphi\cos\Theta\ h' + \sin\Theta\right) \overset{!}{=} 0 \tag{C.1}$$

$$\frac{\partial f}{\partial \varphi} = -R\sin\Theta\sin\varphi\ h' \overset{!}{=} 0 \tag{C.2}$$

Since h is non constant I obtain from equation C.2

1. $\sin\Theta = 0 \Rightarrow \Theta = 0, \pi$
2. $\sin\varphi = 0 \Rightarrow \varphi = 0, \pi$

Plugging these into equation C.1 gives:

1. $\sin\Theta = 0$

   $$\Rightarrow \cos\varphi\ h'(x) = 0$$

   from this follows

   a) $h'(x) \neq 0$: $\cos\varphi = 0$

   b) $h'(x) = 0$: no condition for φ

2. $\sin\varphi = 0$

   $$\Rightarrow \pm\cos\Theta\ h'(x \pm R\sin\Theta) + \sin\Theta = 0$$

   One can distinguish:

   a) $\sin\Theta = 0$

   $$\Rightarrow h'(x) = 0$$

   This is the same situation as 1b. Note that therefore $\sin\varphi = 0$ is not a restricting condition.

   b) $\sin\Theta \neq 0$

   $$\pm\cot\Theta\ h'(x \pm R\sin\Theta) + 1 = 0$$

Putting all together I distinguish the following cases:

1. $\Theta = 0, \pi$
   - $h'(x) \neq 0$: $\varphi = \frac{\pi}{2}, \frac{3\pi}{2}$
   - $h'(x) = 0$: no condition for φ
2. $\pm \cot\Theta \ h'(x \pm R\sin\Theta) + 1 = 0$, $\varphi = 0, \pi$

Now I show that classifying the extrema by the Hessian is not straightforward:

$$\begin{aligned}
\frac{\partial^2 f}{\partial \Theta^2} &= R\left(R\cos^2\varphi\cos^2\Theta\ h'' + \cos\Theta - \cos\varphi\sin\Theta h'\right)\\
\frac{\partial^2 f}{\partial \varphi^2} &= -R\sin\Theta\left(\cos\varphi h' - R\sin\Theta\sin^2\varphi\ h''\right)\\
\frac{\partial^2 f}{\partial \Theta \partial \varphi} &= -R\sin\varphi\left(\cos\Theta h' + R\cos\varphi\cos\Theta\sin\Theta\ h''\right)
\end{aligned}$$

So the Hessian

$$H = \begin{pmatrix} \frac{\partial^2 f}{\partial \Theta^2} & \frac{\partial^2 f}{\partial \Theta \partial \varphi} \\ \frac{\partial^2 f}{\partial \Theta \partial \varphi} & \frac{\partial^2 f}{\partial \varphi^2} \end{pmatrix}$$

is

1. $\Theta = 0, \pi$

   $$H = \begin{pmatrix} R^2\cos^2\varphi\ h'' \pm R & \mp R\sin\varphi h'(x) \\ \mp R\sin\varphi h'(x) & 0 \end{pmatrix}$$

   And therefore $\det H = -\left(R\sin\varphi h'(x)\right)^2$. Ergo

   - $h'(x) \neq 0$: $\varphi = \frac{\pi}{2}, \frac{3\pi}{2}$, $\det H < 0$, $H_{xx} = \pm R$, and therefore a saddle point.
   - $h'(x) = 0$: no condition for φ, $\det H = 0$ and therefore inconclusive.

2. $\pm \cot\Theta \ h'(x \pm R\sin\Theta) + 1 = 0$, $\varphi = 0, \pi$

$$\begin{aligned}
H &= \begin{pmatrix} R\left(R\cos^2\Theta h''(x \pm R\sin\Theta) + \cos\Theta \mp \sin\Theta h'(x \pm R\sin\Theta)\right) & 0 \\ 0 & \mp R\sin\Theta h'(x \pm R\sin\Theta) \end{pmatrix}\\
&= \begin{pmatrix} R\left(R\cos^2\Theta h''(x \pm R\sin\Theta) + \cos\Theta + R\frac{\sin^2\Theta}{\cos\Theta}\right) & 0 \\ 0 & R\frac{\sin^2\Theta}{\cos\Theta} \end{pmatrix}
\end{aligned}$$

> and $\det H$ is quite complicated. Since $H_{\varphi\varphi} = R\frac{\sin^2\Theta}{\cos\Theta}$ and we know from geometry that the constricting theta should be $\frac{\pi}{2} \leq \Theta \leq \pi$, there exists only a maximum if $H_{\Theta\Theta} < 0$.

Since the direct classification of the extrema is difficult the best method is to compute f for all (Θ, φ) which extremize f and subsequently obtain the largest value. Therefore, the bacterium is placed in tangential contact for

$$\begin{aligned} s &= \max\{h(x) - 2R, h(x), h(x \pm R\sin\Theta) - R\,(\cos\Theta + 1)\} \\ &= \max\{h(x), h(x \pm R\sin\Theta) - R\,(\cos\Theta + 1)\}\ , \end{aligned}$$

where Θ needs to be determined from $\pm\cot\Theta\ h'(x \pm R\sin\Theta) + 1 = 0$.

D Minimal distance to surface

To find for a given position above the surface (x_p, y_p, z_p) the point on the surface with the shortest distance between them, I minimize in principle the euclidean distance d of (x_p, y_p, z_p) and an arbitrary surface point (x, y, z) under the condition that $z = h(x, y)$. For calculations, it's however easier to minimize directly $E = d^2$. This is possible because the square root is strictly monotonous. The squared euclidean distance with Lagrange multiplier λ is

$$E = (x - x_p)^2 + (y - y_p)^2 + (z - z_p)^2 + \lambda\,(z - h(x, y)) \ .$$

Taking the derivatives leads to

$$\begin{aligned}
\frac{\partial E}{\partial x} &= 2\,(x - x_p) - \lambda h_x \overset{!}{=} 0 \Rightarrow x = \frac{\lambda}{2} h_x + x_p \\
\frac{\partial E}{\partial y} &= 2\,(y - y_p) - \lambda h_y \overset{!}{=} 0 \Rightarrow y = \frac{\lambda}{2} h_y + y_p \\
\frac{\partial E}{\partial z} &= 2\,(z - z_p) + \lambda \overset{!}{=} 0 \Rightarrow \lambda = 2\,(z_p - z) \\
\frac{\partial E}{\partial \lambda} &= z - h(x, y) \overset{!}{=} 0 \Rightarrow z = h(x, y)
\end{aligned}$$

from which

$$\begin{aligned}
x &= x_p + (z_p - h(x, y))\, h_x(x, y) \\
y &= y_p + (z_p - h(x, y))\, h_y(x, y) \\
z &= h(x, y)
\end{aligned}$$

is obtained. These are implicit equations in (x, y). The corresponding shortest distance is

$$d = \sqrt{E(x, y, z)} = |z_p - h(x, y)| \sqrt{h_x^2(x, y) + h_y^2(x, y) + 1} \ .$$

Acknowledgement

Foremost, I would like to thank my supervisor Prof. Santen for his constant support, discussions and advice. I have greatly benefited from his expertise, the academic freedom he provided and his ability to bring a research project to a publishable outcome. To this end, I also like to mention my research collaborators. In particular, I like to extend my gratitude to Prof. Jacobs and Dr. Christian Spengler, for the fruitful discussions and hard work in drafting and improving the manuscripts.

Furthermore, I like to thank the German Research Foundation (DFG) for financial support within the Collaborative Research Center SFB 1027, and especially the integrated research training group (IRTG) for organising informative seminars, training and summer camps. In particular, I like to thank Dr. Hendrik Hähl for his constant efforts in improving the research environment.

Just as importantly, I like to thank my colleagues, especially Dr. Robin Jose, Gina Monzon, Daniel Bahr, Neda Safari and Jonas Bosche for the pleasant working environment, discussions, relentless proofreading and just occasional laughs.

Sapere aude!